論文 / 著書情報
Article / Book Information

題目(和文)	分子設計に基づく強い交換相互作用及び強いπ-d相互作用
Title(English)	Strong exchange magnetic interaction and strong π-d interaction achieved by molecular design
著者(和文)	西條純一
Author(English)	
出典(和文)	学位:博士(理学), 学位授与機関:東京工業大学, 報告番号:甲第5621号, 授与年月日:2004年3月26日, 学位の種別:課程博士, 審査員:
Citation(English)	Degree:Doctor (Science), Conferring organization: Tokyo Institute of Technology, Report number:甲第5621号, Conferred date:2004/3/26, Degree Type:Course doctor, Examiner:
学位種別(和文)	博士論文
Type(English)	Doctoral Thesis

Thesis

Strong exchange magnetic interaction and strong π-d interaction achieved by molecular design

A Thesis Submitted
to
Tokyo Institute of Technology
for
the Doctor's Degree in Science
(Hakushi (Rigaku))

by

Junichi NISHIJO

Department of Chemistry,
Graduate School of Science and Engineering
Tokyo Institute of Technology
March, 2004

Supervised by Professor Toshiaki Enoki

Acknowledgement

The present work has been carried out in Enoki and Fukui's laboratory in Tokyo Institute of Technology. The author is deeply grateful to Professor Toshiaki Enoki for suggesting the interesting subject of research, having the fruitful discussion and looking over the manuscript carefully.

The author is sincerely gratitude to Professor Masahiko Iyoda (Tokyo Metropolitan University) and the peoples in his laboratory for supplying the halogenated TTF donors EDT-TTFBr_2 and EDO-TTFI_2 in early stages of our research. The author is grateful to Professor Takehiko Mori (Tokyo Institute of Technology). The programs coded by Prof. Mori and collaborators for calculating molecular orbitals, overlap integrals and band structure are convenient and useful to understand the physical properties of the organic conductors. The author is indebted to Dr. Junichi Yamaura (Institute for Solid State Physics) for measuring the low-temperature X-ray analysis of (EDO-TTFBr_2)$_2$[M(mnt)$_2$]. The author expresses their gratitude to Dr. Kengo Enomoto and Dr. Shinya Uji (National Institute for Materials Science) for measuring the high-field magnetoresistance of (EDT-TTFBr_2)$_2$$FeBr_4$. The author also expresses his gratitude to professor Yuri Sushko (University of Kentucky) for measuring the high-pressure magnetic susceptibility of (EDO-TTFI_2)$_2$[Pt(mnt)$_2$]. The author wishes to thank Professor Hidekazu Tanaka (Tokyo Institute of Technology) for making the discussion on the results of EPR spectra of (EDT-TTFBr_2)$_2$$FeBr_4$ and the results of AC susceptibility of (EDO-TTFI_2)$_2$[Pt(mnt)$_2$].

The author appreciates Dr. Yoshiyuki Shibayama (Keio University) for appropriate guidance of the measurements. The author would like to appreciates Dr. Akira Miyazaki (Professor Enoki and Fukui's group) for his suitable suggestions on the synthesis and the characterizations of the samples. The author also appreciates Dr. Kazuyuki Takai for helpful advices in the measurement (Professor Enoki and Fukui's group). The author thanks to all the member of Professor Enoki and Fukui's group for their considerable discussion and support.

Finally, I would like to profoundly gratitudes to my relatives who make me as I am.

Publication list

"Molecular metals with ferromagnetic interaction between localized magnetic moments"

J. Nishijo, E. Ogura, J. Yamaura, A. Miyazaki, T. Enoki, T. Takano, Y. Kuwatani and M. Iyoda, *Solid State Communications*, **116**, 661 (2000).

"Ferromagnetic Interaction and Metallic Conductivity of Radical Ion Salts $(DIEDO)_2M(mnt)_2$ (M=Ni, Pt)"

J. Nishijo, E. Ogura, J. Yamaura, A. Miyazaki, T. Enoki, T. Takano, Y. Kuwatani, and M. Iyoda, *Synthetic Metals*, **133-134**, 539 (2003).

"Weak-ferromagnetism in molecular magnets based on transition metal complexes of crown thioether"

J. Nishijo, A. Miyazaki, T. Enoki, *Polyhedron*, **22**, 1755 (2003).

"Structure and Physical Properties of Molecular Magnets Based on Transition Metal Complexes of Crown Thioether"

J. Nishijo, A. Miyazaki and T. Enoki, *Bulletin of the Chemical Society of Japan*, *in press*, 2004.

"Strong π-d Interaction Based on Brominated TTF-type Donor EDT-$TTFBr_2$"

J. Nishijo, A. Miyazaki, T. Enoki, R. Watanabe, Y. Kuwatani and M. Iyoda, *Journal de Physique IV*, *in press*, 2004.

"Radical-Cation Salts Based on Brominated and Chlorinated Ethylenedioxytetrathiafulvalenes"

M. Iyoda, E. Ogura, T. Takano, K. Hara, Y. Kuwatani, T. Kato, N. Yoneyama, J. Nishijo, A. Miyazaki, T. Enoki, *Chemistry letters*, **6**, 680 (2000).

"Syntheses, structure and conducting properties of halogenated ethylenedioxy-tetrathiafulvalenes"

M. Iyoda, Y. Kuwatani, E. Ogura, K. Hara, H. Suzuki, T. Takano, K. Takeda, J.-I. Takano, K. Ugawa, M. Yoshida, H. Matsuyama, H. Nishikawa, I. Ikemoto, T. Kato, N. Yoneyama, J. Nishijo, A. Miyazaki and T. Enoki, *Heterocycles*, **54**, 833 (2001).

"Conducting Molecular Magnets based on TTF-Derivatives"

A. Miyazaki, K. Enomoto, K. Okabe, H. Yamazaki, J. Nishijo, T. Enoki, E. Ogura, K. Ugawa, Y. Kuwatani, and M. Iyoda, *Journal of Solid State Chemistry*, **168**, 547 (2002).

"π-d interaction-based molecular magnets in TTF-type salts"

A. Miyazaki, M. Enomoto, K. Enomoto, J. Nishijo, T. Enoki, E. Ogura, Y. Kuwatani, and M. Iyoda, *Molecular Crystals and Liquid Crystals*, **376**, 535 (2002).

"Magnetism in new classes of TTF-based charge transfer complexes"

T. Enoki, H. Yamazaki, K. Okabe, J. Nishijo, K. Enomoto, M. Enomoto, A. Miyazaki, *Molecular Crystals and Liquid Crystals*,379, 131 (2002).

"Novel Magnetism of EDO-TTFX_2 Salts (X = Br, I)"

T. Enoki, H. Yamazaki, J. Nishijo, K. Ugawa, E. Ogura, Y. Kuwatani, M. Iyoda, Y. V. Sushko, *Synthetic Metals*, **137**, 1173 (2003).

"π-d Interaction-based Molecular Magnets"

A. Miyazaki, K. Okabe, K. Enomoto, J. Nishijo, T. Enoki, F. Setifi, S. Golhen, L. Ouahab, T. Toita, J. Yamada, *Polyhedron*, **22**, 2227 (2003).

"Unconventional Properties of TTF-Based Organic Magnetic Conductors"

T. Enoki, M. Aimatsu, H. Yamazaki, K. Okabe, J. Nishijo, K. Enomoto, A. Miyazaki, K. Ugawa, E. Ogura, Y. Kuwatani, M. Iyoda, O. Naumenko and Y. V. Sushko, *NATO ASI series*, *in press*, 2004.

Contents

Chapter 1

Introduction

Since the discovery of high-photoconductivity in π-electron system such as anthracene, the investigation of organic conductors has brought us to the world of conducting organic materials with high-conductivity [1], metallic conductivity [2] and eventually superconductivity [3]. In the organic conductors, transfer integral t of the conductive electrons are nearly same as the on-site Coulomb interaction U [4, 5], therefore strong electron-electron interaction affects the transport and magnetic properties of the materials [6–10].

In recent years, hybrid "π-d system" including conductive π-electrons interacting with localized magnetic d-electrons has been intensively focused from the points of basic science of strongly correlated electron systems [11–13] and application for molecular or mesoscopic-size devices where the conductivity can be controlled by the magnetic field [14–18].

These organic magnetic conductors have several interesting electronic features;

- strong electron correlation and resulting in many-body effect,
- low dimensional molecular arrangement owing to the anisotropic orbitals of flat-shaped constituents organic molecules,
- easiness of systematic investigation by using chemical modification.

These features are interesting and useful from the view points mentioned above.

However, at the same time, organic magnetic conductors have some weak points in their electronic properties and applying them to electronic devices, in comparison with traditional inorganic materials;

- difficulty in obtaining a large crystal,
- hardship to obtain a hybrid system only by "mixing" two components, in a word, "alloy", which is a common method in traditional inorganic materials,
- instability at high temperature,
- weakness of the π-d interaction.

These weak points are not serious for the theoretical interest. But when the application to molecular-size device is considered, the weakness of π-d interaction is the critical problem, while the others are left out of consideration for using such a small electro-magnetic device. The molecule-based device is the promising way to construct multi-functional, smaller size devices [19, 20], therefore, the objective of the present work is placed most importantly to how to enhance the π-d interaction by using chemical modification.

Before discussing the features of the physical properties of the organic materials presented in this thesis, the theoretical background on magnetism, electronic structure and electron transport necessary in analyzing experimental results is presented in this chapter, in addition to the history on the research of molecule-based electronic and magnetic materials

1.1 Magnetism

In this section, we deal with the basis of magnetism to understand the magnetic properties of materials. Magnetism of a material is mainly comes from *spin* angular momentum $\boldsymbol{S}$ which is a genuine quantum internal degree of freedom and affected by orbital angular momentum $\boldsymbol{L}$ of the electron. The total angular momentum $\boldsymbol{J}$ of a magnetic atom such as transition metal ion (d-electron systems), lanthanide and actinoid (f-electron systems) is the sum of all unpaired electrons described as

$$\boldsymbol{J} = \sum_i \left(\boldsymbol{S}_i + \boldsymbol{L}_i\right), \tag{1.1}$$

where $\boldsymbol{S}_i$ and $\boldsymbol{L}_i$ are *spin* and orbital angular momentum of an electron i, and the summation takes over all magnetic electrons in the atom.

The value of the spin depends on the structure of an elementary particle, where an electron has $S = 1/2$ with the spin angular momentum being $+1/2$ (up) or $-1/2$ (down). The effect of the orbital angular momentum $\boldsymbol{L}$ is large in f-electron system, where the magnetism is subjected to the large $\boldsymbol{L}$ in the total angular momentum $\boldsymbol{J}$. Contrary to the f-electron system, the orbital angular momentum of the d-electron in transition metal complexes often disappears due to the interaction between the d-orbitals and the molecular orbitals of surrounding ligands, where the magnetism is well described as the sum of the spin angular momenta in individual electrons;

$$\boldsymbol{J} = \sum_i \boldsymbol{S}_i. \tag{1.2}$$

The magnetism of a single particle is simply described as a behavior of $\boldsymbol{J}$, where there is no interaction and no magnetic transition. On the other hand, the "magnets", which means the magnetic materials, shows the large variety of the useful and interesting magnetism thanks to inter-atom or inter-molecular spin-spin interactions.

1.1.1 Paramagnetism of localized magnetic moment

In this subsection, we treat the behavior of well-separated molecules having magnetic moment J in magnetic field B_0. In this case, the energies of the molecules

E are split in $2J$+1 states by magnetic field,

$$E = g\mu_{\rm B} B_0 J_{\rm z}, \tag{1.3}$$

where $J_{\rm z} = J, J-1, \cdots -J$ are the z-components of J. Since the thermal distribution in the energy levels is represented by the Boltzmann distribution, the magnetization M at a temperature T, in a field of B_0 is described as

$$M = Ng\mu_{\rm B} J B_{\rm J}(x), \tag{1.4}$$

where N is the number of spins and $B_{\rm J}(x)$ is the Brillouin function which is defined as

$$B_{\rm J}(x) = \frac{2J+1}{2J}\coth\frac{2J+1}{2J}x - \frac{1}{2J}\coth\frac{1}{2J}x, \tag{1.5}$$

$$x = \frac{Jg\mu_{\rm B}B_0}{k_{\rm B}T}. \tag{1.6}$$

At the limit $B_0 \ll 1/k_{\rm B}T$, eq.(1.4) can be simplified as

$$M = \frac{Ng^2\mu_{\rm B}^2 J(J+1)}{3k_{\rm B}T}B_0 = \frac{C}{T}B_0. \tag{1.7}$$

This equation means that the magnetization is in inverse proportion to the temperature. Eq. (1.7) is called *Curie law*.

1.1.2 Mean field approximation of ferromagnet

In the previous subsection, we assume that molecules have no magnetic interaction. However, in the actual case, there are some magnetic interactions with different strengths between the magnetic moments of molecules constituting a system. The spin Hamiltonian of such a magnetically interacting system in external magnetic field $\boldsymbol{B}_0$ is written as

$$H = \sum_i g\mu_{\rm B}\boldsymbol{B}_0\cdot\boldsymbol{S}_i - \sum_{\langle ij\rangle} 2J_{ij}\boldsymbol{S}_i\cdot\boldsymbol{S}_i, \tag{1.8}$$

where the first and the second terms are the Zeeman and exchange interaction* contributions, respectively, and the summation in the second term is taken for all pairs

*Of course, there are other interactions between spins, for example, dipole-dipole interaction, but they are weaker than the exchange magnetic interaction in usual cases.

of sites $\langle ij \rangle$. In general case, the eigen equation of the many-body Hamiltonian given as eq. (1.8) cannot be solved, therefore we must use some approximation.

Mean field approximation is one of the simplest approximations for such a spin Hamiltonian, in which we employ a mean field $\langle \boldsymbol{S}_j \rangle$ as a one-body parameter, which is the thermal average of spin $\boldsymbol{S}_i$, for considering the effect of surrounding spins of the spin concerned. Based on the approximation, we obtain the one body Hamiltonian,

$$H = \sum_i \left(g\mu_{\rm B} \boldsymbol{B}_0 - \sum_j J_{ij} \langle \boldsymbol{S}_j \rangle \right) \boldsymbol{S}_i. \tag{1.9}$$

The Hamiltonian (1.9) can be regarded as that of non-interacting paramagnetic spins in the effective magnetic field $\boldsymbol{B}$;

$$\boldsymbol{B} = \boldsymbol{B}_0 - \boldsymbol{B}_m(i), \tag{1.10}$$

$$\boldsymbol{B}_m(i) \equiv \frac{1}{g\mu_{\rm B}} \sum_j J_{ij} \langle \boldsymbol{S}_j \rangle, \tag{1.11}$$

where $\boldsymbol{B}_m(i)$ is a mean field at the site i. Therefore, eq. (1.9) can be easily solved as a one-body problem.

When we consider the case of $J_{ij} = J > 0$ (ferromagnetic), the magnetization of the spin system is obtained by substituting $\boldsymbol{B}_0 + \boldsymbol{B}_{\rm m}(i)$ for $\boldsymbol{B}_0$ of eq.(1.7)

$$M = \frac{C}{T}(\boldsymbol{B}_0 + \boldsymbol{B}_m(i)) \tag{1.12}$$

$$= \frac{C}{T}(\boldsymbol{B}_0 + \gamma M), \tag{1.13}$$

where

$$\gamma = \frac{1}{N g^2 \mu_{\rm B}^2} \sum_j J_{ij}. \tag{1.14}$$

Therefore, the magnetic susceptibility χ is described as

$$\chi = \frac{M}{B_0} = \frac{C}{T - \Theta} \quad (\Theta = \gamma C). \tag{1.15}$$

This equation means that the high temperature magnetic susceptibility of a ferromagnetic system is well fitted with eq.(1.15), *Curie-Weiss law*. Eventually, we can estimate the strength of the magnetic interaction J from the Weiss temperature Θ.

1.1.3 Mean field approximation of antiferromagnet

In the following discussion, we treat the case of antiferromagnet, $J_{\rm ij} = J < 0$, in which spins are allocated to two sublattices which are antiparallelly aligned to each other. At first, we treat the magnetization in the high temperature regime above N el temperature in an antiferromagnet which consists of two sublattices "a" and "b", the magnetizations of these sublattices being $\boldsymbol{M}_{\rm a}$ and $\boldsymbol{M}_{\rm b}$. Each sublattice is affected by the mean field $\boldsymbol{B}_m(i)$ at the sublattice i,

$$\boldsymbol{B}_{\rm m}(a) = \gamma_1 \boldsymbol{M}_{\rm b} + \gamma_2 \boldsymbol{M}_{\rm a}, \tag{1.16}$$

$$\boldsymbol{B}_{\rm m}(b) = \gamma_1 \boldsymbol{M}_{\rm a} + \gamma_2 \boldsymbol{M}_{\rm b}, \tag{1.17}$$

where

$$\gamma_1 \equiv \frac{1}{Ng^2\mu_{\rm B}^2} \sum_{i\in a, j\in b} J_{ij} \tag{1.18}$$

$$\gamma_2 \equiv \frac{1}{Ng^2\mu_{\rm B}^2} \sum_{i,j\in a} J_{ij} = \frac{1}{Ng^2\mu_{\rm B}^2} \sum_{i,j\in b} J_{ij}. \tag{1.19}$$

Therefore, the sublattice magnetizations in external field $\boldsymbol{B}_0$ are described as

$$\boldsymbol{M}_{\rm a} = \frac{C}{2T}\{\boldsymbol{B_0} + \boldsymbol{B}_{\rm m}(a)\} = \boldsymbol{B_0} + \gamma_1 \boldsymbol{M}_{\rm b} + \gamma_2 \boldsymbol{M}_{\rm a}, \tag{1.20}$$

$$\boldsymbol{M}_{\rm b} = \frac{C}{2T}\{\boldsymbol{B_0} + \boldsymbol{B}_{\rm m}(b)\} = \boldsymbol{B_0} + \gamma_1 \boldsymbol{M}_{\rm a} + \gamma_2 \boldsymbol{M}_{\rm b}. \tag{1.21}$$

Then, the susceptibility χ is calculated as

$$\chi = \frac{\boldsymbol{M}_{\rm a} + \boldsymbol{M}_{\rm b}}{\boldsymbol{B_0}} = \frac{C}{T-\theta}, \tag{1.22}$$

where

$$\theta = \frac{1}{2}(\gamma_2 + \gamma_1)C. \tag{1.23}$$

In ordinary antiferromagnet, $\gamma_1 \gg \gamma_2$, $\theta < 0$ and θ is in proportion to exchange interaction J.

In the next step, we treat the magnetization of antiferromagnet below N el temperature $T_{\rm N}$, where the magnetizations show angular dependence. In a lot of antiferromagnets, there is a spin anisotropy, the spins tend to direct to a peculiar direction called easy axis. When we apply the external magnetic field aligned perpendicular to the easy axis, it is obvious that the sublattice magnetization is

aligned in parallel to the sum of the external field and the internal field, $\boldsymbol{B}_0 + \boldsymbol{B}_\mathrm{m}$, as shown in Fig. 1.1. From the geometrical conditions,

$$|B_0| = 2|B_\mathrm{m}(a)| \sin\theta = 2\gamma_1 M \sin\theta. \tag{1.24}$$

At the same time, as the observed magnetization becomes $2M\sin\theta$, the magnetic susceptibility $\chi_\perp$ for B_0 $\perp$easy axis is given as

$$\chi_\perp = \frac{2M\sin\theta}{B_0} = \frac{1}{\gamma_1}, \tag{1.25}$$

which is independent of temperature. In contrast, the magnetization for B_0 $\|$easy axis is

$$M = \frac{N}{2} g\mu_\mathrm{B} S B_\mathrm{S}\left\{\frac{g\mu_\mathrm{B} S(B_\mathrm{m}(a) \pm B_0)}{kT}\right\}, \tag{1.26}$$

which decreases as the temperature is lowered, as shown in Fig. 1.2.

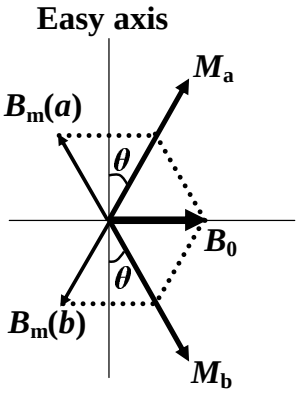

Fig. 1.1. The directions of the internal field of antiferromagnet. $\boldsymbol{M}_a$ and $\boldsymbol{M}_b$ are the magnetization of sublattices a and b, respectively. The magnetization of sublattice a (b) is aligned parallel to the sum of external magnetic field $\boldsymbol{B}_0$ and internal field $\boldsymbol{B}_{\rm m}(a)$ ($\boldsymbol{B}_{\rm m}(b)$) caused by sublattice b (a).

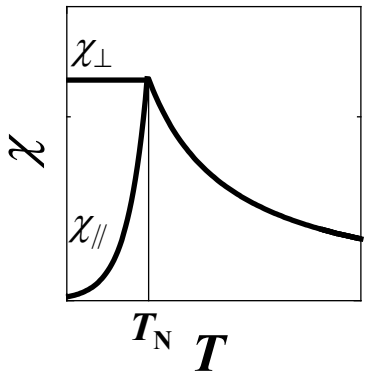

Fig. 1.2. The temperature dependence of magnetization of antiferromagnet.

1.1.4 Ferrimagnetism and weak-ferromagnetism

Ferrimagnets and weak-ferromagnets show, in spite of antiferromagnetic spin-spin interactions, remanent magnetization below transition temperature. The simplest case of the ferrimagnet is produced in case that an alternate chain of $S = 1$ and $S = 1/2$ has intra-chain antiferromagnetic interaction $J < 0$ (Fig. 1.3a)[†]. The sublattice magnetization of $S = 1/2$ spins cannot be compensated with the that of $S = 1$ spins due to the different spin sizes in the chain, where remanent magnetization is observed along the easy axis. The ferrimagnetism is produced also in a system, which consists of sublattices having different numbers of spins, as shown in Fig. 1.3b. In this case, the sizes of spins can be the same although the net magnetic moment of a sublattice is not equal to that of the other sublattice.

On the other hand, weak-ferromagnetism is caused by *spin canting* which means that the spins are directed in different directions between two sublattices (Fig. 1.3c). There are some origins of the spin canting, for example, Dzyaloshinskii-Moriya interaction [21], the coexistence of different magnetic sites having different anisotropy axes [22], etc. In ordinary weak-ferromagnets, the origin of the weak-ferromagnetism is Dzyaloshinskii-Moriya interaction where their remanent magnetization is quite small, the typical value of which is ca. few percent of the saturated magnetization.

[†]Strictly speaking, fully one-dimensional systems does not take any transition at finite temperature. But we consider "ordered one-dimensional system" for simplicity.

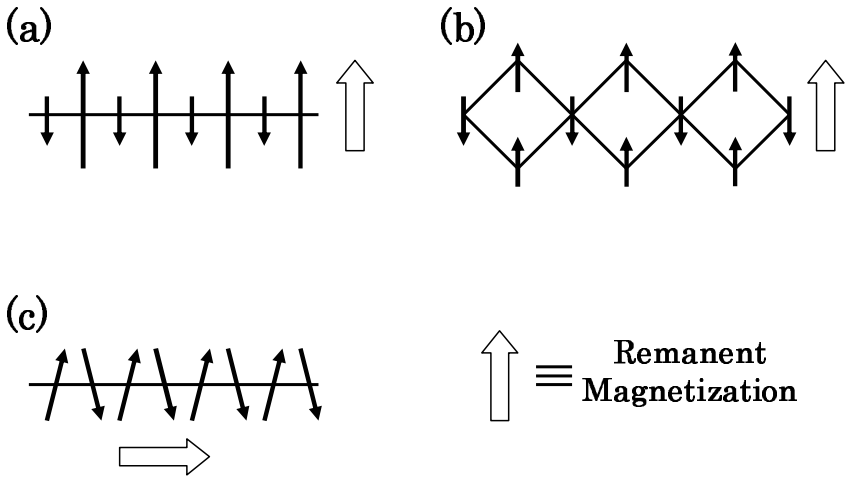

Fig. 1.3. Ferrimagnetism of multi-spin systems having **(a)** different spin sizes and **(b)** different numbers of spins in sublattices. **(c)** weak-ferromagnetism.

1.1.5 Magnetization curve

The behavior of the magnetization plotted as a function of magnetic field is called magnetization curve, which depends on the type of magnetism.

In ferromagnets below the Curie temperature, ferromagnetic domains are formed where the magnetization of each domain is directed randomly in the absence of the magnetic field, the total magnetization being zero to reduce the magnetic static energy. Since domains are stable in weak external field, only a small magnetization is observed in low field region. When the strong external magnetic field is applied, the domains having the magnetization parallel to the external field are expanded, and the magnetization rapidly increases. The magnetization does not disappear even when we remove the external field (Fig. 1.4).

The magnetization curves of antiferromagnets are quite different from those of ferromagnets. Below the N el temperature, the magnetic susceptibility depends on the direction of the external magnetic field. The magnetization in external magnetic field $H \parallel$ hard-axis slowly increases monotonously, as shown in eq. (1.25), and reaches saturated magnetization at $H_{\rm sat}$. In contrast, the magnetization in $H \parallel$ easy axis shows a sudden increase at the spin flop field $H_{\rm SF}$, in which the difference between the Zeeman energy $\boldsymbol{H} \cdot \boldsymbol{M}$ along the easy and the hard-axes surpasses the anisotropic energy of the spin resulting in the spins being rotated (Fig. 1.5). The spin flop field $H_{\rm SF}$ is described as

$$H_{\rm SF} = \sqrt{\frac{K}{\chi_\perp - \chi_\parallel}}, \tag{1.27}$$

where K, $\chi_\perp$ and $\chi_\parallel$ are the anisotropic energy and the susceptibility along the perpendicular and parallel to the easy axes, respectively.

The magnetization curves of ferrimagnets and weak-ferromagnets are described as the magnetization of antiferromagnet with remanent magnetization in $H \parallel$ easy-axis and $H \parallel$ hard-axis for ferrimagnets and weak-ferromagnets, respectively (Fig. 1.6). In the case of weak-ferromagnet, remanent magnetization is perpendicular to the easy axis. On the other hand, ferrimagnet shows a remanent magnetization in the easy axis.

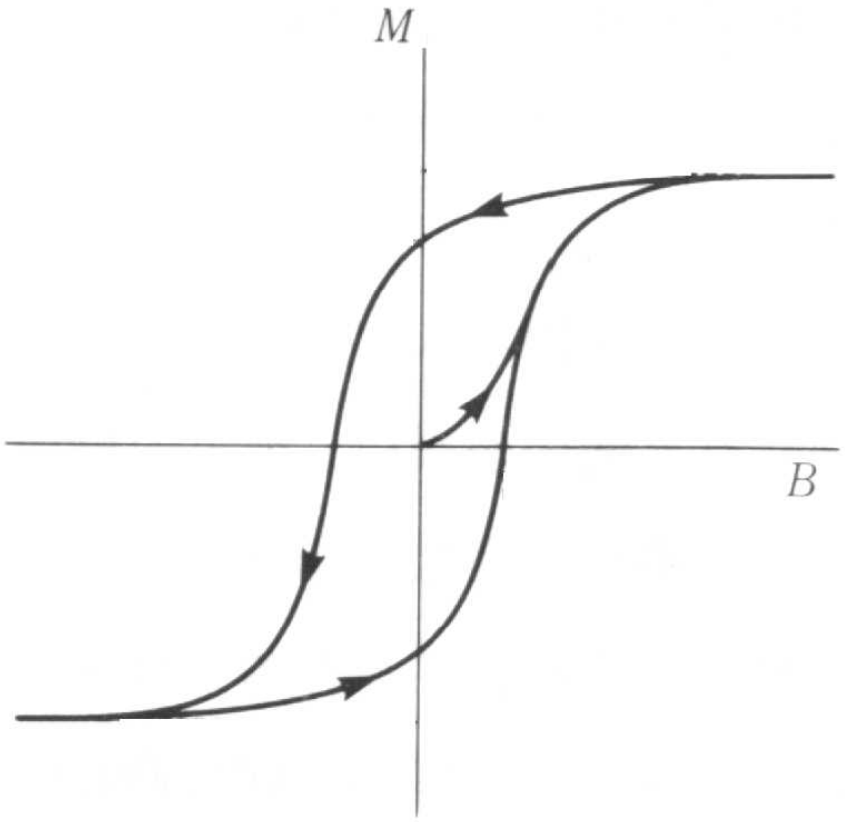

Fig. 1.4. The magnetization curve of ferromagnet.

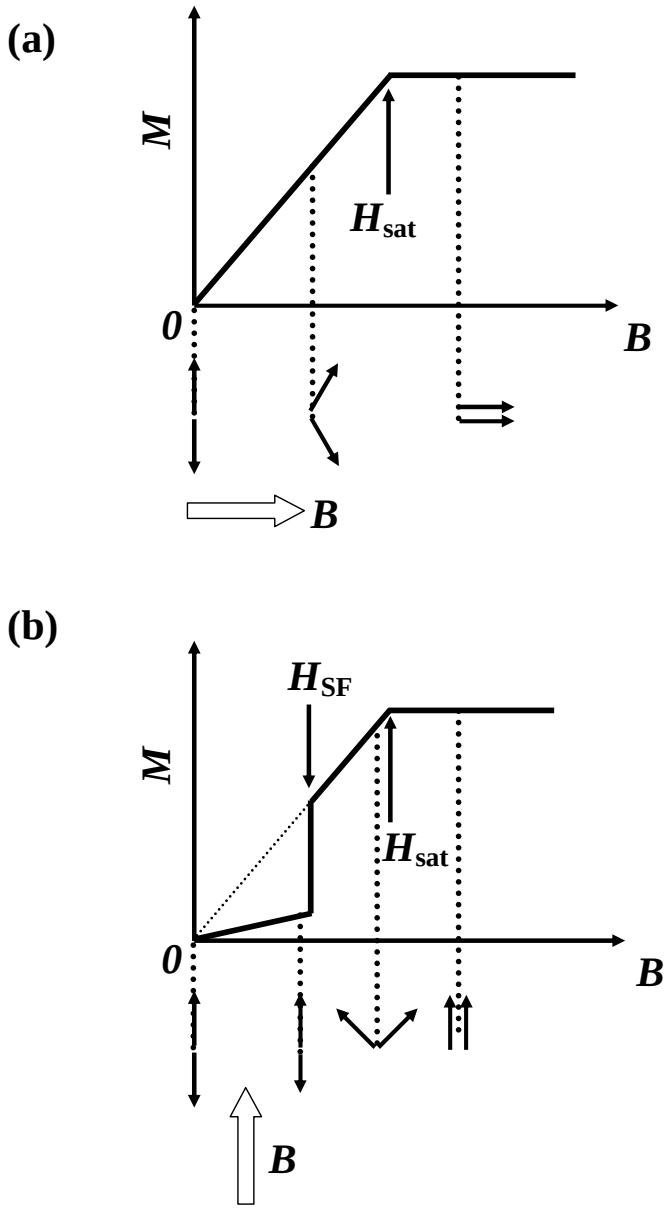

Fig. 1.5. The magnetization curve of antiferromagnet in **(a)** $H \parallel$ hard axis and **(b)** $H \parallel$ easy axis. Arrows below the magnetization curves, $H_{\rm SF}$ and $H_{\rm sat}$ represent the magnetization of the sublattices, spin flop field and saturation field, respectively.

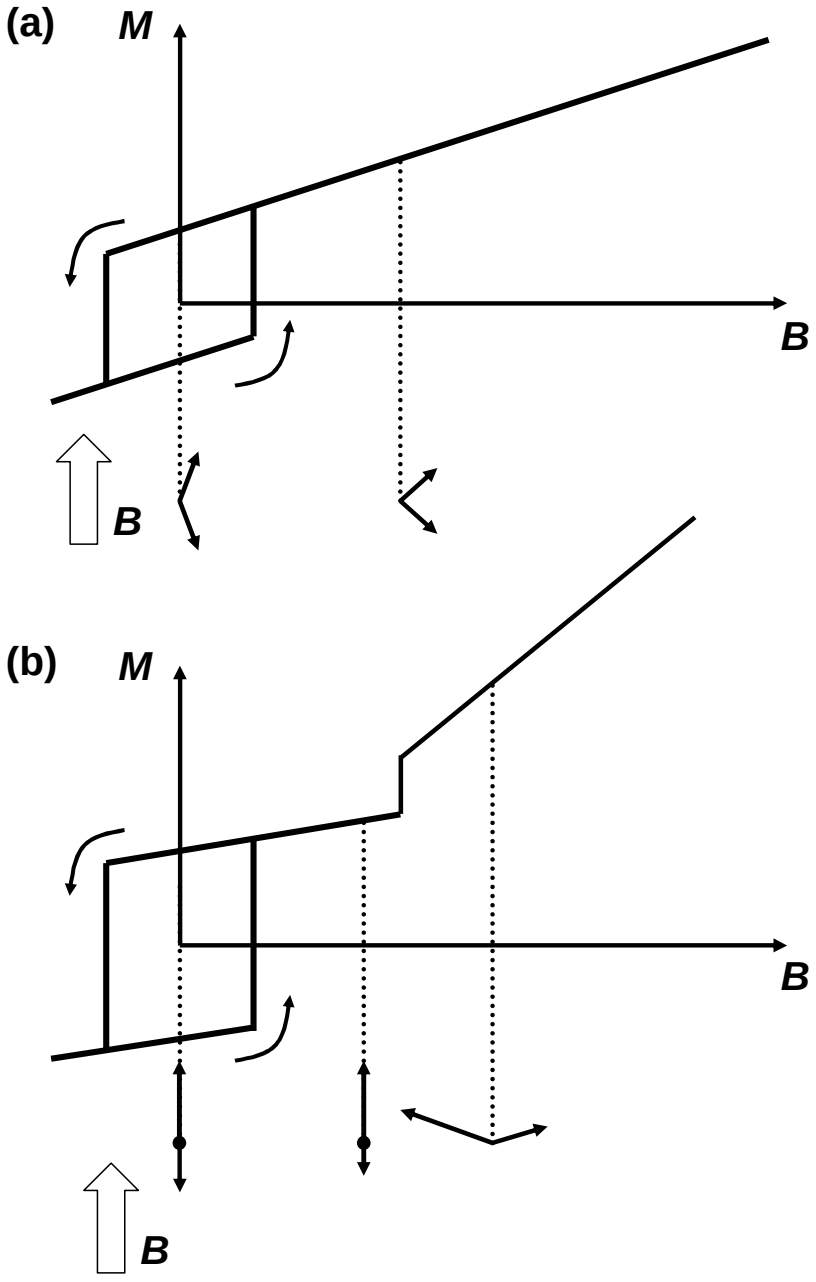

Fig. 1.6. The magnetization curves of **(a)** weak-ferromagnet in $H \parallel$ weak-ferromagnetic axis (hard axis) and that of **(b)** ferrimagnet in $H \parallel$ easy axis.

1.1.6 Low dimensional magnet

Generally speaking, most of traditional inorganic magnets are three-dimensional (3D) because its constituents are small and their atomic orbitals are isotropic. For example, in pure transition metals or isotropic transition metal oxides, spins can interact with each other in every direction. On the contrary to such traditional magnets, molecule-based magnets frequently show low-dimensionality. In the molecule-based magnets, interaction paths are governed by the anisotropic structure and/or inequable distribution of spin density of molecules.

The mean field approximation mentioned in the previous section takes the thermally averaged value of the magnetic moment for all the spins surrounding a spin concerned. This approximation is correct only when each spin interact with a large number of neighbouring spins. In other words, the mean field approximation neglects the spin fluctuation. The fluctuation is usually not so serious in three-dimensionally arranged magnets with a large numbers of neighbouring sites. However, the fluctuation plays an important role in low dimensional molecule-based magnets which have only a small number of neighbouring sites. Actually, the fluctuations in low dimensional systems suppress long range magnetic order. For example, it is revealed that 1D and 2D ferromagnetic and antiferromagnetic Heisenberg spin systems do not have long range ordering [23] [‡]. Furthermore, 1D Ising spin system has no magnetic long range ordering though the spin fluctuation affects less than Heisenberg systems [26].

Reflecting the presence of a spin fluctuation, the short range order prevails in the wide temperature range which is otherwise hidden behind the rapid development of the long range order, such as 3D magnets. Figure 1.7 shows the magnetic susceptibility χ of 2D magnet (BEDT-TTF)$_2$ICl$_2$ as an example of low dimensional magnets. In the χ vs temperature plot, a broad hump is observed as a short range order effect above N el temperature $T_{\mathrm{N}} = 22$ K. The correlation between neighbouring spins becomes strong as the temperature is lowered, resulting in the development of the short range order around the susceptibility hump at ca. 100 K.

[‡]Strictly speaking, 1D integer-spin system causes another type transition which is similar to the singlet-triplet transition [24]. Furthermore, it is noted that the case of 2D Heisenberg antiferromagnet is an unsolved problem. Some theoretical investigations claim that the system has finis transition temperature [25].

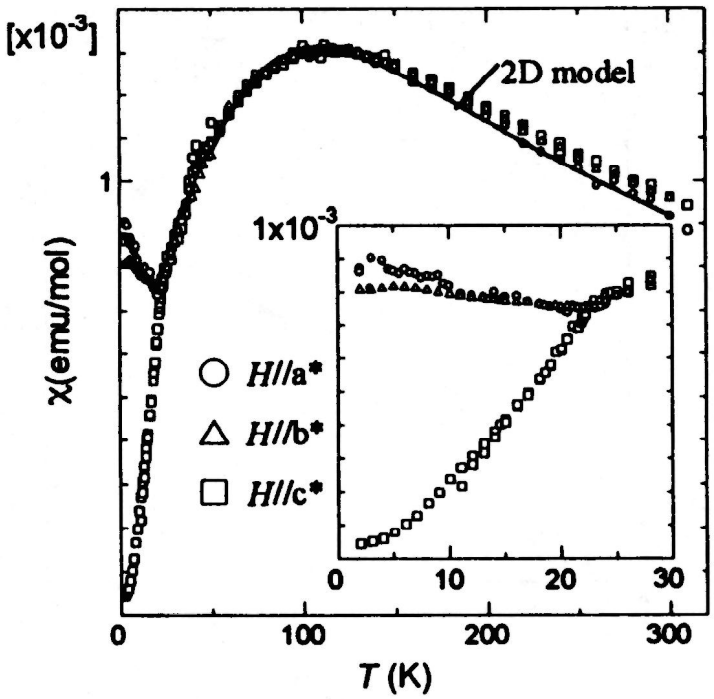

Fig. 1.7. The magnetic susceptibility of 2D magnet β'-(BEDT-TTF)$_2$ICl$_2$ [27].

1.1.7 Diamagnetism of core electrons

The susceptibility of a closed-shell atom only show Langevin diamagnetism. The diamagnetism is the consequence of the Larmour precession of electrons, where the value of diamagnetism is in proportion to external magnetic field and roughly in proportion to the number of electron of the atom. The diamagnetism of a molecule can be roughly estimated as

$$\chi_{\rm dia} = \sum \chi_{\rm atom} + \sum \chi_{\rm structure}, \tag{1.28}$$

where $\chi_{\rm atom}$, called the Pascal constant, is the diamagnetism of the constituent atom of the molecule, while $\chi_{\rm structure}$ is characteristic of molecular structure, such as alkyl chain, six-membered ring, etc.

1.1.8 Pauli paramagnetism of metals

In metallic materials, almost all of conducting electron spins in the conduction band do not show paramagnetism except electrons around the Fermi level, since the spins are antiparallelly coupled, in addition that the band width is much larger than the Zeeman energy caused by ordinary external magnetic field.

When we apply the external magnetic field B_0 to a metal, the electron density of state (DOS) $D(\varepsilon)$, DOS of up spin electron $D_\uparrow(\varepsilon)$ and down spin electron $D_\downarrow(\varepsilon)$ are changed as

$$D_\uparrow(\varepsilon) = \frac{1}{2}D(\varepsilon + \mu_{\rm B}B_0), \tag{1.29}$$

$$D_\downarrow(\varepsilon) = \frac{1}{2}D(\varepsilon - \mu_{\rm B}B_0), \tag{1.30}$$

because the energy of up spin electrons and down spin electrons are changed as $\varepsilon - \mu_{\rm B}B_0$ and $\varepsilon + \mu_{\rm B}B_0$, respectively. The total number of up spin electrons ($N_\uparrow$) and down spin electrons ($N_\downarrow$) are given by

$$N_\uparrow = \int D_\uparrow(\varepsilon) f(\varepsilon) d\varepsilon \tag{1.31}$$

$$N_\downarrow = \int D_\downarrow(\varepsilon) f(\varepsilon) d\varepsilon, \tag{1.32}$$

respectively, where $f(\varepsilon)$ is the Fermi distribution function and $N_\uparrow + N_\downarrow = N_{\rm total}$. In ordinary case, as the Zeeman energy $\mu_{\rm B}B_0 \ll \varepsilon$, eq. (1.29) and (1.30) can be

expanded as

$$D_{\uparrow} = \frac{1}{2}D(\varepsilon) + \frac{1}{2}\mu_{\mathrm{B}}B_0\frac{\partial D(\varepsilon)}{\partial \varepsilon}, \tag{1.33}$$

$$D_{\downarrow} = \frac{1}{2}D(\varepsilon) - \frac{1}{2}\mu_{\mathrm{B}}B_0\frac{\partial D(\varepsilon)}{\partial \varepsilon}. \tag{1.34}$$

The susceptibility of the conduction electron spins χ_{Pauli} is given by

$$\chi_{\mathrm{Pauli}} = \frac{\mu_{\mathrm{B}}(N_{\uparrow} - N_{\downarrow})}{V}/B_0 \tag{1.35}$$

$$= \frac{\mu_{\mathrm{B}}^2}{V}\int_0^{\infty}\frac{\partial D(\varepsilon)}{\partial \varepsilon}f(\varepsilon)d\varepsilon \tag{1.36}$$

$$= \frac{\mu_{\mathrm{B}}^2}{V}\int_0^{\infty}D(\varepsilon)\left(-\frac{\partial f(\varepsilon)}{\partial \varepsilon}\right)d\varepsilon, \tag{1.37}$$

where V is the volume of the system, and the last expression is obtained by integration by parts. When the condition of the Fermi energy $\varepsilon_{\mathrm{F}} \gg k_{\mathrm{B}}T$, which is satisfied in ordinary condition with ε_{F} ∼few eV, eq. (1.37) can be rewritten as

$$\chi_{\mathrm{Pauli}} = \frac{\mu_{\mathrm{B}}^2}{V}int_0^{\infty}D(\varepsilon)\delta(\varepsilon_{\mathrm{F}})d\varepsilon \tag{1.38}$$

$$= \frac{\mu_{\mathrm{B}}^2}{V}D(\varepsilon_{\mathrm{F}}). \tag{1.39}$$

The eq. (1.39) is the expression of Pauli paramagnetism, which is independent from temperature and in proportion to the density of state at the Fermi energy.

1.1.9 History of molecule-based magnets

Most of organic molecules have closed shell electronic structure which shows only diamagnetism, but stable radicals which have localized spins are present as magnetic materials [28]. The development of EPR measurement technique stimulated the research of organic radicals, resulting in finding organic magnetic materials. Among the materials, compounds having $S = 2$ high spin ground state [29,30] have been discovered as shown in Fig. 1.8a. This result suggests a possibility of high spin polymer shown in Fig. 1.8b and 1.8c, then the research has been extended to polycarbenes [31–34]. These molecules shows a high-spin character, but the almost all of the polycarbene does not show a 3D magnetic transition due to the weakness of the inter-molecular interaction.

The inter-molecular interaction is usually antiferromagnetic because of the inter-molecular overlap between SOMOs of adjacent molecules, therefore it is natural that the many chemists tried to achieve a ferromagnetic interaction. The persistent effort to produce ferromagnetic inter-molecular interaction finally achieved pure organic ferromagnet *p*-NPNN whose $T_C = 0.6$ K in 1991 [35]. In 1993, another pure organic ferromagnet *N*, *N*′-dioxy-1,3,5,7-tetramethyl-2,6-diazaadamantane [38] with $T_C = 1.48$ K was also obtained. These molecules clearly show the ferromagnetic transition as confirmed by heat capacity (Fig. 1.9a), magnetic susceptibility (Fig. 1.9b), AC susceptibilities (Figs. 1.10a and 1.11b) and magnetization curves (Figs. 1.10b, 1.12a and c). Though the ferromagnetic materials were obtained, the weak inter-molecular interaction, the typical value of which is few Kelvin, is the fatal drawback of the pure organic magnets. Indeed, organic materials have points to be specially considered; that is, many functional groups are able to be incorporated into organic molecules by chemical modification. The feature is a great advantage for molecule-based devices, but the weakness of the inter-molecular interaction spoils the advantage of the pure organic system. What we need is a system which has both the flexible modifiability like as organic magnets, and the strong inter-molecular interaction like as inorganic magnets.

The weakness of the organic magnets is owing to the small overlaps between SOMOs, which is necessary to protect the reactive organic radicals. In contrary to the organic magnets, the source of the magnetism in traditional inorganic magnets is *d*-electrons which are not chemically reactive. Therefore, it is concluded that the molecule suitable for molecule-based device is a something having both the *d*-electron, which is a source of the magnetic moment, and the organic system, which gives a modifiability; that is, using "transition metal complexes" are the smart choice.

In the field of the transition metal complex magnets, many innovative materials have been developed in the last few decades thanks to the development of the design guide for controlling intra- and inter-molecular interactions [39, 40]. In the transition metal complexes, we can easily obtain bi-, tri- and poly-nuclear transition metal complexes by using the bridging ligand, for examples, oxalato [41], N_3^- [42] and dithiooxalato [43] (Fig. 1.13). In the multi-nuclear transition metal complexes,

intra-molecular interaction is easily modified by the chemical design of the ligand. As suggested by the O. Kahn [44, 45], interaction between transition metals of a multi-nuclear complex is determined by the relation between the magnetic orbitals of the metals. The simplest examples consisting two d^9 $S = 1/2$ metals demonstrate the importance of the symmetry of the magnetic orbitals, as shown in Fig. 1.14 [49–51]. The magnetic orbital of the right (left) half of the binuclear complex is described as antibonding orbital between the right (left) side central metal d-orbital and HOMO of the right (left) side ligand, as shown in Fig. 1.14b. According to the interaction model [44, 45] (Fig. 1.14c), the interaction J between two magnetic orbitals is approximately described as

$$J = 2k + 4\beta S, \tag{1.40}$$

where k, β and S are Coulomb integral, resonance integral and overlap integral, respectively, between the two magnetic orbitals. The first term gives a weak ferromagnetic interaction, while the second term gives a strongly antiferromagnetic interaction. Consequently, intra-molecular interaction of binuclear complex depends on the overlap between the orbitals. If the overlap is large as shown in Fig. 1.14d, intra-molecular interaction is strong antiferromagnetic, while the small overlap (Fig. 1.14e) and no-overlap (Fig. 1.14f) give a weak and no antiferromagnetic interaction, respectively. Since the proof of the controlling the intra-molecular interaction, many superior poly-nuclear transition metal complexes have been derived from the chemical design of intra- and inter-molecular interaction of the magnetic molecules [28, 46–48, 52, 53]. Nowadays, the chemical design is the indispensable tool for constructing novel molecule-based magnets [28, 39].

At the end of this subsection, I will briefly note the recent trends of the molecule-based magnet; that is, low dimensional magnets, frustrated systems and hybrid-systems.

The recent development of the transition-metal-complex-based magnets produced a lot of low dimensional magnets, such as single molecule magnets [54–58] and single chain magnets [59–62]. In these low-dimensional system, quantum behavior of the spin can be observed in the magnetism. Similarly, the frustrated system also shows the quantum effect [63–67], in which the spins cannot be arranged as that in the classical spin system due to the quantization of the spin.

These quantum effect is interesting from the view point of the theoretical investigation.

On the other hand, "hybrid magnetic system" is investigated mainly from the view point of the application, where the magnet shows not only a magnetism but also the other feature such as optical [68–72], electronic [73–75] or thermal [76] property. Though almost all of the hybrid systems just show the two functions independently, the existence of the correlation between the magnetism and the other function in some cases suggests the promise of the hybrid system in application.

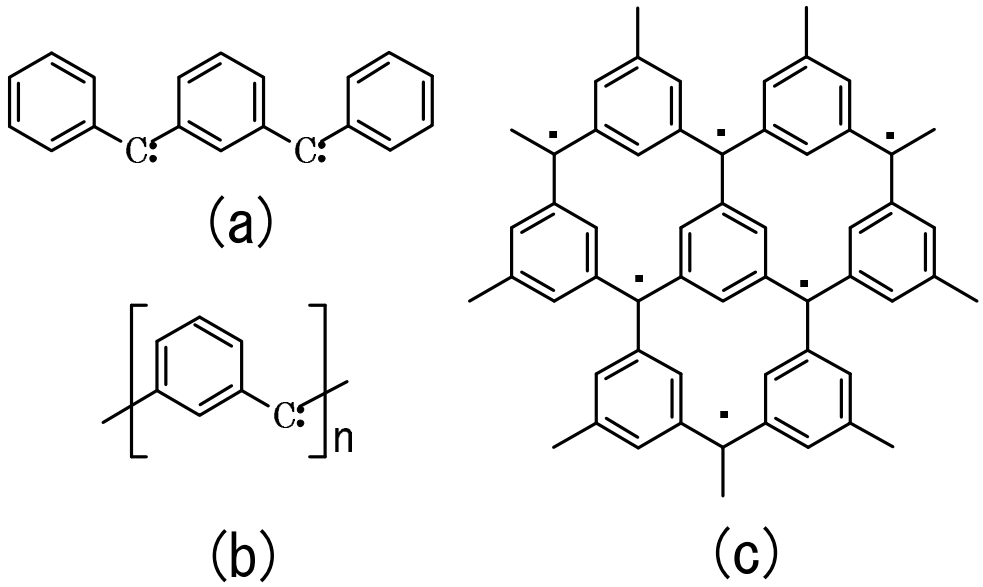

Fig. 1.8. Organic high spin radicals with magnetic moment **(a)** $S = 1$ [30], **(b)** $S = n/2$ [32, 36, 36] and **(c)** a part of $S = \inf$ polymer (not obtained).

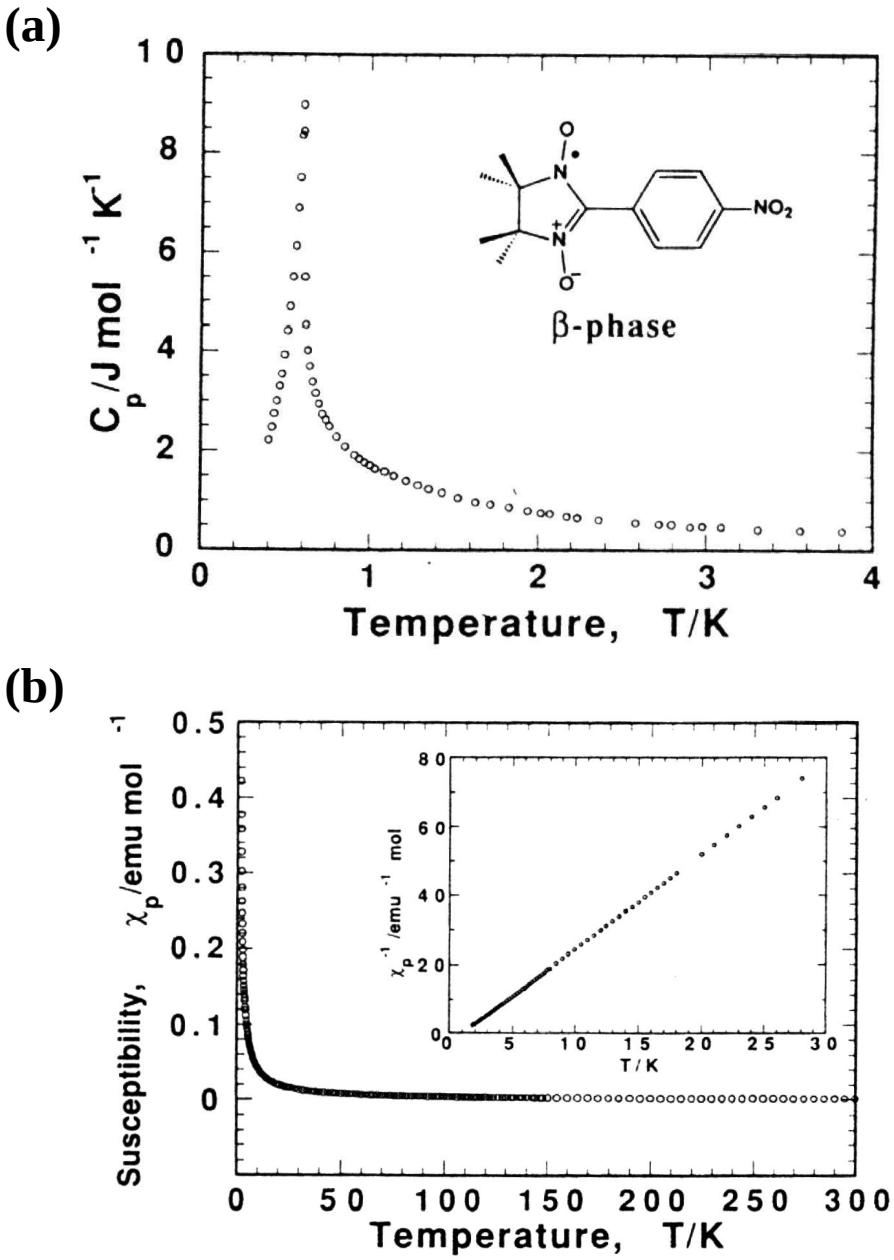

Fig. 1.9. The **(a)** molecular structure, **(b)** specific heat and **(b)** magnetic susceptibility of first pure organic ferromagnet *p*-NPNN (β-phase) [35] ! ☠Specific heat indicates a transition at 0.6 K, and susceptibility suggests the ferromagnetic interaction.

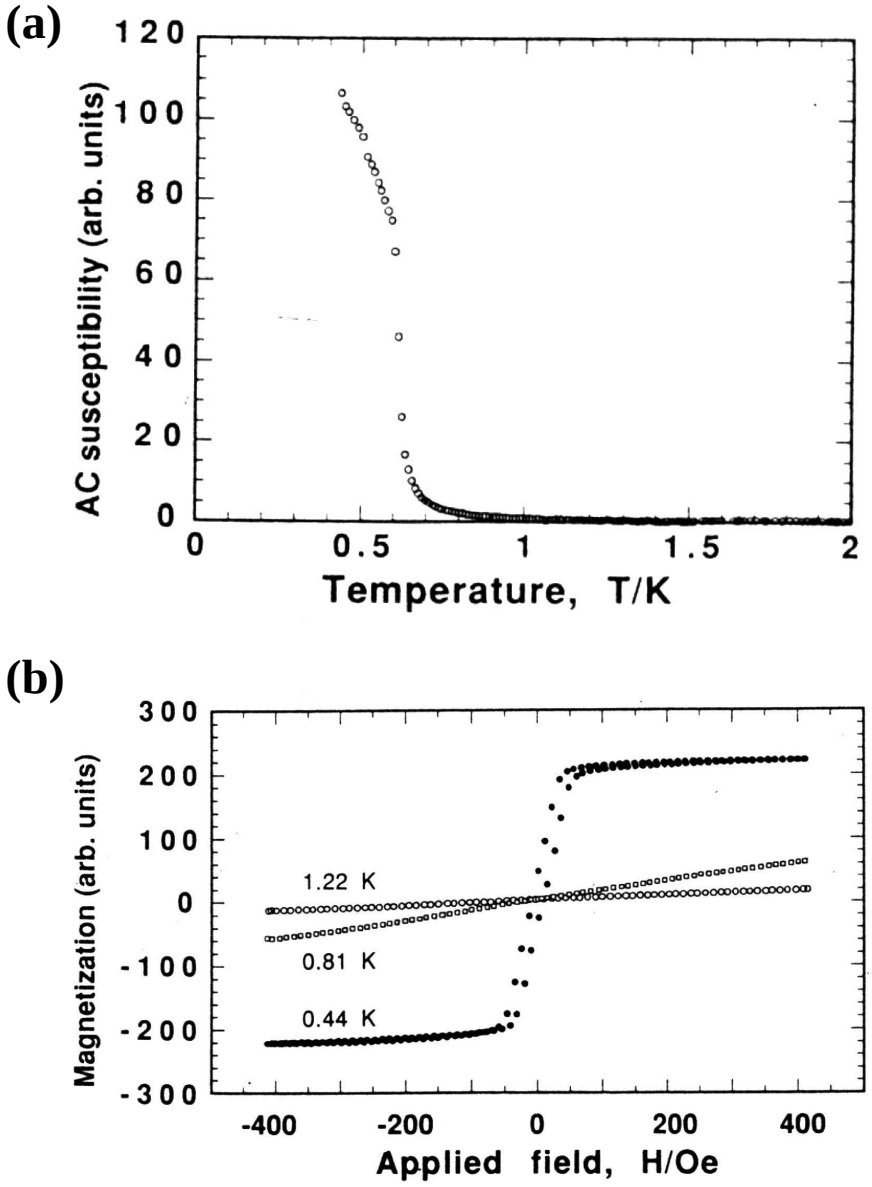

Fig. 1.10. **(a)** AC susceptibility (30 mT) and magnetization curve of *p*-NPNN.

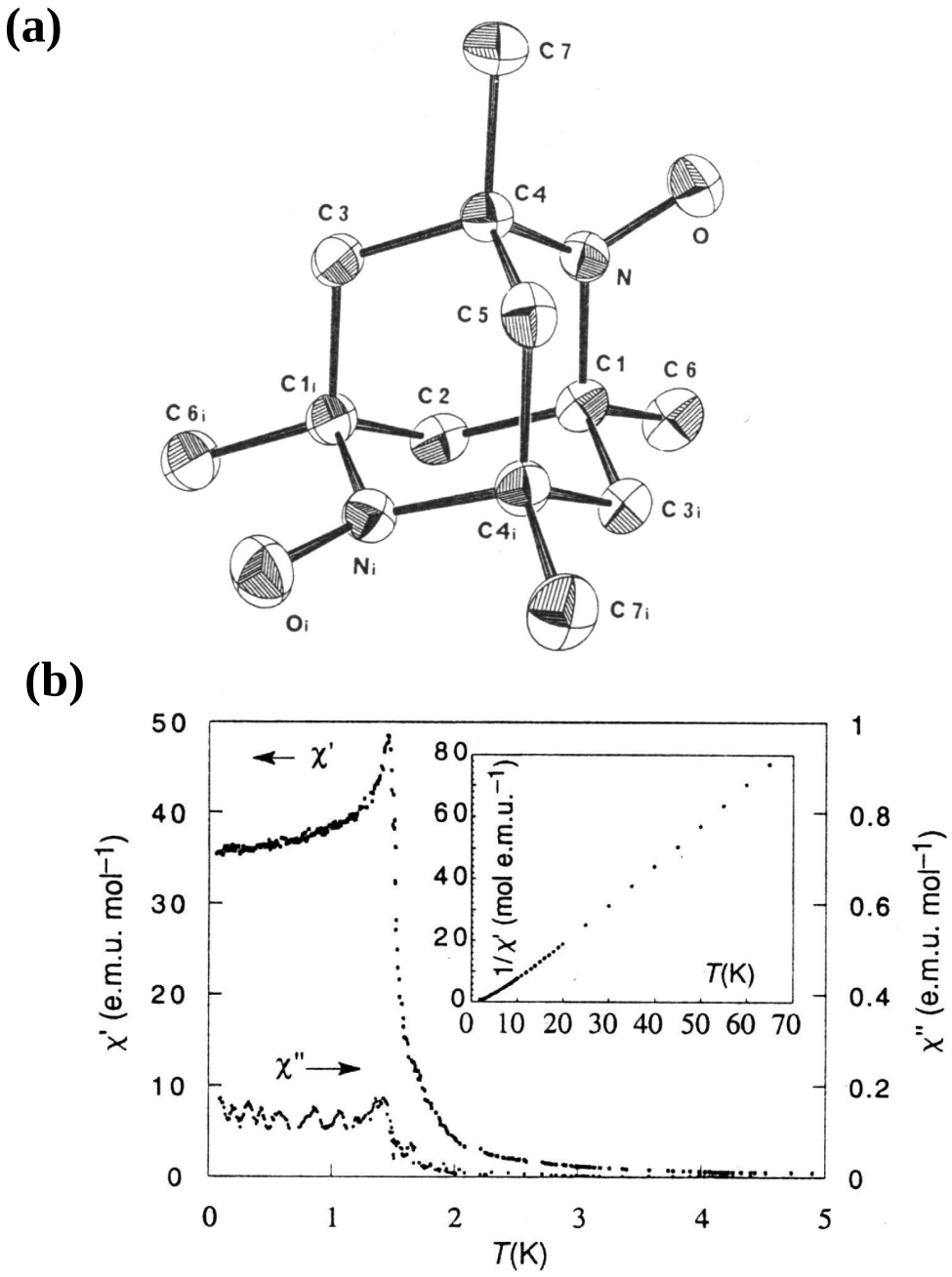

Fig. 1.11. **(a)** Structure and **(b)** AC susceptibility of N, N'-dioxy-1,3,5,7-tetramethyl-2,6-diazaadamantane [38].

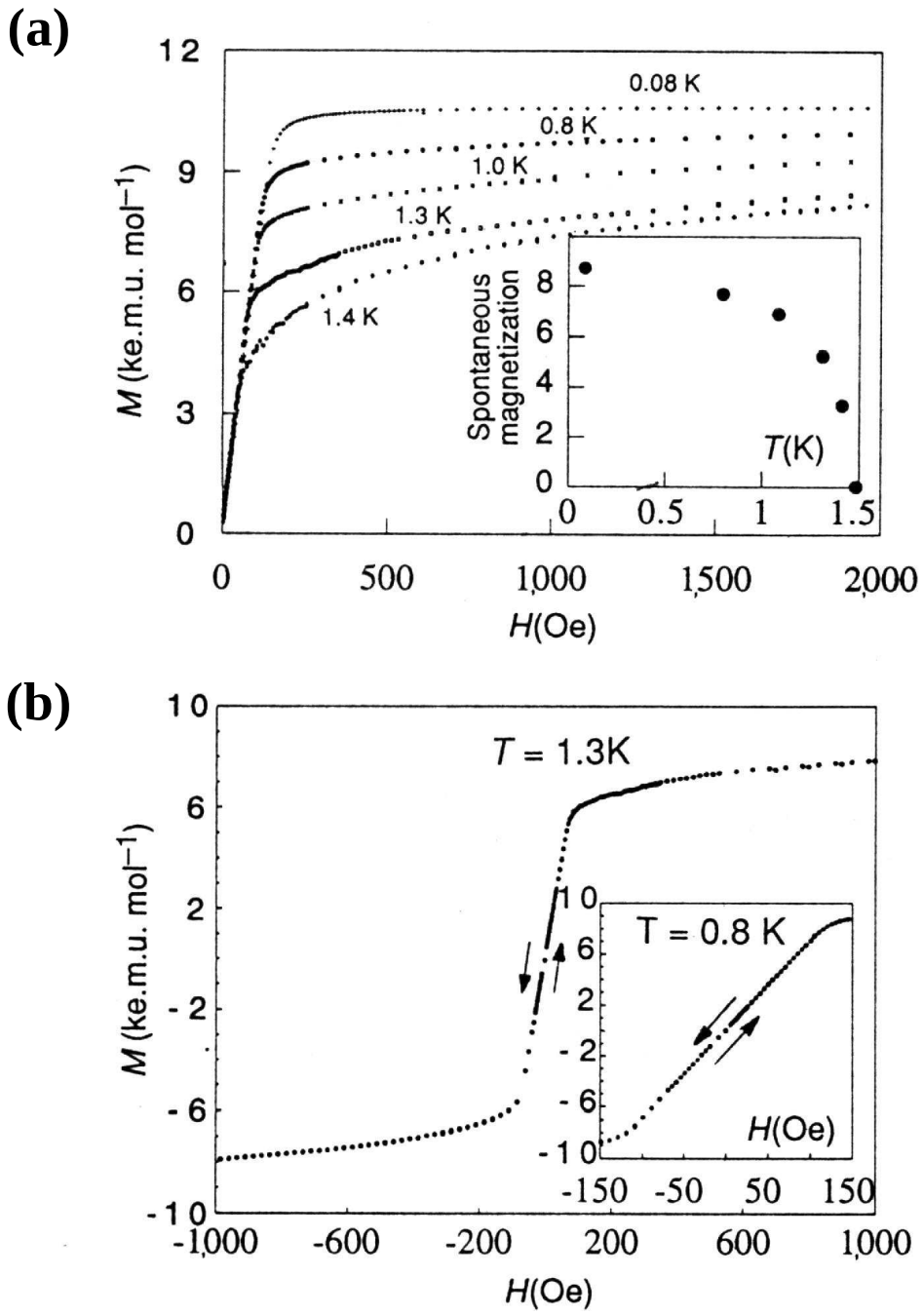

Fig. 1.12. Magnetization curve of N, N'-dioxy-1,3,5,7-tetramethyl-2,6-diazaadamantane [38].

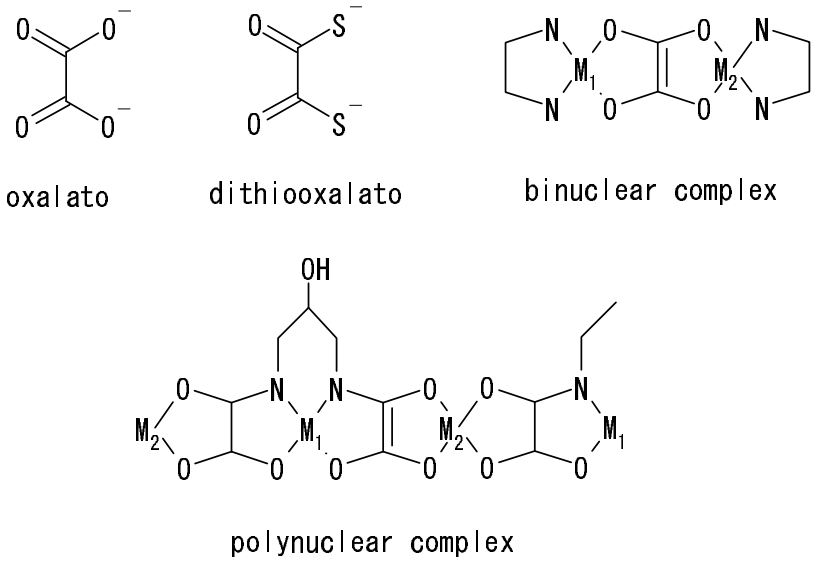

Fig. 1.13. The structure of the ligands and examples of the bi- and polynuclear complexes.

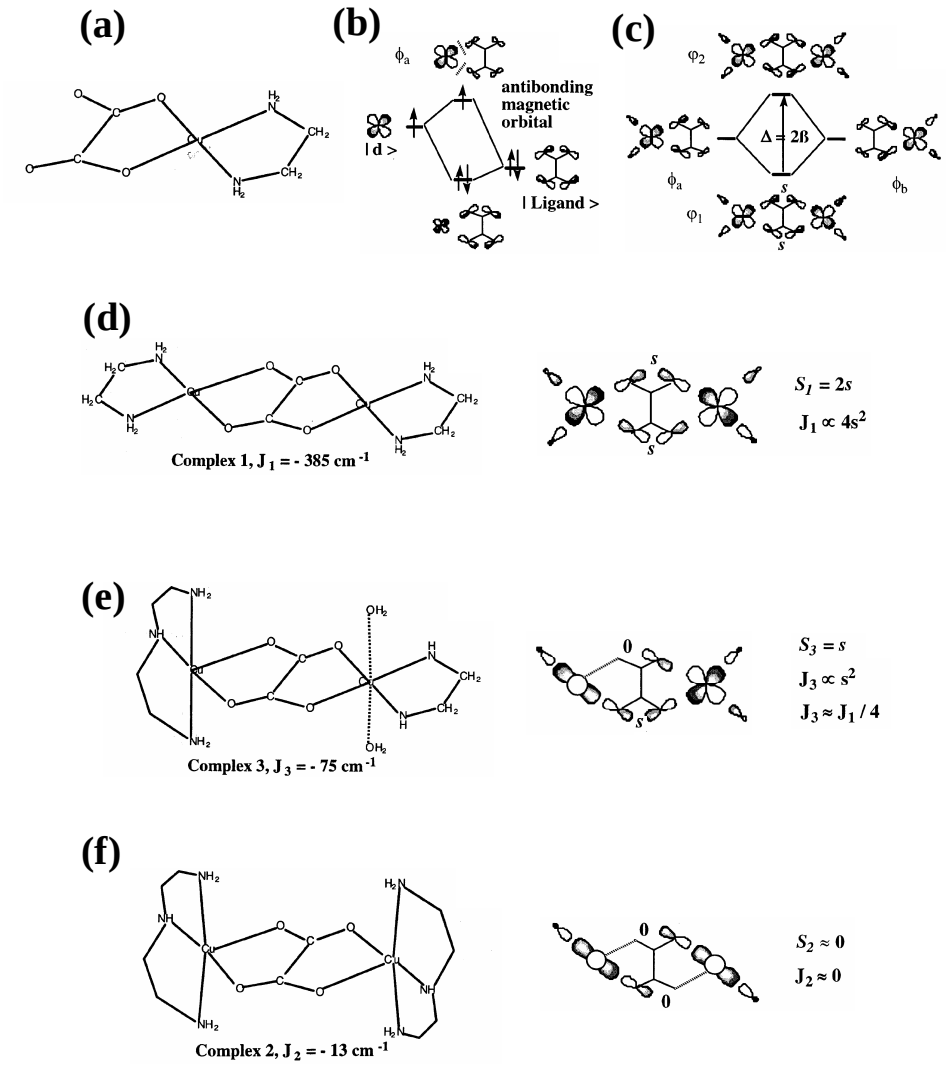

Fig. 1.14. The demonstration of the controlling the intra-molecular interaction [40, 49–51]. **(a)** The base unit of the Cu^{2+} binuclear complexes. **(b)** The magnetic orbital of the half side of the binuclear complex is antibonding orbital between a metal and a ligand. **(c)** Inter-molecular interaction J is equal to the energy gap between the bonding state and antibonding state between the two magnetic orbitals. **(d)** If the overlap between the magnetic orbitals is large, intra-molecular interaction is strong antiferromagnetic. In contrary, the overlap is **(e)** small or **(f)** negligible, the interaction is weak or negligible, respectively.

1.2 Electric conductivity

In this section, we deal with electron transport phenomenon. The simplest consideration of electron transport is based on *nearly free electron model*, where we start from the free electron described as plane wave. The nearly free electron model shows good agreement with the transport properties of simple metals, such as alkaline metals, because of high mobility of electron and small electron-electron interaction. In the model, band structure and energy gap, the basic features of electrons in metallic materials, are easily understood. On the other hand, we can draw an another picture of electrons named *tight-binding model*, where we deal with the electronic state starting from the localized atomic orbitals. In comparison to the nearly free electron model, the tight-binding model is frequently more realistic when we deal with molecule-based electronic systems because of low mobility of the electrons in organic conductors.

1.2.1 Nearly free electron model

When we consider the motion of electrons in solids, we must solve the many-body Shr dinger equation including electron-electron interaction. However, the many-body problem is quite difficult and the electron correlation effect is small in the traditional metals. Therefore we treat the nearly free electron model on the basis of one-electron approximation at first. According to the Bloch's theorem, the solutions of Schr dinger equation in a periodic potential is described as

$$\psi_{\mathbf{k}}(\mathbf{r}) = u_{\mathbf{k}}(\mathbf{r}) \exp(\mathrm{i}\mathbf{k} \cdot \mathbf{r}), \tag{1.41}$$

where $u_{\mathbf{k}}$ has the same periodicity as the potential, and

$$\mathbf{k} = \frac{2\pi n}{L} \ (n : \text{integer}) \tag{1.42}$$

when we assume the periodic boundary condition of crystal size L. To investigate the electronic properties, it is necessary to know the *band structure of electron*, the wave-number dependence of energy. At first, we consider the energy of a free electron in the weak potential limit. In this limit, we obtain the energy dispersion of an electron

$$\varepsilon_{\mathbf{k}} \ = \ \int \psi_{\mathbf{k}}(\mathbf{r})^* \left(-\frac{\hbar^2}{2m} \nabla^2 \right) \psi_{\mathrm{k}}(\mathbf{r})$$

$$= \frac{\hbar^2}{2m}\mathbf{k}^2. \tag{1.43}$$

Here, we introduce the weak potential of the lattice $V(\mathbf{r})$ as a perturbation. $V(\mathbf{r})$ satisfies the following relation due to the periodicity of the lattice;

$$V(\mathbf{r}+\mathbf{R}) = V(\mathbf{r}), \tag{1.44}$$

where $\mathbf{R}$ is the lattice vector. The energy is modified by the potential as given by

$$\varepsilon'_{\mathbf{k}} = \varepsilon_{\mathbf{k}} + \sum_{\mathbf{K}'} H'_{\mathbf{k}\mathbf{k}'} + \sum_{\mathbf{k}'} \frac{|H'_{\mathbf{k}\mathbf{k}'}|^2}{\varepsilon_{\mathbf{K}} - \varepsilon_{\mathbf{k}'}}, \tag{1.45}$$

using the perturbation theory, where

$$H'_{\mathbf{k}\mathbf{k}'} = \int \psi^*_{\mathbf{k}}(\mathbf{r}) V(\mathbf{r}) \psi_{\mathbf{k}'}(\mathbf{r}) d\mathbf{r}. \tag{1.46}$$

Because the potential has the same periodicity to the lattice, the potential term can be expanded by the Fourier transformation;

$$V(\mathbf{r}) = \sum_{\mathbf{G}} V_{\mathbf{G}} \exp(-i\mathbf{G}\cdot\mathbf{r}). \tag{1.47}$$

Therefore, eq. (1.46) is transformed as

$$H'_{\mathbf{k}\mathbf{k}'} = \frac{1}{V}\int V_{\mathbf{G}} \exp(\mathrm{i}(\mathbf{k}'+\mathbf{G}-\mathbf{k})\cdot\mathbf{r}) d\mathbf{r}, \tag{1.48}$$

where $\mathbf{G}$ is the reciprocal lattice vector. The term has non zero value only in the condition of $\mathbf{k}' = \mathbf{k} - \mathbf{G}$ in the second order perturbation, while electrons behave as free electron in other wave number. The difference between free electrons and nearly free electrons is one of our interests. At $\mathbf{k}' = \mathbf{k} - \mathbf{G}$, $\psi_{\mathbf{k}}(\mathbf{r})$ and $\psi_{\mathbf{k}'}(\mathbf{r})$ are not orthogonal to each other in the Hamiltonian as following.

$$H' \equiv -\frac{\hbar^2}{2m}\nabla^2 + \sum_{\mathbf{G}} V_{\mathbf{G}} \exp(\mathrm{i}\mathbf{G}\mathbf{r}) \tag{1.49}$$

$$\begin{aligned}\int \psi^*_{\mathbf{k}}(\mathbf{r}) H' \psi_{\mathbf{k}-\mathbf{G}}(\mathbf{r}) &= \int \psi^*_{\mathbf{k}}(\mathbf{r}) \left(-\frac{\hbar^2}{2m}\nabla\right) \psi_{\mathbf{k}-\mathbf{G}}(\mathbf{r}) \\ &\quad + \int \psi^*_{\mathbf{k}}(\mathbf{r}) \left(\sum_{\mathbf{G}} V_{\mathbf{G}} \exp(\mathrm{i}\mathbf{G}\mathbf{r})\right) \psi_{\mathbf{k}-\mathbf{G}}(\mathbf{r}) \qquad (1.50)\\ &= \int |u(\mathbf{r})|^2 \left(\sum_{\mathbf{G}} V_{\mathbf{G}}\right) \neq 0 \qquad (1.51)\end{aligned}$$

Therefore the new basis of H' are given as the linear combinations of these non-perturbated wave functions. For simplicity, we focus on the smallest wave number, $\mathbf{k} = -\mathbf{k}' = \mathbf{G}$ and use

$$\psi'_{\mathbf{k}}(\mathbf{r}) = C_1\psi_{\mathbf{k}}(\mathbf{r}) + C_2\psi_{-\mathbf{k}}(\mathbf{r}) \tag{1.52}$$

as trial function. The energy of the trial function is given by solving the secular equations

$$\begin{aligned} \int \psi_{\mathbf{k}}(\mathbf{r})H'\psi'_{\mathbf{k}}(\mathbf{r}) &= C_1(H_{\mathbf{kk}} - \varepsilon) + C_2H_{\mathbf{k}-\mathbf{k}} = 0 & (1.53)\\ \int \psi_{-\mathbf{k}}(\mathbf{r})H'\psi'_{\mathbf{k}}(\mathbf{r}) &= C_1(H_{-\mathbf{kk}} - \varepsilon) + C_2H_{-\mathbf{k}-\mathbf{k}} = 0, & (1.54) \end{aligned}$$

and we obtain the perturbated energy

$$\begin{aligned} \varepsilon &= \frac{(\varepsilon_{\mathbf{k}} + \varepsilon_{-\mathbf{k}}) \pm \sqrt{(\varepsilon_{\mathbf{k}} - \varepsilon_{-\mathbf{k}})^2 + 4|V_{\mathbf{G}}|^2}}{2} \\ &= \varepsilon_{\mathbf{k}} \pm |V_{\mathbf{G}}|, \end{aligned} \tag{1.55}$$

which means that a band of crystal has a gap at the midpoint of reciprocal lattice (Fig. 1.15).

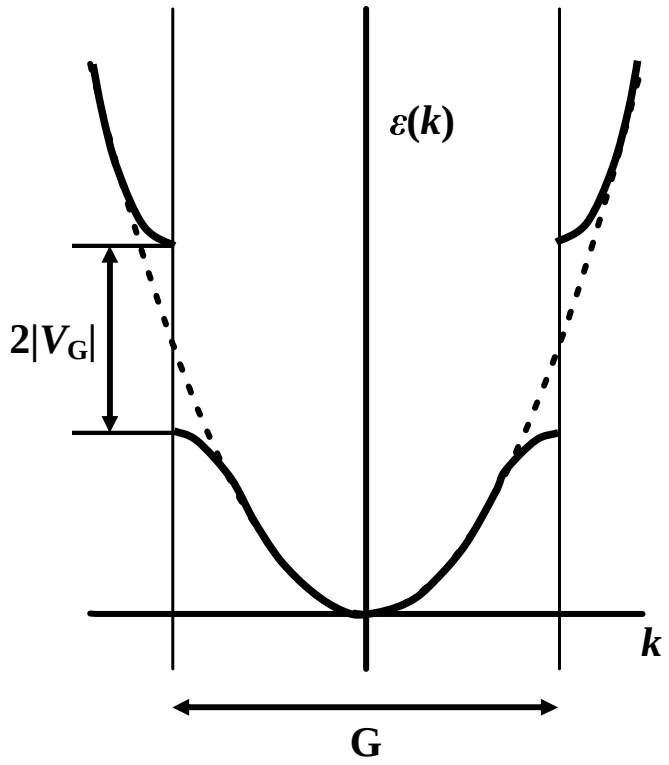

Fig. 1.15. The band structure of free electron (dotted line) and nearly free electron (solid line). V_G is the strength of perturbation potential.

1.2.2 Tight binding model

In the cases of nearly localized electron such as organic conductors, the nearly free electron model is no longer a good model for conduction electrons. For this case, it is better to use the linear combination of the wave functions localized on atoms or molecules for expressing the electronic states of solids. The model based on localized wave function is called "tight binding model", where the wave function of electrons $\phi_{\mathbf{k}}(\mathbf{r})$ is represented as

$$\phi_{\mathbf{k}}(\mathbf{r}) = \sum_{\mathbf{l}} \exp(\mathrm{i}\mathbf{k}\cdot\mathbf{l})\cdot\phi_{\mathrm{a}}(\mathbf{r}-\mathbf{l}), \tag{1.56}$$

where $\phi_{\mathrm{a}}(\mathbf{r}-\mathbf{l})$ is the wave function of an atom at site $\mathbf{l}$. For simplification, we assume that $\phi_{\mathrm{a}}(\mathbf{r}-\mathbf{l})$ is not modified by the neighboring atoms, in other words, $\phi_{\mathrm{a}}(\mathbf{r}-\mathbf{l})$ is the same as the atomic orbital. In this situation, the electron energy is calculated as follows.

$$\begin{aligned}
\varepsilon(\mathbf{k}) &= \int \phi_{\mathbf{k}}^{*}\left\{-\frac{\hbar^2}{2m}\nabla^2 + V(\mathbf{r})\right\}\phi_{\mathbf{k}}d\mathbf{r} && (1.57)\\
&= \int \phi_{\mathbf{k}}^{*}\left\{\left(-\frac{\hbar^2}{2m}\nabla^2 + v_{\mathrm{a}}(\mathbf{r})\right) + (V(\mathbf{r}) - v_{\mathrm{a}}(\mathbf{r}))\right\}\phi_{\mathbf{k}}d\mathbf{r} && (1.58)\\
&= \int \phi_{\mathbf{k}}^{*}\left\{H_{\mathrm{a}} + (V(\mathbf{r}) - v_{\mathrm{a}}(\mathbf{r}))\right\}\phi_{\mathbf{k}}d\mathbf{r} && (1.59)\\
&= \frac{1}{v_{\mathrm{c}}}\sum_{\mathbf{h}}\exp(i\mathbf{k}\cdot\mathbf{h})\int \phi_{\mathrm{a}}^{*}(\mathbf{r}+\mathbf{h})\left\{H_{\mathrm{a}} + (V(\mathbf{r}) - v_{\mathrm{a}}(\mathbf{r}))\right\}\phi_{\mathrm{a}}(\mathbf{r})d\mathbf{r} && (1.60)\\
&= \varepsilon_{\mathrm{a}} + \frac{1}{v_{\mathrm{c}}}\sum_{\mathbf{h}}\int \phi_{\mathrm{a}}^{*}(\mathbf{r}+\mathbf{h})\left\{V(\mathbf{r}) - v_{\mathrm{a}}(\mathbf{r})\right\}\phi_{\mathrm{a}}(\mathbf{r})d\mathbf{r}, && (1.61)
\end{aligned}$$

where H_{a} is the Hamiltonian of an atom, v_{a} is the potential of an atom, $\mathbf{h}$ is inter-atomic vector and ε is the energy of an electron on an isolated atom. Owing to the localized nature of atomic orbitals and, in addition, the weakness of atomic potential due to the screening effect, the last integral term has a large value only between adjacent atoms ($\mathbf{h} = \pm 1$) and an atom itself ($\mathbf{h} = 0$). So, electron energy is described as

$$\varepsilon_{\mathbf{k}} = \varepsilon_{\mathrm{a}} - \alpha - \sum_{\mathbf{h}}\beta_{\mathbf{h}}\exp(\mathrm{i}\mathbf{k}\cdot\mathbf{h}), \tag{1.62}$$

where

$$\alpha = -\int \phi_{\mathrm{a_i}}^{*}V(\mathbf{r}) - v_{\mathrm{a}}(\mathbf{r})\phi_{\mathrm{a_i}} \tag{1.63}$$

and

$$\beta = -\int \phi^*_{\mathrm{a_j}} V(\mathbf{r}) - v_{\mathrm{a}}(\mathbf{r})\phi_{\mathrm{a_i}} \tag{1.64}$$

are the Coulomb integral and resonance integral, respectively. When we calculate the band structure of organic conductors, at first, we calculate the molecular orbitals by the extend H ckel approximation, and use the molecular orbitals as $\phi_{\mathrm{a_i}}$ of eqs. (1.63) and (1.64) in the next step.

1.3 Peierls instability

It was shown by Peierls that one-dimensional metal has inherent electronic instability [77], which causes a metal-insulator (MI) transition taking place at low temperatures. Such instability and MI transition are observed commonly in organic conductors due to their low dimensionality. As mentioned above, the electronic state of one dimensional system is described as

$$\psi_{\mathrm{k}}(r) = u_{\mathrm{k}}(r) \cdot \exp(ikr). \tag{1.65}$$

When we introduce the periodic potential

$$V(q, r) = V_{\mathrm{q}} \exp(\mathrm{i}qr) \tag{1.66}$$

as a perturbation potential, we obtain the electronic state as follows by using the perturbation theory.

$$\psi'_{\mathrm{k}}(r) = \psi_{\mathrm{k}}(r) + a_{\mathrm{k+q}}\psi_{\mathrm{k+q}}(r), \tag{1.67}$$

where

$$a_{\mathrm{k+q}} = \frac{V_{\mathrm{q}}}{E_{\mathrm{k}} - E_{\mathrm{k+q}}}. \tag{1.68}$$

To sum up the norms of wave functions gives the electron density $\rho(r)$,

$$\rho(r) = \frac{1}{N}\sum_k |\psi'_{\mathrm{k}}(r)|^2 \tag{1.69}$$

$$= \simeq \frac{1}{NV}\sum_k (1 + a_{\mathrm{k+q}} \exp(\mathrm{i}kq) + a^*_{\mathrm{k}} \exp(-\mathrm{i}kq), \tag{1.70}$$

where we ignore the higher order term and normalized by the total electron number N. By omitting the first term which is independent of the periodic potential, the susceptibility is defined $\chi(r)$ in the following.

$$\chi(r) = \frac{1}{NV}\sum_k \left(\frac{V_{\rm q}}{E_{\rm k} - E_{\rm k+q}} \exp({\rm i}qr) + \frac{V_{\rm q}}{E_{\rm k} - E_{\rm k+q}} \exp(-{\rm i}qr) \right) \tag{1.71}$$

$$= \frac{1}{NV}\sum_k \frac{1}{E_{\rm k} - E_{\rm k+q}} V_{\rm q}(\exp({\rm i}qr) + \exp(-{\rm i}qr)) \tag{1.72}$$

For taking a *real* potential, we redefine the potential as

$$V(q, r) = V_{\rm q}\exp({\rm i}qr) + V_{\rm q}\exp(-{\rm i}qr). \tag{1.73}$$

Then,

$$\chi(r) = \frac{1}{NV}\sum_k \left(\frac{1}{E_{\rm k} - E_{\rm k+q}} \frac{1}{E_{\rm k} - E_{\rm k-q}} \right) V_{\rm q}(\exp({\rm i}qr) + \exp(-{\rm i}qr)). \tag{1.74}$$

To mix $\psi_{\rm k}$ and $\psi_{\rm k+q}$, it is necessary that one of these two orbitals is occupied whereas the other unoccupied. Then, we introduce the Fermi distribution function at a finis temperature.

$$\chi(r) = \frac{1}{NV}\sum_k \left(\frac{f_{\rm k}(1 - f_{\rm k+q})}{E_{\rm k} - E_{\rm k+q}} \frac{f_{\rm k}(1 - f_{\rm k-q})}{E_{\rm k} - E_{\rm k-q}} \right) V_{\rm q}(\exp({\rm i}qr) + \exp(-{\rm i}qr)). \tag{1.75}$$

We can take the replacements $k \to k + q$, $k - q \to k$ in the second term, which are justified by taking the summation of all k.

$$\chi(r) = \frac{1}{NV}\sum_k \frac{f_{\rm k} - f_{\rm k+q}}{E_{\rm k} - E_{\rm k+q}} V_{\rm q}(\exp({\rm i}qr) + \exp(-{\rm i}qr)). \tag{1.76}$$

In a usual case, we can regard k as continuous variable. Therefore, the summation is changed to integral. Taking into account the Fermi distribution function at low temperatures, we obtain

$$\chi(r) = \int \frac{f_{\rm k} - f_{\rm k+q}}{E_{\rm k} - E_{\rm k+q}} V_{\rm q}(\exp({\rm i}qr) + \exp(-{\rm i}qr))dk \tag{1.77}$$

$$= \frac{2mV_{\rm q}}{\pi n\hbar^2 qV} \{\exp({\rm i}qr) + \exp(-{\rm i}qr)\} \ln\left|\frac{q + 2k_{\rm F}}{q - 2k_{\rm F}}\right|. \tag{1.78}$$

If the periodicity of the potential differ from $q = \pm 2k_{\rm F}$, the magnitude of the modulation of electron density is roughly in proportion to $V_{\rm q}/q$, and no singularity

is observed. However, at the point of $q = \pm 2k_{\mathrm{F}}$, the susceptibility diverges. The divergence implies that the electron density is spatially modulated with the wave vector $k = 2k_{\mathrm{F}}$ spontaneously, even if the periodic potential is weak. Weak periodic potentials always exist, such as phonon except 0 K, and if once the periodic electron density occurs, the electron itself causes the periodic potential with periodicity $2k_{\mathrm{F}}$. Therefore the oscillating electron density with periodicity $q = 2k_{\mathrm{F}}$ must occurs in one dimensional systems in the low temperature region. In addition, the periodic potential with wave vector $2k_{\mathrm{F}}$ generates a band gap at $k = k_{\mathrm{F}}$ as shown in the previous section, resulting in the generation of MI transition.

The insulating state is characterized by the periodic oscillation of charge density with wave vector $2k_{\mathrm{F}}$, so called $2k_{\mathrm{F}}$-*Charge Density Wave* (CDW) state.

In the CDW state, there are charge-rich sites which are destabilized by the existence of the on-site Coulomb potential U. Consequently, the another phase becomes a insulating ground state when the U is significantly large. Similar to the former discussion, we can deal with up spin electrons and down spin electrons independently. The on-site Coulomb energy E_{c} of the solid is described as

$$E_{\mathrm{c}} = \sum_i U_i a_{i\uparrow} a_{i\downarrow} \tag{1.79}$$

where i, $a_{i\uparrow}$ and $a_{i\downarrow}$ are index of the site, annihilation operator of up and down spin electron at i-th site, respectively. Eq. 1.79 indicates that the U exists only the case of up and down spin electrons sharing a same site. Therefore, up and down spin electrons tend to occupy different sites when the U is large. In this case, both up spin electrons and down spin electrons cause CDW with same wave vector $k = 2k_{\mathrm{F}}$ and different "phase". If the "phases" of these two "waves" are same, the state of total electrons is CDW itself. However, if one of the phases is π shifted from one another, the state has charge density modulation with wave vector k_{F} and spin density modulation with wave vector $2k_{\mathrm{F}}$. In this case, not a charge modulation but a spin density modulation maintain the periodic modulated state. This is called *Spin Density Wave* (SDW) state. When we assume the up spin and down spin electron density ($n_{\uparrow\downarrow}$) described as

$$n_{\uparrow} = \sin(k_{\mathrm{F}} \cdot r), \tag{1.80}$$

$$n_{\downarrow} = \sin(k_{\mathrm{F}} \cdot r + \theta_0), \tag{1.81}$$

The CDW state ($\theta_0 = 0$) has only charge modulation, while the SDW state ($\theta_0 = \pi$) has only spin density modulation. If the value of θ_0 is intermediate between 0 and π, CDW and SDW are coexist.

Which state is the ground state? The result of the question depends on many parameters. Since CDW state is accompanied by charge-rich sites, large on-site Coulomb repulsion destabilizes the CDW state. On the other hand, inter-site Coulomb repulsion V destabilizes SDW state because each site has the same electron density, while adjacent sites of charge-rich site have low charge density in the CDW state. Therefore, it is difficult to forecast which state (CDW, SDW or mixture of them) is the ground state of a one dimensional system, though the determination of ground state is comparatively easy. In the CDW state, there is charge density modulation frequently accompanied by lattice distortion, which can be detected by X-ray diffraction. On the other hand, the SDW state shows finis magnetic susceptibility below the transition temperature. It is noted that these distinction methods are powerful but not always effective, for example, it is difficult to detect a small charge disproportionation of CDW or small magnetic susceptibility of SDW.

In contrary to the 1D metal mentioned above, the ground state at 0 K for 2D or 3D metals depends on the band structure. The MI transition in the 1D metal is owing to the band structure of the 1D metal where the all electrons stabilized by the mixing of the states with a nesting vector $k = 2k_{\mathrm{F}}$ as shown in Fig. 1.16. On the other hand, only a small part of the electrons in the typical 2D Fermi surface (ellipse) are mixed and stabilized by a nesting vector as shown in Fig. 1.17. As a result of these features, the susceptibility χ does not diverge in isotropic 2D and 3D metals as shown in Fig. 1.18, resulting in the absence of the MI transition in these materials. It is noted that there are the 2D metals having the special shaped Fermi surfaces, for example, as shown in Fig. 1.19, where the majority part of the Fermi surface is nested by a nesting vector, resulting in the MI transition.

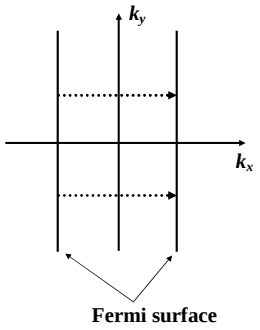

Fig. 1.16. Nesting vector in quasi one dimensional metal (broken line). All electrons at the Fermi surface are mixed and stabilized by the nesting vector.

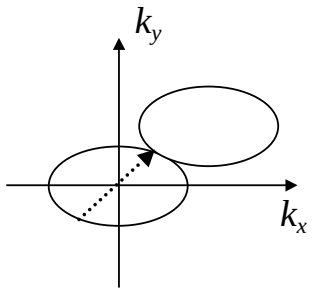

Fig. 1.17. Fermi surface of quasi 2D system. The Fermi surface cannot be nested by a nesting vector, resulting in the only a small energy stabilization with a distortion.

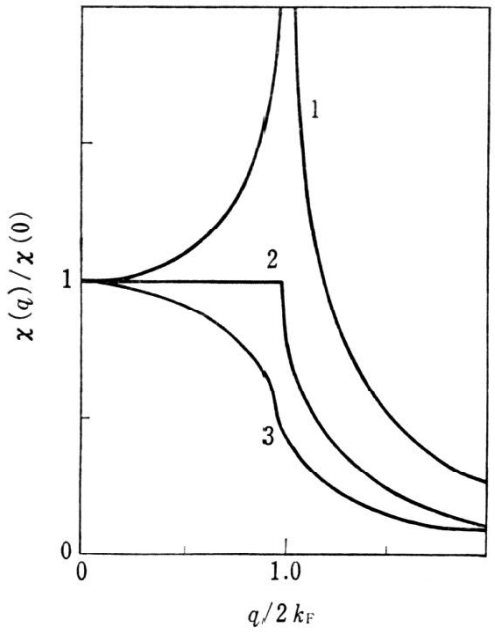

Fig. 1.18. Susceptibilities as a function of wave vector in 1D, 2D and 3D systems. k_{F} is the Fermi wave vector.

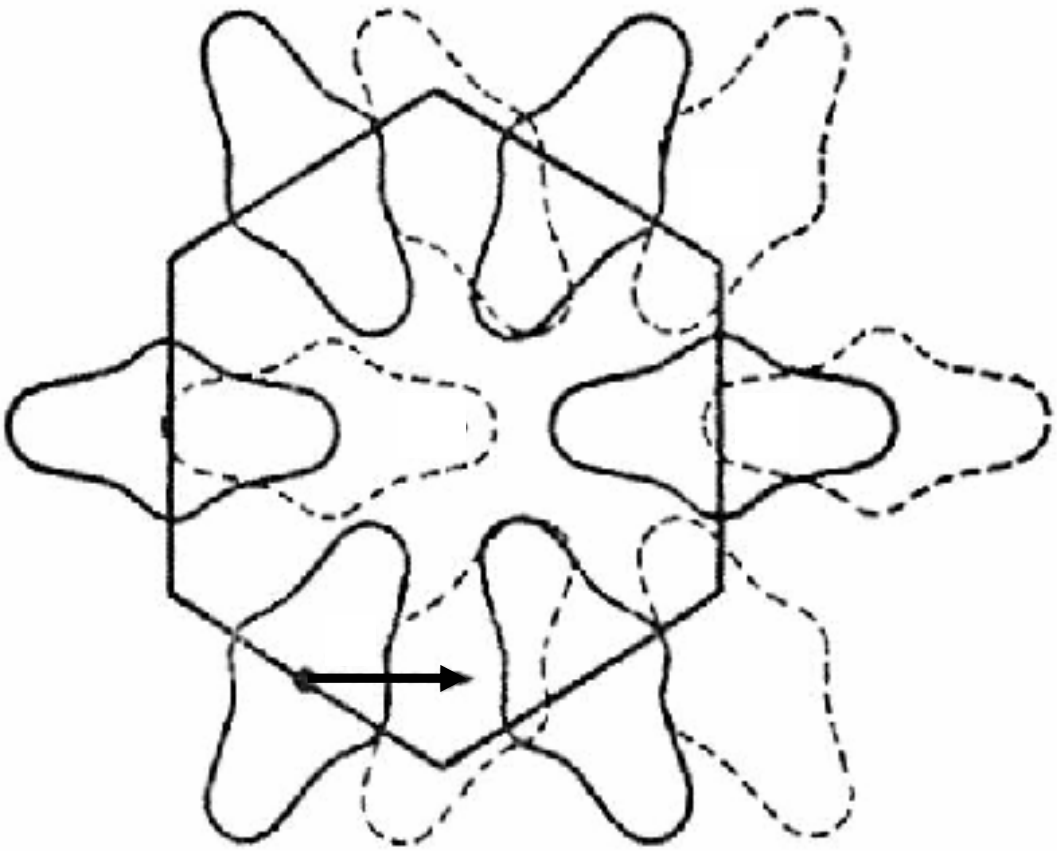

Fig. 1.19. A model of the special shaped 2D Fermi surface, a majority part of which can be nested by the one nesting vector (arrow).

1.3.1 Mott insulator

Transfer integral and Coulomb interaction

The electron-electron interaction is negligible in "good" metals, such as alkaline metals and alkaline-earth metals, but the interaction plays an important role in strongly correlated systems, such as lanthanides and actinoid compounds, some transition metal compounds, high T_C superconductors and organic conductors due to their small transfer integrals and/or low dimensionality. In these strongly correlated systems, (one electron) mean field approximation no longer gives appropriate results. For example, de Boer and Verwey reported that partially occupied transition metal oxides show insulating behavior [78] in spite of the prediction of the band calculation giving metallic band structure. The insulator is understood as a result of electron-electron Coulomb interaction; this is called *Mott insulator* [79]. In this subsection, we discuss about the effect of intra-site electron-electron interaction U, the typical value of which is in the range of ca. 1 eV [80] which is comparable to transfer integrals [81].

Let us arrange hydrogen atoms one-dimensionally with an electron per one hydrogen atom as shown in Fig. 1.20, which is called "half-filled state" having the same numbers of electrons and sites. We treat this one-dimensional arrangement of hydrogen atoms as a model of the Mott insulator. When an electron jumps to the neighbouring site, the total energy of the system is reduced by the transfer integral t and increased by the on-site Coulomb interaction U. When the inter-atomic distance is sufficiently short, the overlap of atomic orbitals between neighbouring atoms raises, resulting in the elevation of transfer integral t. In this case, the energy decrement by t is larger than the energy increment by U, therefore electrons can move from site to site. In other words, the system is metallic. On the other hand, when the atoms are well separated, the decrease of transfer integral t makes the electrons tend to be localized on each atom because the effect of U becomes larger than that of t. As a result, the reduction of transfer integrals brings about localization of electrons, and finally the electrons perfectly localized (called Mott insulator). In the Mott insulating state, each electron has localized magnetic mo-

ment $S = 1/2$ [§], where the activation energy of the system is smaller than that of typical band insulator in ordinary cases.

[§]In the original advocate of Mott insulator, all of the insulators whose MI transition originates from electron-electron interaction are called Mott insulator, therefore it is not necessary that all sites have one electron with $S = 1/2$ magnetic moment, for example, charge disproportion state. However, in the present thesis, "Mott insulator" is defined as insulators where each site has one electron with magnetic moment $S = 1/2$, origin of MI transition being on-site Coulomb interaction U.

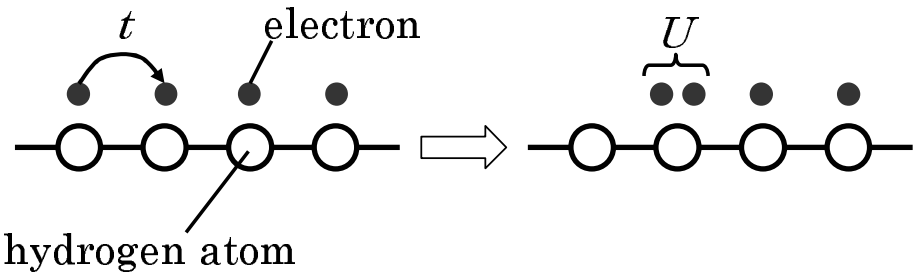

Fig. 1.20. Transfer integral t and on-site Coulomb energy U. The large white circles and small black circles represent 1D aligned hydrogen atoms and electrons, respectively. Electron transfer causes the energy stabilization t and destabilization U at the same time.

Hubbard model

As mentioned in §1.3.1, the system of $t \simeq U$ is in the range of the localized electron system. Consequently the electronic state of the system is well described by using the tight binding approximation with on-site Coulomb repulsion U, which acts between two electrons when they are located on the same site simultaneously. For the description of this electronic state, the simplest model is the Hubbard Hamiltonian

$$\hat{H} = \sum_{i\sigma} E_0 c_{i\sigma}^{\dagger} c_{i\sigma} + \sum_{i \neq j,\sigma} t_{ij} c_{i\sigma}^{\dagger} c_{j\sigma} + \frac{1}{2} \sum_{i\sigma} U c_{i\sigma}^{\dagger} c_{i\sigma} c_{i\bar{\sigma}}^{\dagger} c_{i\bar{\sigma}} \tag{1.82}$$

where i, j is are the site indices, σ is the spin quantum number, $c^{\dagger}$ and c are the creation and annihilation operators, respectively, and t_{ij} is the transfer integral from j to i site. One electron at site i has the energy E_0, and the coexistence of two electrons at the same site gives an additional energy U. Here, we consider a half-filled state with $t_{ij} = t$ working between the nearest neighbour sites, where t is much smaller than U. The reduction in energy from the second perturbation approximation gives rise to an antiparallel spin arrangement between adjacent spins based on the Pauli principle, which is estimated as

$$\Delta E_{ij} = -\frac{2t^2}{U}. \tag{1.83}$$

We can reexpress eq. (1.82) with the following form

$$\hat{H} = -\sum_{\langle i,j \rangle} 2J_{ij} \left\{ \boldsymbol{S}_i \cdot \boldsymbol{S}_j - \frac{1}{4} \right\}, \tag{1.84}$$

$$J_{ij} = -\frac{|t_{ij}|^2}{U}, \tag{1.85}$$

where $\boldsymbol{S}_i$ denotes the spin of the electron at site i. Eqs. (1.84) and (1.85) indicate the equivalence between the Hubbard Hamiltonian under the condition $U \gg t$ and the $S = 1/2$ Heisenberg antiferromagnetic Hamiltonian for a localized spin system.

1.4 Organic conductors

1.4.1 Charge transfer salt and partially oxidized salt

Insulating state of ordinary organic compounds are due to its closed shell structure and small overlap between HOMOs of neighbouring molecules. The former brings about the completely occupied band, while the latter gives a small energy dispersion of the band. Therefore, we must stabilize an open shell structure in organic molecules and enhance the inter-molecular orverlaps if we want to produce metallic organic materials. Using charge transfer salts such as TTF-TCNQ or partially oxidized organic donors is a successful method to obtain stable open shell molecules.

In the charge transfer salts, electron donatable molecule (D; donor) and electron acceptable molecule (A; acceptor) are stabilized by forming charge transfer state ($D^{\delta+}$-$A^{\delta-}$) which is realized by mixing the neutral (D-A) and ionic (D^{+}-A^{-}) states. The mixed valence charge transfer state is no longer closed shell system, therefore there is a possibility that the donor-acceptor system shows metallic conductivity. Well, what condition causes a large charge transfer? The wave function of charge transfer state is described as

$$\psi_{\mathrm{CT}} = a\psi_{\mathrm{DA}} + b\psi \mathrm{D}^{+}\mathrm{A}^{-}, \tag{1.86}$$

where ψ_{DA} and $\psi_{\mathrm{D^{+}A^{-}}}$ represent neutral and ionic wave function, respectively. When charge transfer interaction is weak ($a \gg b$), the energy of the ψ_{CT} can be estimated by perturbation theory in the following;

$$E_{\mathrm{CT}} = E_{\mathrm{DA}} - \frac{(H - S \cdot E_{\mathrm{DA}})^2}{E_{\mathrm{D^{+}A^{-}}} - E_{\mathrm{DA}}}, \tag{1.87}$$

where

$$H = \int \psi^{*}_{\mathrm{DA}} \hat{H} \psi_{\mathrm{D^{+}A^{-}}} d\tau \tag{1.88}$$

$$S = \int \psi^{*}_{\mathrm{DA}} \psi_{\mathrm{D^{+}A^{-}}} d\tau. \tag{1.89}$$

It is necessary for sufficiently large charge transfer that the second term of eq. (1.87) has a large value, which requires two conditions; $E_{\mathrm{DA}} - E_{\mathrm{D^{+}A^{-}}}$ is small, and $H - S \cdot E_{\mathrm{DA}}$ is large. The first condition means that the energy difference between

neutral state and ionic state should be small, which is achieved when the ionization energy of donor molecules is small, while acceptor molecule has a large electron affinity. The condition is satisfied in the typical TTF-type donors and TCNQ-type acceptors, where donors have 7-π electrons showing 6-π stabilization in oxidized state, and cyano groups enhance the electron affinity of acceptors. The second condition is achieved by increasing the inter-molecular orbital overlaps, which is also satisfied in TTF-type donors due to its widely extended p and d orbitals of sulfur atoms.

In partially oxidized salts, the mixing of not D-A but D-D^+ play a important role. In usual partially oxidized salt, anion is described as A^- due to its quite strong electron affinity. On the other hand, the valence of donor molecule is not integer because the typical ratio of donor to anion is 2:1, 3:1, etc. In the following discussion, we consider the partially oxidized salt with donor-anion ratio 2:1 for simplicity¶. The ground state is described as the mixture of the two states, D-D^+-D-D^+ and D^+-D-D^+-D because the energy of these two states are equivalent. The mixed state is formally described as $D^{\frac{1}{2}}$-$D^{\frac{1}{2}}$-$D^{\frac{1}{2}}$-$D^{\frac{1}{2}}$, the partially oxidized state. To realize the partially oxidized state, we need large inter-molecular orbital overlaps between donors, which are achieved in TTF-type organic conductors owing to planar shape of TTF. TTF-type donors have π-orbitals extended on both edges of the TTF plane, and the stacking of these "plates" causes the large inter-donor orbital overlaps.

1.4.2 History of organic conductors

As mentioned in the beginning of this chapter, the researches of organic conductors [82] started from the high-conductive perylene iodine [1]. The early stage of the researches in organic conductors simply aimed to achieve high conductivity. The researches have successfully produced the first organic metal TTF-TCNQ [2](see, Fig. 1.21), but its one-dimensionality causes a MI transition at low temperature. With this result, one new course of researches arisen; low dimensional physics and physics on the strong electron-electron correlation in organic

¶1:1 salt also gives the open shell system, but the small inter-molecular orbital overlaps and large on-site Coulomb interaction causes the Mott transition in typical organic conductors (see, §1.3.1).

conductors [7, 12, 106–109]. Since organic conductors essentially have low dimensionality, it is easy to investigate low dimensional instabilities in them, such as spin Peierls [83–86], CDW [2, 87–89], SDW [90–92] etc.

On the other hand, chemists have tried to increase the dimension of conductive part aiming at higher conductivity even at lower temperatures, like inorganic materials. To enhance the inter-chain interaction which is necessary to achieve 2D or 3D metals, selenium atoms were introduced to TTF framework, resulting the organic superconductors $(TMTSF)_2X$ [3](see, Fig. 1.21). A selenium has a ca. 10 % larger van der Waals radius than that of a sulfur atom, which enhances the inter-chain overlaps and suppresses MI transition under high pressure. The first two dimensional organic metal $(BEDT\text{-}TTF)_2ClO_4(TCE)_{0.5}$ was obtained in 1982 [93], where the donor molecule BEDT-TTF (see, Fig. 1.21) has sulfur atoms in the outer six-membered ring which enhances inter-molecular overlaps by sulfur-sulfur contacts resulting in achieving the two dimensionality. Especially, κ-type, which is a perfectly 2D structure, BEDT-TTF salts often gives a superconductivity [94–97]. In contrary to 2D metals, it is difficult to achieve a 3D metal because TTF-type molecules have only small inter-molecular overlap along the long axis of the molecule. Consequently, there are only few 3D organic metals, such as DCNQI-type metals [98] and $[Ni(tmdt)_2]$, the single-component 3D metal [99]. In the DCNQI-type metals, the π-orbital of DCNQI molecule and the d-orbital of $Cu^{4/3+}$ atom are hybridized and form the 3D Fermi surface. On the other hand, $[Ni(tmdt)_2]$ molecules are stacked with a slippage of a half of the molecular length. The "slipped stack" brings about the inter-chain overlap even in the molecular length axis, while the intra-chain overlap is kept due to the extremely long molecular length.

The conductivity of the organic materials has been improved as mentioned above, indeed, but existing organic conductors are not so appropriate in application of conducting materials in comparison with inorganic materials or conductive polymers [100, 101]. The advantage of the organic conductors is not a conductivity itself, but a high design-ability of a organic molecules which allows us to hybridize the several properties in a material; that is, a conductivity is combined with other properties. In constructing a hybrid system, magnetic-conductors are the promis-

ing materials, while it is hard for the optics [102] or dielectrics [103–105] to be compatible with a high conductivity. The history and features of the π-d system will be mentioned in the next subsection.

1.4.3 π-d systems

Recent works on organic conductors including transition-metal complexes as magnetic anion have revealed the correlated phenomena between electron transport and magnetism, in which the interaction between the π-conduction electron and the localized d-electron spin (π-d interaction) plays an important role [13, 14, 16, 18, 110–115]. The π-d interaction is an analogue of s-d interaction of transition-metal based materials, such as (diluted) magnetic alloy and rare-earth alloy. These π-d interactions are interesting from the points of theoretical aspect of strongly correlated electron systems [11–13] and application for molecular devices [14–18]. Actually, these π-d systems show various phenomena, for example, negative magnetoresistance [115–118], field induced MI transition [119, 120], field induced superconductivity [74] and so forth.

In the early stage of investigation of the π-d systems, it is revealed that localized d-electrons interact with each other through the π-electrons of the ligands in $[CuPc]_3I_3$ (Pc = Phthalocyanine, see, Fig. 1.22) [121], where only a single EPR signal is observed though the salt containing two kinds of electrons π and d. The π-d interaction brings about antiferromagnetic interaction between localized spins of Cu^{2+}, but no magnetic order is observed down to 2 K because of the weakness of the interaction. In 1992, P. Day and coworkers achieved a new π-d salt (BEDT-TTF)$_3$CuCl$_4$·H$_2$O, where the magnetic moment of Cu^{2+} ion coexists with the metallic conductivity in the whole temperature range investigated (4∼300 K). The salt shows a weak ferromagnetic interaction between Cu^{2+} ions owing to π-d interaction. In 1995, the first paramagnetic superconductor β''-(BEDT-TTF)$_4$(H$_2$O)[Fe(C$_2$O$_4$)$_3$]·(C$_6$H$_5$CN) [122] was discovered, but π-d interaction is as weak as the salts mentioned above.

In contrary to the salts mentioned above, it is known that the several π-d salts show a strong π-d interaction though the weak interaction is common [123–128].

In the strong π-d interaction system (BEDT-TTF)$_3$CuBr$_4$ (Fig. 1.23), the

Weiss temperature becomes considerably high in the range of 100 K despite long distances between magnetic anions (Fig. 1.24), and even in the low temperature region where magnetic donors form dimers and become non-magnetic, magnetic interaction between anions is $J = -15.7$ K which is quite high among molecule-based magnets based on TTF-type donors (Fig. 1.25) [129]. The strong magnetic interaction is regarded as being caused by donor-anion interaction through short donor-anion contacts (Fig. 1.26).

(DMe-DCNQI)$_2$Cu [98] is the π-d system investigated in detail, where DMe-DCNQI molecules form coordination bond with $Cu^{4/3+}$ atoms, resulting in the short π-d contacts as shown in Fig. 1.28. The salt shows metallic conductivity down to 1.3 K despite its 1D structure of DMe-DCNQI molecules. The reason why the salt shows metallic conductivity in low temperature is the strong hybridization effect between the π-orbital of DMe-DCNQI molecules and d-orbital of $Cu^{4/3+}$ atoms, while the orbitals have nearly same energies. The π-d hybridization bridges 1D-conductive columns and makes the Fermi surface three dimensional [130]. When the weak pressure ($\sim$0.1 kbar) is applied to the crystal, an insulating phase is stabilized at low temperature as shown in Fig. 1.29a. The detail of the MI transition has been investigated by the chemical modification which can expand or reduce inter-molecular distances as weak pressures is applied, as shown in Figs. 1.29, 1.30, 1.31. Some researches reveal the importance of the orbital hybridization which largely depends on the angles of N-Cu-N [134, 135]. The physical properties of the DCNQI-type salts are owing to the π-d hybridization, however, the magnetism does not coexist with metallic conductivity. In the metallic phase, not only π-electrons of DCNQI molecules but also d-electrons of the $Cu^{4/3+}$ atoms contribute the metallic conductivity, therefore no localized magnetic moment is observed. On the other hand, in the insulating phase, there are localized magnetic moments of d-electrons with Weiss temperature ~ -13 K suggesting the presence of the π-d interaction, but the conductivity is very low.

In the recent researches, there are some π-d interaction systems having direct interaction between the conductivity and the magnetism , where the conductivities can be controlled by the magnetic field.

(DMET)$_2$FeBr$_4$ consists of a TTF-type conductive donor molecule DMET (see,

Fig. 1.21) and magnetic anion $FeBr_4^-$ as shown in Figs. 1.32. The fields of the magnetic susceptibility having anomalies (Figs. 1.33a and 1.34a) are in good agreement with those the magnetoresistance (Figs. 1.33b and 1.34b), suggesting an important role of the magnetism in the electron transport. The origin of the negative magnetoresistance is the enhancement of the SDW gap caused by the periodic magnetic potential of antiferromagnetically aligned $FeBr_4^-$ anion.

The phthalocyanine complexes of Fe^{3+} ($S = 1/2$) and Co^{3+} ($S = 0$) show a quite different behaviors despite the same crystal structure, as shown in Fig. 1.35. The resistivity of the magnetic salt rapidly increases as the temperature is lowered, while that of the non-magnetic salts salts increases more gradually. The difference between these two salts suggests that the random potential of the paramagnetic localized magnetic moments scatters the conductive electrons. This hypothesis is evidenced by the magnetoresistance of the Fe^{3+} salt as shown in Fig. 1.36. The magnetic salt shows a large negative magnetoresistances explained by that the random magnetic potential is weakened in high field region where the magnetic moments are aligned parallelly.

At last, the most stimulating phenomenon is the field induced superconductivity of λ-$(BETS)_2FeCl_4$ [18] (BEST; see, Fig. 1.21). λ-$(BETS)_2FeCl_4$ takes place an antiferromagnetic transition of anions accompanied by a MI transition of π-electrons, whereas the non-magnetic analogue λ-$(BETS)_2GaCl_4$ causes the metal-superconductor transition at ca. 5 K (Fig. 1.37). The suppression of the superconductivity in $FeCl_4^-$ salt is owing to the strong internal field at the π-electron system caused by the localized magnetic moments of anions. When the strong magnetic field is applied to the salt, the resistance rapidly decreases in the low field region ($H < 12$ T) suggesting a field induced insulator-metal (IM) transition. Above the IM transition, the resistance gradually increases as the field is raised, followed by a steep drop of the resistance; that is, the field induced metal-superconductor transition. The origin of the transition is as follows. At first, the superconductivity is suppressed by the internal field caused by the anions, where the internal field is antiparallel to the external field due to the antiferromagnetic π-d interaction. The internal field is stronger than the external field below ca. 15 T and does not change in the high field region because the field is higher than the

saturation field of the anions. Consequently, when the external field is raised, the external field just cancel the internal field at the point, resulting in the restoration of the superconductivity.

As mentioned above, the discoveries of the new π-d systems have deepened our understanding of π-d systems. However, the weakness of the π-d interaction ($\sim$ few Kelvin) is a critical weak point for applications.

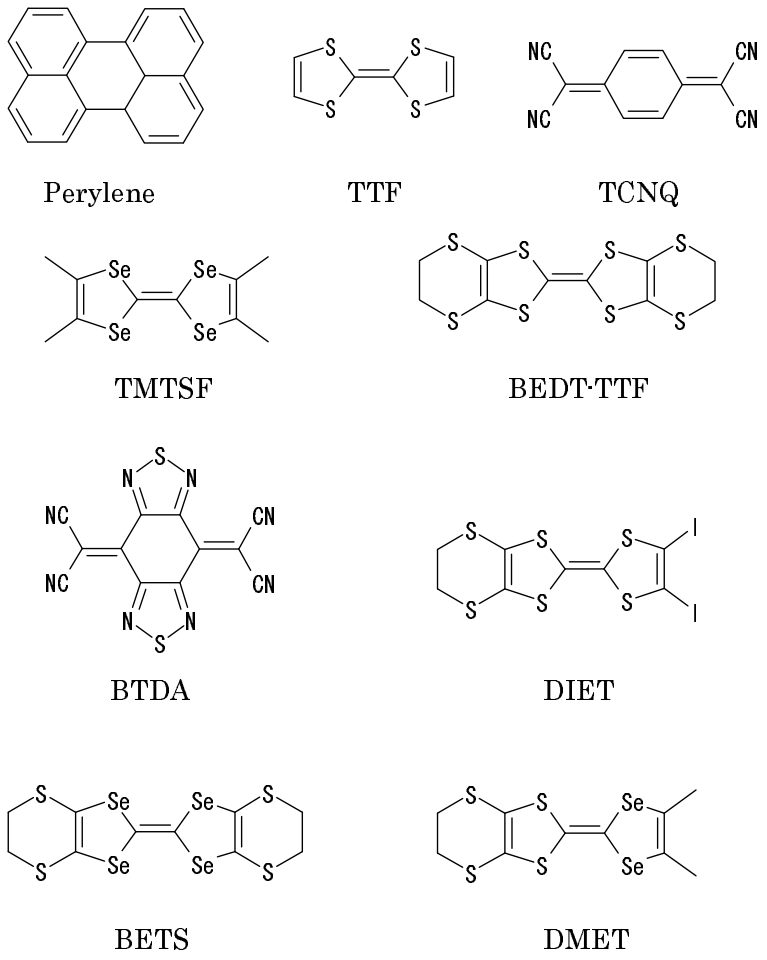

Fig. 1.21. The structure of typical donor and acceptor molecules. Perylene, the first high-conductive organic molecule, first pure organic metal TTF·TCNQ, first organic superconductor TMTSF, base of many organic metal/superconductors BEDT-TTF, BTDA and DIET which have structure control function groups!%

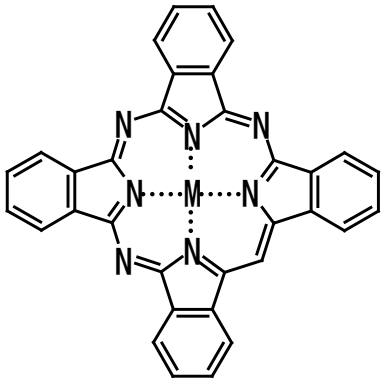

Fig. 1.22. The structure of MPc(Pc=Phthalocyanine).

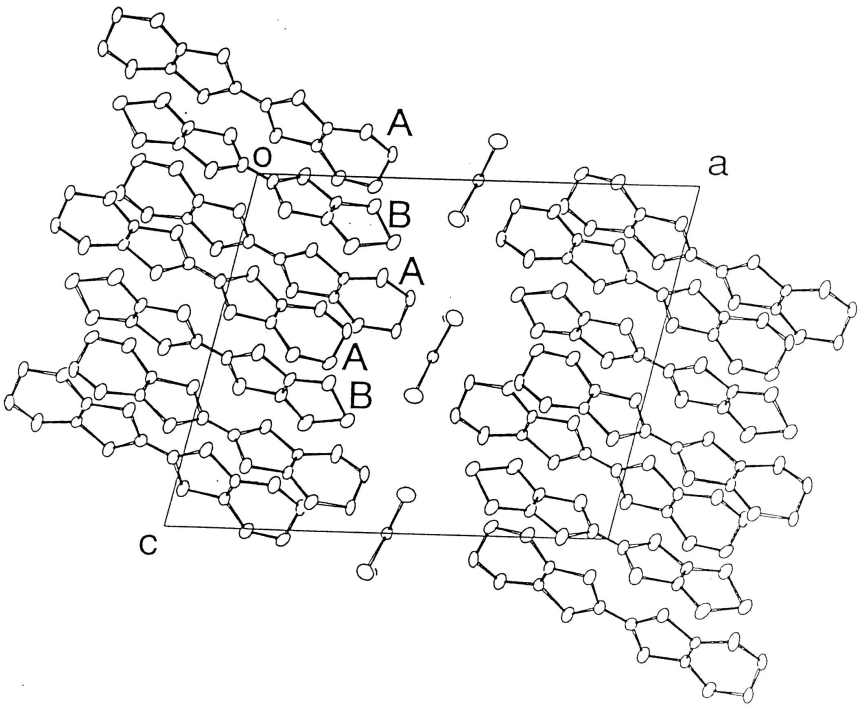

Fig. 1.23. The crystal structure of BEDT-TTF_3CuBr_4 [129].

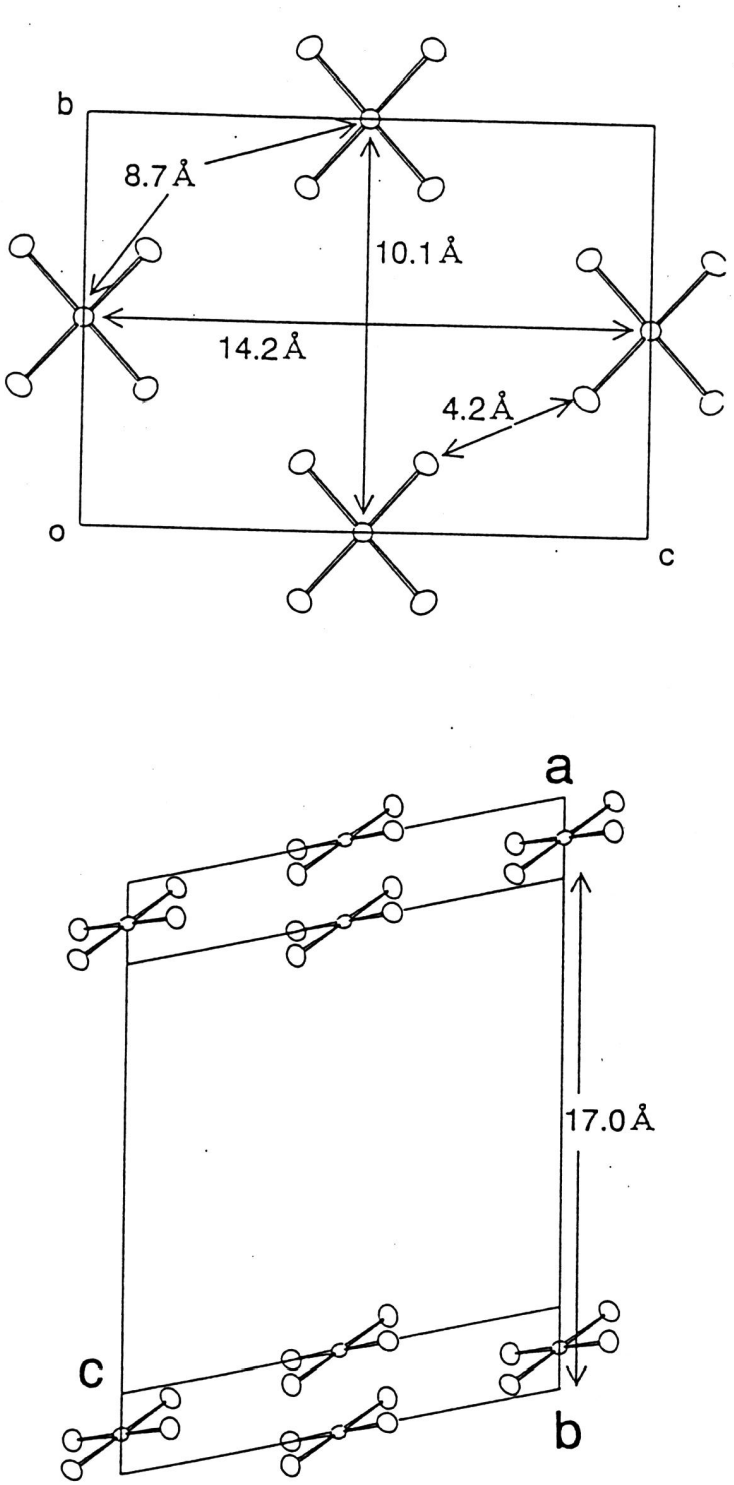

Fig. 1.24. Anion-anion distances of BEDT-TTF_3CuBr_4 [129]. Anion-anion direct interaction is weak due to long anion-anion distances.

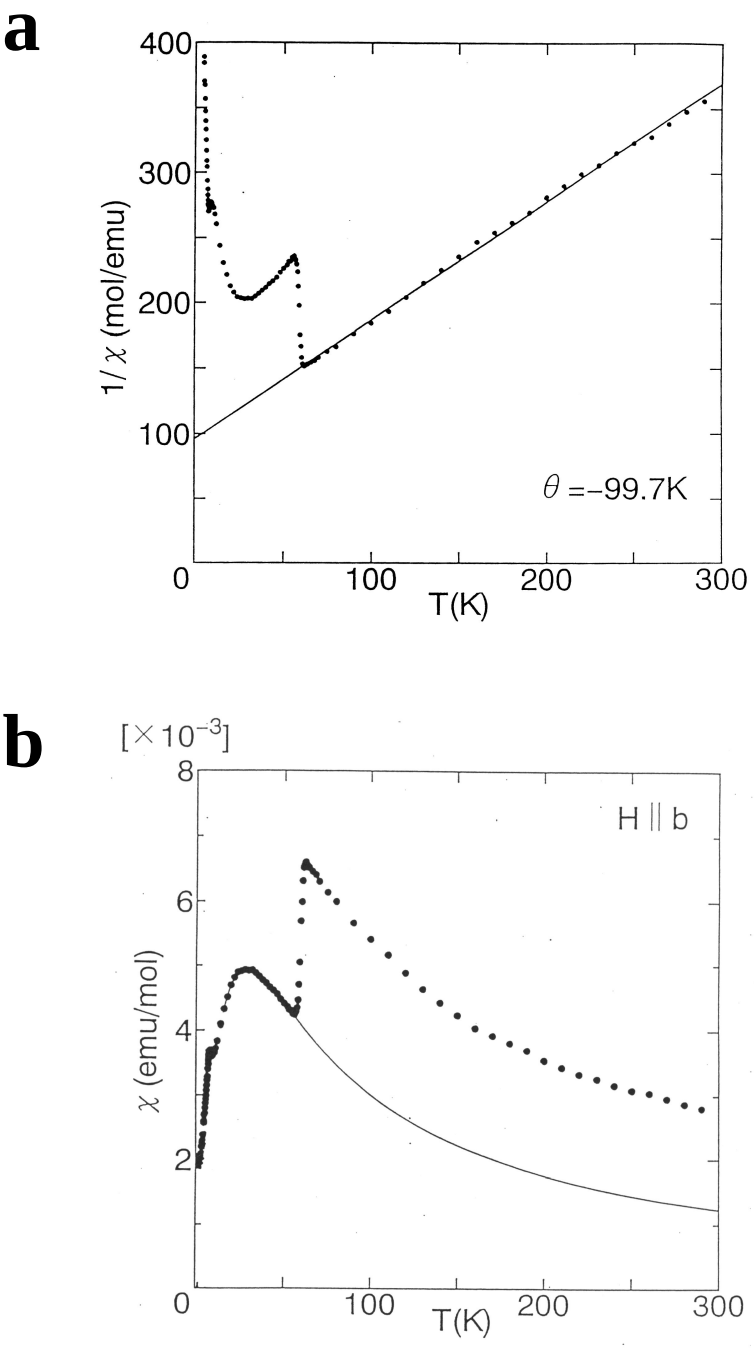

Fig. 1.25. **(a)** Inverse susceptibility of BEDT-TTF$_3$CuBr$_4$ fitted by Curie-Weiss low ($\theta = -99.7$ K) in the high temperature region and **(b)** magnetic susceptibility fitted by 2D square lattice Heisenberg model ($J = -15.7$ K) [129]. A sudden decrease of the susceptibility at around 60 K is due to the dimerization of magnetic donor molecules.

atom-atom	distance	van der waals radius
Br-Br	4.4	3.7
Br-C	3.651	3.65
Br-S	3.699	3.80
Cu-S	3.478	3.15(Å)

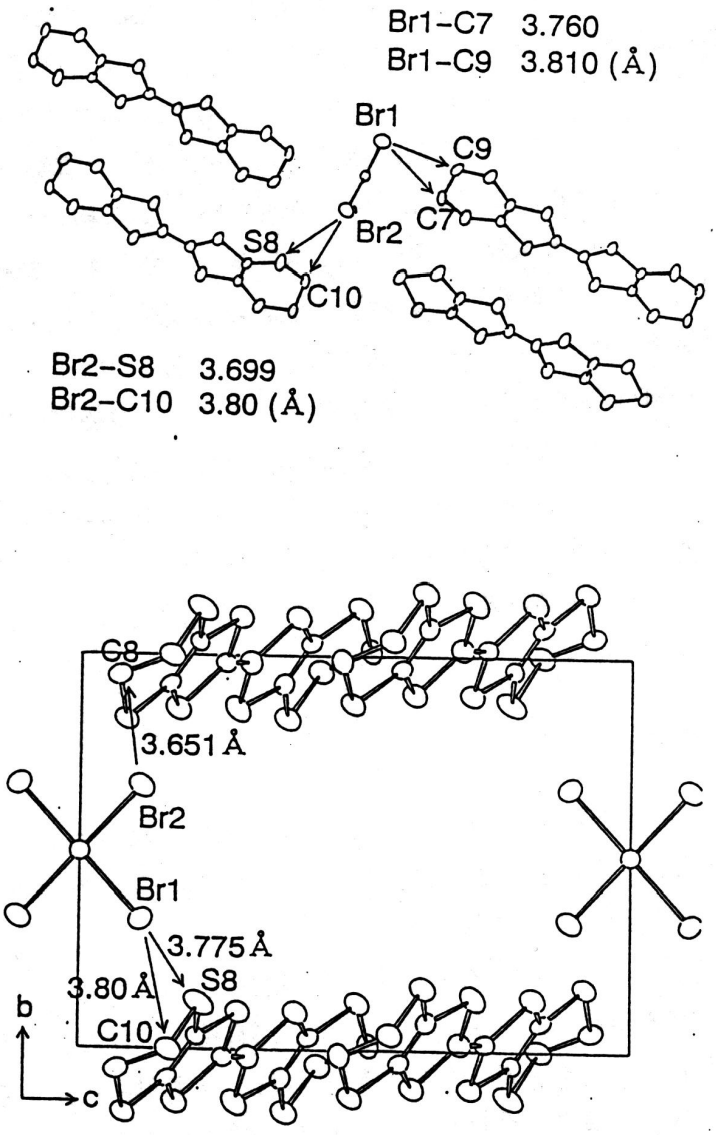

Fig. 1.26. Anion-donor distances of BEDT-TTF_3CuBr_4 [129].

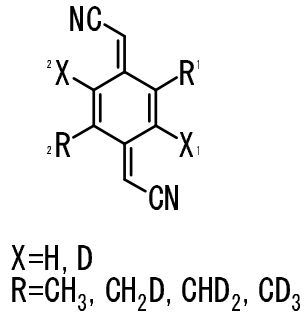

Fig. 1.27. Molecular structure of DMe-DCNQI.

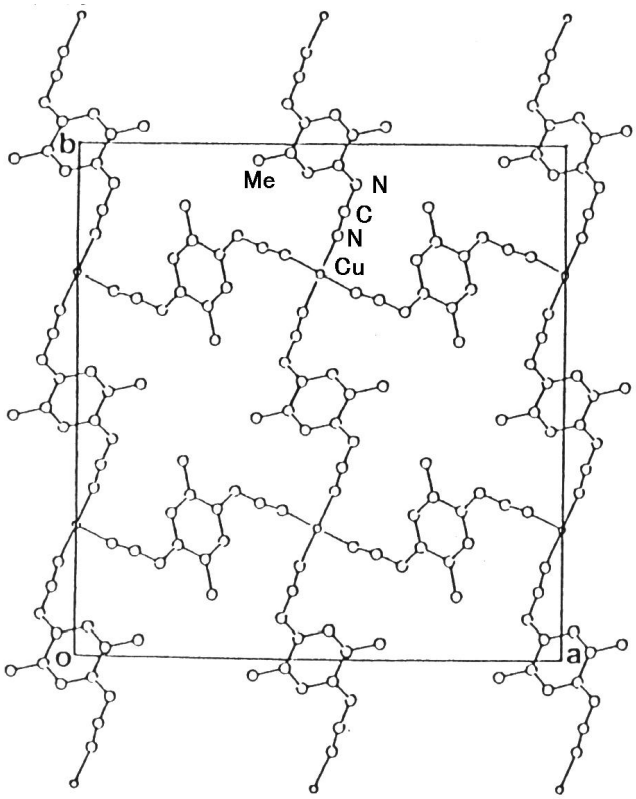

Fig. 1.28. The structure of DCNQI-Cu [131]. Both Cu atoms and DCNQI form conductive 1D chain structure elongated parallel to *c*-axis. These materials are the first series of organic 3D metal, where Cu atoms bridge DCNQI molecules in *a*- and *b*-directions. This bridging structure and $Cu^{+4/3}$ having localized magnetic moment causes the strong π-*d* interaction.

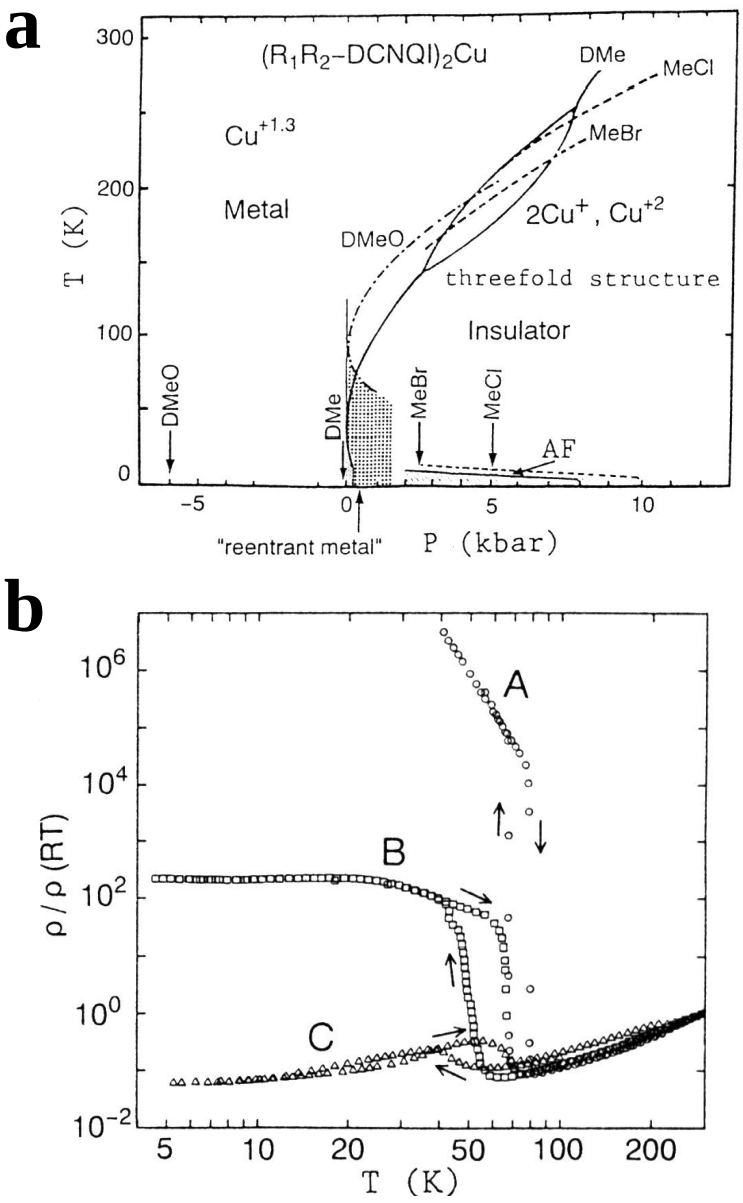

Fig. 1.29. **(a)**Phase diagram of DCNQI [131]. Substituting two methyl group of DMe-DCNQI causes the change of MI phase boundary. **(b)** Functional group dependency of conductivity. A, B and C represent $x \sim 0.1$, $x \sim 0.08$ and $x \sim 0.05$ of (DMe-DCNQI$_{1-x}$DBr-DCNQI$_x$)$_2$Cu,Cuespectively.

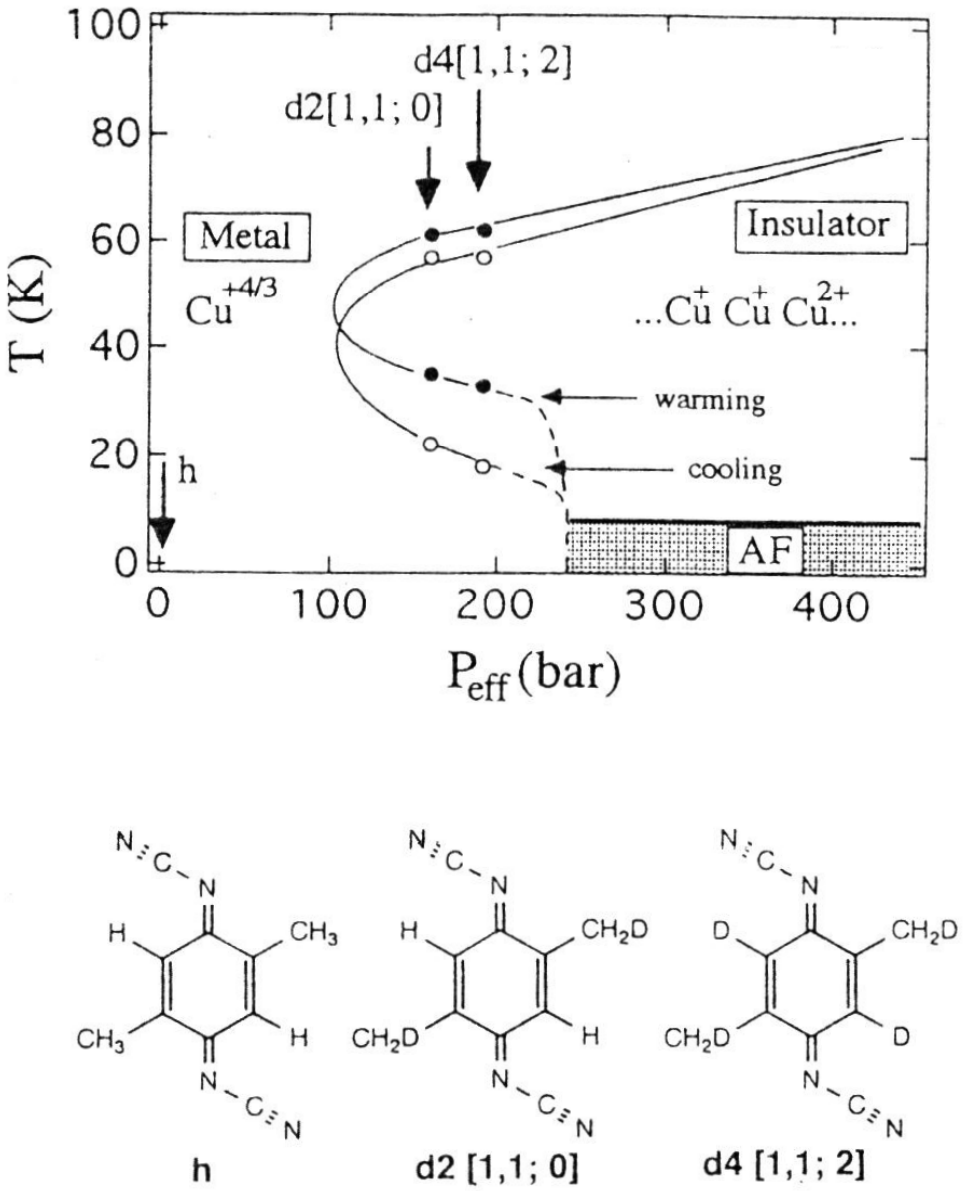

Fig. 1.30. Chemical pressure caused by deuterium substitution [132]. The chemical pressure stabilizes the insulating state at low temperature. The antiferromagnetic transition is observed lower temperature region of insulating state.

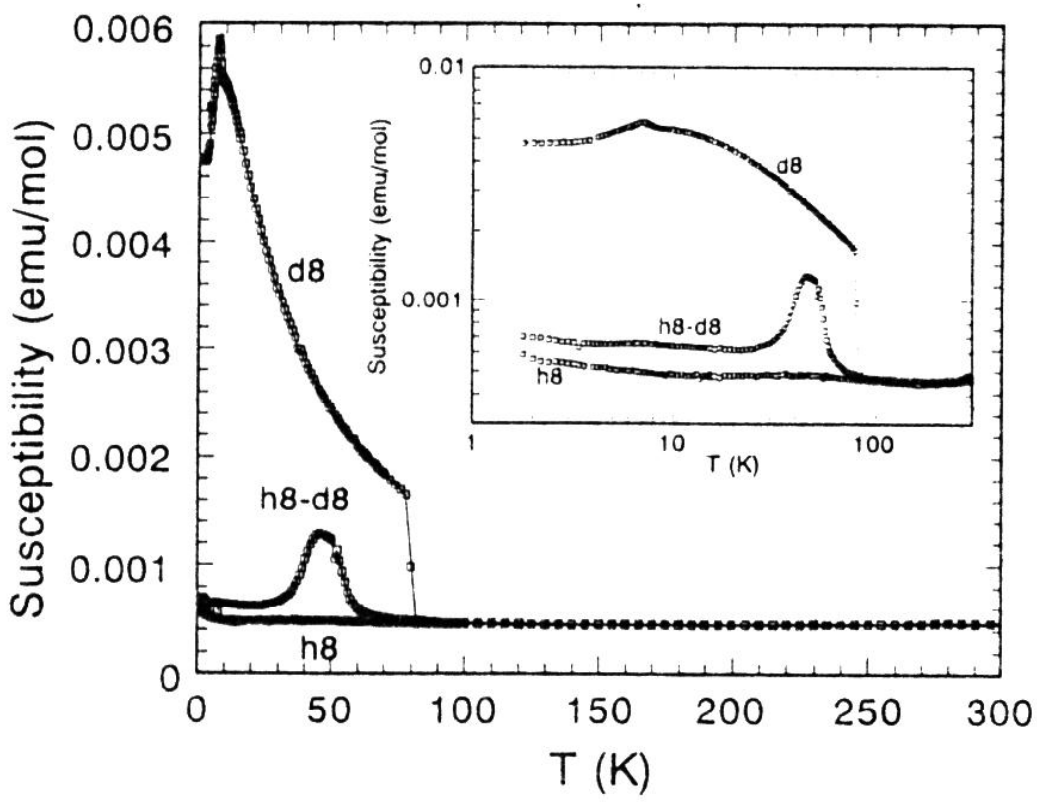

Fig. 1.31. The magnetic susceptibility of (DMe-DCNQI$_{1-x}$DMe-DCNQI-$d8_x$)$_2$Cu [133]. $d8\,!\,\$h8$-$d8\,!\,\$h8$ represent $x = 1\,!\,\$0.29\,!\,\$0$, respectively. MI transition causes the appearance of large localized magnetic moment, and the localized magnetic moment disappears in reentrant metallic phase.

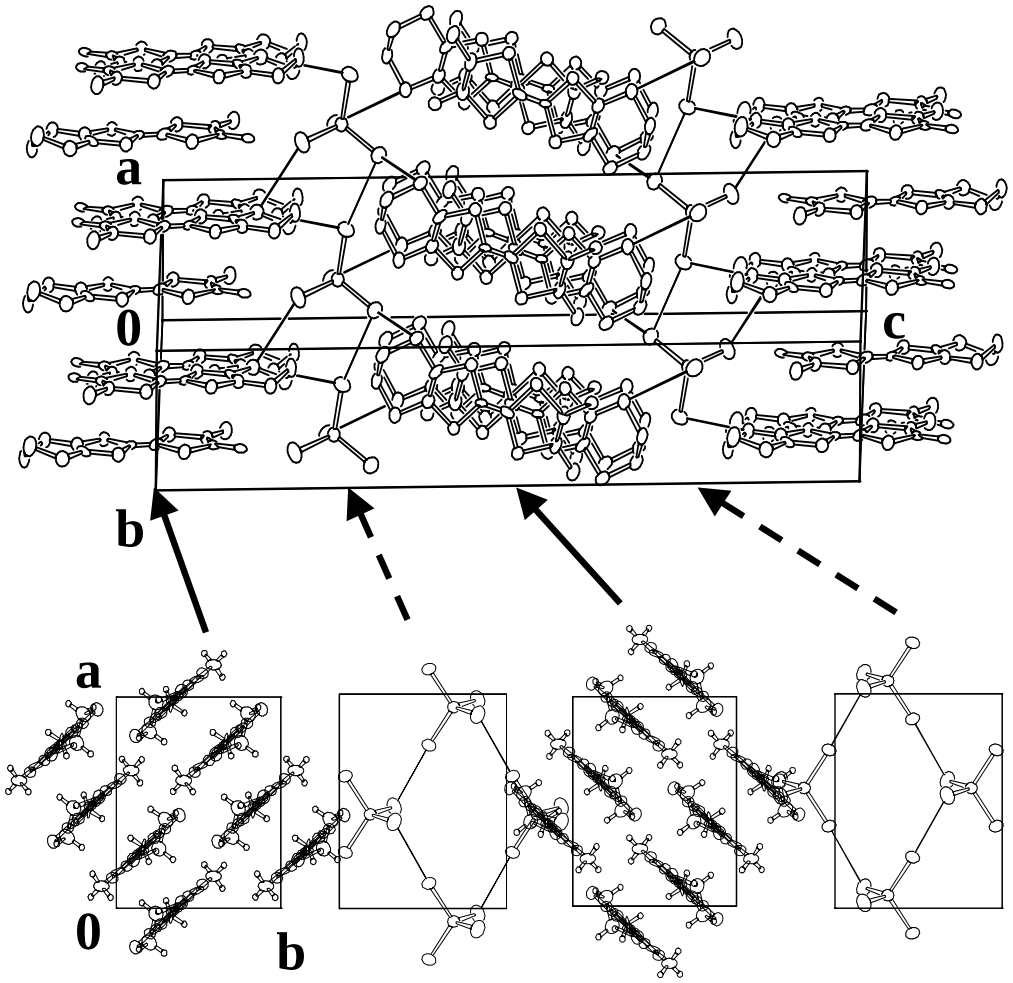

Fig. 1.32. The structure of $(DMET)_2FeBr_4$. The sheets of donor molecules and those of anion molecules are alternately stacked [113].

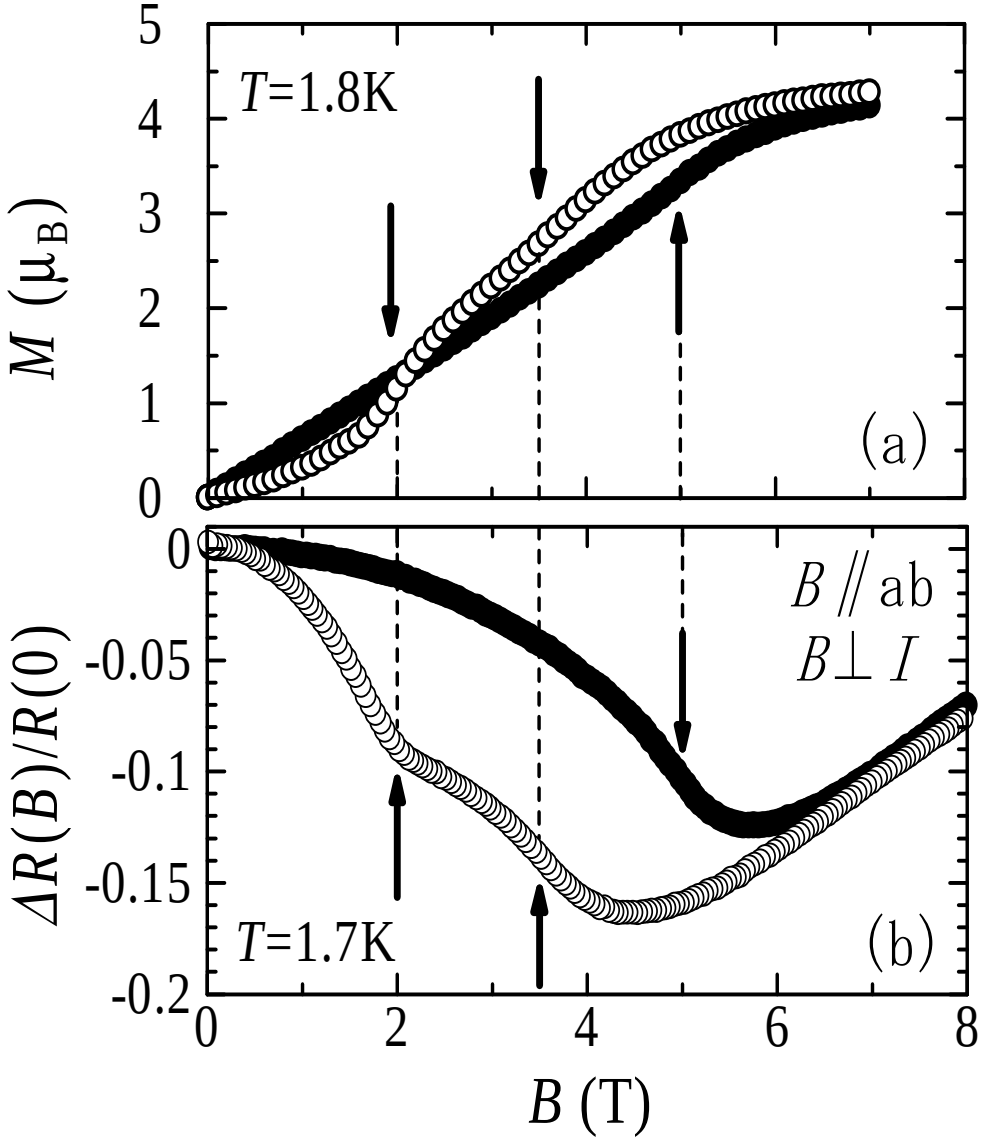

Fig. 1.33. **(a)**Magnetic susceptibility and **(b)**magnetoresistance [113] of $DMET_2FeBr_4$. The position of the anomalies of these two properties shows good agreement.

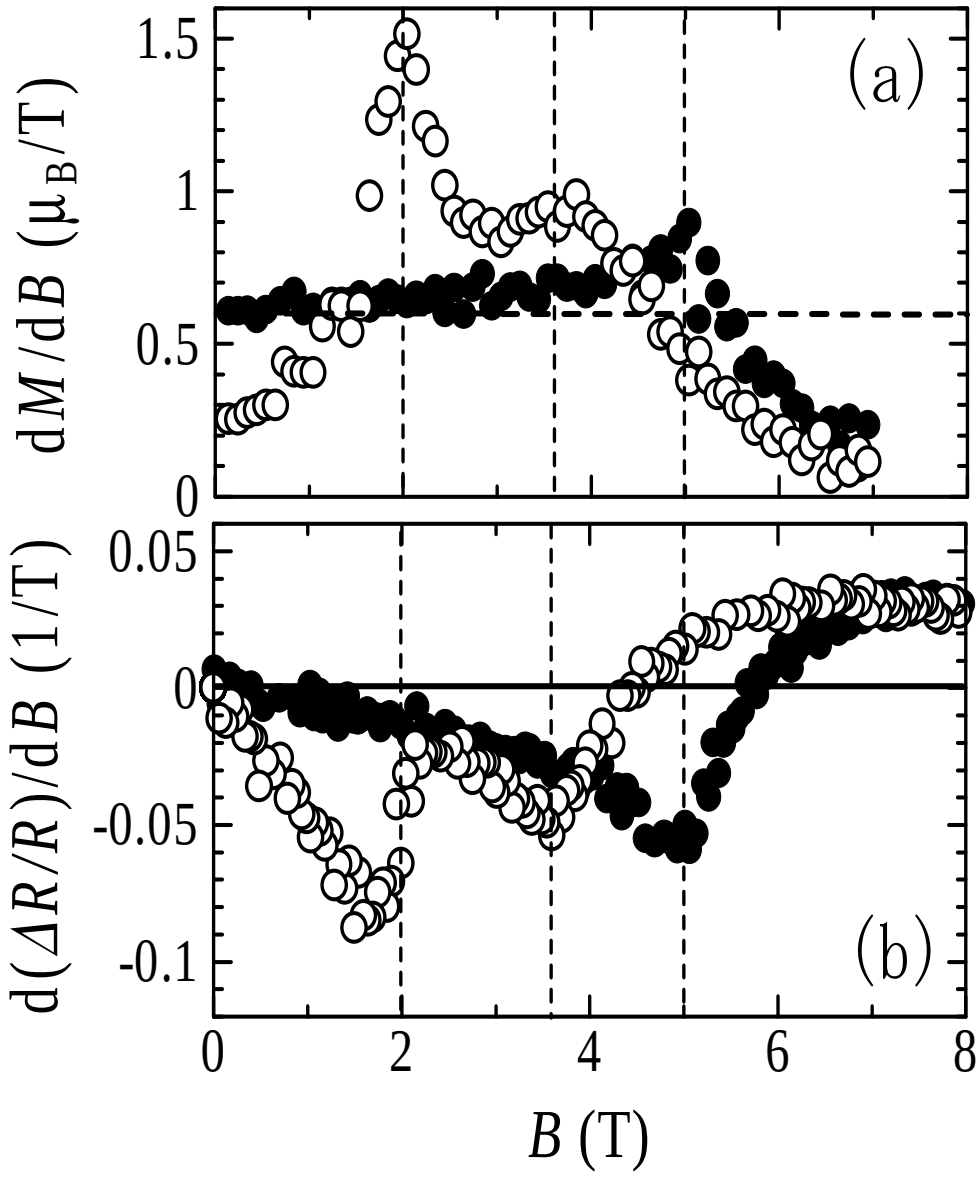

Fig. 1.34. The differential plot of Fig. 1.33 for emphasize the position of the anomalies [113].

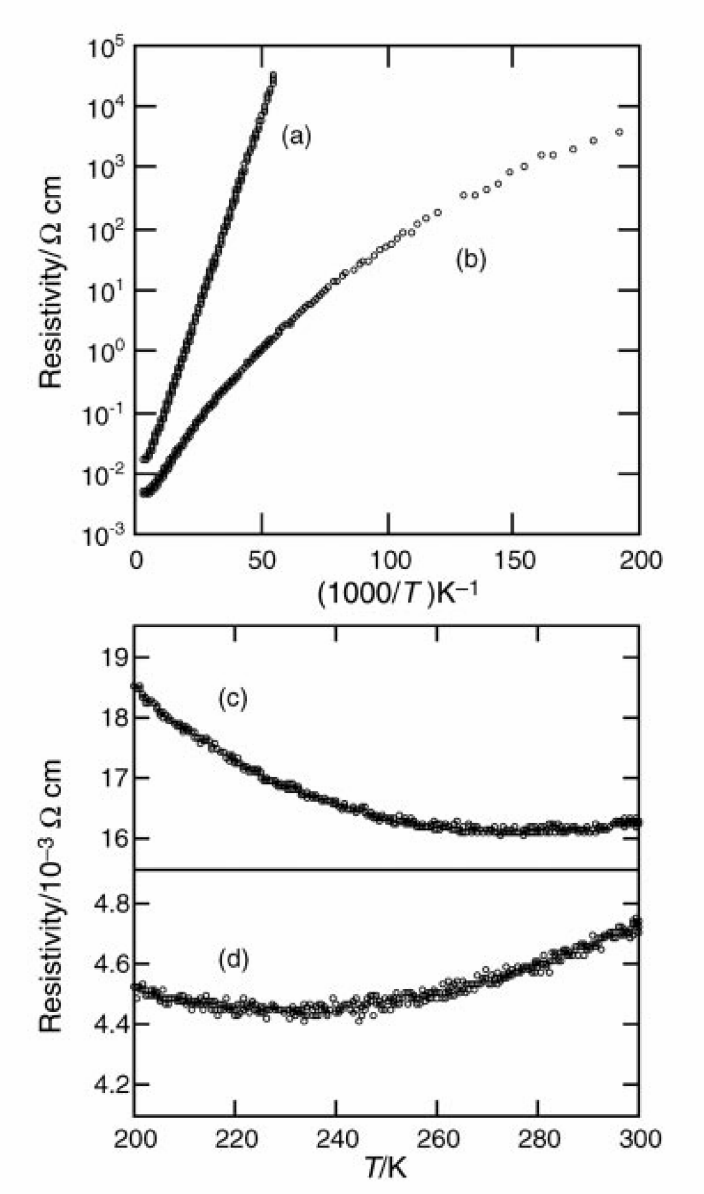

Fig. 1.35. Temperature dependence of the single-crystal resistivity of **(a)** $(PTMA)_x[Fe^{III}(Pc)(CN)2]_y(MeCN)$ and **(b)** $(PTMA)_x[Co^{III}(Pc)(CN)_2]_y(MeCN)$, and corresponding curves in the high temperature region, **(c)** and **(d)** [136].

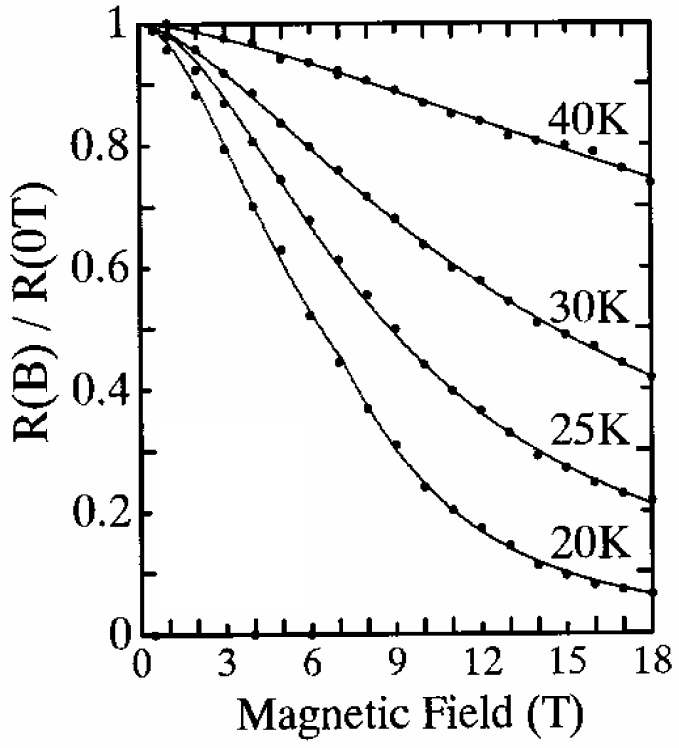

Fig. 1.36. Field dependence of the resistivity of Fe^{III} salt [13].

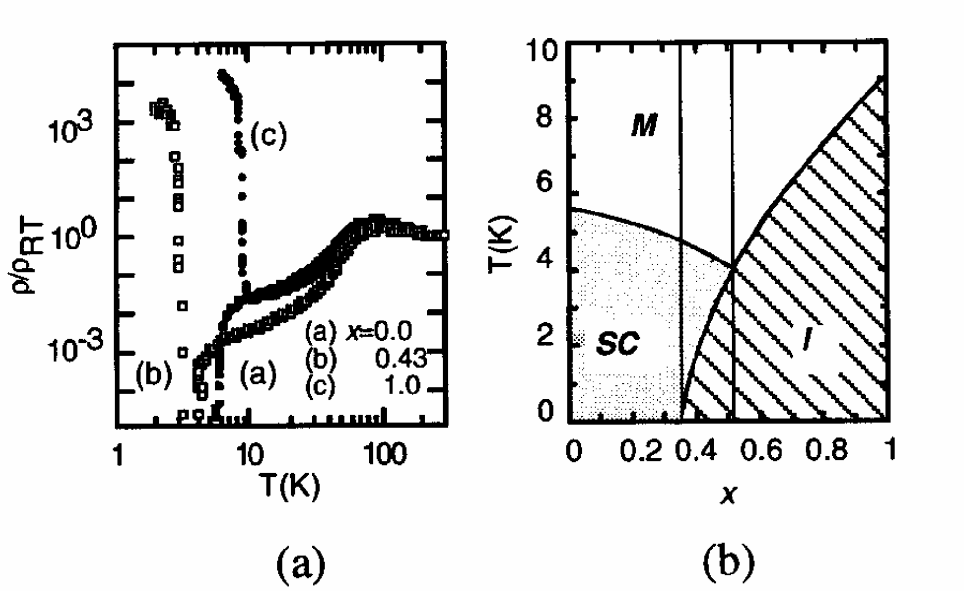

Fig. 1.37. **(a)** The $FeCl_4^-$ concentration dependence of the resistivity, and **(b)** phase diagram.

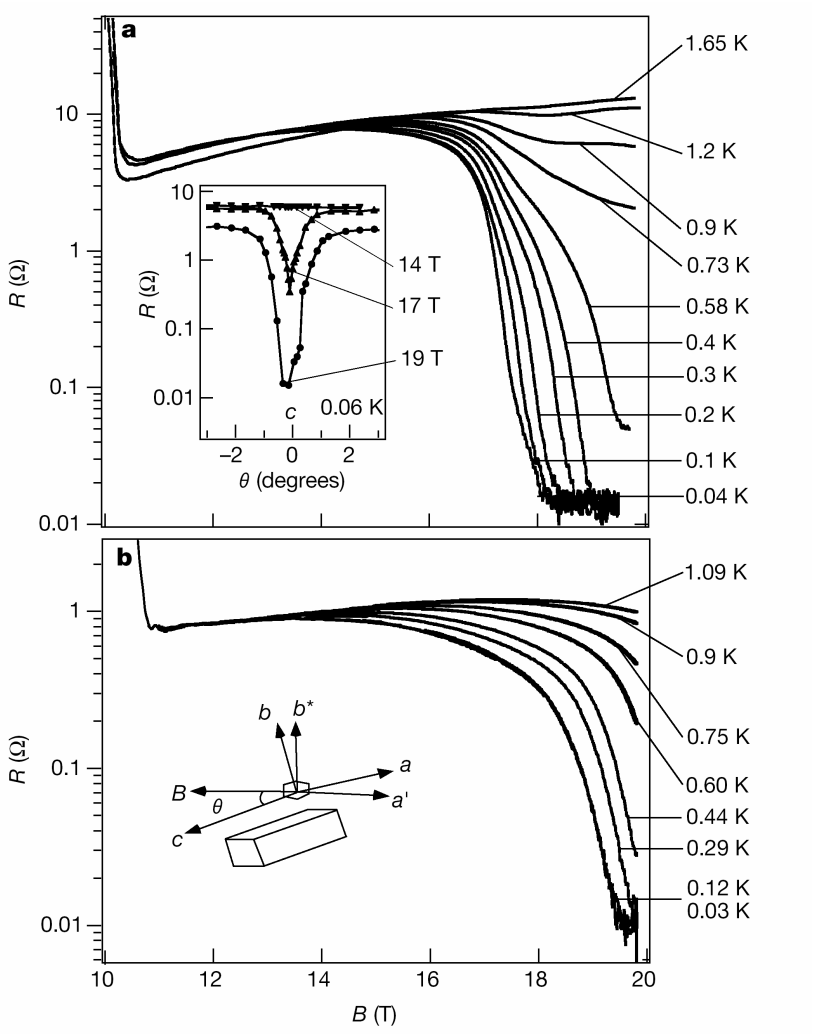

Fig. 1.38. Inter-layer resistance (for current parallel to the b^*-axis) when the magnetic field is exactly parallel to the conduction layers. A steep decrease is evident at high fields, suggesting a superconducting transition. **(a)** Resistance when the magnetic field is parallel to the c-axis. The inset shows the field-direction dependence of the resistance under the field in the $b^* \pm c$-plane. **(b)** Resistance when the magnetic field is parallel to the a^*-axis.

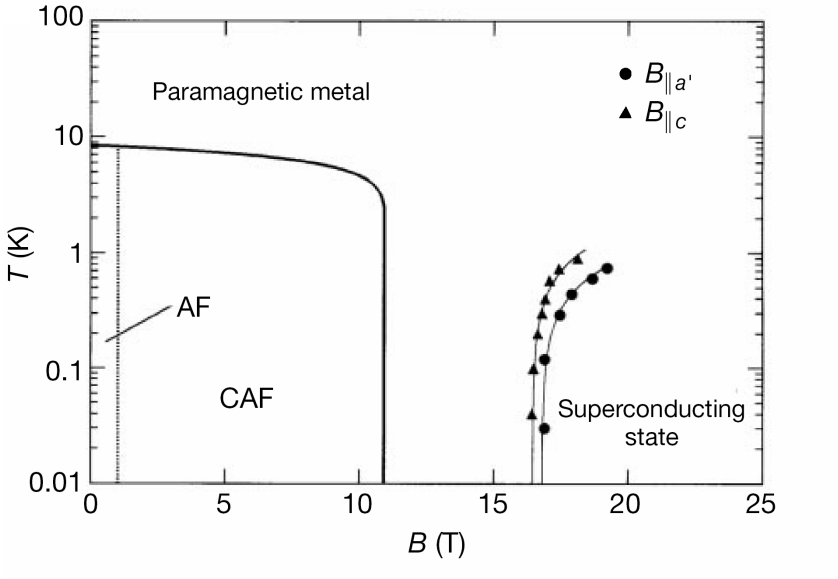

Fig. 1.39. The phase diagram of the λ-$(BETS)_2FeCl_4$.

1.5 Aim of the present research

Organic conductors having π-d interaction show many interesting features, though their π-d interactions are, regrettably, very weak in comparison with s-d interaction in traditional metal magnets because localized magnetic electrons and conductive electrons are separatedly placed on different molecules. Molecule-based device is a promising tool to achieve smaller, highly-integrated multi-functional devices. To apply the π-d systems to molecule-based devices, it is necessary to strengthen the π-d interaction as mentioned in the beginning of this chapter. Therefore, the aim of this work is to establish the method which increase the π-d interaction.

To increase the effect of π-d interaction, there are five useful strategies. The first is to take the conductive π-electron system to the MI phase boundary[‖]. In the vicinity of the phase boundary, two phases are competing, even a small perturbation can cause a large change in the electronic state including phase transition. In other words, this strategy can enhance the effect of π-d interaction. The second is using anions which have large magnetic moment. Magnetic interaction is described as $-J\boldsymbol{S}_\pi \cdot \boldsymbol{S}_\mathrm{d}$, therefore large $\boldsymbol{S}_\mathrm{d}$ causes strong interaction. The third is increasing spin density of magnetic anion at the point of contact between donor and anion molecules, which also causes strong interaction as same as the second strategy. The forth is increasing orbital overlap between conductive donors and magnetic anions, which increases the interaction $|J|$. The fifth is shortening the distance between π and d-systems, which also increases the interaction $|J|$. Achieving the above four strategies at the same time is, however, difficult due to several trade-off between these strategies. For example, when we try to increase donor-anion inter-molecular overlap by introducing the atom which has a large van der Waals radius into TTF-type conductive donor, the atom also also increases donor-donor inter-molecular overlaps which stabilize metallic state of π-electrons. This works contrary to the first strategy. Similarly, the second strategy frequently conflicts with the third strategy. When we want to use an anion having large magnetic

[‖]Of course, we can use other type of phase boundary, for example metal-superconductor phase boundary such as λ-$(\mathrm{BETS})_2\mathrm{FeBr}_4$ [16]. However, it is easier to achieve the phase boundary between metal and insulator rather than that of metal and superconductor.

moment, it is easy way to use high-spin transition metal complexes. However, high-spin state is stable only when the ligand field is weak. This means that d-orbital is not so hybridized with orbital of ligand. In contrast, f-orbital is too small to be hybridized with the orbital of ligand, therefore inter-molecular interaction is weak [137, 138]. These facts indicate that high-spin complexes and, especially, lanthanide or actinide complexes have only small spin density at the ligand sites. What we want is the method which achieves these strategies without any conflict with other strategies.

To achieve the request mentioned above, I used the two types of molecules; that is, halogenated TTF-type donors, EDT-TTFBr_2 and EDO-TTFI_2, and sulfur-containing transition metal complexes of crown thioethers (see, Fig. 1.40).

1.5.1 Halogenated TTF-type donors

Different from the other strategies, the fifth strategy, shortening the distance between π and d-systems, has no conflict with other strategies. What this strategy do is only to increase the overlap between donor and anion molecular orbitals, therefore it is suitable for our purpose. According to the recent works of "Crystal Engineering", which aims to control a crystal structure by chemical-designed molecules, it is revealed that halogenated TTF donors shorten distances between halogen atom of donor and halogen atom or cyano group of anion [139–143]. Therefore, it is expected that we can obtain strong π-d interaction system by using halogenated donors and halogen or cyano group coordinated transition metal complexes.

Under this plan, I build the new π-d systems (EDT-TTFBr_2)$_2$FeBr_4 (see, Chapter 3) and (EDO-TTFI_2)$_2$[M(mnt)$_2$] (M = Ni, Pt) (see, Chapter 5).

EDT-TTFBr_2 [145, 146] is a TTF-type donor molecule having bromine atoms as structure controlling groups. The counter anion of the donor is $FeBr_4^-$ having a large magnetic moment $S = 5/2$, while the bromine atoms of the anion are strongly attracted by the bromine atoms of the donor molecule. Consequently, a strong π-d interaction between through the short donor-anion contacts is expected in this material.

On the other hand, EDO-TTFI_2 [144] is also a halogenated TTF-type donor,

while the $[M(mnt)_2]^-$ anion is a dithiolate complex having cyano group and magnetic moment $S = 1/2$. The strong attractive interaction between iodine atoms of the donor and cyano groups of the anion also causes a short donor-anion contacts similarly to (EDT-TTFBr_2)$_2$FeBr_4. In addition, $[M(mnt)_2]^-$ is a well known anion as giving ferromagnetic interaction [147, 148], therefore not only strong π-d interaction but also ferromagnetic metal is expected in the crystal (EDO-TTFI_2)$_2$[M(mnt)$_2$].

1.5.2 Crown Thioether Complexes

There is a possibility of achieving the forth strategy, to increase inter-molecular overlaps between conductive molecule and magnetic molecule, without any conflict by chemical modification of magnetic transition metal complexes. The chemical modification of magnetic complexes can enhance the inter-molecular overlaps between conductive molecule and magnetic complexes, while inter-molecular overlaps between conductive molecules are unchanged. To enhance the inter-molecular overlaps, it is a useful method to introduce sulfur atoms in ligands of the transition metal complexes as proved in the results of BEDT-TTF mentioned above and dithiadiazolyl pure organic radicals having an extraordinary high transition temperature (36 K at ambient pressure [149] and 65 K under high pressure [150]).

In the surveying sulfur-containing ligands, I found out about the π-acidity of crown thioethers [151,152] which is suitable for the building block of the molecule-based magnets because the feature enhances the spin density at ligand and strengthen the inter-molecular interaction. As a result of the potential of a strong inter-molecular interaction, it is expected that the crown thioether complexes of transition metals gives not only a strong d-d interaction but also strong π-d interaction.

To confirm the ability of a strong interaction of crown thioether complexes, I build new series of molecule-based magnets [M(9S3)$_2$](TCNQ)$_n$ (M = Co, Ni; n = 2, 3), [M(9S3)Br_2] (M = $Cu_{1-x}Ni_x$; x = 0, 0.05) and [M(9S3)$_2$][Ni(bdt)$_2$]$_2$ (M = Ni, Co) having strong inter-molecular interactions as will be discussed in Chapter 4.

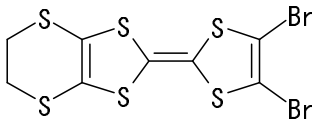

EDT-TTFBr$_2$

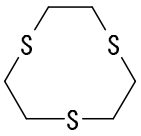

9S3

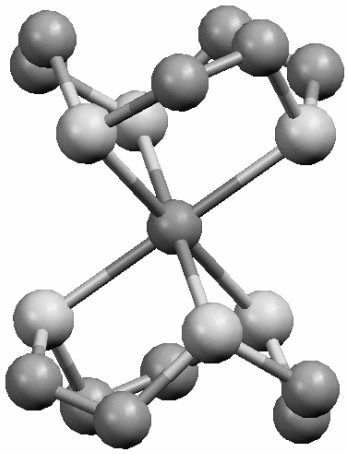

M(9S3)$_2^{2+}$

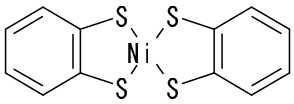

[Ni(bdt)$_2$]$^-$

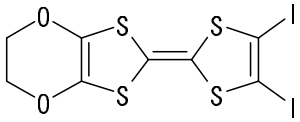

EDO-TTFI$_2$

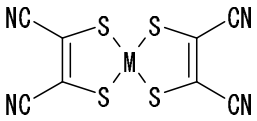

[M(mnt)$_2$]$^-$

Fig. 1.40. The molecular structures of EDT-TTFBr$_2$, 9S3, M(9S3)$_2^{2+}$, [Ni(bdt)$_2$]$^-$, EDO-TTFI$_2$ and [M(mnt)$_2$]$^-$.

References

[1] H. Akamatu, H. Inokuchi, Y. Matsunaga, *Nature*, **173**, 168 (1954).

[2] J. Ferraris, D. O. Cowan, V. Walatka Jr. and J. H. Perlstein, *J. Am. Chem. Soc.*, **95**, 948 (1973).

[3] D. Jerome, A. Mazaud, M. Ribault and K. Bechgaard, *J. Phys. Lett.*, **41**, 95 (1980).

[4] *Handbook of Organic Conductive Molecules and Polymers*, vol. 1, ed. H. S. Nalwa, Wiley-VCH, New York, 1997.

[5] P. Cassoux and J. S. Miller, in *Chemistry of Advanced Materials, An Overview*, ed. L. V. Interrante, M. J. Hampden-Smith, Wiley-VCH, New York, 1998, and references therein.

[6] *The Physics and Chemistry of Organic Superconductors*, ed. G. Saito and S. Kagoshima, Springer-Verlag, Berlin, 1990.

[7] *Low-Dimensional Conductors and Superconductors*, ed. D. J rome and L. G. Caron, NATO ASI series, series B: Physics vol. 155, Plenum Press, New York, 1985.

[8] R. Wesoowski, J. T. Haraldsen, J. L. Musfeldt, T. Barnes, M. Mas-Torrent, C. Rovira, R. T. Henriques and M. Almeida *Phys. Rev. B* **68**, 134405 (2003).

[9] A. Miyazaki, T. Kato, H. Yamazaki, T. Enoki, E. Ogura, Y. Kuwatani, M. Iyoda, J. Yamaura, *Phys. Rev. B*, **68**, 085108 (2003).

[10] Y. Imamura, S. Ten-no, K. Yonemitsu, and Y. Tanimura, *Chem. Phys. Lett.*, **298**, 15 (1998).

[11] Kawakami, Y. Kitagawa, S. Nakano, T. Taniguchi and K.Yamaguchi, *Mol.Cryst. Liq. Cryst.*, **379**, 489 (2002).

[12] H. Fukuyama, *Strong Correlation in Low-Dimensional Systems*, ed. A. Okaji and N. Kawakami, p128 (Springer, 1994).

[13] N. Hanasaki, H. Tajima, M. Matsuda, T. Naito and T. Inabe *Phys. Rev. B*, **62**, 5839 (2000).

[14] A. Miyazaki, K. Enomoto, K. Okabe, H. Yamazaki, J. Nishijo, T. Enoki, E. Ogura, K. Ugawa, Y. Kuwatani and M. Iyoda, *J. Solid State Chem.*, **168**, 547 (2002).

[15] H. Tajima, N. Hanasaki., M. Matsuda, F. Sakai, T. Naito and T. Inabe, *J. Solid State Chem.*, **168**, 509 (2002).

[16] H. Kobayashi, A. Kobayashi and Patrick Cassoux, *Chem. Soc. Rev.*, **29**, 325 (2000).

[17] M. Matsuda, N. Hanasaki, H. Tajima, T. Naito and T. Inabe, *Synthetic Metals*, **133**, 547 (2003).

[18] S. Uji, H. Shinagawa, T. Terashima, T. Yakabe, Y. Terai, M. Tokumoto, A. Kobayashi, H. Tanaka and H. Kobayashi, *Nature*, **410**, 908 (2001).

[19] *Functionality of Molecular System: From Molecular Systems to Molecular Devices*, ed. K. Honda, Springer Verlag, 1999.

[20] *Nanoelectronics and Nanosystems: From Transistors to Molecular and Quantum Devices*, ed. P. Glosekotter, J. Dienstuhl and K. Goser, Springer Verlag, 2004.

[21] I. Dzyaloshinskii, *Sov. Phys. JETP*, **5**, 1259 (1957). and T. Moriya, *Phys. Rev.*, **120**, 91 (1960).

[22] A. Miyazaki, K. Okabe, T. Enoki, F. Setifi, S. Golhen, L. Ouahab, T. Toita and J. Yamada, *Synth. Metals*, **137**, 1195 (2003).

[23] D. Mermin and H. Wagner, *Phys. Rev. Lett.* **17**, 1133 (1966).

[24] D. M. Haldane, *Phys. Rev. Lett.*, **50**, 1153 (1983).

[25] T. Koma and H. Tasaki, *Phys. Rev. Lett.*, **70**, 93 (1993), and the references therein.

[26] E. Ising, *Zeits. Physik* **49**, 619 (1928).

[27] T. Enoki, M. Enomoto, M. Enomoto, K. Yamaguchi, N. Yoneyama, J. Yamaura, A. Miyazaki and G. Saito, *Mol. Crys. Liq. Cryst.* **285**, 19 (1996).

[28] For example, *Magnetism: Molecules to Materials*, vol. II, Molecule-Based Materials, ed. J. S. Miller and M. Drillon, Wiley-VCH, Weinheim.

[29] K. Itoh, *Chem. Phys. Lett.*, **1** 235 (1967).

[30] L. Wasserman, R. W. Murray, W. A. Yager, A. M. Trozzolo and G. J. Somolinsky, *J. Am. Chem. Soc.*, **89**, 5076 (1967).

[31] I. Fujita, Y. Teki, T. Takui, T. Kinoshita, K. Itoh, F. Miko, Y. Sawaki, H. Iwamura, A. Izuoka and T. Sugawara, *J. Am. Chem. Soc.*, **112**, 4074 (1990).

[32] N. Nakamura, K. Inoue and H. Iwamura, *Angew. Chem. Int. Ed. Engl.*, **32**, 872 (1993).

[33] K. Inoue, N. Koga and H. Iwamura, *J. Am. Chem. Soc.*, **113**, 9803 (1991).

[34] T. Ishida, K. Inoue, N. Koga, N. Nakamura and H. Iwamura, *Mat. Res. Symp. Proc.*, **247**, 407 (1992).

[35] M. Tamura, Y. Nakazawa, D. Shiomi, K. Nozawa, Y. Hosokoshi, M. Ishikawa, M. Takahashi and M. Kinoshita, *Chem. Phys. Lett.*, **186**, 401 (1991).

[36] N. Nakamura, K. Inoue, H. Iwamura, T. Fujioka and Y. Sawaki, *J. Am. Chem. Soc.*, **114**, 1484 (1992)

[37] T. Sugawara, S. Bandow, K. Kimura, H. Iwamura and K. Itoh, *J. Am. Chem. Soc.*, **108**, 368 (1986).

[38] R. Chiarelli, M. A. Novak, A. Rassat and J. L. Tholence, *Nature* **363**, 147 (1993).

[39] O. Kahn, *Molecular Magnetism*, Wiley-VCH, New York, 1993.

[40] M. Verdaguer, *Polyhedron*, **20**, 1115 (2001).

[41] J. Cano, P. Alemany, S. Alvarez, M. Verdaguer and E. Ruiz, *Chem. Eur. J.*, **4**, 476 (1998).

[42] E. Ruiz, J. Cano, S. Alvarez and P. Alemany, *J. Am. Chem. Soc.*, **120**, 11122 (1998).

[43] J. Cui, C. Peng, D. Liao, Z. Jiang, S. Yan, G. Wang, X. Huang, *Polyhedron*, **17**, 2517 (1998).

[44] O. Kahn and B. Briat, *J. Chem. Soc. Faraday Trans.*, **72**, 268 and 1441 (1976).

[45] J.J. Girerd, Y. Journaux and O. Kahn, *Chem. Phys. Lett.*, **82**, 534 (1981).

[46] D. Babel, *Comm. Inorg. Chem.*, **5**, 285 (1986).

[47] K. Inoue and H. Iwamura, *J. Chem. Soc., Chem. Commun.*, 2273 (1994)

[48] M. Ohba, N. Usuki, N. Fukita and H. Okawa, *Angew. Chem. Int. Ed. Engl.*, **38**, 1795 (1999).

[49] M. Julve, M. Verdaguer, O. Kahn, A. Gleizes and M. Philoche-Levisalles, *Inorg. Chem.*, **22**, 368 (1983).

[50] M. Julve, M. Verdaguer, O. Kahn, A. Gleizes and M. Philoche-Levisalles, *Inorg. Chem.*, **23**, 3808 (1984).

[51] J. Cano, P. Alemany, S. Alvarez, M. Verdaguer and E. Ruiz, *Chem. Eur. J.*, **4**, 472 (1998).

[52] O. Kahn, Y. Pei, M. Verdaguer, J. P. Renard and J. Sletten, *J. Am. Chem. Soc.*, **110**, 782 (1988)

[53] J. S. Miller, J. C. Calabrese, H. Rommelmann, S. R. Chittipedi, J. H. Zhang, W. M. Reiff and A. J. Epstein, *J. Am. Chem. Soc.*, **109**, 769 (1987).

[54] R. Sessoli, D. Gatteschi, A. Caneschi and M. A. Novak, *Nature*, **365**, 141 (1993).

[55] C. Paulsen, J. G. Park, B. Barbara, R. Sessoli and A. Caneschi, *J. Magn. Magn. Mater.*, **140-144**, 1891 (1995).

[56] C. Delfs, D. Gatteschi, L. Pardi, R. Sessoli, K. Wieghardt and D. Hanke, *Inorg. Chem.*, **32**, 3099 (1993).

[57] A. L. Barra, P. Debrunner, D. Gatteschi, Ch. E. Shultz and R. Sessoli, *Europhys Lett.*, **35**, 133 (1996).

[58] N. Ishikawa, M. Sugita, T. Ishikawa, S. Koshihara and Y. Kaizu, *J. Am. Chem. Soc.*, **125**, 8694 (2003).

[59] A. Caneschi, D. Gatteschi, N. Lalioti, C. Sangregorio, R. Sessoli, G. Venturi, A. Vindigni, A. Rettori, M. G. Pini and M. A. Novak, *Angew. Chem. Int. Ed. Engl.* **40**, 1760 (2001).

[60] A. Caneschi, D. Gatteschi, N. Lalioti, C. Sangregorio and R. Sessoli, *J. Chem. Soc. Dalton Trans.*, 3907 (2000).

[61] R. Cl rac, H. Miyasaka, M. Yamashita and C. Coulon, *J. Am. Chem.Soc.*, **124**, 12837 (2002).

[62] A. Kamiyama, T. Noguchi, T. Kajiwara and T. Ito, *Inorg. Chem.*, **41**, 507 (2002),

[63] P. Fazekas and P. W. Anderson, *Phylos. Mag.*, **30**, 423 (1974).

[64] X. G. Wen, F. Wilczek and A. Zee, *Phys. Rev. B*, **39**, 11413 (1989).

[65] P. Chandra and P. Coleman, *Phys. Rev. Lett.* **66**, 100 (1991).

[66] K. Awaga, T. Okuno, A. Yamaguchi, M. Hasegawa, T. Inabe, Y. Maruyama and N. Wada, *Phys. Rev. B*, **49**, 3975 (1994).

[67] M. Tamura and R. Kato, *J. Phys.: Condens. Matter*, **14**, L729 (2002).

[68] E. Coronado, J. R. Galan-Mascaros, C. J. G mez-García and J. M. Martinez-Agugo, *Inorg. Chem.*, **40**, 113 (2001).

[69] D. Armentano, G. D. Munno, F. Lloret, A. V. Palii and M. Julve, *Inorg. Chem.*, **41**, 2007 (2002).

[70] M. Minguet, D. Luneau, E. Lhotel, V. Villar, C. Paulsen, D. B. Amabilino and J. Veciana, *Angew. Chem., Int. Ed.*, **40**, 586 (2002).

[71] S. Karasawa, H. Kumada, N. Koga and H. Iwamura, *J. Am. Chem. Soc.*, **123**, 9685 (2001).

[72] H. Kumagai and K. Inoue, *Angew. Chem., Int. Ed.*, **40**, 4242 (2001)

[73] M. Kuemoo, A. W. Graham, P. Day, S. J. Coles, M. B. Hursthouse, J. L. Caulfied, J. Singleton, F. L. Pratt, W. Hayes, L. Ducasse and Ph. Guionneau, *J. Am. Chem. Soc.*, **117**, 12209 (1995).

[74] S. Uji, H. Shinagawa, T. Terashima, T. Yakabe, Y. Terai, M. Tokumoto, A. Kobayashi, H. Tanaka and H. Kobayashi, *Nature*, **410**, 908 (2001).

[75] E. Coronado, J. R. Galan-Mascaros, C. J. Gomez-Garcia and V. Laukhin, *Nature*, **408**, 447 (2000).

[76] Y. Wang, N. S. Rogado, R. J. Cava and N. P. Ong, *Nature*, **423**, 425 (2003).

[77] R.E. Peierls, *Quantum Theory of Solids* p108, Oxford University Press, London (1955).

[78] J. H. de Boer, E. J. W. Verwey, *Proc. Plug. Soc.*, **49**, 59 (1937).

[79] N. Mott, *Proc. Phys. Soc.*, **A62**, 416 (1949).

[80] J. B. Torrance, *"Low Dimensional Conductors and Superconductors"*, Edited by D. J rome and L. G. Caron (NATO ASI Series B: Physics Vol.155, 1987)

[81] T. Mori, A. Kobayashi, Y. Sasaki and H. Kobayashi, *Bull. Chem. Soc. Jpn.*, **56**, 3376 (1983).

[82] *Chemistry of Advanced Materials, An Overview*, P. Cassoux and J. S. Miller, ed. L. V. Interrante, M. J. Hampden-Smith, Wiley-VCH, New York, 1998.

[83] J. W. Bray, H. R. Hart, Jr., L. V. Interrante, I. S. Jacobs, J. S. Kasper, G. D. Watkins, S. H. Wei and J. C. Bonner, *Phys. Rev. Lett.*, **35**, 744 (1975).

[84] I. S. Jacobs, J. W. Bray, H. R. Hart, Jr., L. V. Interrante, J. S. Kasper, G. D. Watkins, D. E. Prober and J. C. Bonner, *Phys. Rev. B*, **14**, 3036 (1976).

[85] S. Huizinga, J. Kommandeur, G. A. Sawatzky, B. T. Thole, K. Kopinga, W. J. M. de Jonge and J. Roos, *Phys. Rev. B*, **19**, 4723 (1979).

[86] B. W. Lovett, S. J. Blundell, F. L. Pratt, T. Jestadt, W. Hayes, S. Tagaki and M. Kurmoo, *Phys. Rev. B*, **61**, 12241 (2000).

[87] Y. Lin and J.E. Eldridge, *Phys. Rev. B* **58**, 3477 (1998).

[88] L. P. Gor'kov and A. G. Lebed, *J. Phys. Lett.*, **45**, L433 (1984).

[89] P. M. Chaikin, *Phys. Rev. B*, **31**, 4770 (1985).

[90] T. Ishiguro, K. Yamaji and G. Saito, *Organic Superconductors*, Second Edition, Springer-Verlag, Heidelberg, 1998.

[91] P. M. Chaikin, *J. Phys.*, **6**, 1875 (1996).

[92] K. Kanoda, T. Takahashi, T. Tokiwa, K. Kikuchi, K. Saito, I. Ikemoto and K. Kobayashi, *Phys. Rev. B*, **38**, 39 (1988).

[93] G. Saito, T. Enoki, K. Toriumi and H. Inokuchi, *Sold State Commun.*, **42**, 557 (1982).

[94] M. Bousseau, L. Valade, M. F. Bruniquel, P. Cassoux, M. Garbauskas, L. Interrante and J. Kasper, *Nouv. J. Chim.*, **4**, 3 (1984).

[95] T. Komatsu, T. Nakamura, N. Matsushita, H. Yamochi, G. Saito, H. Ito, T. Ishiguro, M. Kusunoki and K. Sakaguchi, *Solid State Commun.*, **80**, 843 (1991).

[96] A. Kobayashi, R. Kato, H. Kobayashi, S. Moriyama, Y. Nishino, K. Kajita and W. Sasaki, *Chem. Lett.*, 459 (1987).

[97] R. P. Shibaeva and L. P. Rozenberg, *Sov. Phys. Crystallogr.*, **33**, 834 (1988)

[98] A. Aum ller, P. Erk, G. Klebe, S. H nig, J. U. von Sch tz and H. P. Werner, *Angew. Chem. Int. Ed. Engle.*, **25**, 740 (1986).

[99] H. Tanaka, Y. Okano, H. Kobayashi, W. Suzuki and A. Kobayashi, *Science*, **291**, 285 (2001).

[100] *Handbook of Organic Conductive molecules and Polymers*, vol. 1, ed. H. S. Nalwa, John Wiley & Sons Inc., Chichester, 1997.

[101] *Science and Applications of Conducting Polymers*, ed. W. R. Salaneck, D. T. Clark and E. J. Samuelsen, Adam Hilger, Bristol, 1990.

[102] K. Nakatsu, N. Yoshie, H. Yoshioka, T. Nogami, Y. Shirota, Y. Shimizu, T. Uemiya and N. Yasuda, *Mol. Cryst. Liq. Cryst.*, **182A**, 59 (1990).

[103] S. Koshihara, Y. Ogawa, T. Ishikawa, M. Takesada, A. Oiwa, H. Munekata, T. Komori and J. Yoshino *Curr. App. Phys.* **1**, 21 (2001).

[104] F.Nad, P.Monceau and S. Brazovskii, *Phys. Rev. Lett.*, **86**, 4080 (2001).

[105] S.Horiuchi, R.Kumai, and Y.Tokura, *J. Am. Chem. Soc.*, **120**, 7379 (1998).

[106] P. A. Lee, T. M. Rice and P. W. Anderson, *Solid State Commun.*, **14**, 703 (1974).

[107] S. Kagoshima, H. Anzai, K. Kajimura and T. Ishiguro, *J. Phys. Soc. Jpn.*, **39**, 1143 (1975)

[108] D. Jŕome and H. J. Schulz, *Adv. Phys.*, **31**, 299 (1982).

[109] K. Kajita, T. Ojiro, H. Fujii, Y. Nishio, H. Kobayashi, A. Kobayashi and R. Kato, *J. Phys. Soc. Jpn.*, **61**, 23 (1992).

[110] T. Enoki, J.-I. Yamaura and A. Miyazaki, *Bull. Chem. Soc. Jpn.*, **70**, 2005 (1997).

[111] A. Sato, E. Ojima, H. Akutsu, Y. Nakazawa, H. Kobayashi, H. Tanaka, A. Kobayashi and P. Cassoux, *Phys. Rev. B*, **61**, 111 (2000).

[112] J. Nishijo, E. Ogura, J. Yamaura, A. Miyazaki, T. Enoki, T. Takano, Y. Kuwatani and M. Iyoda, *Solid State Comm.*, **116**, 661 (2000).

[113] K. Enomoto, J.-I. Yamaura, A. Miyazaki and T. Enoki, *Bull. Chem. Soc. Jpn.*, **76**, 945 (2003).

[114] M. Enomoto, A. Miyazaki, and T. Enoki, *Bull. Chem. Soc. Jpn.*, **74**, 459 (2001).

[115] K. Okabe, K. Enomoto, A. Miyazaki and T. Enoki, *Mol. Cryst. Liq. Cryst.*, **376**, 513 (2002).

[116] N. Hanasaki, H. Tajima, M. Matsuda, T. Naito and T.Inabe, *Phys. Rev. B*, **62**, 5839 (2000).

[117] N. Harrison, C.H. Mielke, D.G. Rickel, L.K. Montgomery,C. Gerst, J.D. Thompson, *Phys. Rev. B* **57**, 8751 (1998).

[118] A. K. Klehe, A. A. House, J. Singleton, W. Hayes, C. J. Kepert and P. Day, *Synth. Met.* **86**, 2003 (1997).

[119] J. Wosnitza, S. Wanka, J. Hagel, H. v. Lohneysen, J. S. Brooks, E. Balthes, J. A. Schlueter, U. Geiser, J. Mohtasham, R.W. Winter and G. L. Gard *Phys. Rev. Lett.* **86**, 508 (2001).

[120] L. Brossard, R. Clerac, C. Coulon, M. Tokumoto, T. Ziman, D. K. Petrov, V. N. Laukhin, M. J. Naughton, A. Audouard, F. Goze, A. Kobayashi, H. Kobayashi and P. Cassoux, *Eur. Phys. J. B* **1**, 439 (1998)

[121] M. Y. Ogawa, B. M. Hoffman, S. Lee, M. Yudkowsky and W. P. Halperin, *Phys. Rev. Lett.*, **57**, 1177 (1986).

[122] P. Day, *C. R. Acad. Sci., Ser. IIc: Chim.*, **2**, 675 (1999) and references therein.

[123] T. Sugano, H. Takenouchi, D. Shiomi and M. Kinoshita, *Synth. Met.* **41**, 2217 (1991).

[124] C. J. Kepert, M. Kurmoo, P. Day and M. R. Truter, *Synth. Met.* **70**, 781 (1995).

[125] P. Day and M. Kurmoo, *Synth. Met.*, **85**, 1445 (1997)

[126] M. Kurmoo, P. Day, P. Guionneau, G. Bravic, D. Chasseau, L. Ducasse, M. L. Allan, I. D. Marsden and R. H. Friend, *Inorg. Chem.*, **35**, 4719 (1996).

[127] H. Oshio, E. Ino, I. Mogi, T. Ito, *Inorg. Chem.*, **32** 5697 (1993).

[128] T. Mallah, C. Hollis, S. Bott, M. Kurmoo and P. Day, *J. Chem. Soc.*, Dalton Trans., 859 (1990).

[129] K. Suzuki, J. Yamaura, N. Sugiyasu and T.Enoki, *Synth. Metals*, **55**, 2191 (1993).

[130] S. Uji, T. Terashima, H. Aoki, J. S. Brooks, R. Kato, H. Sawa, S. Aonuma, M. Tamura, and M. Kinoshita, *Phys. Rev. B*, **50**, 15597 (1994).

[131] H. Kobayashi, A. Miyamoto, R. Kato, F. Sakai, A. Kobayashi, Y.Yamakita, Y.Fukukawa, M. Tasimi and T. Watanabe, *Phys. Rev. B*, **47**, 3500 (1993).

[132] S. Uji, T. Terashima, H. Aoki, R. Kato, H. Sawa, S. Aonuma, M. Tamura and M. Kinoshita, *Solid State Commun.*, **93**, 203 (1995).

[133] R. Kato, H. Sawa, S. Aonuma, R. Kato, M. Kinoshita and H. Kobayashi, *Solid State Commun.*, **85**, 831 (1993).

[134] H. Kobayashi, H. Sawa, S. Aonuma, and R. Kato, *J. Am. Chem. Soc.*, **115**, 7870 (1993).

[135] S. H nig, *J. Mater. Chem.*, **5**, 1469 (1995) and references therein.

[136] M. Matsuda, T. Naito, T. Inabe, N. Hanasaki and H. Tajima, *J. Mater. Chem.*, **11**, 2493 (2001).

[137] M. Tamura, F. Matsuzaki, Y. Nishio, K. Kajita, T. Kitazawa, H. Mori and S. Tanaka, *Synth. Metals*, **102** 1716 (1999).

[138] M. Tamura, K. Yamanaka, Y. Mori, Y. Nishio, K. Kajita, H. Mori, S. Tanaka, J.-I. Yamaura, T. Imakubo, R. Kato, Y. Misaki and K. Tanaka, *Synth. Metals*, **120** 1041 (2001).

[139] T. Imakubo, H. Sawa and R. Kato, *J. Chem. Soc., Chem. Commun.*, 1097 and 1667 (1995).

[140] R. Gompper, J. Hock, K. Ploborn, E. Dormann and H. Winter, *Adv. Mater.*, **7**, 41 (1995).

[141] M. Iyoda, Y. Kuwatani, K. Hara, E. Ogura, H. Suzuki, H. Ito and T. Mori, *Chem. Lett.*, 599 (1997).

[142] M. Iyoda, Y. Kuwatani, E. Ogura, K. Hara, H. Suzuki, T. Takano, K. Takeda, J.-I. Takano, K. Ugawa, M. Yoshida, H. Matsuyama, H. Nishikawa, I. Ikemoto, T. Kato, N. Yoneyama, J. Nishijo A. Miyazaki and T. Enoki, *Heterocycles*, **54**, 833 (2001).

[143] T. Imakubo, N. Tajima, M. Tamura, R. Kato, Y. Nishio, and K. Kajita, *J. Mater. Chem.*, **12**, 159 (2002).

[144] Y. Kuwatani, E. Ogura, H. Nishikawa, I. Ikemoto and M. Iyoda, *Chem. Lett.* 817 (1997).

[145] U. Kux, H. Suzuki, S. Sasaki, M. Iyoda, *Chem. Lett.*, 183 (1995).

[146] B. Domercq, T. Devic, M. Fourmigu , P. Auban-Senzier and E. Canadell, *J. Meter. Chem.*, **11**, 1570 (2001).

[147] M. Uruichi, K. Yakushi, Y. Yamashita and J. Qin, *J. Mater. Chem.*, **8**, 141 (1998).

[148] A. T. Coomber, D. Beljonne, R. H. Friend, J. L. Br das, A. Charlton, N. Robertson, A. E. Underhill, M. Kurmoo and P. Day, *Nature*, **380**, 144 (1996).

[149] F. Palacio, G. Antorrena, M. Castro, R. Burriel, J. Rawson, J. N. B. Smith, N. Bricklebank, J. Novoa and C. Ritter, *Phys. Rev. Lett.*, **79**, 2336 (1997).

[150] M. Mito, T. Kawae, K. Takeda, S. Takagi, Y. Matsushita, H. Deguchi, J. M. Rawson and F. Palacio, *Polyhedron* **20** 1509 (2001).

[151] J. R. Hartman and S. R. Cooper, *J. Am. Chem. Soc.*, **108**, 1202 (1986).

[152] N. Gallego-Planas and M. A. Whitehead, *J. Mol. Struc.; Theochem,* **428**, 67 (1998)

Chapter 2

Experimental

2.1 Syntheses

2.1.1 Syntheses and preparation of organic donors and transition metal complexes

Organic donor EDO-TTFI_2 [1] was supplied from Iyoda lab., Tokyo Metropolitan University. The donor EDT-TTFBr_2 was synthesized according to the literatures [2] as shown in scheme2.1-2.4, and partially supplied from Iyoda lab [3]. The crown thioether ligand 9S3 = 1,4,7-trithiacyclononane, 7,7,8,8-tetracyanoquinodimethane and 1,2-benzenedithiole are commercially available (Sigma-Aldrich Co. Inc.).

1,3-dithiol-2-thione (5)

25 g of ethylene trithiocarbonate **(1)** and 25 ml of dimethyl acetylene dicarboxylate **(2)** were dissolved in ca. 100 ml of toluene. The solution was heated and refluxed for ca. 6 h, then the solution was cooled. Adding ca. 400 ml of hexane gave the precipitate of 2-Thioxo-1,3-dithiole-4,5-dicarboxylic acid dimethyl ester **(3)**.

After filtration, a mixture of 210 ml of water, 150 ml of conc. HCl and 70 ml of acetic acid was added to 35 g of the residual. The solution was refluxed for ca. 2 h, then the solution was iced and filtered. We obtained the small crystals of 2-thioxo-1,3dithiole-4,5-dicarboxylic acid **(4)** as residual. The filtrated was concentrated and filtered again to obtain more compound.

31.5 g of **4** dissolved in 150 ml of pyridine was refluxed for ca. 3 h. The solution

was cooled and concentrated by evaporation. Then the tar like residual was put in a Soxhlet extractor, and extracted with hexane for few days. The obtained solution was cooled by a mixture of methanol and liquid nitrogen. Filtering the cooled solution gave yellow crystals of **(5)** (7.5 g, 31 % yield).

4,5-dibromo-1,3-dithiole-2-one (7)

2.5 g of **5** was dissolved in 30 ml of dehydrated THF, and the solution was cooled down to −78 °C. The mixture of 8.4 ml of diisopropylamine, 24.3 ml of *n*-butyllithium in *n*-hexane (1.57 mol/l) and 15 ml of dehydrated THF was slowly dropped into the cooled solution. The solution was stirred for 3 h at the temperature, then the solution of 21.1 g of 1,2-dibromo-1,1,2,2-tetrachloroethane in 8 ml of dehydrated THF was added within ca. 10 minutes. After 3 h stirring at −78 °C, the solution was slowly warmed to room temperature and ca. 200 ml of saturated aqueous solution of Na_2SO_3 was added. The compound was extracted by $CHCl_2$, and washed by saturated NaCl aqueous solution followed by water. The solution was dried by $MgSO_4$ and concentrated. Column chromatography on silica gel eluting with carbon disulfide gave **6** as red crystals (2.6 g, 48 % yield).

2 g of **6** was dissolved in 40 ml of chloroform, then 40 ml of acetic acid and 5.2 g of mercury (II) acetate was added and stirred for 1 h. The solution was filtered, and the filtrate was washed with twice water, aqueous $NaHCO_3$ and water again. The solution was dried by magnesium sulfate. Column chromatography on silica gel eluting with carbon disulfide gave **7** as yellow crystals (2.3 g, 93 % yield).

5,6-dihydro-1,3-dithiolo-[4,5-b]-1,4-dithiin-2-one (11)

10.6 g of sodium was cut and added to 90 ml of carbon disulfide, then 100 ml of N,N-dimethylformamide was slowly dropped into the solution. After ca. 6 h stirring, the solution was gently heated to volatilize surplus carbon disulfide. The solution was cooled by ice, and the mixture of 300 ml of methanol and 50 ml of water was added in ice bath. 17.6 g of zinc chloride dissolved in the mixture of 250 ml of methanol and 100 ml of 25 % ammonia water was added. 44.9 g of tetrabutylammonium bromide dissolved in 100 ml of water was added, and stirring ca. a day gave red precipitate. The solution was filtered, then the residual was

dissolved in acetone and filtered. Concentration of the mixture of the filtrate and ca. 300 ml of 2-propanol gave red crystals of tetrabutylammonium bis(1,3-dithiole-2-thione-4,5-dithiolato)zincate (II) **(8)** (78.5 g, 67 % yield). All of obtained **8** was dissolved in 400 ml of acetone, then 75 ml of benzoyl chloride was slowly poured and stirred for ca. 30 minutes. The solution was filtered, and yellow crystals of 4,5-bis(benzoylthio)-1,3-dithiol-2-thione **(9)** was obtained by recrystallization of the residual from chloroform/methanol (62.4 g, 92 % yield). 10 g of **9** was suspended in 50 ml of methanol under an argon atmosphere. 7ml of 28 % sodium methoxide followed by 4 ml of 1,2-dibromoethane was added and stirred for a day. The solution was filtered, and recrystallization of the residual from ca. 300 ml of hot ethanol gave the yellow crystal of 5,6-dihydro-1,3-dithiolo-[4,5-b]-1,4-dithiin-2-thione **(10)** (6.2 g, 87 % yield). 6 g of **10** was dissolved in 120 ml of chloroform, then 160 ml of acetic acid and 20.0 g of mercury (II) acetate was added and stirred for 1 h. The solution was filtered, and the filtrate was washed twice with water, aqueous $NaHCO_3$ and water again. The solution was dried by magnesium sulfate. Concentration of the solution gave **11** as white crystals (5.3 g, 95 % yield).

4,5-dibromo-4',5'-ethylenedithiotetrathiafulvalene (12, EDT-TTFBr_2)

1 g of **11** and 1 g of **7** was dissolved in 40 ml of toluene under an argon atmosphere. 20 ml of triethyl phosphite dried by sodium was added, then the solution was heated and refluxed for a day. The solution was cooled to room temperature and concentrated. The residual was dissolved in acetone and filtered, then the filtrate was concentrated. Column chromatography on silica gel eluting with carbon disulfide gave **12** as red crystals (0.4 g, 24 % yield).

tetrabutylammonium bis(1,2-benzenedithiolato)nickelate (III)

This anion, TBA[Ni$(bdt)_2$], was synthesized according to the literatures [4]. 0.5 g of 1,2-benzenedithiol was dissolved in the mixture of 2 ml of 28 % sodium methoxide and 8 ml of ethanol, then 0.42g of $NiCl{\cdot}6H_2O$/3ml of ethanol followed by 0.6 g of tetrabutyl ammonium bromide/3 ml of ethanol was added. The nickel (II) complex in the solution was oxidized by stirring for 3 h in air. After stirring, the solution was filtered, then the residual was recrystallized from ethanol (0.85 g,

83 % yield).

crown thioether complexes of nickel (II) ($[Ni(9S3)_2](BF_4)_2$) [5]

A solution of 137 mg of nickel (II) tetrafluoroborate hexahydrate in 10 ml of ethanol was added to a solution of 212 mg of 9S3 (=1,4,7-trithiacyclononane). The solution was heated to gentle reflux for 10 minutes. The crystal of $Ni(9S3)_2(BF_4)_2$ was obtained by adding ca. 50 ml of diethyl ether to the solution (331 mg, 95 % yield).

crown thioether complexes of cobalt (II) ($[Co(9S3)_2](BF_4)_2$) [5]

A solution of 327 mg of cobalt (II) tetrafluoroborate hexahydrate in 50ml of ethanol was added to a solution of 346 mg of 9S3 in 50 ml of ethanol. The solution was filtered, then the residual was washed with ethanol and recrystallized from nitromethane/diethyl ether (217 mg, 45 % yield).

crown thioether complexes of copper (II) ($[Cu(9S3)_2](BF_4)_2$) [5]

A solution of 478 mg of copper (II) tetrafuloroborate hydrate in 40 ml of ethanol was added to a solution of 500 mg of 9S3 in 50 ml ethanol, and the solution was stirred for ca. 1 h. The precipitate was filtered and washed with ethanol, and recrystallized from acetonitrile/diethylether to give brown small crystals of $[Cu(9S3)_2](BF_4)_2$ (640 mg, 80 % yield).

tetrabutylammonium iron (III) tetrabromide ($TBAFeBr_4$)

25 ml of ethanol solution of 1.5 g of iron (III) bromide was added to 25 ml of ethanol solution of 1.7 g of tetrabutylammonium bromide. The mixture was stirred for 30 minutes, then the solution was evaporated and the residual was recrystallized by ethanol (2.1g, 68 % yield).

tetrabutylammonium gallium (III) tetrabromide ($TBAGaBr_4$)

25 ml of ethanol solution of 1.6 g of gallium (III) bromide was added to 25 ml of ethanol solution of 1.7 g of tetrabutylammonium bromide. The mixture

was stirred for 30 minutes, then the solution was evaporated and the residual was recrystallized by ethanol (2.3g, 73 % yield).

lithium tetracyanoquinodimethane (LiTCNQ)

10 ml of acetonitrile solution of 4 g of lithium iodide was added to 200 ml of acetonitrile solution of 2.04 g of tetracyanoquinodimethane (TCNQ). The solution was refluxed for ca. 1 h, then a precipitate was obtained after 4 h standing at room temperature. After filtration, the residual was washed by acetonitrile till the filtrate became green. The powder of LiTCNQ was washed by diethylether and dried in vacuo (0.78 g, 37 % yield).

tetrabutylammonium bis{(Z)-1,2-dicyanoethylene-1,2-dithiolato}metalate (III) (TBA[M(mnt)$_2$], M = Ni, Pt)

The anion was synthesized according to the literatures [6–8]. 4.9 g of NaCN was dissolved in the 50 ml of N,N-dimethylfolmamido, then the 7.6 g of CS_2 was dropped into the solution at 0 °C. 50 ml of 1-butanol was added, then the solution was heated at 100 °C for 20 minutes followed by filtration at the temperature, then the solution was cooled to 0 °C. The solution was filtered and the residual was dissolved in ca. 100 ml of chloroform. The solution was filtered. Putting the filtrate in a cool and dark spot for 3 days gives a yellow powder of $Na_2S_2C_2(CN)_2$. 6.15 g of $Na_2S_2C_2(CN)_2$ was dissolved into the mixture of 70 ml of water and 70 ml of ethanol, then 15 mmol of $NiCl{\cdot}6H_2O$ or K_2PtCl_4 dissolved in 30 ml of ethanol was added to the solution. The solution was filtered, then 10 g of tetrabutylammonium bromide dissolved in ca. 30 ml of ethanol was added to the filtrate. The solution was stirred for 10 minutes, then the solution was filtered and the residual was washed with 20 ml of water followed by 20 ml of ethanol. 8.24 g of the crystal, $TBA_2[M(mnt)_2]$, was dissolved into 60 ml of dimethylsulfoxide, then 4.0 g of iodine dissolved in 8ml of dimethylsulfoxide was added and stirred for ca. 10 minutes. After stirring, the solution was poured into 200 ml of ethanol, then the solution was stirred for ca. 1 hour. The filtration of the solution and washing the residual with 10 ml of ethanol 10 times gives a black powder of TBA[M(mnt)$_2$] (4.07 g, 28 % yield for M = Ni, 3.58 g, 20 % yield for M = Pt, respectively).

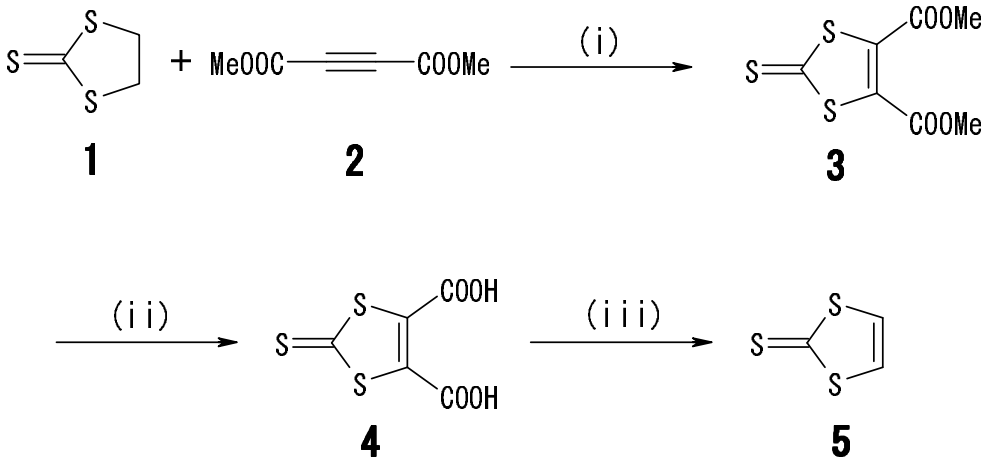

Scheme 2.1. (i) Δ/toluene, (ii) conc. HCl, CH_3COOH, Δ/H_2O, (iii) Δ/pyridine

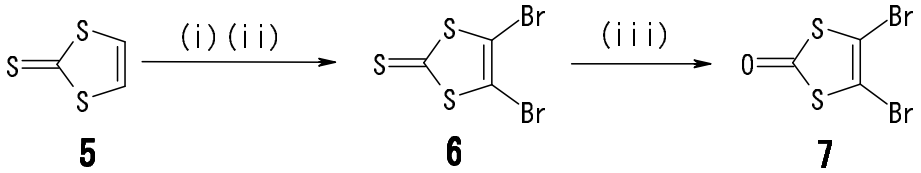

Scheme 2.2. (i) LDA, (ii) 1,2-dibromo-1,1,2,2-tetrachloroethane

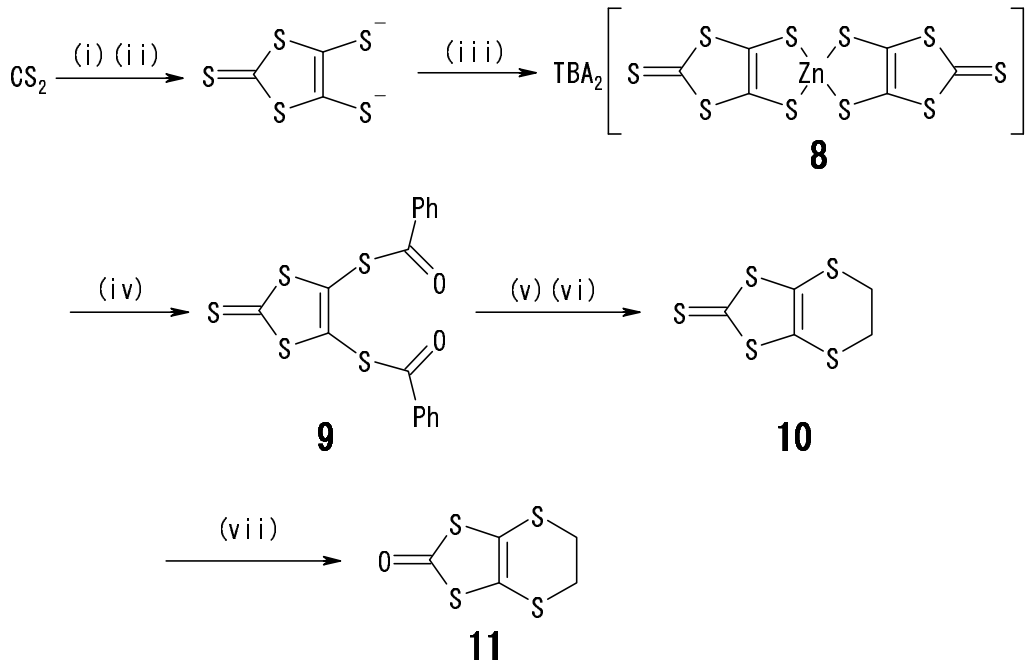

Scheme 2.3. (i) Na, (ii) DMF, (iii) $ZnCl_2$, TBABr / MeOH, H_2O, (iv) PhCOCl, (v) EtONa/EtOH, (vi) 1,2-dibromoethane, (vii) $Hg(OAc)_2$ / $CHCl_3$, CH_3COOH

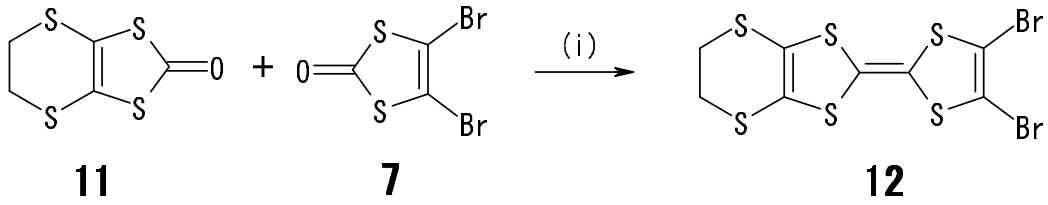

Scheme 2.4. (i) $P(OEt)_3$, Δ

2.1.2 Sample preparations

Electrocrystallization

(EDT-TTFBr$_2$)$_2$MBr$_4$ (M = Fe, Ga) were prepared by electrochemical oxidation with a H-shape glass tube containing ca. 10 mg of EDT-TTFBr$_2$ and ca. 30 mg of TBAMBr$_4$ in each side of the H-tube, and benzene chloride was was used as the solvent (Fig. 2.1). The donor molecule was electrochemically oxidized with constant current $I = 0.20$ μA at 5 °C. After 2 weeks, black needle shape crystals were obtained. Typical crystal sizes were $2 \times 0.1 \times 0.05$ mm^3 and $1 \times 0.05 \times 0.03$ mm^3 for M = Fe and Ga, respectively.

(EDO-TTFI$_2$)$_2$[M(mnt)$_2$] (M = Ni, Pt) were also prepared by the method with ca. 7 mg of EDO-TTFI$_2$ and ca. 40 mg of TBA[M(mnt)$_2$], and the solvent was 1,2-dichloroethane. The condition of the electro oxidation is $I = 0.25$ μA at 40 °C for a week. Typical crystal sizes were 1.8×0.15×0.09 mm^3 and 2.5×0.25×0.1 mm^3 for M = Ni and Pt, respectively.

Diffusion method

Single crystals of [M(9S3)$_2$](TCNQ)$_n$ (M = Ni, Co; n = 2, 3) and [M(9S3)Br$_2$] (M = Cu, Cu$_{1-x}$Ni$_x$) were prepared using the diffusion method. In the method, cation and anion were placed in the each side of the tube, and they were mixed and the crystals were deposited at the midpoint of the tube (Fig. 2.2). The conditions of the crystal growths are listed in table 2.1 Typical crystal sizes were 0.6×0.6×2 mm^3, $3 \times 3 \times 0.2$ mm^3, $1.5 \times 1 \times 0.1$ mm^3 and $2.2 \times 1.5 \times 0.2$ mm^3 for [Ni(9S3)$_2$](TCNQ)$_2$, [Ni(9S3)$_2$](TCNQ)$_3$, [Cu(9S3)Br$_2$] and [Cu$_{1-x}$Ni$_x$(9S3)Br$_2$], respectively, and samples [Co(9S3)$_2$](TCNQ)$_n$ were obtained as powder.

Crystal growth of [M(9S3)$_2$][Ni(bdt)$_2$]$_2$ (M = Ni, Co)

A 50 ml acetonitrile solution of 50 mg [M(9S3)$_2$](BF$_4$)$_2$ was added to a 50 ml acetonitrile solution of 50 mg TBA[Ni(bdt)$_2$] at room temperature, and was slowly cooled to 0 °C. After standing for 4 hours at 0 °C, black elongated thin plate crystals of [M(9S3)$_2$][Ni(bdt)$_2$]$_2$ (M = Ni, Co) were obtained. Typical crystal sizes were $3 \times 1 \times 0.1$ mm^3 and $1.4 \times 0.8 \times 0.03$ mm^3 for [Ni(9S3)$_2$][Ni(bdt)$_2$]$_2$ and [Co(9S3)$_2$][Ni(bdt)$_2$]$_2$, respectively.

2.2 Structure analyses and measurement

2.2.1 X-ray structure analysis

The crystal structures of (EDT-TTFBr$_2$)$_2$MBr$_4$ (M = Fe, Ga), [Ni(9S3)$_2$]-(TCNQ)$_n$ (n = 2, 3), [M(9S3)Br$_2$] (M = Cu$_{1-x}$Ni$_x$; x = 0, 0.05) and [M(9S3)$_2$]-[Ni(bdt)$_2$]$_2$ (M = Ni, Co) were determined by single crystal X-ray diffraction with a *Rigaku* AFC-7R four-circle diffractometer at 293K, using Mo $K\alpha$ radiation (λ = 0.71069 Å), where a suitable crystal was mounted on a glass fiber.

The structures were solved using direct methods (SHELXS-86) [9], then refined with a full-matrix least-squares method (SHELXL-93) [10]. An absorption correction based on a Ψ-scan was introduced. All non-hydrogen atoms were refined anisotropically, while hydrogen atoms were placed in their calculated positions and refined by the riding model.

We used the crystals shown below, which were suitable for structural determinations.

(EDT-TTFBr$_2$)$_2$FeBr$_4$ (needle, black, 2×0.1×0.05 mm^3)

(EDT-TTFBr$_2$)$_2$GaBr$_4$ (needle, black, 1×0.05×0.03 mm^3),

[Ni(9S3)$_2$](TCNQ)$_2$ (triangular prism, red, 0.2×0.2×0.5 mm^3)

[Ni(9S3)$_2$](TCNQ)$_3$ (plate, black, 0.5×0.5×0.1 mm^3)

[Cu(9S3)Br$_2$] (plate, black, 0.2×0.1×0.05 mm^3)

[Cu$_{1-x}$Ni$_x$(9S3)Br$_2$] (plate, black, 0.4×0.3×0.1 mm^3)

[Ni(9S3)$_2$][Ni(bdt)$_2$]$_2$ (elongated plate, black, 0.7×0.2×0.1 mm^3)

[Co(9S3)$_2$][Ni(bdt)$_2$]$_2$ (elongated plate, black, 0.5×0.2×0.03 mm^3)

(EDO-TTFI$_2$)$_2$[Ni(mnt)$_2$] (needle, black, 1×0.1×0.07 mm^3)

(EDO-TTFI$_2$)$_2$[Pt(mnt)$_2$] (needle, black, 1×0.15×0.1 mm^3)

Crystals of [Co(9S3)$_2$](TCNQ)$_2$ and [Co(9S3)$_2$](TCNQ)$_3$ were confirmed to be isostructural to those of [Ni(9S3)$_2$](TCNQ)$_2$ and [Ni(9S3)$_2$](TCNQ)$_3$, respectively, by X-ray powder diffraction pattern with *Rigaku* RINT-2400 diffractometer.

2.2.2 Overlap integrals and band calculation

The molecular orbitals and inter-molecular overlap integrals between HOMOs were calculated based on extended H ckel method [11]. The band structures of (EDT-TTFBr_2)$_2$$MBr_4$ were calculated by tight binding method.

2.2.3 Electrical resistivity

The resistivity measurements were carried out using a standard four terminal method for (EDT-TTFBr_2)$_2$$MBr_4$ and (EDO-TTFI_2)$_2$[M(mnt)$_2$], and two terminal method for the other materials, respectively, where gold wires of 15 $\mu\phi$ were attached to crystals as the electrical terminals with carbon paste (DOTITE XC-12, JEOL Inc.).

2.2.4 Electrical resistivity under high pressure

The resistivities of (EDT-TTFBr_2)$_2$$MBr_4$ and (EDO-TTFI_2)$_2$[M(mnt)$_2$] under high pressure were measured using a clamp-type cell made of CuBe alloy, which was designed for the maximum pressure of ∼15 kbar. Fig. 2.3 shows the schematic view of the cross section of the clamp-type cell and the apparatus for the resistivity measurement with the four terminal method. For the setting of the measurement, a pressure medium of Daphne 7243 oil was filled in the Teflon jacket (5 $\phi\times$ 30 mm) located in the center of the cell, where a hydrostatic pressure was applied. The pressure was set and clamped at room temperature, and the exact values of pressure were determined by the change of the resistivity of a manganin wire (0.05 $\phi\times$ 40 cm, ∼80 Ω) in the sample space. It is known that the resistivity of a manganin wire which is annealed at 200 °C for 24 h can be described as

$$R = R_0 \left(1 + C \cdot P\cdot\right), \tag{2.1}$$

where R_0, C and P are resistivity at ambient pressure, constant value which is characteristic of each manganin wire and applied pressure [12]. The constant value C of a manganin wire was determined from the resistivities at ambient pressure and 3.605 kbar where NH_3F causes the structural change.

2.2.5 Magnetic susceptibility and magnetization

The magnetic susceptibilities were measured by using SQUID magnetometers, *Quantum Design* MPMS-5 and MPMS-XL, with the maximum magnetic field of 5.5 and 7 Tesla, respectively, in the temperature range 1.7-300 K. In the measurements, I used an assembly of single crystals of $[Ni(9S3)_2](TCNQ)_n$, $M(9S3)Br_2$, $(EDT\text{-}TTFBr_2)_2MBr_4$ and $(EDO\text{-}TTFI_2)_2[M(mnt)_2]$ where the crystals were well aligned using Apiezon N grease, a packet of powder sample of $[Co(9S3)_2](TCNQ)_n$ and one single crystal of $[M(9S3)_2][Ni(bdt)_2]_2$. Typical weights of the samples used in the measurements were 1 mg for aligned single crystals and 1 to 1.5 mg for powder samples, respectively. The crystal weights and sizes of $[M(9S3)_2][Ni(bdt)_2]_2$ were $1.6 \times 0.4 \times 0.1$ mm^3 and 0.1 mg for M = Ni and $1.2 \times 0.4 \times 0.1$ mm^3 and 0.08 mg for M = Co, respectively.

An observed susceptibility is generally considered to be the summation of several contributions,

$$\chi = \chi_{\rm spin} + \chi_{\rm dia} + \chi_{\rm impurity}, \tag{2.2}$$

where χ, $\chi_{\rm spin}$, $\chi_{\rm dia}$ and $\chi_{\rm impulity}$ are the net observed susceptibility, the spin susceptibility of localized and delocalized electrons, the core diamagnetic contribution and the fractional Curie-tail coming from magnetic impurities. The experimental results shown later are after subtraction of the Pascal's diamagnetic core contribution ($\chi_{\rm dia}$) and, if any, and $S = 1/2$ Curie term associated with a trace of magnetic impurities ($\chi_{\rm impulity}$) as summarized in table 2.2

The AC-susceptibilities of $[M(9S3)_2][Ni(bdt)_2]_2$ and $(EDO\text{-}TTFI_2)_2[M(mnt)_2]$ were measured using a *Quantum Design* MPMS-XL SQUID magnetometer with an AC option for an assembly of aligned single crystals whose total weight was about 5 mg.

2.2.6 Magnetic susceptibility under high pressure

The magnetic susceptibility of $[Ni(9S3)_2][Ni(bdt)_2]_2$ under high pressure was measured using a clamp-type cell made of CuBe alloy, which was designed for the maximum pressure of $\sim$10 kbar. Fig. 2.4 shows the schematic cross section of the clamp-type cell for the magnetic susceptibility measurement. For the setting of

the measurement, a pressure medium of Daphne 7373 oil was filled in the sample space located in the center of the cell, where a hydrostatic pressure was applied. The pressure was set and clamped at room temperature, and the exact values of pressure were determined by the superconductive transition temperature of Sn depending on the applied pressure.

2.2.7 EPR measurement

EPR measurements were carried out with an assembly of single crystals arranged in the same directions pasted up on the Teflon rod by *Toray-Dow corning Silicone* SH111 silicone compound, using an X-band EPR spectrometer (*JEOL* JES-TE200 having a microwave power of 0.1 μW-200 mW and the maximum magnetic field $\sim$1300mT) with a He cryostat (*Oxford* ESR910) in the temperature range 4.2-300 K.

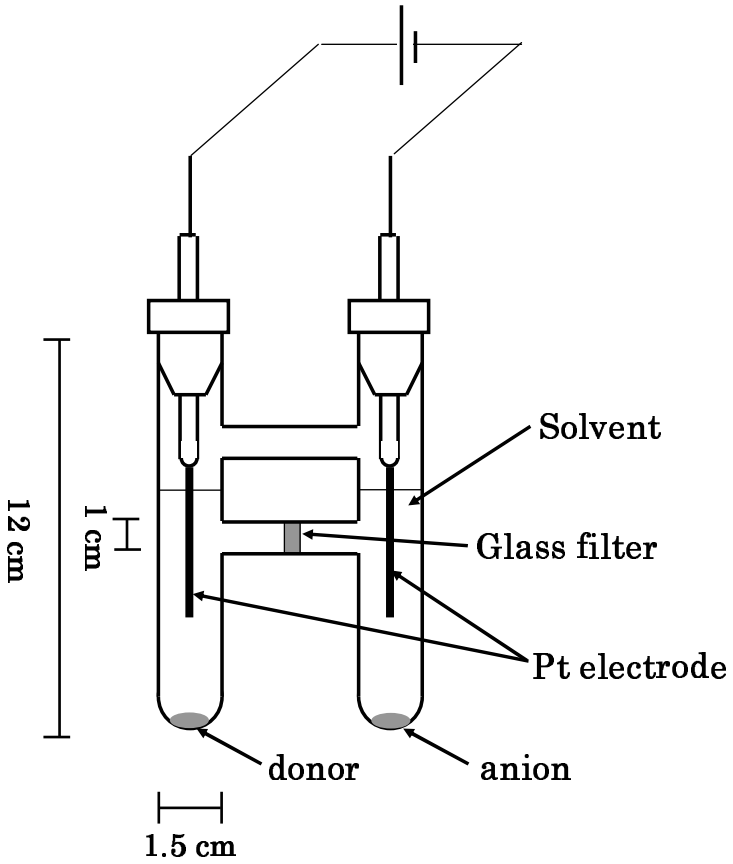

Fig. 2.1. Electrochemical oxidation method

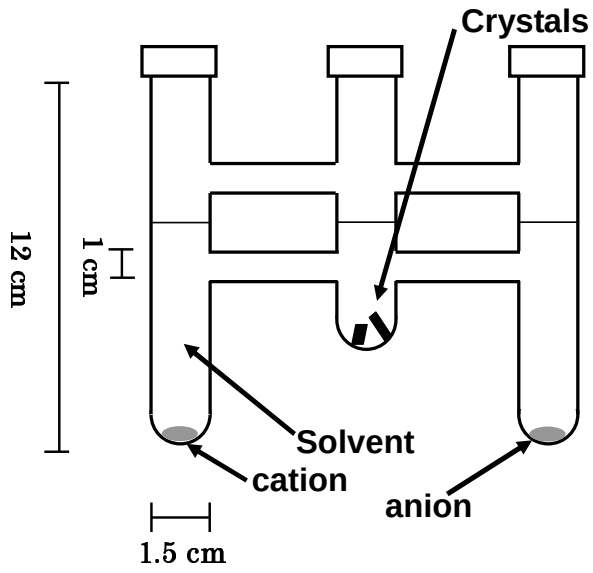

Fig. 2.2. Schematic draw of diffusion method.

Table 2.1. The conditions of crystal growth.

Material	Cation	Anion	Solvent	Temp.	Time
$[Ni(9S3)_2](TCNQ)_2$	$[Ni(9S3)_2](BF_4)_2$ 50 mg	LiTCNQ 50 mg	CH_3CN 30 ml	r. t.	2 weeks
$[Co(9S3)_2](TCNQ)_2$	$[Co(9S3)_2](BF_4)_2$ 50 mg	LiTCNQ 50 mg	CH_3CN 30 ml	5 °C	2 weeks
$[Ni(9S3)_2](TCNQ)_3$	$[Ni(9S3)_2](BF_4)_2$ 50 mg	LiTCNQ 50 mg	CH_3CN 30 ml	r. t.	2 weeks
$[Co(9S3)_2](TCNQ)_2$	$[Co(9S3)_3](BF_4)_2$ 50 mg	LiTCNQ 50 mg	CH_3CN 30 ml	45 °C	2 weeks
$[Cu(9S3)Br_2]$	$[Cu(9S3)_2](BF_4)_2$ 30 mg	$CuBr_2$ 30 mg	CH_3CN 30 ml	5 °C	6 weeks
$[Cu_{1-x}Ni_x(9S3)Br_2]$	$[Cu(9S3)_2](BF_4)_2$ 30 mg	$NiBr_2$ 50 mg	CH_3CN 30 ml	5 °C	1 weeks

Table 2.2. Core diamagnetic susceptibilities and Curie contribution of impurities.

	$\chi_{\rm dia}$ (10^{-4} emu/mol)	impurity $S = 1/2$ spin
$(EDT\text{-}TTFBr_2)_2FeBr_4$	−5.59	–
$(EDT\text{-}TTFBr_2)_2GaBr_4$	−5.57	0.18 %
$[Ni(9S3)_2](TCNQ)_2$	−4.09	–
$[Co(9S3)_2](TCNQ)_2$	−4.10	–
$[Ni(9S3)_2](TCNQ)_3$	−4.90	–
$[Co(9S3)_2](TCNQ)_3$	−4.91	–
$[Cu(9S3)Br_2]$	−2.01	–
$[Cu_{1-x}Ni_x(9S3)Br_2]$	−2.01	–
$[Ni(9S3)_2][Ni(bdt)_2]_2$	−5.07	–
$[Co(9S3)_2][Ni(bdt)_2]_2$	−5.08	–
$(EDO\text{-}TTFI_2)_2[Ni(mnt)_2]$	−5.19	–
$(EDO\text{-}TTFI_2)_2[Pt(mnt)_2]$	−5.38	–

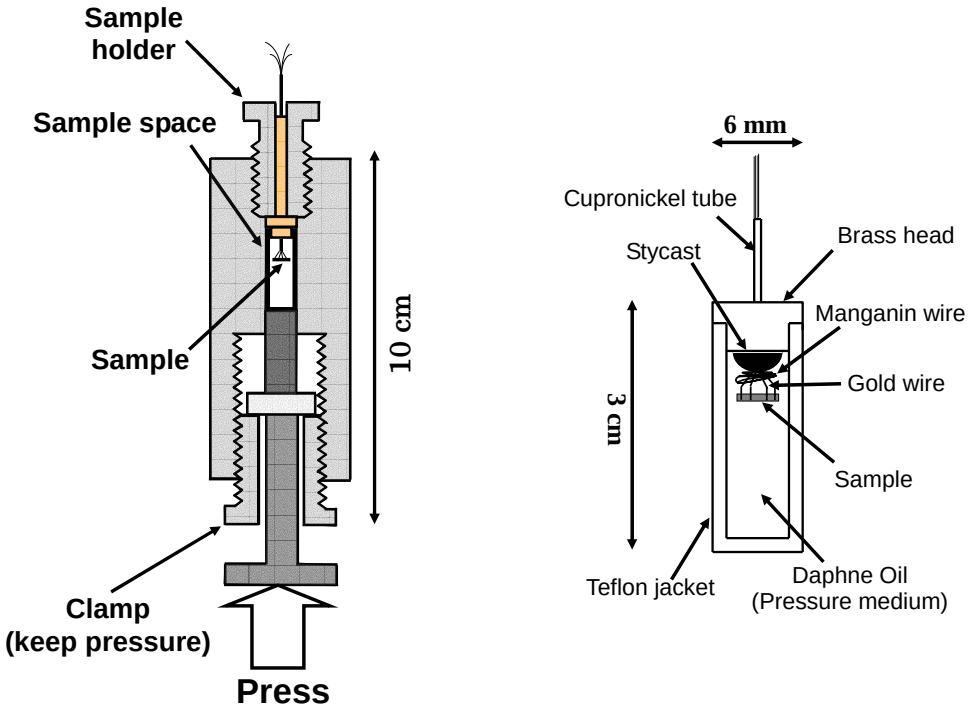

Fig. 2.3. Schematic view of the clamp-type cell for high pressure resistivity measurement (left) and the enlargement of the sample space.

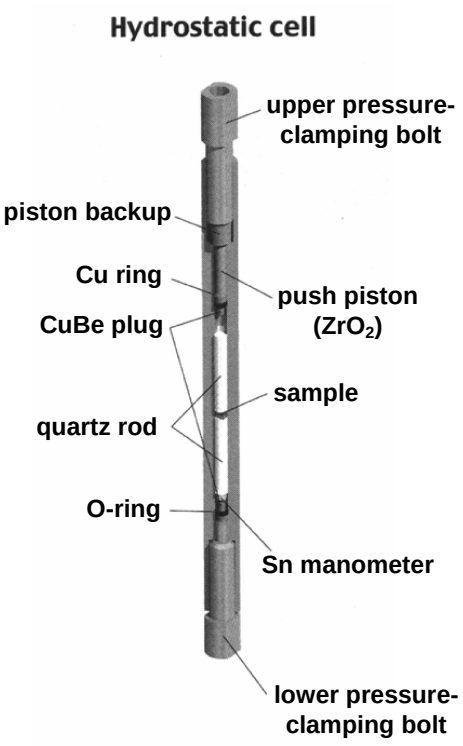

Fig. 2.4. Schematic view of the clamp-type cell for high pressure magnetic susceptibility measurement [13].

2.3 Tight-binding calculation

In the Chapter 3, the electronic structure of the π-d system (EDT-TTFBr$_2$)$_2$-FeBr$_4$ will be calculated based on the tight-binding calculation. As mentioned in Chapter 1, the tight-binding calculation is appropriate to calculate the electronic structure of organic conductors. In the calculation, the Hamiltonian of the conductive electronic system is described as

$$H = \sum_{\langle i,j \rangle} \left(t_{i,j} a^{\dagger}_{\pi i} a_{\pi j} + \text{h.c.} \right), \tag{2.3}$$

where $\langle i, j \rangle$ denotes the neighboring site pair, $a_{\pi i}$ and $a^{\dagger}_{\pi i}$ are the annihilation operator and the creation operator for the π-electron at the i-th donor site, respectively.

The Hamiltonian (2.3) Fourier transformed in the k-space is given by

$$H = \sum_{k} \begin{pmatrix} a_{\pi 1k} \\ \vdots \\ a_{\pi nk} \end{pmatrix}^{\dagger} \begin{pmatrix} t_{11} & \cdots & t_{1n} \\ \vdots & \ddots & \vdots \\ t_{n1} & \cdots & t_{nn} \end{pmatrix} \begin{pmatrix} a_{\pi 1k} \\ \vdots \\ a_{\pi nk} \end{pmatrix}, \tag{2.4}$$

where n, $a_{\nu k}$ and t_{ij} are the number of the site in a unit cell, the Fourier transformation of a_i and transfer integral from the i-th site to j-th site, respectively.

The energy $\varepsilon(k)$ and the eigenvector $\psi(k) = (a_{1k}, \cdots, a_{nk})$ of the electron with wave number k are obtained by solving the eigenequation,

$$H\psi_{\pi}(k) = \varepsilon_{\pi}(k)\psi_{\pi}(k). \tag{2.5}$$

In the calculation, the Fermi energy ε_{F} are calculated as the following equation is satisfied;

$$N_{\pi \text{e}} = \frac{1}{N_{\text{cell}}} N_{\varepsilon_{\pi}(k) \leq \varepsilon_{\text{F}}}, \tag{2.6}$$

where $N_{\pi \text{e}}$, N_{cell} and $N_{\varepsilon_{\pi}(k) \leq \varepsilon_{\text{F}}}$ are the electron number in a unit cell, the number of the unit cell being considered in the calculation and the number of the electron having the energy $\varepsilon_{\pi}(k) \leq \varepsilon_{\text{F}}$, respectively.

The electron density of the i-th site n_i can be estimated as

$$n_{\pi i} = \frac{1}{N_{\text{cell}}} \sum_{k \in \{\varepsilon_{\pi}(k) \leq \varepsilon_{\text{F}}\}} \langle a^{\dagger}_{\pi ik} a_{\pi ik} \rangle. \tag{2.7}$$

2.3.1 Tight-binding calculation including the on-site and inter-site Coulomb interaction U

The Hamiltonian (2.3) is not suitable for treating the insulating state caused by the electron-electron interaction such as SDW or CDW because the Hamiltonian contains no electron-electron interaction term. Introducing the electron-electron interaction term makes the Hamiltonian insolvable, therefore using an approximation is necessary.

In 1996 and 1997, Kino, Seo and Fukuyama used mean field approximation, and they can explain the effect of the on-site and inter-site Coulomb interaction U and V in qualitative level [14,15]. In their calculation, they introduce U and V as a function of the average π-electron density $n_{\pi i}$. In this condition, the Hartree-Fock Hamiltonian in the k-space is given by

$$H_{\rm HF} = H_0 + \sum_{k\sigma} \begin{pmatrix} a_{\pi 1k\sigma} \\ \vdots \\ a_{\pi nk\sigma} \end{pmatrix}^{\dagger} \left\{ U \begin{pmatrix} n_{\pi 1\sigma'} & & 0 \\ & \ddots & \\ 0 & & n_{\pi n\sigma'} \end{pmatrix} + \begin{pmatrix} \sum_j V_{1j} n_{\pi j} & & 0 \\ & \ddots & \\ 0 & & \sum_j V_{nj} n_{\pi n} \end{pmatrix} \right\} \begin{pmatrix} a_{\pi 1k\sigma} \\ \vdots \\ a_{\pi nk\sigma} \end{pmatrix}, \tag{2.8}$$

where σ, σ', U, V_{ij} and H_0 are a spin index ($\uparrow$, $\downarrow$), opposite to σ, the on-site Coulomb repulsion, the inter-site Coulomb repulsion between i- and j-th sites and the transfer matrix which is same as the Hamiltonian (2.4). In eq. (2.8), the average density of electrons with spin σ $n_{i\sigma}$ at i-th site is determined self-consistently by

$$n_{\pi i\sigma} = \frac{1}{N_{\rm cell}} \sum_{k\in\{\varepsilon_\pi(k\sigma)\le\varepsilon_{\rm F}\}} \langle a^{\dagger}_{\pi ik\sigma} a_{\pi ik\sigma} \rangle. \tag{2.9}$$

At first, a constant values U and V is assumed and a set of $n_{\pi i\sigma}$ are given randomly, then the set of $a_{\pi ik\sigma}$ is obtained in the condition of given $n_{\pi i\sigma}$ by solving the eigen value equation (2.8). In the next step, the new set of $n_{\pi i\sigma}$ is calculated based on eq. (2.9) from calculated $a_{\pi ik\sigma}$. The operations are repeated till $n_{\pi i\sigma}$ becomes self-consistent under the constants U and V. In the calculation, the self-consistent HF calculation was carried out at 270×270 k-points. By using the $n_{\pi i\sigma}$, the average π-electron density $n_{i\pi}$ and average spin density $S_{\pi i}$ are given as

$$n_{\pi i} = n_{\pi i\uparrow} + n_{\pi i\downarrow} \tag{2.10}$$

$$S_{\pi i} = \frac{1}{2} \cdot (n_{\pi i\uparrow} - n_{\pi i\downarrow}). \tag{2.11}$$

2.3.2 Tight-binding calculation including a π-d interaction $J_{\pi d}$

To calculate the effect of the π-d interaction, I also introduce the π-d interaction term and the Zeeman energy term of π-electrons into the tight-binding calculation. In the following calculation, z-direction is defined as the parallel to the up spin of the π-electrons which is assumed to be unchanged even in the external field. The Zeeman energy is $E_{\rm Zeeman}$ simply given as

$$E_{\rm Zeeman} = S_{\rm e} g_\pi \mu_{\rm B} H_{\rm ex}, \tag{2.12}$$

where S_e, g_π, $\mu_{\rm B}$ and $H_{\rm ex}$ are the spin of electron ($S_e = \pm 1/2$), the g-value of the π-electron, the Bohr magneton and the z-component of the external field. The energy of the π-d interaction at the i-th site of the π-electron system is described as

$$E_{\pi d}(i) = -2J \sum_j J_{ij} \boldsymbol{S}_{\pi i} \cdot \boldsymbol{S}_{dj}, \tag{2.13}$$

where $\boldsymbol{S}_\pi$ and $\boldsymbol{S}_{dj}$ are the spin of the π-electron and that of the d-electron at the j-th site of the d-electron system, and J_{ij} is the strength of the π-d interaction between i-th site of the π-electron system and j-th site of the d-spin system. If J_{ij} is independent of the sites with a value $J_{\pi d}$ and a site of the π-electron system is affected only by one d-spin, which is the case of (EDT-TTFBr$_2$)$_2$FeBr$_4$, eq. (2.13) is simplified as

$$E_{\pi d}(i) = -2J_{\pi d} \boldsymbol{S}_\pi \cdot \boldsymbol{S}_d \tag{2.14}$$

$$= -2J_{\pi d} S_\pi \cdot S_{dzi}, \tag{2.15}$$

where S_{dzi} is the z-component of the d-spin interacting the π-electron at the i-th site of the π-electron system.

By using the eqs. (2.12) and (2.15), the Hamiltonian of the π-electron system including the π-d interaction in the k-space is given by

$$H = H_{\rm HF}$$

$$+ \quad \begin{pmatrix} a_{\pi 1k\sigma} \\ \vdots \\ a_{\pi nk\sigma} \end{pmatrix}^{\dagger} (-1)^{l} \left\{ 2J_{\pi d} \begin{pmatrix} S_{dz1} & & 0 \\ & \ddots & \\ 0 & & S_{dzn} \end{pmatrix} - \frac{g_{\pi}\mu_{\mathrm{B}}H_{\mathrm{ex}}}{2} \right\} \begin{pmatrix} a_{\pi 1k\sigma} \\ \vdots \\ a_{\pi nk\sigma} \end{pmatrix}, \tag{2.16}$$

where $l = 1$ for $\sigma = \uparrow$ and 0 for $\downarrow$, and H_{HF} is the HF Hamiltonian given by eq. (2.8) not including the π-d interaction. Solving the eigenequation (2.16) self-consistently as same as the subsection (2.3.1) gives a electron density $n_{\pi i\sigma}$ and spin density of the π-electrons at i-th site $S_{\pi i}$. From this calculation, $n_{\pi i}$, $S_{\pi i}$ and energy gap can be calculated under constant values of $J_{\pi d}$ and U.

The self-consistent HF calculation of this calculation was also carried out at 270×270 k-points.

References

[1] Y. Kuwatani, E. Ogura, H. Nishikawa, I. Ikemoto and M. Iyoda, *Chem. Lett.* 817 (1997).

[2] B. Domercq, T. Devic, M. Fourmigu , P. Auban-Senzier and E. Canadell, *J. Meter. Chem.*, **11**, 1570 (2001).

[3] U. Kux, H. Suzuki, S. Sasaki, M. Iyoda, *Chem. Lett.*, 183 (1995).

[4] M. J. Baker-Hawkes, E. Billing and H. B. Gray, *J. Am. Chem. Soc.*, **88**, 4870 (1966).

[5] W. N. Setzer, C. A. Ogle, G. S. Wilson and R. S. Glass, *Inorg. Chem.*, **22**, 266 (1983).

[6] "Inorg. Synth.", vol. X (1967), p11, 13 and 15.

[7] "Inorg. Synth.", vol. XIII (1972), p187.

[8] J. Locker and J. A. McCleverty, *Inorg. Chem.*, **5**, 1157 (1966).

[9] G. M. Sheldrick, *SHELXS86*, program for crystal structure determination. Univ. of G ttingen, Federal Republic of Germany (1986).

[10] G. M. Sheldrick, *SHELXL93*, program for refinement of crystal structures. Univ. of G ttingen, Federal Republic of Germany (1993).

[11] T. Mori, A. Kobayashi, Y. Sasaki, H. Kobayashi, G. Saito and H. Inokuchi, *Bull. Chem. Soc. Jpn.*, **57**, 627 (1984)

[12] J. Mizuki and Y. Endo, *Kotai-Butsuri*, **15**, 551 (1980).

[13] Y. Uwatoko, T. Hotta, E. Matsumoto, H. Mori, T. Ohki, J. L. Sarrao, J. D. Thompson, N. Mori and G. Oomi, *Rev. High Pressure Sci. Technol.*, **7**, 1508 (1998)

[14] H. Kino and H. Fukuyama, *J. Phys. Soc. Jpn.*, **65**, 235 (1996).

[15] H. Seo and H. Fukuyama, *J. Phys. Soc. Jpn.*, **66**, 1249 (1997).

Chapter 3

$(EDT\text{-}TTFBr_2)_2MBr_4$

3.1 Introduction

As discussed in Chapter 1, to build short donor-anion atomic contacts is a promising way to increase the strength of the π-d interaction when magnetic anions are incorporated into TTF-type organic conductors. However, it is not so easy to achieve a short donor-anion contacts. In the early stage of researches on organic magnetic conductors, many researchers have tried to make appropriate electronic systems by using the molecular design which can control the properties of organic donor molecule itself, resulting in bringing various kinds of electronic systems. However, the physical properties are governed by not only a character of a molecule but also the arrangement of the molecules. Unfortunately, it is difficult to control the molecular arrangement intentionally in organic conductors because inter-molecular interaction is very weak, where small changes of the inter-molecular interaction and the condition of the crystal growth cause the change of the molecular arrangement. In short, the weakness of the inter-molecular interaction is the key factor in the difficulty in controlling molecular arrangements. To solve the difficulty, several works have been made revealing that the interaction, which is stronger than van der Waals interaction (but weaker than chemical bond), can be produced by introducing the coordination-bond-like interaction [1–7], which is built with structure controlling group. It is still difficult to control the crystal structure, but we can control the donor-anion distance by using such *designed molecules*.

Among the donor molecules having structure-controlling-group, I selected the bromine-bonded TTF-type donor EDT-$TTFBr_2$ whose structure is shown in Fig.

1.40. On the same side of the TTF-moiety, the donor molecule has two bromine atoms which cause attractive interaction with a halogen atom of a counter anion, when halogen-coordinated anions are employed, resulting in the formation of short donor anion contacts, which are an advantage to achieve a strong π-d interaction. The other side of TTF-moiety is substituted with ethylenedithio bridge which expands the π-orbital and stabilizes metallic state.

Meanwhile, I used $FeBr_4^-$ anion as magnetic anion. The anion has a large magnetic moment $S = 5/2$ and a small size, where the former is suitable for producing strong π-d interaction and the latter is preferable for donor molecules to be stacked in forming high-conductive donor column. Indeed, it is known that the several salts of the anion are metallic with and π-d interaction [8–13]. In addition, there is a non-magnetic analogue of the anion, $GaBr_4^-$, having a quite similar ionic radii (0.49 Å for Fe^{3+} and 0.47 Å for Ga^{3+}, respectively), resulting in giving the isostructural crystal [8–13]. The existence of the non-magnetic analogue is useful to investigate comprehensively the effect of π-d interaction.

In this Chapter, I will report the new π-d interaction system (EDT-$TTFBr_2)_2$-$FeBr_4$ and its non-magnetic anion analogue (EDT-$TTFBr_2)_2GaBr_4$. At first, I will show the crystal structures of these two salts, which provide basis to discuss the physical properties. Then, the electronic and magnetic properties are discussed on the basis of the behavior of the magnetic susceptibilities, electrical resistivities, magnetoresistances and electron paramagnetic resonance spectra (EPR). In the $FeBr_4^-$ salt, the magnetic susceptibility and EPR mainly depends on the behavior of d-electrons, while the behavior of the electrical resistivity is mainly owing to the π-electron system. In contrast, the behavior of the $GaBr_4^-$ salt clarified the electronic state of the donor π-electrons, which is similar to that of the $FeBr_4^-$ salt because of the structural similarity. In addition, the effect of π-d interaction is studied by comparing the magnetoresistances between the $FeBr_4^-$ salt and the $GaBr_4^-$ salt. At last, I analyze the magnetic structure, magnetization curves and magnetoresistance based on the tight-binding calculation.

3.2 Crystal structures

Fig. 3.1 shows the crystal structure of (EDT-TTFBr$_2$)$_2$MBr$_4$ (M = Fe, Ga), which is isostructural regardless of counter anions due to similar sizes of anions. The structure is similar to π-d interaction system (EDO-TTFBr$_2$)$_2$FeBr$_4$ [10] except a difference in the conformation of the ethylenedichalcogen group. In the crystals, donors are stacked in a head-to-tail manner to form quasi one-dimensional (1D) columns elongated parallel to the a-axis. The adjacent donor molecules in a donor column of the EDT-TTFBr$_2$ salts are related by 2-fold screw symmetry with the screw axis parallel to a-axis, whereas those of the EDO-TTFBr$_2$ salt are related by the glide symmetry with a glide axis being parallel to a donor column and glide plane being perpendicular to the long axis of the donor molecular plane. A unit cell contains crystallographically independent one donor molecule and a half of anion shown in Fig. 3.1a. The atom positions, anisotropic/isotropic thermal factors, bond lengths and bond angles are summarized in Tables 3.1-3.9. An anion has two crystallographically different bromine atoms with M^{3+}-Br^- distances 2.316 and 2.331 for M = Fe and 2.275 and 2.332 for M = Ga, respectively, while Br-M-Br angles are 108.29, 108.43 and 107.82 for M = Fe and 110.5, 108.2 and 108.4 for M = Ga, respectively. The intra-anion structure of the $FeBr_4^-$ anion has no significant distortion, while the $GaBr_4^-$ anion seems to have large uniaxital distortion. But it is noted that the absolute values of the atomic positions of the $GaBr_4^-$ is not so reliable because of the large R-factor R_1 = 21.1 %.

In the arrangement of the anions, the inter-anion Br1-Br2 contacts r_a (= 4.01 and 4.00 Å for M = Fe and Ga, respectively) are ca. 3 % longer than the sum of van der Waals radii of bromine atoms (3.90 Å), while inter-molecular Br1-Br2 contacts r_b (= 5.09 and 5.13 Å for M= Fe and Ga, respectively) are much longer than the sum of van der Waals radii. Thus, anions also form 1D chains elongated parallel to the b-axis which is perpendicular to the donor columns. In contrast to the structure of (EDO-TTFBr$_2$)$_2$FeBr$_4$ having the intra-chain Br-Br distances 3.87 Å, that of (EDT-TTFBr$_2$)$_2$MBr$_4$ is significantly long. These long anion-anion distances suggest that the direct anion-anion exchange magnetic interaction is not so strong.

On the contrary to the long anion-anion distances, attractive interaction between bromine atoms of donor and anion (see, section 3.1) shortens the donor-anion distance; that is, the short atomic contacts r_{c1} between Br3-Br1 (= 3.66 and 3.68 Å for M = Fe and Ga, respectively), r_{c2} between Br4-Br2 (= 3.67 and 3.68 Å for M = Fe and Ga, respectively) are ca. 7 % shorter than the sum of van der Waals radii of bromine atoms. In addition, the attractive inter-molecular interaction also causes short S5-Br1 atomic contacts r_d, the values of which, 3.69 Å for both M= Fe and Ga is ca. 3 % shorter than the sum of van der Waals radii of bromine and sulfur atoms (3.80 Å). It is noted that each anion molecule has four short Br-Br donor-anion contacts (two r_{c1} and two r_{c2}) and two short S-Br contacts (two r_d) due to the symmetry of the crystal. The long anion-anion distances and the short donor-anion distances enhance the importance of π-d interaction in the magnetism of the $FeBr_4^-$ salt.

The overlap integrals, band structure and Fermi surface calculated based on the extended H ckel method and the tight-binding method [18] are shown in Fig. 3.2, where the values of the overlap integrals are $p = -29.8 \times 10^{-3}$, $q_1 = -1.39 \times 10^{-3}$, $q_2 = -1.43 \times 10^{-3}$, $r_1 = 6.71 \times 10^{-3}$ and $r_2 = 6.42 \times 10^{-3}$, respectively, and I assume the transfer integral $t = ES$ in calculating the band structure, where S is the overlap integral and $E = 10$ eV [18]. In addition, it is expected that the overlap integral between a donor and an anion takes a finite value because of short donor-anion contacts. For characterizing the electronic features of the donor-anion contacts, information on the wave function distribution of HOMO of a donor molecule is particularly important since the interaction is generated by the wave function overlaps between donor and anion. For this purpose, the wave function distribution is calculated for a EDT-TTFBr_2 molecule on the basis of PM3 method [17], and the result is shown in Fig. 3.3. The HOMO electron is distributed mainly in the TTF moiety in addition to the sulfur atoms of the ethylenedithio group. However, no electron is present on the bromine atoms attached to the TTF skeleton. This fact indicates that the Br-Br contacts between a donor and an anion do not contribute to the electronic state such as π-d interaction or electron transfer, while the S-Br contact between a donor and an anion can contribute to it. Indeed, the sum of the five overlap integrals between the HOMO of a donor molecule and

the five SOMOs of an anion [15] calculated based on extended H ckel method has the finite value 9.3×10^{-4} only at the short donor-anion S5-Br1 contact r_{d}, while that of the short donor-anion Br-Br contacts, $r_{\mathrm{c1}} and r_{\mathrm{c2}}$, have the values ~ 0.

The electronic structure of the π electrons is quasi 1D featured with two lens-shaped Fermi surfaces, which is quite similar to that of (EDO-TTF$\mathrm{Br_2}$)$_2$Fe$\mathrm{Br_4}$ with no obvious difference. The π-electron system of the present salts is little more one-dimensional than that of (EDO-TTF$\mathrm{Br_2}$)$_2$Fe$\mathrm{Br_4}$, where the ratio between intra- and inter-chain overlap integrals $t_{\mathrm{intra}}/t_{\mathrm{inter}}$ are 4.43 and 3.56 for (EDT-TTF$\mathrm{Br_2}$)$_2$Fe$\mathrm{Br_4}$ and (EDO-TTF$\mathrm{Br_2}$)$_2$Fe$\mathrm{Br_4}$, respectively. From the structure of the Fermi surfaces, a nesting vector $Q \sim a^*/2$ is present, as shown in Fig. 3.2b.

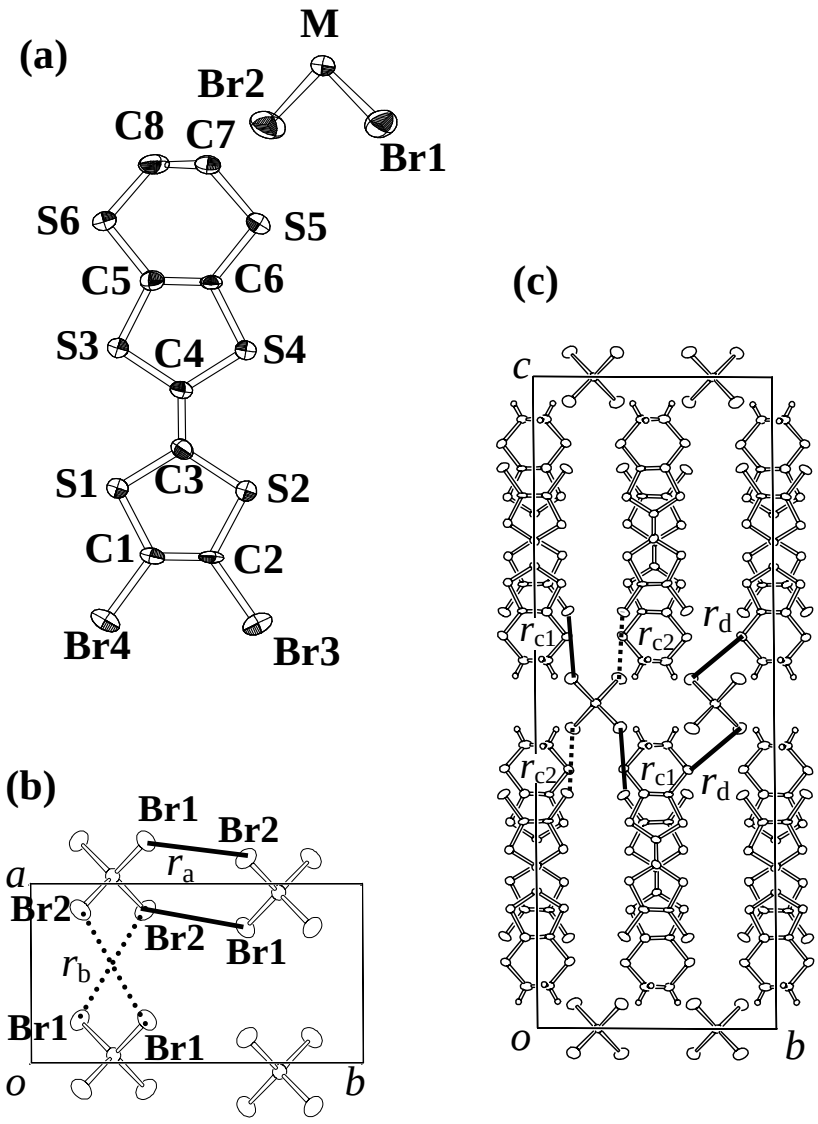

Fig. 3.1. The crystal structure of $(EDT\text{-}TTFBr_2)_2MBr_4$ (M = Fe, Ga). **(a)** Thermal ellipsoid plot (50 % probability) of $(EDT\text{-}TTFBr_2)_2FeBr_4$ drawn by ORTEP-III [16]. **(b)** The arrangement of anions placed on the $c/2$ plane projected on the ab-plane. Solid lines r_a (= 4.01 and 4.00) Å for M = Fe and Ga) and the dotted lines r_b (= 5.09 and 5.13 Å for M = Fe and Ga) represent the anion-anion intra-chain and inter-chain Br1-Br2 contacts, respectively. **(c)** Crystal structure of $(EDT\text{-}TTFBr_2)_2MBr_4$ projected on the bc-plane. Solid lines r_{c1} (= 3.66 and 3.68 Å for M = Fe and Ga), dotted lines r_{c2} (= 3.67 and 3.68 Å for M = Fe and Ga) and solid lines r_d (= 3.69 Å for both M = Fe and Ga) represent the short donor-anion Br3-Br1, Br4-Br2 and S5-Br1 contacts, respectively.

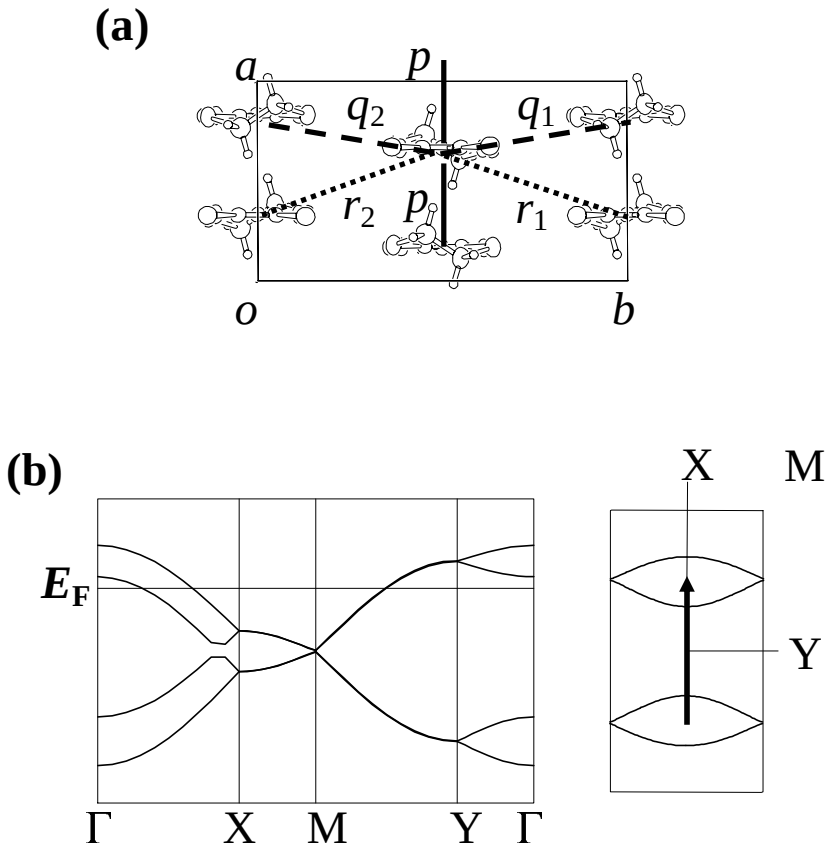

Fig. 3.2. **(a)** The arrangement of donor molecules. Solid, dashed and dotted lines represent the overlap integrals between HOMOs of adjacent donor molecules (see, text). **(b)** Band structure (left) and Fermi surface (right) where the arrow indicates the nesting vector $Q = a^*/2$.

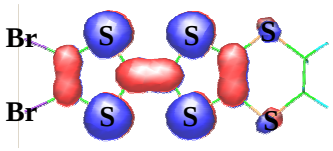

Fig. 3.3. HOMO of EDT-TTFBr_2 molecule calculated by using PM3 method [17]. Bromine atoms do not contribute to the orbital.

Table 3.1. Crystallographic data of (EDT-TTFBr$_2$)$_2$MBr$_4$.

	(EDT-TTFBr$_2$)$_2$FeBr$_4$	(EDT-TTFBr$_2$)$_2$GaBr$_4$
space group	$I_{2/\mathrm{b}11}$	$I_{2/\mathrm{b}11}$
a,Å	7.066(10)	7.078(4)
b,Å	13.10(2)	13.146(11)
c,Å	35.65(9)	35.74(3)
α,deg	90.26(16)	90.72(7)
β,deg	89.93(18)	89.98(5)
γ,deg	89.4(2)	90.06(5)
V,Å^3	3300(11)	3326(4)
Z	4	4
reflections collected ($2\theta < 55^{\mathrm{o}}$)	7286	7277
reflections unique	3205	3382
R_1 for all data	0.0899	0.2114
wR_2 for all data	0.1321	0.4467

Table 3.2. Atom positions of (EDT-TTFBr_2)$_2$FeBr_4.

atom	x	y	z	B_{eq} (Å^3)
Fe1	0.04663(16)	0.2500	0.5000	0.0306(3)
Br1	0.24164(12)	0.35100(7)	0.46231(3)	0.0553(3)
Br2	-0.14427(11)	0.15203(7)	0.46164(3)	0.0588(3)
Br3	0.32338(9)	0.12945(6)	0.13917(2)	0.0392(2)
Br4	0.32894(9)	-0.13594(5)	0.14111(2)	0.0391(2)
C1	0.3306(7)	-0.0531(5)	0.18279(19)	0.0253(12)
C2	0.3312(7)	0.0495(5)	0.18213(18)	0.0236(12)
C3	0.3337(7)	0.0001(5)	0.2519(2)	0.0265(13)
C4	0.3333(7)	-0.0003(4)	0.29009(19)	0.0249(12)
C5	0.3259(7)	-0.0500(5)	0.3605(2)	0.0273(13)
C6	0.3291(7)	0.0532(4)	0.35953(18)	0.0223(12)
C7	0.3859(10)	0.0487(5)	0.4353(2)	0.0380(15)
H7A	0.5180	0.0282	0.4334	0.046
H7B	0.3695	0.0843	0.4590	0.046
C8	0.2662(10)	-0.0457(6)	0.4356(2)	0.0427(17)
H8A	0.1341	-0.0255	0.4337	0.051
H8B	0.2831	-0.0801	0.4595	0.051
S1	0.3351(2)	-0.11346(12)	0.22653(5)	0.0316(4)
S2	0.3335(2)	0.11175(12)	0.22497(5)	0.0312(4)
S3	0.3290(2)	-0.11072(12)	0.31698(5)	0.0295(3)
S4	0.3341(2)	0.11247(11)	0.31579(5)	0.0286(3)
S5	0.3314(2)	0.13592(13)	0.39757(6)	0.0360(4)
S6	0.3207(2)	-0.13282(13)	0.39881(5)	0.0343(4)

Table 3.3. Anisotropic thermal factors of (EDT-TTFBr_2)$_2$FeBr_4.

atom	U_{11}	U_{22}	U_{33}	U_{23}	U_{13}	U_{12}
Fe1	0.0367(6)	0.0324(7)	0.0228(8)	-0.0014(5)	0.000	0.000
Br1	0.0679(5)	0.0568(5)	0.0417(6)	0.0075(4)	0.0111(4)	-0.0182(4)
Br2	0.0665(5)	0.0686(6)	0.0417(6)	-0.0126(4)	-0.0094(4)	-0.0227(4)
Br3	0.0429(4)	0.0473(4)	0.0274(4)	0.0132(3)	0.0003(3)	-0.0009(3)
Br4	0.0430(4)	0.0460(4)	0.0281(5)	-0.0150(3)	0.0003(3)	0.0009(2)
C1	0.028(3)	0.034(3)	0.015(3)	-0.005(3)	-0.001(2)	0.002(2)
C2	0.029(3)	0.034(3)	0.008(3)	-0.001(2)	0.002(2)	-0.002(2)
C3	0.029(3)	0.027(3)	0.023(4)	-0.005(3)	-0.003(2)	0.0040(19)
C4	0.030(3)	0.028(3)	0.017(4)	-0.002(3)	-0.002(2)	0.000(2)
C5	0.026(3)	0.033(3)	0.023(4)	0.002(3)	-0.002(2)	0.003(2)
C6	0.029(3)	0.028(3)	0.010(3)	0.000(2)	-0.004(2)	0.004(2)
C7	0.059(4)	0.036(4)	0.019(4)	-0.002(3)	-0.014(3)	-0.002(3)
C8	0.055(4)	0.052(5)	0.021(4)	0.002(3)	0.008(3)	0.003(3)
S1	0.0478(9)	0.0255(8)	0.0216(10)	-0.0011(7)	0.0001(6)	0.0002(6)
S2	0.0463(9)	0.0240(8)	0.0233(10)	0.0000(7)	0.0006(6)	-0.0009(5)
S3	0.0431(8)	0.0243(8)	0.0213(10)	-0.0008(6)	-0.0006(6)	-0.0002(5)
S4	0.0410(8)	0.0244(8)	0.0202(9)	-0.0004(6)	-0.0009(6)	0.0002(5)
S5	0.0521(10)	0.0312(9)	0.0247(11)	-0.0065(7)	-0.0012(7)	0.0020(6)
S6	0.0517(9)	0.0313(9)	0.0201(10)	0.0040(7)	-0.0014(6)	-0.0007(6)

Table 3.4. Bond length of (EDT-TTFBr_2)$_2$FeBr_4 (Å).

Fe1-Br2	2.316(5)
Fe1-Br1	2.331(5)
Br3-C2	1.860(7)
Br4-C1	1.836(7)
C1-C2	1.345(9)
C1-S1	1.751(8)
C2-S2	1.728(7)
C3-C4	1.362(10)
C3-S1	1.738(7)
C3-S2	1.753(8)
C4-S4	1.735(7)
C4-S3	1.740(7)
C5-C6	1.353(9)
C5-S3	1.742(8)
C5-S6	1.748(8)
C6-S5	1.732(7)
C6-S4	1.745(8)
C7-C8	1.506(10)
C7-S5	1.809(8)
C8-S6	1.775(9)

Table 3.5. Bond angle of (EDT-TTFBr_2)$_2$FeBr_4 (deg).

Br2-Fe1-Br1	108.29(18)
Br2-Fe1-Br2	108.43(15)
Br1-Fe1-Br1	107.82(15)
C2-C1-S1	118.1(5)
C2-C1-Br4	125.0(6)
S1-C1-Br4	116.9(4)
C1-C2-S2	116.9(5)
C1-C2-Br3	125.5(5)
S2-C2-Br3	117.6(4)
C4-C3-S1	120.8(5)
C4-C3-S2	123.7(5)
S1-C3-S2	115.5(4)
C3-C4-S4	121.4(5)
C3-C4-S3	123.9(5)
S4-C4-S3	114.7(4)
C6-C5-S3	115.4(6)
C6-C5-S6	130.2(6)
S3-C5-S6	114.4(4)
C5-C6-S5	127.0(6)
C5-C6-S4	118.2(5)
S5-C6-S4	114.8(4)
C8-C7-S5	114.1(5)
C7-C8-S6	113.6(5)
C3-S1-C1	94.2(4)
C2-S2-C3	95.3(3)
C4-S3-C5	96.5(3)
C4-S4-C6	95.2(3)
C6-S5-C7	101.0(4)
C5-S6-C8	100.5(4)

Table 3.6. Atom positions of (EDT-TTFBr_2)$_2$GaBr_4.

atom	x	y	z	B_{eq} (Å^3)
Ga1	0.0397(10)	0.2500	0.5000	0.0533(16)
Br1	0.2326(7)	0.3497(4)	0.46226(13)	0.0658(13)
Br2	-0.1436(7)	0.1507(4)	0.46215(12)	0.0684(14)
Br3	0.3258(4)	0.1309(3)	0.13985(9)	0.0396(9)
Br4	0.3300(5)	-0.1343(3)	0.14049(9)	0.0402(8)
C1	0.327(4)	-0.057(3)	0.1829(9)	0.040(8)
C2	0.324(4)	0.050(2)	0.1819(8)	0.032(6)
C3	0.334(4)	-0.002(2)	0.2516(7)	0.026(5)
C4	0.338(5)	0.003(2)	0.2905(8)	0.033(6)
C5	0.334(4)	-0.049(2)	0.3593(8)	0.030(6)
C6	0.332(3)	0.052(2)	0.3595(7)	0.028(6)
C7	0.375(6)	0.045(3)	0.4350(11)	0.057(10)
H7A	0.5090	0.0285	0.4345	0.068
H7B	0.3512	0.0799	0.4586	0.068
C8	0.277(5)	-0.047(3)	0.4358(10)	0.049(9)
H8A	0.1431	-0.0316	0.4359	0.058
H8B	0.3063	-0.0800	0.4592	0.058
S1	0.3356(12)	-0.1133(6)	0.2263(2)	0.0340(16)
S2	0.3372(11)	0.1121(5)	0.2256(2)	0.0308(15)
S3	0.3338(10)	-0.1114(6)	0.31641(19)	0.0297(15)
S4	0.3342(10)	0.1112(5)	0.3164(2)	0.0287(14)
S5	0.3325(12)	0.1355(6)	0.3977(2)	0.0370(17)
S6	0.3237(11)	-0.1338(6)	0.3983(2)	0.0338(16)

Table 3.7. Anisotropic thermal factors of (EDT-TTFBr_2)$_2$GaBr_4.

atom	U_{11}	U_{22}	U_{33}	U_{23}	U_{13}	U_{12}
Ga1	0.089(5)	0.041(3)	0.031(3)	0.004(2)	0.000	0.000
Br1	0.076(3)	0.072(3)	0.050(3)	0.013(2)	0.012(2)	-0.006(2)
Br2	0.078(3)	0.080(3)	0.047(3)	-0.009(2)	-0.006(2)	-0.020(2)
Br3	0.0367(17)	0.053(2)	0.0295(17)	0.0159(14)	-0.0022(12)	-0.0035(13)
Br4	0.0425(18)	0.049(2)	0.0286(16)	-0.0151(13)	0.0004(12)	-0.0013(13)
C1	0.023(15)	0.06(2)	0.040(18)	0.011(15)	-0.012(12)	0.014(13)
C2	0.031(15)	0.047(18)	0.017(14)	-0.005(11)	0.001(10)	-0.001(12)
C3	0.035(14)	0.030(14)	0.014(12)	-0.005(10)	0.009(9)	0.002(10)
C4	0.054(19)	0.033(16)	0.012(13)	-0.002(11)	-0.009(11)	-0.002(13)
C5	0.042(16)	0.027(15)	0.021(14)	0.001(11)	0.000(11)	0.006(11)
C6	0.018(12)	0.054(17)	0.014(12)	0.015(11)	-0.018(9)	0.002(11)
C7	0.08(3)	0.04(2)	0.05(2)	-0.033(17)	0.008(18)	-0.003(18)
C8	0.05(2)	0.05(2)	0.05(2)	0.021(17)	0.010(15)	0.015(15)
S1	0.055(5)	0.028(4)	0.020(4)	0.002(3)	-0.003(3)	-0.005(3)
S2	0.041(4)	0.028(4)	0.023(4)	-0.005(3)	0.002(3)	0.003(3)
S3	0.035(4)	0.035(4)	0.020(3)	0.001(3)	0.001(3)	-0.001(3)
S4	0.038(4)	0.023(3)	0.026(4)	-0.001(3)	0.002(3)	0.002(3)
S5	0.051(5)	0.034(4)	0.026(4)	-0.006(3)	0.002(3)	0.001(3)
S6	0.042(4)	0.039(4)	0.020(3)	0.007(3)	0.002(3)	0.004(3)

Table 3.8. Bond length of (EDT-TTFBr_2)$_2$$GaBr_4$ (Å).

Ga1-Br2	2.275(6)
Ga1-Br1	2.332(6)
Br3-C2	1.85(3)
Br4-C1	1.82(4)
C1-C2	1.41(4)
C1-S1	1.73(3)
C2-S2	1.75(3)
C3-C4	1.39(4)
C3-S1	1.71(3)
C3-S2	1.78(3)
C4-S4	1.68(3)
C4-S3	1.78(3)
C5-C6	1.32(4)
C5-S3	1.73(3)
C5-S6	1.80(3)
C6-S4	1.74(2)
C6-S5	1.74(3)
C7-C8	1.39(5)
C7-S5	1.83(4)
C8-S6	1.78(4)

Table 3.9. Bond angle of (EDT-TTFBr_2)$_2$$GaBr_4$ (deg).

Br2-Ga1-Br2	110.5(4)
Br2-Ga1-Br1	108.16(18)
Br1-Ga1-Br1	108.4(4)
C2-C1-S1	118(3)
C2-C1-Br4	122(2)
S1-C1-Br4	120.3(19)
C1-C2-S2	115(2)
C1-C2-Br3	127(2)
S2-C2-Br3	117.3(17)
C4-C3-S1	124(2)
C4-C3-S2	119(2)
S1-C3-S2	116.5(15)
C3-C4-S4	126(2)
C3-C4-S3	119(2)
S4-C4-S3	115.4(15)
C6-C5-S3	118(2)
C6-C5-S6	129(2)
S3-C5-S6	113.1(16)
C5-C6-S4	117(2)
C5-C6-S5	129(2)
S4-C6-S5	114.0(16)
C8-C7-S5	120(3)
C7-C8-S6	116(3)
C3-S1-C1	95.8(15)
C2-S2-C3	94.5(14)
C5-S3-C4	93.6(13)
C4-S4-C6	95.8(14)
C6-S5-C7	99.2(14)
C8-S6-C5	100.9(14)

3.3 Magnetic susceptibilities

Fig. 3.4 shows the magnetic susceptibility χ of (EDT-TTFBr$_2$)$_2$GaBr$_4$ in external magnetic field $H = 2$ T applied parallel to the a-axis. No anisotropy was observed in the field applied along the three crystallographic axes. The $GaBr_4^-$ salt shows Pauli paramagnetism with a susceptibility of $\chi = 5 \times 10^{-4}$ emu/mol at room temperature. The absolute value of χ is the typical value in organic conductors, for examples, 13×10^{-4} emu/mol for (BMDT-TTF)$_3$ClO$_4$(1,2-dichloroethane) [18], 0.92×10^{-4} emu/mol for α'-(BEDT-TTF)$_2$AuBr$_2$ [19], 2.5×10^{-4} emu/mol for (DMET)$_2$GaBr$_4$ [11] and 6×10^{-4} emu/mol for TTF·TCNQ [20]. The value decreases as the temperature decreases down to $T_{\rm MI} \sim 70$ K, at which a metal-insulator (MI) transition takes place as will be mentioned later in the results of resistivity and EPR measurements. The susceptibility decreases monotonically as the temperature is lowered down to $T_{\rm MI}$ The large temperature dependence of χ often observed in the organic metals [20–23], though there is no decisive explanation. χ becomes independent of temperature below T_1 with a value of $\chi = 2.7 \times 10^{-4}$ emu/mol. It is difficult to discuss the temperature dependence of χ in the temperature range $T < 10$ K because of the large contribution of the paramagnetic impurities.

On the contrary to the $GaBr_4^-$ salt, the localized magnetic moment of Fe^{3+} is dominant in the magnetic susceptibility χ of the $FeBr_4^-$ salt as shown in Fig. 3.5. χ of the $FeBr_4^-$ salt obeys the Curie-Weiss law in the high temperature region above ca. 150K with Curie constant $C = 4.40$ emu·K/mol and Weiss temperature $\Theta = -3.6$ K, the former of which corresponds to one $S = 5/2$ spin of $FeBr_4^-$ per formula unit. Therefore, the magnetism is governed by the Fe^{3+} localized spins, although the minor contribution of the donor π-electron spins is possible. The susceptibilities take a broad hump of short range order at around 20 K, and below ca. 11 K, anisotropic behavior emerges between the different field directions, where χ increases as the temperature decreases for $H \parallel a$- and c-axes whereas it decreases for $H \parallel b$-axis. The appearance of the anisotropic behavior indicates an onset of an antiferromagnetic (AF) transition at $T_{\rm N} = 11$ K, where the spin easy axis is oriented parallel to the b-axis in the ordered state as evidenced by a decreasing trend of the

susceptibility below $T_{\rm N}$. On the contrary to ordinary antiferromagnets, χ in the directions $H \parallel a$ and c below $T_{\rm N}$ increase after a plateau at $T_{\rm N}$ as the temperature is lowered. It is known that the spin wave excitation causes the increase of χ below $T_{\rm N}$. In general, according to the spin wave theory [25], the susceptibility along the hard axis $\chi_\perp$ including the spin wave is described as

$$\chi_\perp = \frac{N_{\rm A} g^2 \mu_{\rm B}^2}{4s|J|}\left[1 - \frac{1}{2S}(c + c') - \frac{1}{S}\frac{\zeta(2)}{2\pi^2\eta^2}\left(1 - \frac{c}{S}\right)\theta^2 \cdots\right], \tag{3.1}$$

where θ is described as

$$\theta = \frac{k_{\rm B} T}{2s|J|S}, \tag{3.2}$$

and $N_{\rm A}$, g, $\mu_{\rm B}$, S, $\zeta(x)$ $k_{\rm B}$, s and $|J|$ are the Avogadro number, the g-value, the Bohr magneton, the spin value, the Zeta function, the Boltzmann constant, the number of interaction paths and the strength of the antiferromagnetic interaction. c, c', η are structural factors and the values are ca. 0.1, 0.15 and 0.5. In the present case, the small magnetic susceptibility $\chi \sim 0.9$ below $T_{\rm N}$ associated with large $|J|$ and the large value of $S = 5/2$ reduce the contribution of the spin wave resulting in the temperature independent feature of eq. (3.1) below $T_{\rm N}$ in hard axes. Therefore, the spin wave contribution is excluded for a possible explanation of the susceptibility behavior. The increase below $T_{\rm N}$ is also found in λ-$(BETS)_2FeCl_4$ and $(EDO\text{-}TTFBr_2)_2FeBr_4$ [10, 24], though the origin of the increase is unclear.

$T_{\rm N}$ are quite higher than those expected from the crystal structure, in which the anion-anion distances are considerably longer than the sum of van der Waals radii. Therefore, such high $T_{\rm N}$ suggests that magnetic moments of the anions are connected by π-d indirect interaction which is strong enough to produce such a high transition temperature.

The magnetization curves of the $FeBr_4^-$ salt at 2 K are shown in Fig. 3.6. The crystal has small magnetizations in the whole observed field range even up to 7 T, which are only ca. 1/5 to 1/4 of the saturated value (5 $\mu_{\rm B}$) at the maximum field investigated. Here, the saturation field is roughly estimated as 27 T, which is obtained by extrapolating the linear fitting line of the magnetization of $H \parallel c$-axis in the low field range ($0 \leq H \leq 3$ T) to the saturation magnetization value (5 $\mu_{\rm B}$). The large saturation field is caused by π-d interaction, suggesting the presence of

the strong antiferromagnetic π-d interaction acting between the d-electron spins. In the mean field approximation, $T_{\rm N}$ is described as

$$T_{\rm N}/K = \frac{2}{\chi_\perp/\mathrm{emu}\cdot\mathrm{mol}^{-1}}, \tag{3.3}$$

and $T_{\rm N}$ is estimated ca. 22 K from the observed $\chi_\perp$ $\sim$0.09 at $T_{\rm N}$. In the low dimensional system, $T_{\rm N}$ becomes lower than that expected from the mean field approximation owing to a fluctuation. Therefore the temperature $T_{\rm max}$ of the peak of χ is more suitable for employing relation (3.3), the observed value of $T_{\rm max}$ $\sim$20 K being in good agreement with the relation.

In $H \parallel c$ and b-axes, the magnetizations monotonously increase as the magnetic field is raised with convex curvatures. On the other hand, the magnetization in $H \parallel b$-axis shows quite smaller values than that for other two axes in the low field region, which represent the spin easy axis is aligned parallel to the b-axis. In $H \parallel b$-axis, the magnetization shows a sudden increase of a spin flop transition at $H_{\rm SF} \sim 5.5$ T. The magnetization of $H \parallel b$-axis is smaller than that of other two directions even above $H_{\rm SF}$. The observed spin flop field for $H \parallel b$ is considerably large, compared with typical $FeBr_4^-$ salts of TTF-type organic donors [8–10]. The spin flop field $H_{\rm SF}$ is described as

$$H_{\rm SF} = \sqrt{\frac{2K_{\rm u}}{\chi_\perp - \chi_\parallel}}, \tag{3.4}$$

where $K_{\rm u}$ is an anisotropy energy. In the $FeBr_4^-$ salt, $K_{\rm u}$ is not so differ from that of other salts, while $\chi_\perp - \chi_\parallel$ are about 1/5$\sim$1/10 times smaller than the typical $FeBr_4^-$ salts because of strong antiferromagnetic interaction resulting in large spin flop field.

It should be noted that there is a problem remaining unsolved in magnetization curves of the $FeBr_4^-$ salt; large difference between the magnetization along the crystallographic three axes above the spin flop field, where the magnetizations have values of $M = 1.12$, 0.93 and 1.25 $\mu_{\rm B}$ with $H \parallel a$, b and c-axes, respectively, at $H = 7$ T. The difference between a and c-axes are easily understood as a difference of the g-values. These two axes have $g = 1.87$ and 2.00 for a and c-axes, respectively, at 20 K as will be discussed in section 3.6, and the difference of the g-values $\Delta g \sim 0.1$ are roughly same as that of the magnetizations. In contrary

to the small difference mentioned above, that between the a or the c-axis and the b-axis is too large to be explained by the difference of the g-values. The candidate of the large difference is the thermal fluctuation of the spins around the H_{SF}. In the finite temperature, the magnetization along the easy axis takes a larger and smaller values in below and above H_{SF} than that expected at 0 K owing to the thermal fluctuation. Considering this effect, the magnetization along the b-axis probably increases and takes similar value to that along the a or c-axes in higher field region.

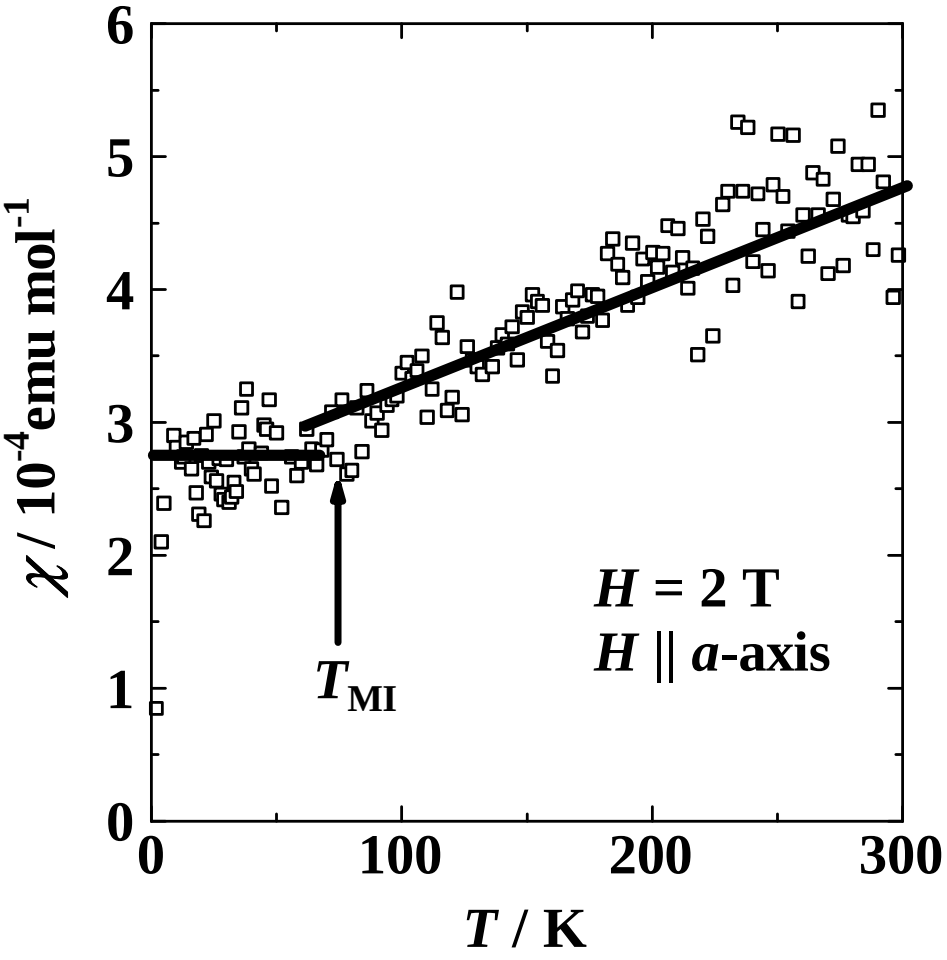

Fig. 3.4. Static susceptibility of (EDT-TTFBr_2)$_2$$GaBr_4$ with external magnetic field $H = 2$ T applied parallel to the a-axis. Two solid lines are obtained with the least square fits above 80 K and below 60 K. $T_{\rm MI}$ denotes the metal-insulator transition temperature. A steep drop of the susceptibility appearing below 10 K is an artifact due to the overestimation of the Curie tail of paramagnetic impurities.

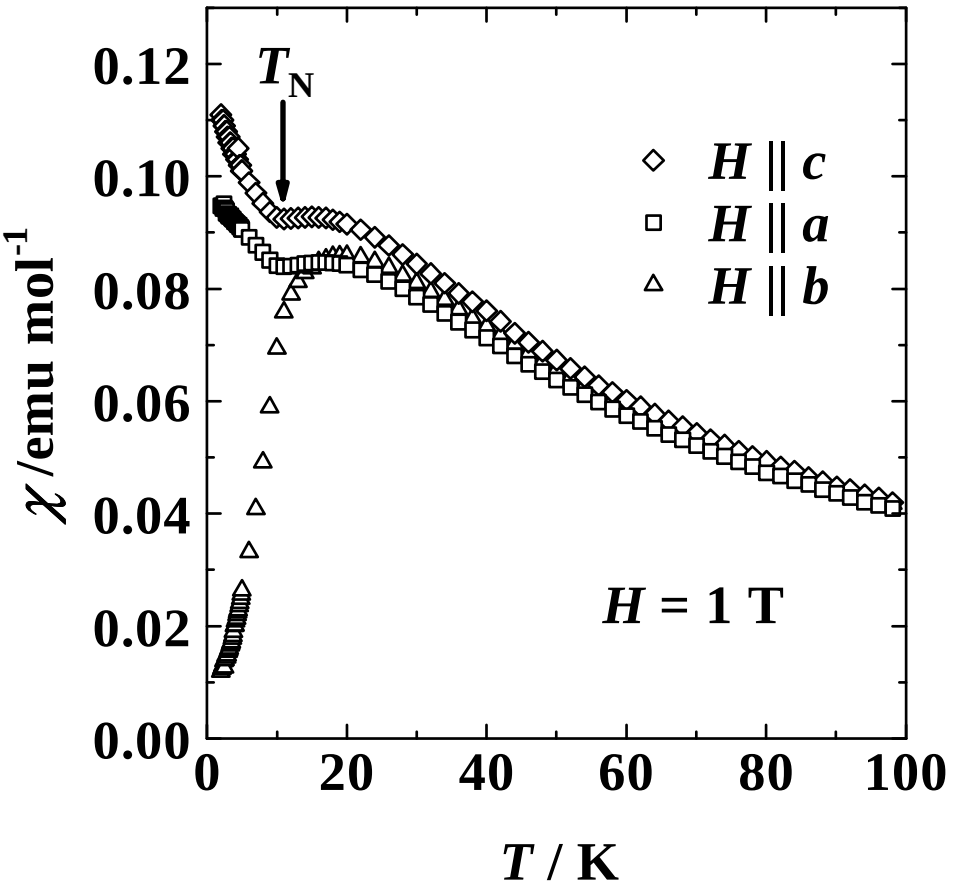

Fig. 3.5. Magnetic susceptibilities of (EDT-TTFBr_2)$_2$$FeBr_4$ in external magnetic field $H = 1$T applied parallel to the three crystallographic directions. $T_N = 11$ K is the antiferromagnetic transition temperature.

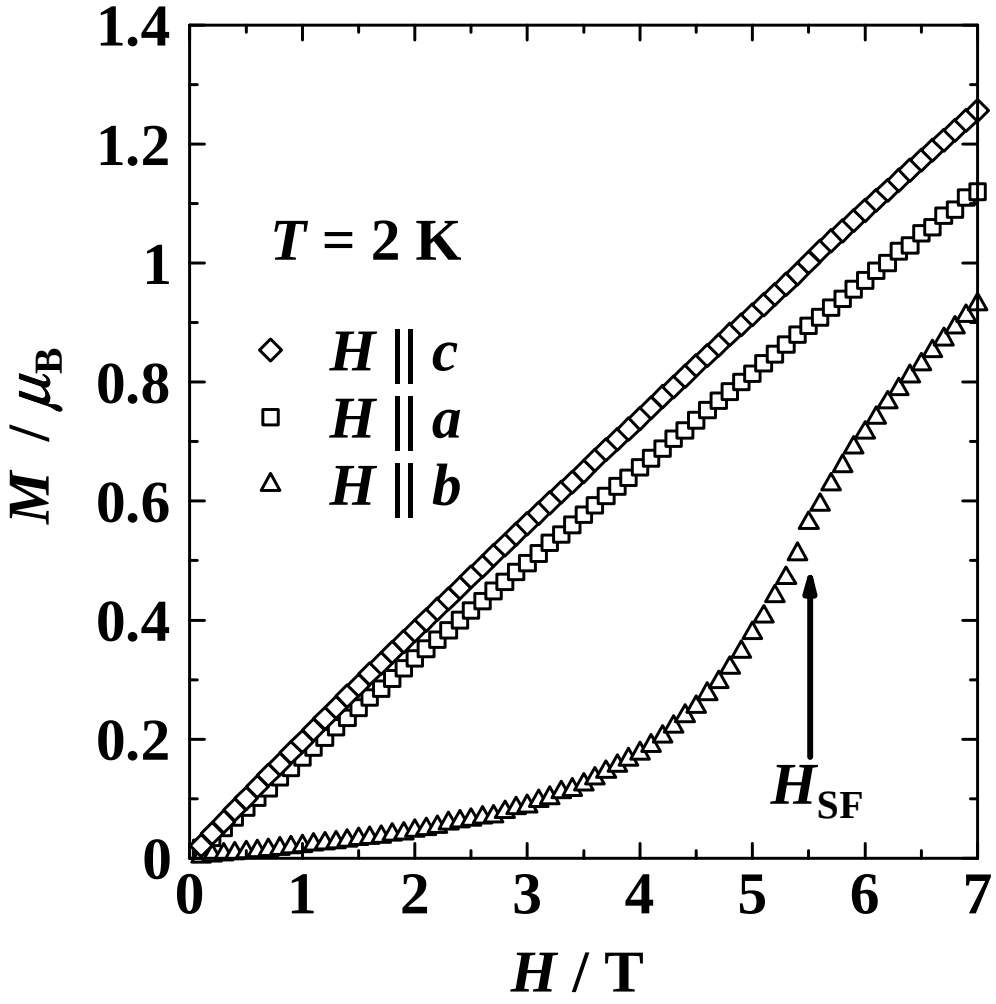

Fig. 3.6. Magnetization curves of (EDT-TTFBr_2)$_2$$FeBr_4$ at $T = 2$ K in the field applied along the three crystallographic axes. A spin flop transition takes place at $H_{\rm SF} = 5.5$ T for $H \parallel b$.

3.4 Electrical resistivities

The electrical resistivities of the $GaBr_4^-$ salt measured along the a-axis, which is parallel to the conducting donor chain, at ambient and high pressures, are shown in Fig. 3.7. The resistivities at room temperature are decreases as pressure is raised in the pressure region $0 \leq P \leq 11.0$ kbar, while no significant difference is observed in the pressure range $11.0 < P$ kbar as shown in Fig. 3.8. At ambient pressure, the salt has metallic conduction with a resistivity minimum at about 130 K. The resistivity slightly increases below the temperature with no singularity observed in contrast to that in the $FeBr_4^-$ salt as will be discussed later. When the high pressure is applied, the resistivity and the temperature of a resistivity minimum are lowered, in spite that the increase of the resistivity at low temperatures does not disappear even at 14.8 kbar.

The behaviors become legible when the derivative of the resistivity, $\Delta E = \Delta \ln(\rho/\Omega\mathrm{cm})/\Delta(1/T)$, is plotted as a function of temperature, as shown in Fig. 3.9. Here, the value ΔE roughly represents the activation energy in the resistivity, where the position of its peak indicates an onset of a MI transition temperature (T_{MI}) in case that an insulating state is stabilized on the low temperature side of the peak. There are two anomalies in the ΔE vs T plot; that is, a peak at higher temperature (T_{p}) and a shoulder (T_{s}) at lower temperature. Figure 3.10 shows the pressure dependencies of T_{p} and T_{s}, where the temperatures are obtained from the maximum and the crossing point between linear fitting lines on both side of the anomaly for the high and low temperature anomalies, respectively. The behavior at ambient pressure is somewhat different from that at high pressure; that is, the appearance of the peak is rather ambiguous and an apparent hump emerges around 48 K. From the technical viewpoint, it should be noted that the resistivity measurement is used to be subjected to the generation of microcracks in the sample in cooling process due to the thermal contraction, in contrast to high quality crack-free measurements in a pressure medium at high pressures. Indeed, the EPR result suggests the onset temperature of the MI transition at 70 K. T_{p} is linearly dependent on the pressure except that at ambient pressure. However, when the anomaly of the EPR results is taken as the MI transition temperature,

the linear dependence is held in the whole pressure range below 11 kbar, while the resistivity becomes pressure independent above the pressure. Therefore, the high temperature peak is assigned to the MI transition. In the meantime, the shoulder observed in lower temperature is independent of the pressure. $T_{\rm s}$ is roughly same as the antiferromagnetic transition of π-electrons, as will be discussed in section 3.6. The small difference of the temperature between $T_{\rm N} = 9$ K estimated from the EPR result and the anomaly of ΔE at 13 K is due to the inaccurate estimation of the latter. Actually, the disappearance of EPR signal firmly indicates the onset of the magnetic transition, although the change of ΔE is considered to be affected by the development of the short range order in the same manner to that in the EPR line width, resulting in higher temperature of the anomaly in the resistivity results.

In contrast to the $GaBr_4^-$ salt, the $FeBr_4^-$ salt shows metallic behavior down to ca. 40 K as shown in Fig. 3.11, and the resistivity increases below 40 K at ambient pressure. The resistivity at room temperature $R_{\rm rt}$ decreases as pressure is raised in the pressure range $0 \leq P \leq 10.1$ kbar, and it takes a roughly constant value in $P > 10.1$ kbar as shown in Fig. 3.12, while the temperature of the resistivity taking a minimum is roughly independent of pressure. For clarifying resistivity anomalies, the derivative of the resistivity is taken as shown in Fig. 3.13. ΔE has a broad hump at ca. 20 K, below which the resistivity clearly increases indicating an onset of a MI transition at this temperature. Thus, the MI transition temperature becomes considerably reduced in the $FeBr_4^-$ salt, in contrast to that in the $GaBr_4^-$ salt. Below the MI transition temperature, an additional ΔE hump at $T_{\rm a} = 11$ K is observed, which is assigned to the magnetic transition of the localized magnetic moment of anions, as mentioned in the previous section. The fact that the magnetic ordering of d-electrons affects the transport properties of π-electrons clearly indicates the important role of the π-d interaction which is caused by the short Br-Br and S-Br contacts between donors and anions.

The temperature positions of the peaks of ΔE largely depend on the pressure; the temperature of broad peak at $T_{\rm MI}$ is lowered from 20 K to 15 K reflecting the decrease of $T_{\rm MI}$ as the pressure increases, while the small peak at $T_{\rm N}$ is elevated from 11 K to 14 K reflecting the increase of $T_{\rm N}$, as shown in Fig. 3.14.

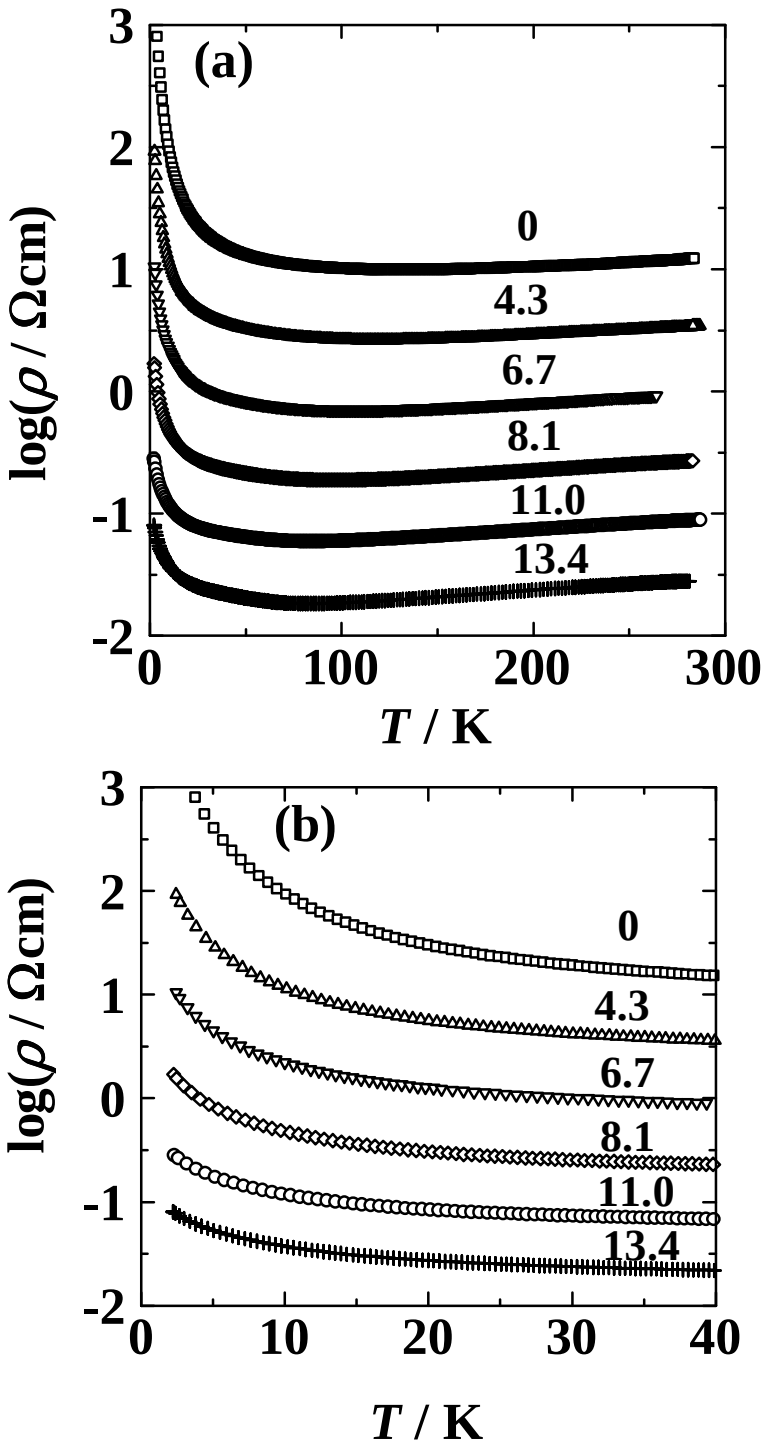

Fig. 3.7. **(a)** Temperature dependence of the electrical resistivity of (EDT-TTFBr$_2$)$_2$GaBr$_4$ at ambient and high pressures measured along the a-axis. **(b)** The enlargement in the low temperature region. The pressure values are given by the numbers indicated, and the data for 0, 4.3, 6.7, 8.1 and 13.4 kbar are vertically shifted up by 0.5, 1, 1.5, 2 and 2.5, respectively, for clarity, in both figures.

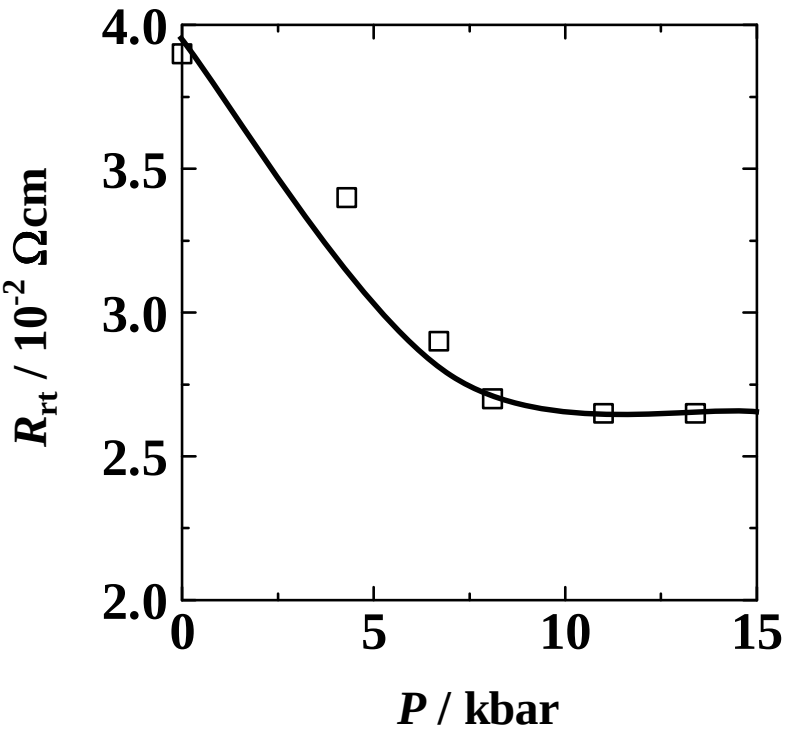

Fig. 3.8. Pressure dependence of the resistivity of (EDT-TTFBr_2)$_2$$GaBr_4$ at room temperature.

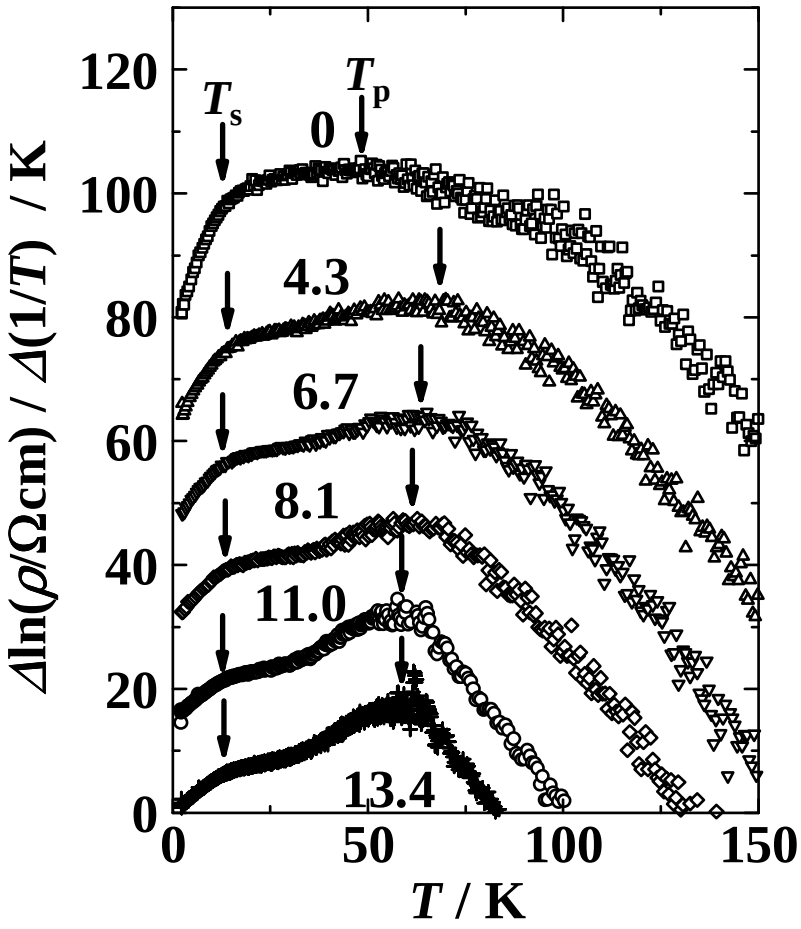

Fig. 3.9. Derivative of the resistivity vs temperature for the $GaBr_4^-$ salt under different pressures. The pressure values are given by the numbers indicated. The data for 0, 4.3, 6.7, 8.1 and 11.0 kbar are vertically shifted up by 75, 60, 45, 30 and 15, respectively, for clarity. The arrows indicate the positions of the peak at high temperature (T_p) and the shoulder at low temperature (T_s).

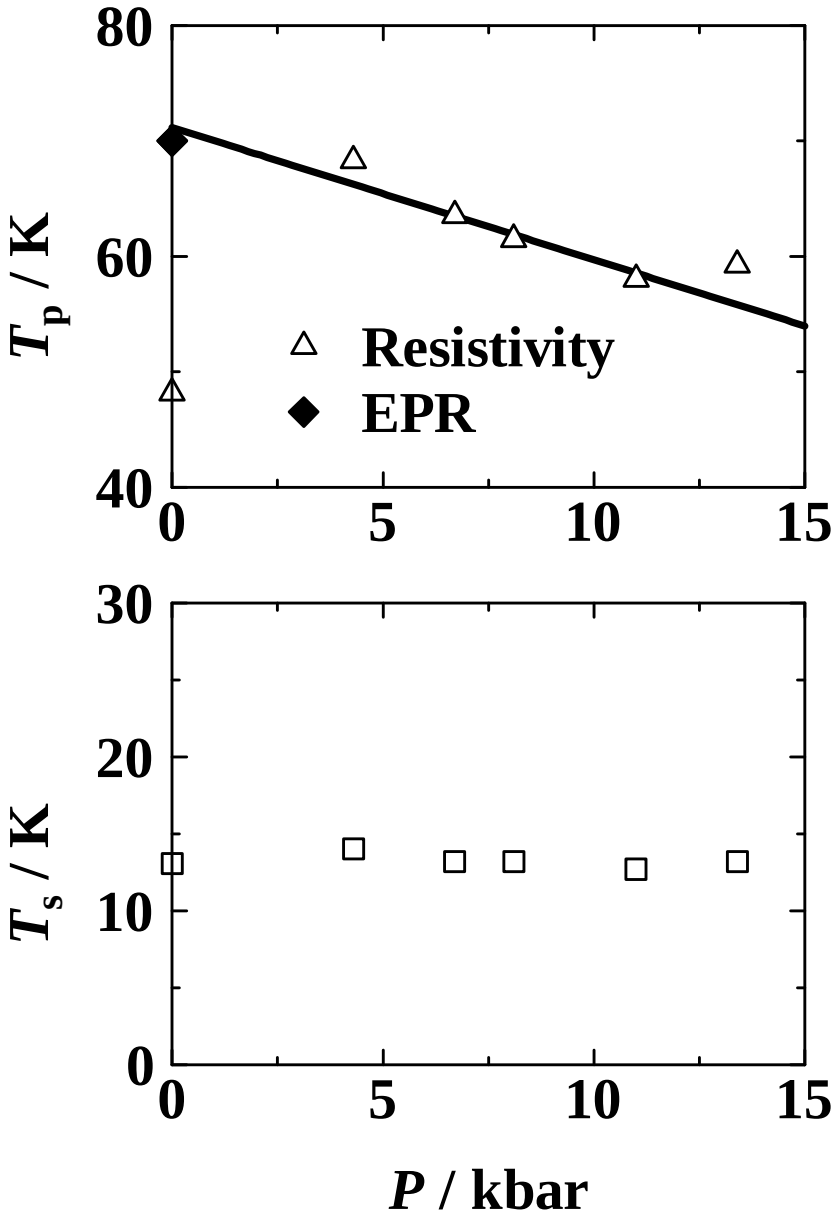

Fig. 3.10. **(a)** Pressure dependence of $T_{\rm p}$. Solid diamond represents the MI transition temperature estimated from the EPR measurement at ambient pressure. The solid line is obtained from the least square fit below 11.0 kbar, where the EPR data is employed for ambient pressure. **(b)** Pressure dependence of $T_{\rm s}$, which is roughly independent of pressure.

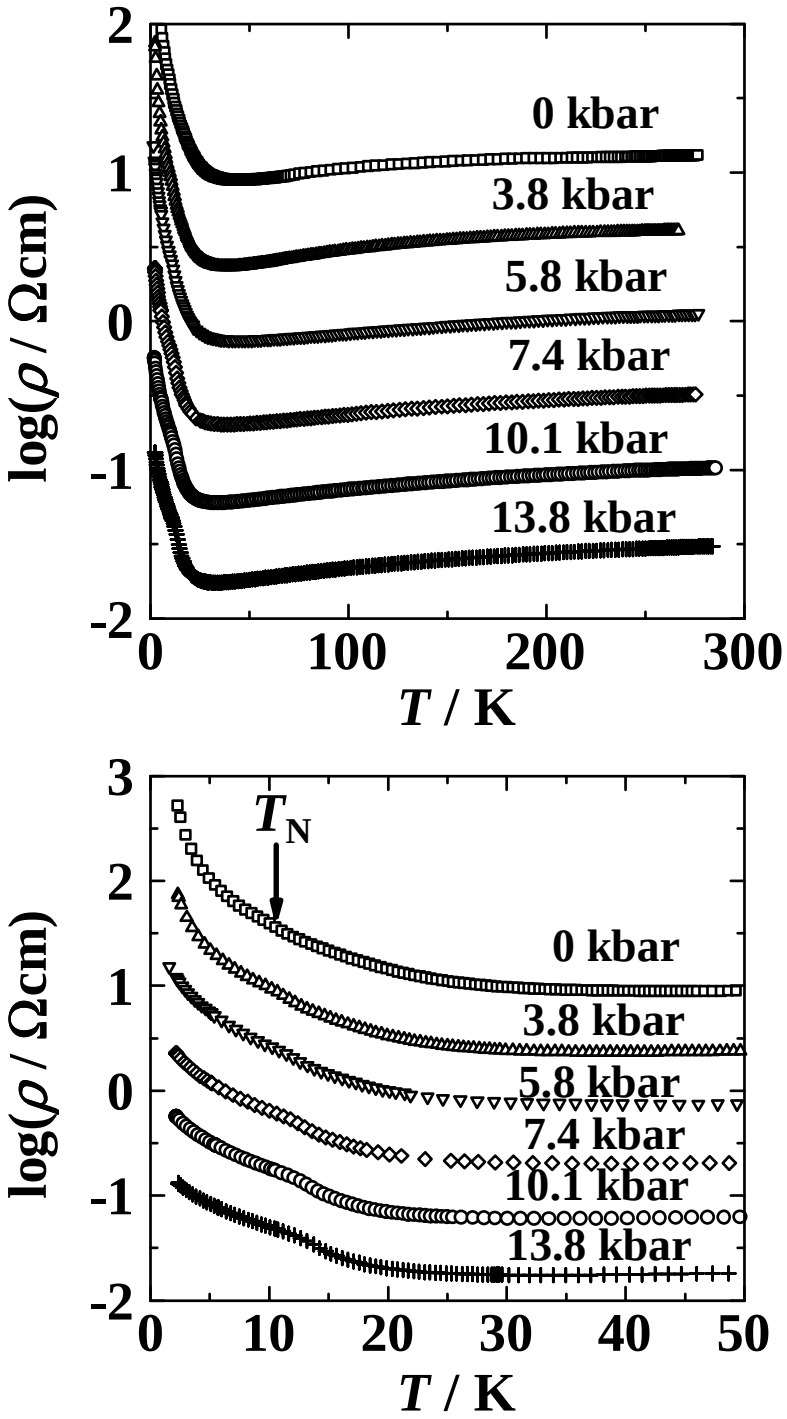

Fig. 3.11. **(a)** Temperature dependence of the electrical resistivity of (EDT-TTFBr$_2$)$_2$FeBr$_4$ at ambient and high pressures measured along the a-axis. (b) The enlargement in the low temperature region. The data for 0, 3.8, 5.8, 7.4 and 10.1 kbar are vertically shifted up by 2.5, 2, 1.5, 1 and 0.5, respectively, for clarity in both figures.

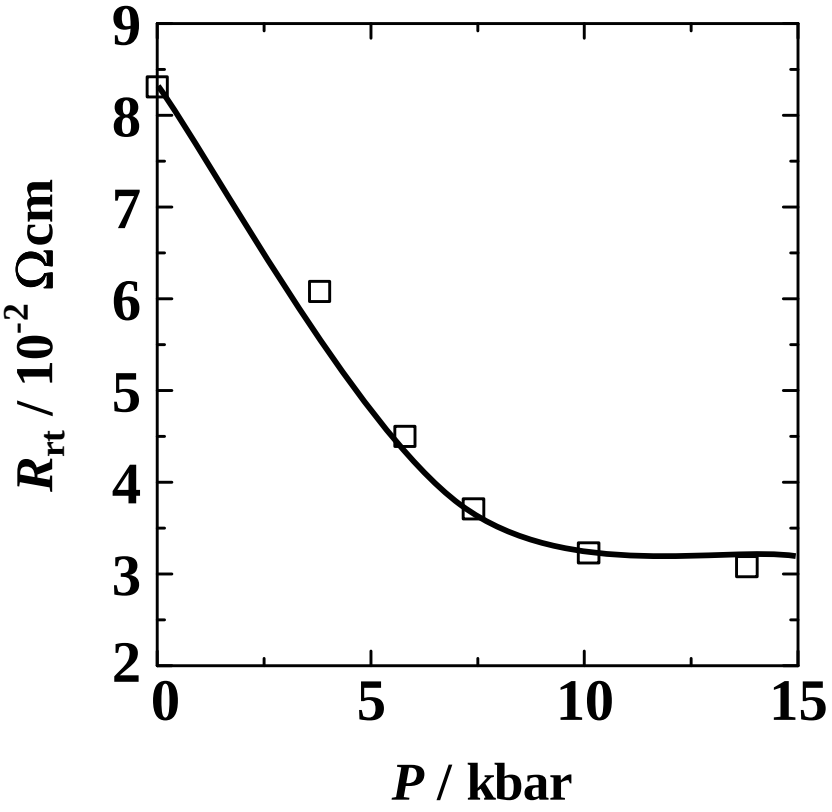

Fig. 3.12. Pressure dependence of the resistivity of (EDT-TTFBr_2)$_2$FeBr_4 at room temperature.

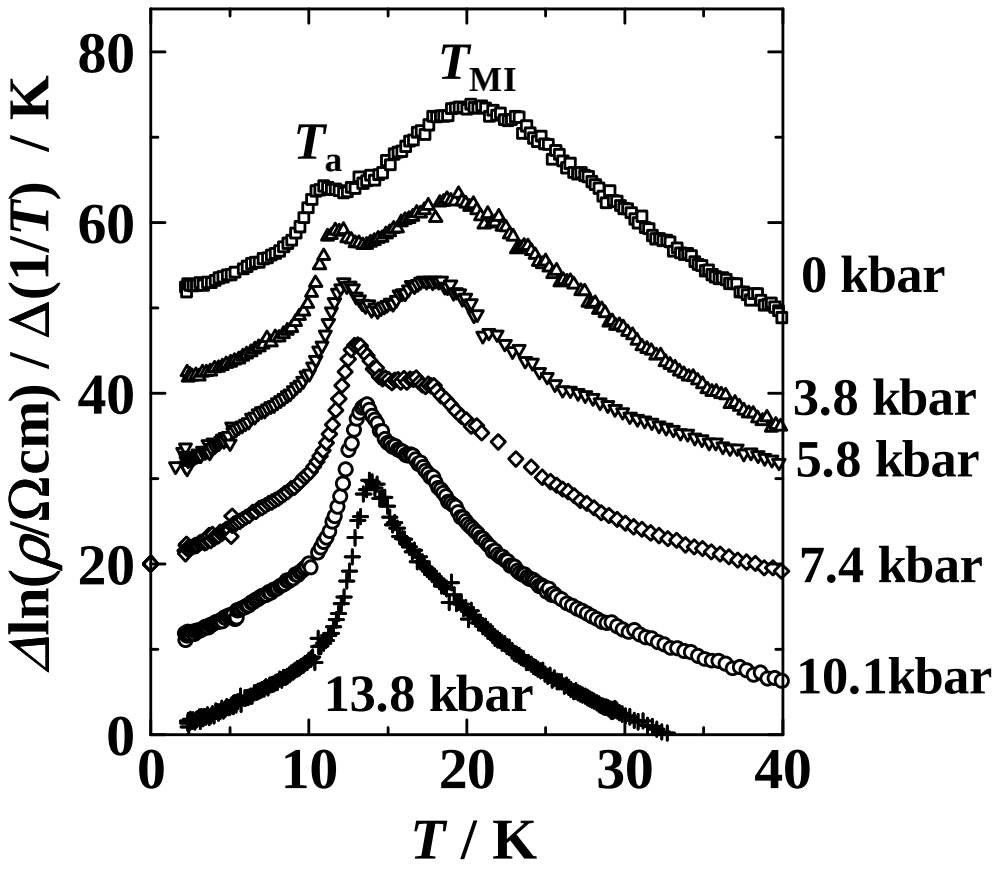

Fig. 3.13. Derivative of the resistivity vs temperature for the $FeBr_4^-$ salt at ambient and high pressure ($0 \leq P \leq 13.8$ kbar). The data for 0, 3.8, 5.8, 7.4 and 10.1 kbar are vertically shifted up by 50, 40, 30, 20 and 10, respectively, for clarity. $T_{\rm MI}$ and $T_{\rm a}$ represent the two peak positions of $\Delta \ln(\rho/\Omega \text{ cm})/\Delta(1/T)$ at higher and lower temperatures, respectively.

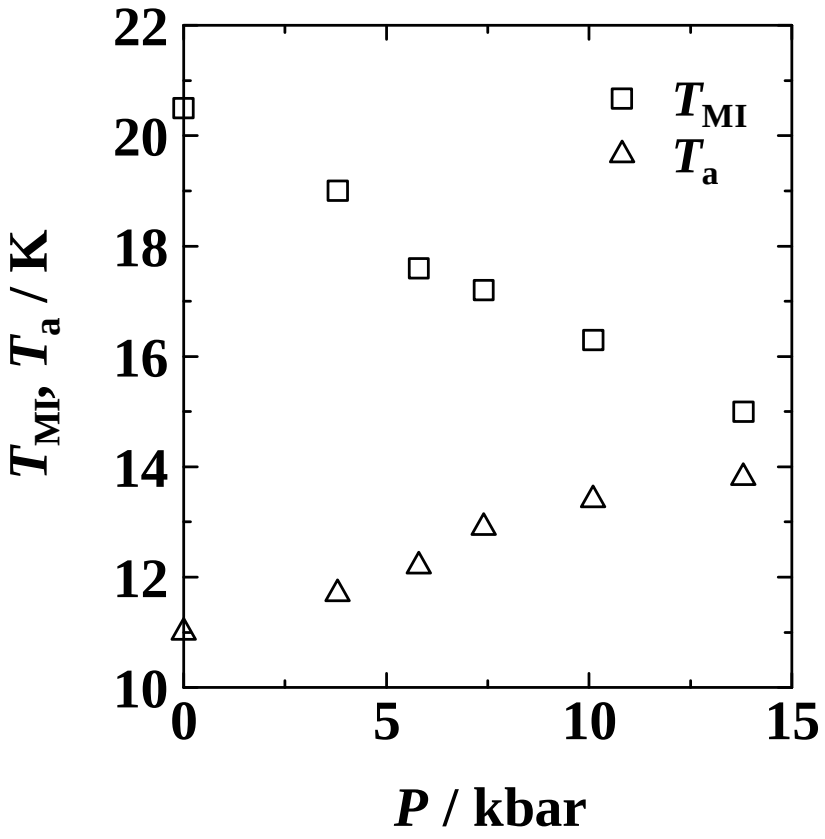

Fig. 3.14. Pressure dependence of T_{MI} and T_{a} shown in Fig. 3.13.

3.5 Magnetoresistances

To investigate the effect of the π-d interaction in different pressures, the magnetoresistances (MR) of (EDT-TTFBr$_2$)$_2$MBr$_4$ (M = Fe, Ga) were measured, where the current I and the magnetic field H are applied parallel to the a-axis (donor stacking axis) and the b-axis ($FeBr_4^-$ spin easy axis), respectively. Figures 3.15 and 3.16 present the field dependence of the MRs of the $GaBr_4^-$ salt and the $FeBr_4^-$ salt at $T = 1.5$ K, respectively.

The $GaBr_4^-$ salt shows only small positive MRs in the whole field range investigated, where the MR increases quadratically regardless of the pressure in the low field region up to ca. 3 T. In the high field region above the field, the slope of the MR vs H plot is gradually reduced giving an S-shaped field dependence, and finally, the MR tends to become saturated. The reduction of the slope and the saturated behavior are weaken by applying pressure, where the MR becomes more linear field dependence in the high field region. The absolute value of the MRs roughly increase as the pressure is elevated up to ca. 7 kbar and then they are lowered above the pressure. In any case, the value of the MR of non-magnetic $GaBr_4^-$ salt is in the range of 2.5$\sim$3.5 % below 15 T at the most.

In contrast, the $FeBr_4^-$ salt shows large pressure-dependent negative MRs. The MR of the $FeBr_4^-$ salt is steeply lowered with a convex curvature followed by the appearance of a kink, at which the spin flop transition takes place, in the low pressure range up to 7.4 kbar. The large negative MR and the anomaly at the spin flop transition are convincing evidences of the existence of the π-d interaction. Above the spin-flop transition, the slope of the MR vs field curve becomes moderate and the MR reaches -23 % at $H = 15$ T in the ambient pressure. Judging from the pressure-induced increase of the field of the kink, the spin flop transition field is elevated from 5.5 to 6.0 T as the pressure goes from 0 to 5.8 kbar as shown in Fig. 3.17. In the pressure range above 7.4 kbar, the kink disappears, although a trace of the kink is evidenced as the presence of the field at which the slope is changed. The disappearance of the kink, which proves the absence of an obvious spin-flop transition, suggests the change in the magnetic structure or the ineffectiveness of the d-electron spins to the π-electron transport in the high pressure range, where

the metallic features are enhanced. This is supported by the reduction of the negative MR as the pressure increases, as shown in Fig. 3.18. The figure clearly shows the reduction of the effect of the d-spins, where the magnitude of the MR monotonous decreases as the pressure increases. The value of MR at $H = 15$ T and the highest pressure $P = 13.8$ kbar is only 19 % of that at ambient pressure.

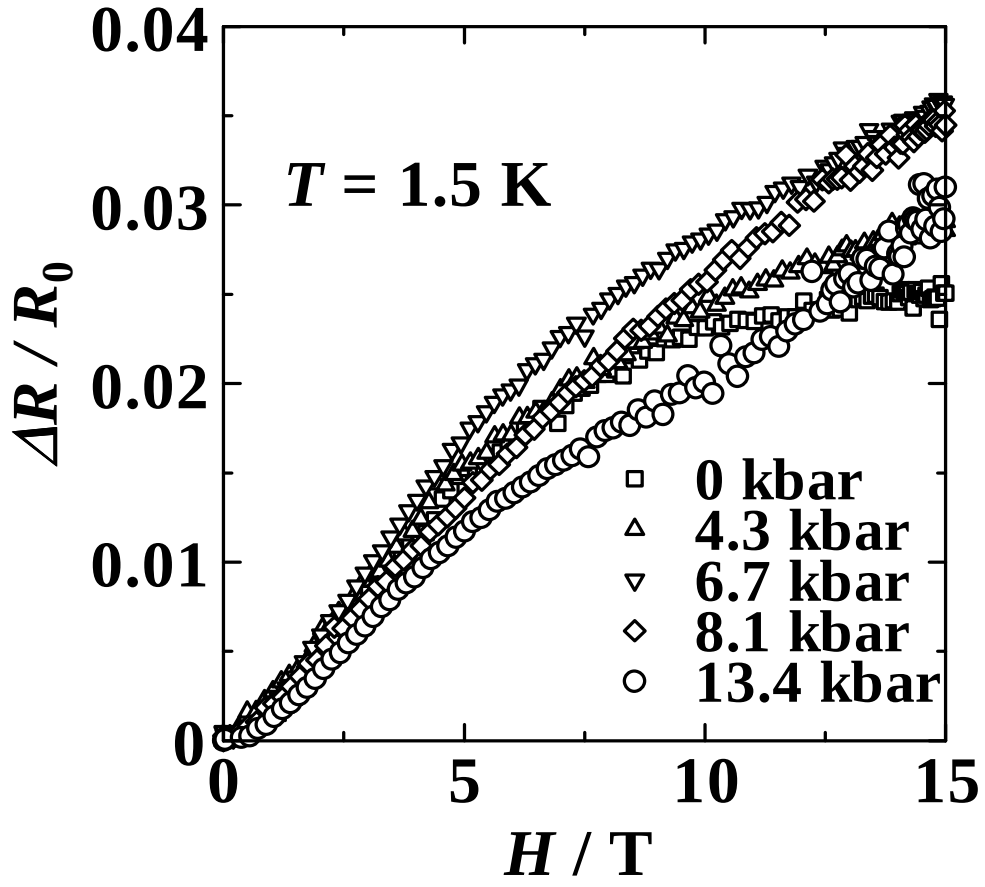

Fig. 3.15. Magnetoresistances of (EDT-TTFBr_2)$_2$$GaBr_4$ in different pressures at 1.5 K. The current and external magnetic field are applied parallel to the a- and b-axes, respectively.

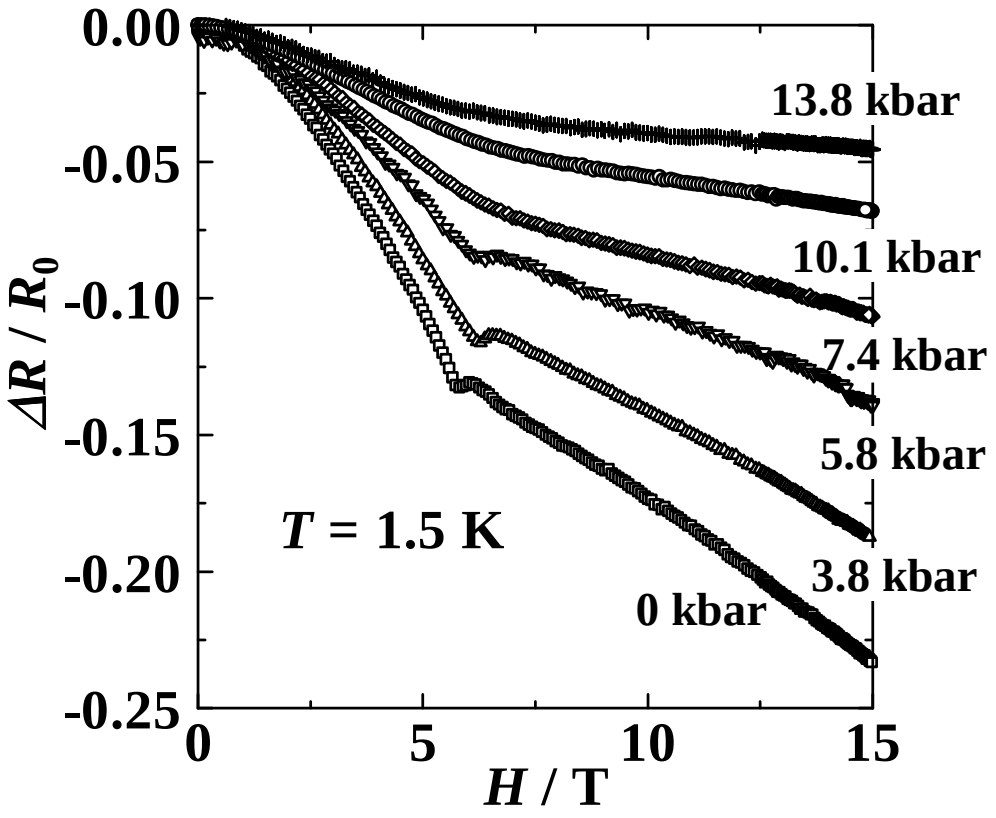

Fig. 3.16. Magnetoresistances of (EDT-TTFBr_2)$_2$$FeBr_4$ at 1.5 K in different pressures. The current and external magnetic field are applied parallel to the a- and the b-axes, respectively.

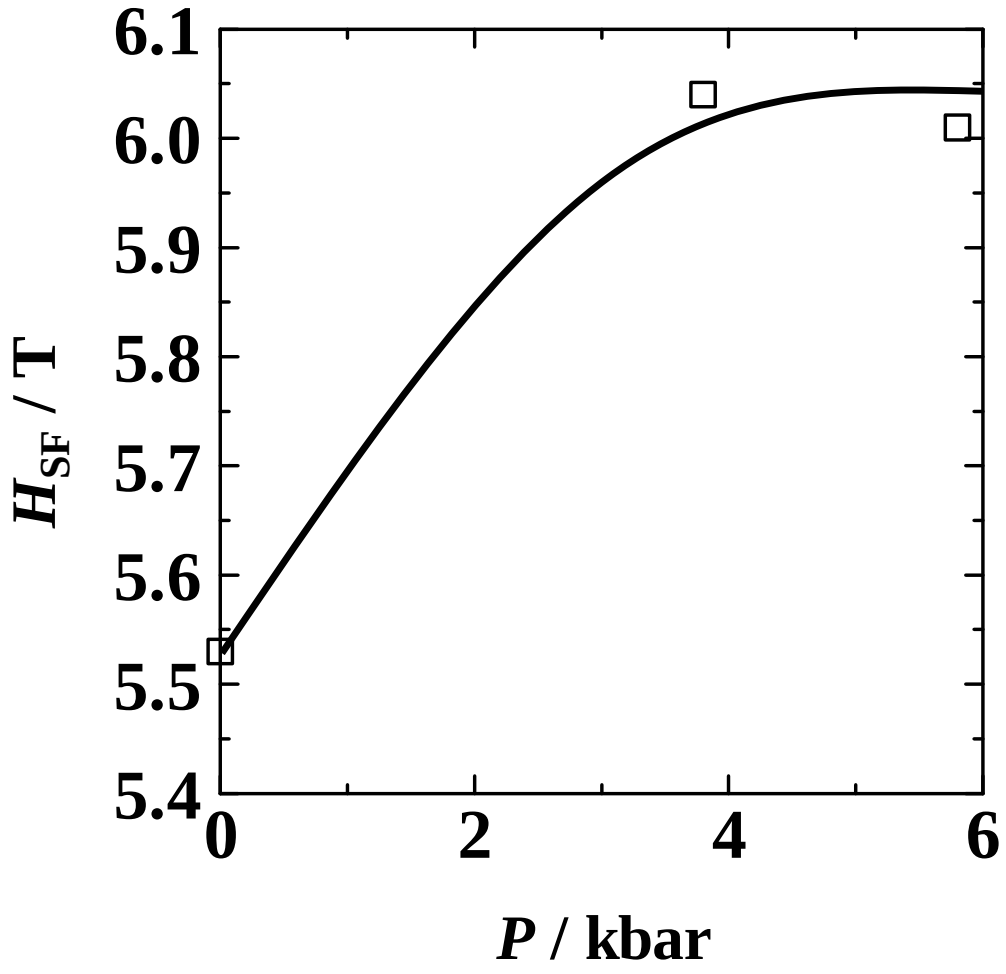

Fig. 3.17. H_{SF} of (EDT-TTFBr_2)$_2$FeBr_4 at 1.5 K estimated from the kink of the MR.

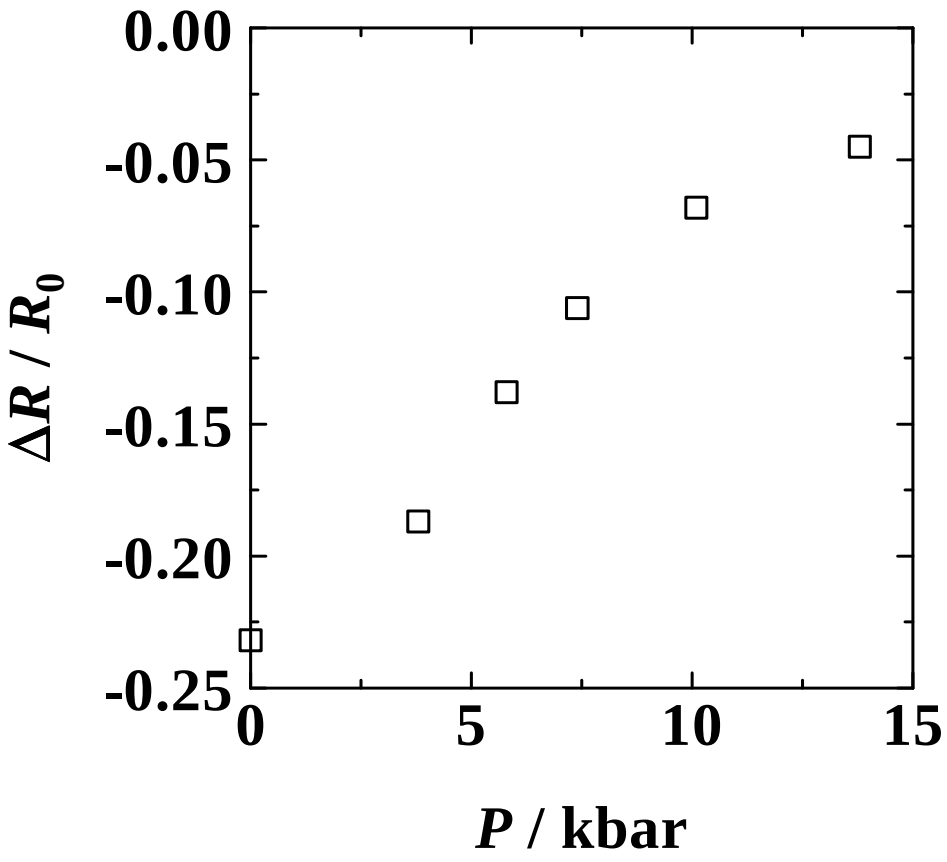

Fig. 3.18. Pressure dependence of MR at $H = 15$ T, $T = 1.5$ K.

3.6 EPR measurement

The results of EPR measurements of (EDT-TTFBr$_2$)GaBr$_4$ are shown in Figs. 3.19-3.21. The salt shows a Lorentzian shape signal with line width $\Delta H_{\rm pp}$ = 7.36, 7.55 and 7.16 and g-value g = 2.0029, 2.0089 and 2.0105 for $H \parallel a$, b and c-axes, respectively, at room temperature. The anisotropy in the g-value is in good agreement with the orientation of donor molecule; that is, the lowest g-value corresponds to the field direction applied perpendicular to the molecular plane, while the g-value becomes the highest in the field applied along the long side of the molecular plane [26]. The spin susceptibility $\chi_{\rm spin}$ shown in Fig. 3.19 gradually decreases as the temperature decreases down to ca. 70 K, which is the MI transition temperature. Below the temperature, $\chi_{\rm spin}$ takes a roughly constant value $\chi_{\rm spin} \sim 2.7 \times 10^{-4}$ emu mol^{-1} followed by the steep decreasing below ca. 25 K, and the EPR signal disappears below ca. 9 K. The existence of the EPR signal below $T_{\rm MI}$ evidences the survival of the spin degree of freedom in the insulating phase, indicating that the insulating ground state above 10 K is neither CDW state nor SDW state. The steep drop of $\chi_{\rm spin}$ is considered to be associated with an onset of an antiferromagnetic transition at $T_{\rm N}$ = 9 K, which is clearly proved by the divergence of the line width $\Delta H_{\rm pp}$ and g-value as will be mentioned below.

The anomalies at $T_{\rm MI}$ and $T_{\rm N}$ of the π-electron system are more clearly seen in the data of $\Delta H_{\rm pp}$. As shown in Fig. 3.20, the values of $\Delta H_{\rm pp}$ keeps the relation $\Delta H_{\rm pp}(b) > \Delta H_{\rm pp}(a) > \Delta H_{\rm pp}(c)$ in the temperature range $T >$ 45 K. They gradually decreases with a convex curvature as the temperature is lowered down to $T_{\rm MI}$, at which it takes an abrupt drop accompanied by a plateau on the low temperature side of $T_{\rm MI}$. In the temperature range $20 < T < T_{\rm MI}$, the $\Delta H_{\rm pp}$ shows a complicated behavior; that is, $\Delta H_{\rm pp}$ along the three axes plateau around 40 K followed by decrease below ca. 35K, where $\Delta H_{\rm pp}$ along the b-axis becomes smaller than that along the a-axis. Judging from the decreasing of the $\chi_{\rm spin}$ below 35 K, the decrease of $\Delta H_{\rm pp}$ below 35 K is originated from the antiferromagnetic short range order, but the detail is unclear. Finally, $\Delta H_{\rm pp}$ starts increasing divergently below 20 K, the EPR signal disappearing at ca. 9 K. The divergent behavior of $\Delta H_{\rm pp}$ is the nature of the precursor of the long range antiferromagnetic ordering

of π-electrons, which is evidenced by the steep decrease of $\chi_{\rm spin}$, followed by an antiferromagnetic long range ordering taking place at $T_{\rm N} \sim 9$ K.

The effects of short range ordering and antiferromagnetic transition are also clearly seen in the change of g-value as shown in Fig. 3.21. The g-values are roughly temperature independent above $T_{\rm MI}$. Below $T_{\rm MI}$, the g-values along the b and the c-axes gradually increases, while that of the a-axis keeps a constant value. The small changes of the g-values in the a and b-axes are considered to be owing to the appearance of the 1D short range order of localized magnetic moment in donor chains, where the g-value along the chain direction (= a-axis in the crystal) gradually decreases and that perpendicular to the chain (= b and c-axes) increase [27,28]. The g-values increase suddenly below 20 K in all the field directions, which are again suggestive of the development of magnetic short range ordering followed by the long range order at 9 K where the g-values diverge.

The angular dependence of $\Delta H_{\rm pp}$ below $T_{\rm MI}$ is quite different from that above $T_{\rm MI}$, as shown in Figs. 3.22 and 3.23. Above $T_{\rm MI}$, the angular dependence of $\Delta H_{\rm pp}$ is described as

$$\Delta H_{\rm pp} = \Delta H_{\rm pp}(1) \cos^2\theta + \Delta H_{\rm pp}(2) \sin^2\theta, \tag{3.5}$$

where $\Delta H_{\rm pp}(1)$ and $\Delta H_{\rm pp}(2)$ represent the line widths in the two different principle axes 1 and 2, and θ is the angle between external field and the principle axis 1. In contrary to the angular dependence of $H_{\rm pp}$ above $T_{\rm MI}$, that below $T_{\rm MI}$ does not obey eq. (3.5) owing to the effect of the magnetic moments of insulating π-electrons as will be discussed in section 3.7.1.

Contrary to the $\Delta H_{\rm pp}$, the angular dependence of the g-value has no significant change between above (100 K) and below (45 K) $T_{\rm MI}$ as shown in Figs. 3.24 and 3.25. The angular dependence of both temperature obeys an ordinary angular dependence of the g-value described as

$$g = g_1 \cos^2\theta + g_2 \sin^2\theta, , \tag{3.6}$$

where g_1 and g_2 are the g-values of the two principle axes, and θ is a angle between the external field and the principle axis 1.

In the case of (EDT-TTFBr_2)$_2$FeBr_4, in spite of the coexistence of the two kinds of magnetic electrons (π and d), only one broad signal was observed in the EPR

spectra in the temperature range , as shown in Fig. 3.26, due to the coalescence of the two signals of π and d-electrons. This suggests the presence of the interaction between these two spins. The values of the line width $\Delta H_{\rm pp}$ at room temperature are 86, 129 and 56 mT for $H \parallel a$, b and c-axes, respectively. The values are in same order of that of the $FeBr_4^-$ solution of CH_3CN (55 mT) [29, 30], and the angular dependence of the $H_{\rm pp}$ is well described by eq. (3.5) as shown later suggesting a small contribution of the dipole-dipole interaction which has different angular dependence as shown in Fig. 3.27. Therefore not a spin-spin relaxation time but a intra-molecular spin-lattice relaxation time T_1 of $FeBr_4^-$ anion is dominant to the line widths.

$\Delta H_{\rm pp}$ has rather simple temperature dependence as shown in Fig. 3.28 compared with that of the $GaBr_4^-$ salt. $\Delta H_{\rm pp}$ along the b and c-axes gradually increases as temperature decreases, while that of a-axis is roughly constant down to ca. 40 K. Below ca. 30 K where the anisotropies in the susceptibilities start appearing, $\Delta H_{\rm pp}$ increases in all the field directions as the temperature is lowered. The increase of the $\Delta H_{\rm pp}$ is related to the development of short range order of $FeBr_4^-$ [31, 32], and $\Delta H_{\rm pp}$ diverges at $T_{\rm N}$.

The g-values take values $g = 2.02$, 1.97 and 2.05 for $H \parallel a$, b and c-axes, respectively. The g-values along the a and b-axes are roughly independent of the temperature down to ca. 150 K, while that along the c-axis gradually increases as the temperature decreases. Below 150 K, the g-values along the a and c-axes gently decrease, followed by the steep decrease below 30 K owing to antiferromagnetic short range ordering [27]. On the contrary to these two axes, the g-value along the b-axis gradually increases, take a maximum at ca. 35 K, and then it decreases. The increase of the g-value along the b-axis is accompanied by the change of the angular dependence of the g-value.

The angular dependence of $\Delta H_{\rm pp}$ is roughly described by the eq. (3.5) in both the ac and bc-planes, as shown in Figs. 3.30 and 3.31 with $\Delta H_{\rm pp}(a) = 85.3$ and 104.3, $\Delta H_{\rm pp}(b) = 123.1$ and 174.2 and $\Delta H_{\rm pp}(c) = 55.9$ and 82.7 mT for $T = 300$ and 40 K, respectively.

Different from the sinusoidal angular dependence of $\Delta H_{\rm pp}$, the angular dependence of the g-value shows anomalous behavior, especially in $H \parallel bc$-plane as

shown in Fig. 3.32. At room temperature, the angular dependence of the g-value in $H \parallel bc$-plane is approximately represented by eq. (3.6) except the presence of a small anomaly observed near $\theta \sim 0$ and 180 °, where a minimum of the g-value exists at around 10 and 170 °. The anomaly becomes larger and more clear at 40 K, where the angular dependence of the g-value is far from the behavior described as eq. (3.6). The observed anomalous angular dependence is also observed in $H \parallel ac$-plane as shown in Fig. 3.33, although the anomaly is not so large in this plane. It may be possible to explain the origin of the anomaly by a small misalignment of crystals in the ac-plane. However, the large discrepancy between eq. (3.6) and the observed value in the bc-plane at $T = 40$ K cannot be explained only by that. In other words, the angular dependence of the g-value cannot be explained by conventional g-tensor, the anomalous angular dependence of g-value remaining unclear.

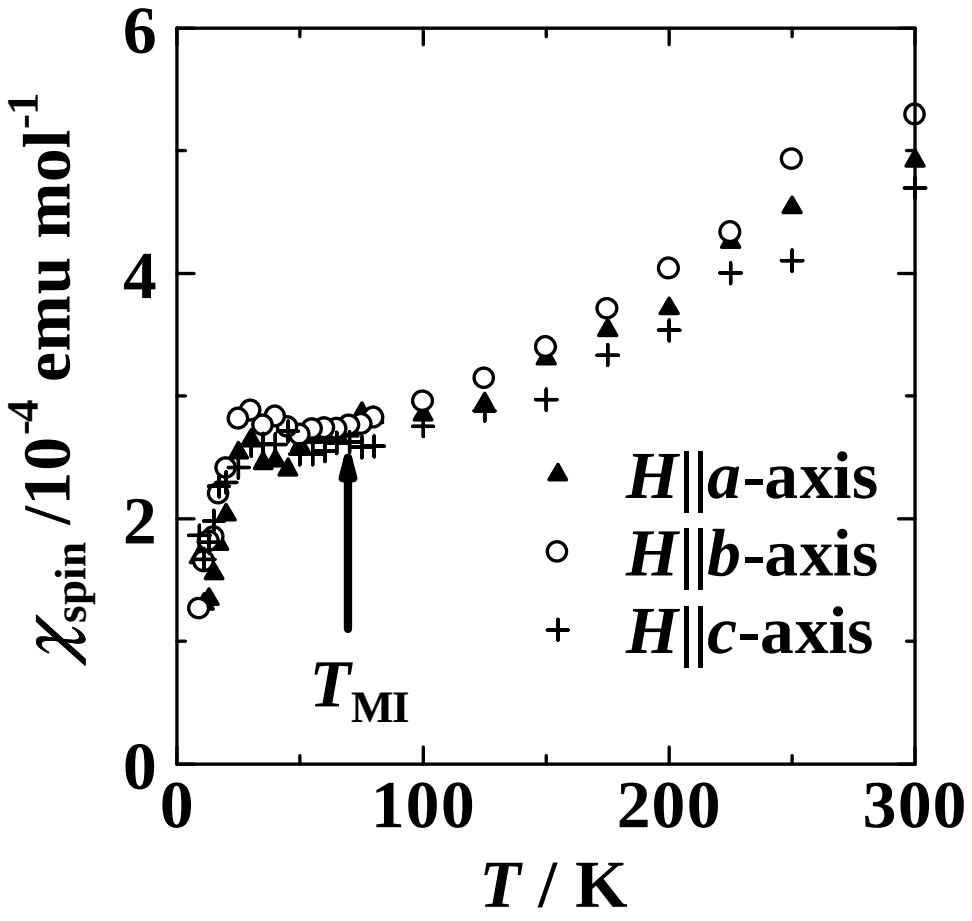

Fig. 3.19. The EPR spin susceptibility $\chi_{\rm spin}$ along the three crystallographic axes for (EDT-TTFBr_2)$_2$GaBr_4. The absolute values are obtained by comparing the EPR intensity and the static susceptibility from the SQUID measurement at room temperature. $T_{\rm MI}$ indicates the metal-insulator transition temperature.

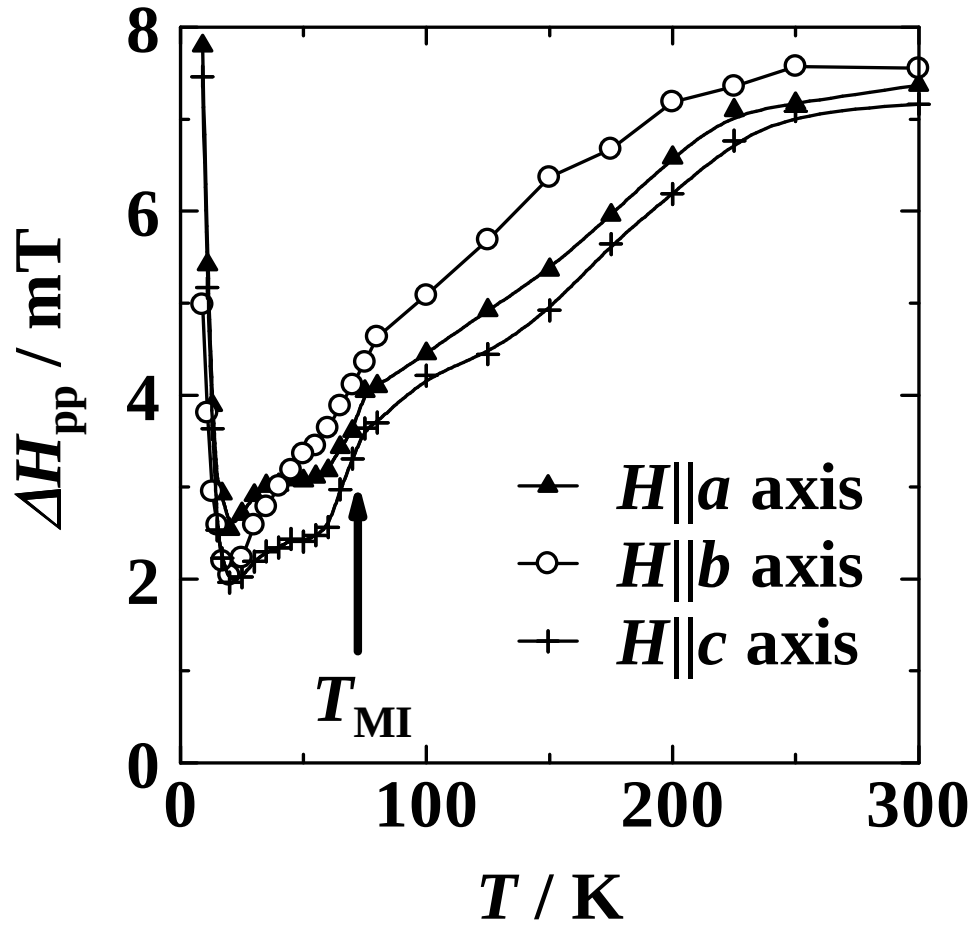

Fig. 3.20. EPR line width along the three crystallographic axes for (EDT-$TTFBr_2)_2GaBr_4$. T_{MI} denotes the metal-insulator transition temperature.

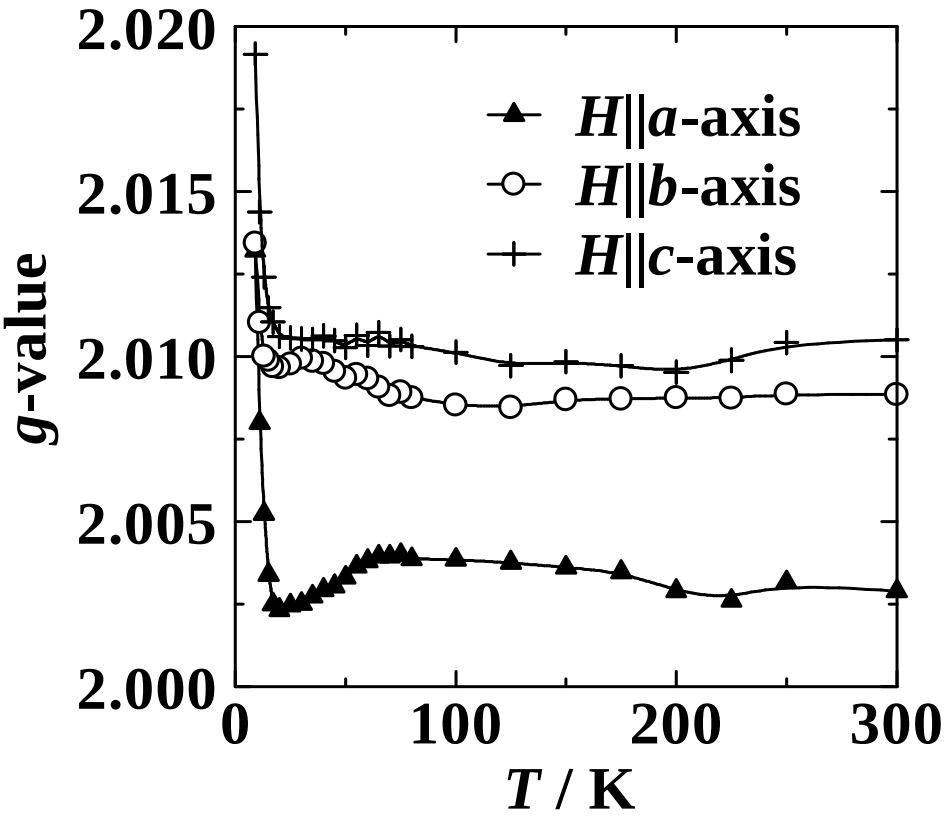

Fig. 3.21. Temperature dependence of the g values along the three crystallographic axes for $(\text{EDT-TTFBr}_2)_2\text{GaBr}_4$.

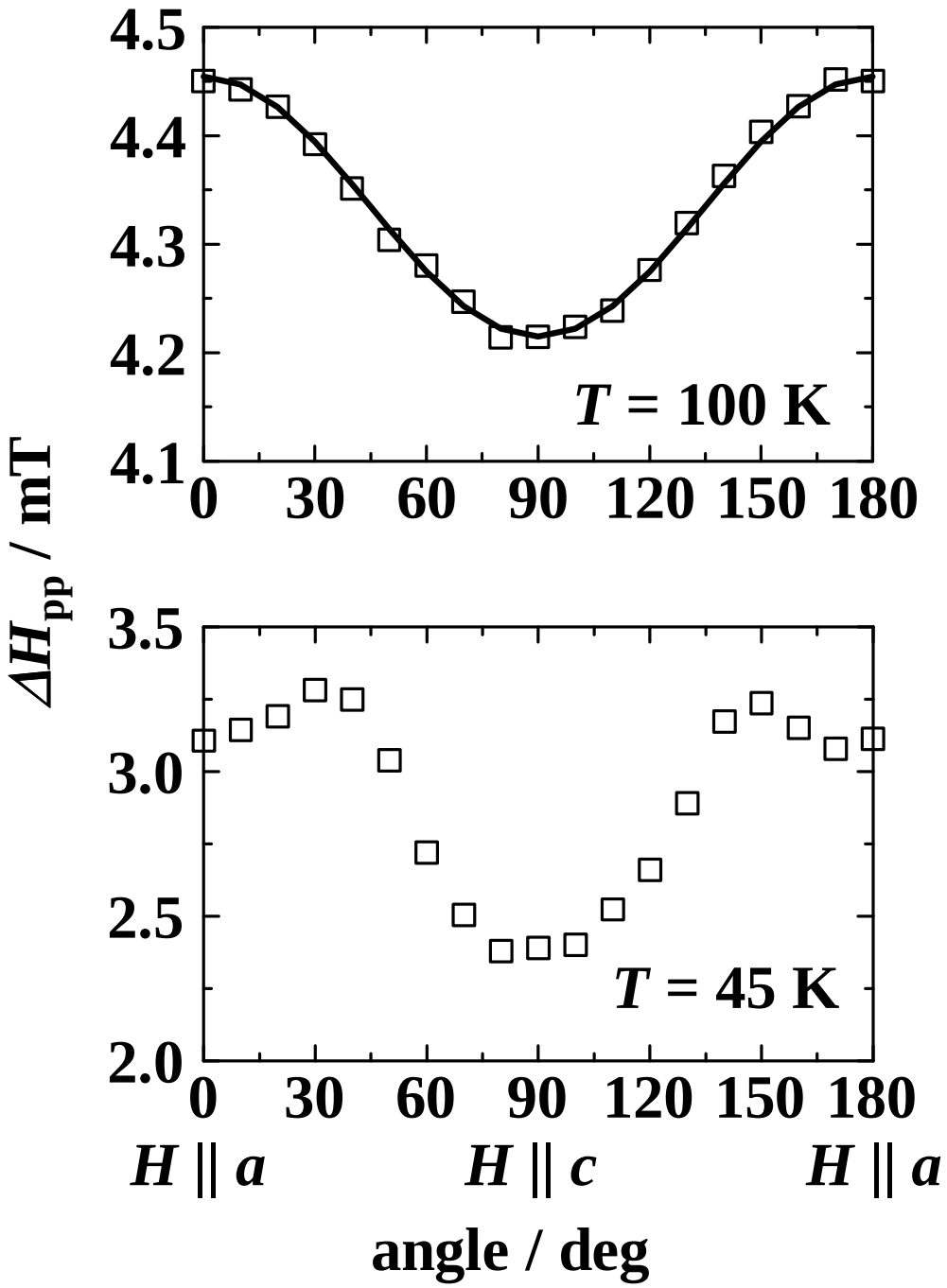

Fig. 3.22. Angular dependence of the EPR line width in the *ac*-plane for (EDT-TTFBr$_2$)$_2$GaBr$_4$ at 100 K and 45 K, which are above and below $T_{\rm MI}$, respectively. Solid line is the fitting curve of eq. (3.5) with $\Delta H_{\rm pp}(a) = 4.454$ and $\Delta H_{\rm pp}(c) = 4.210$ mT, respectively.

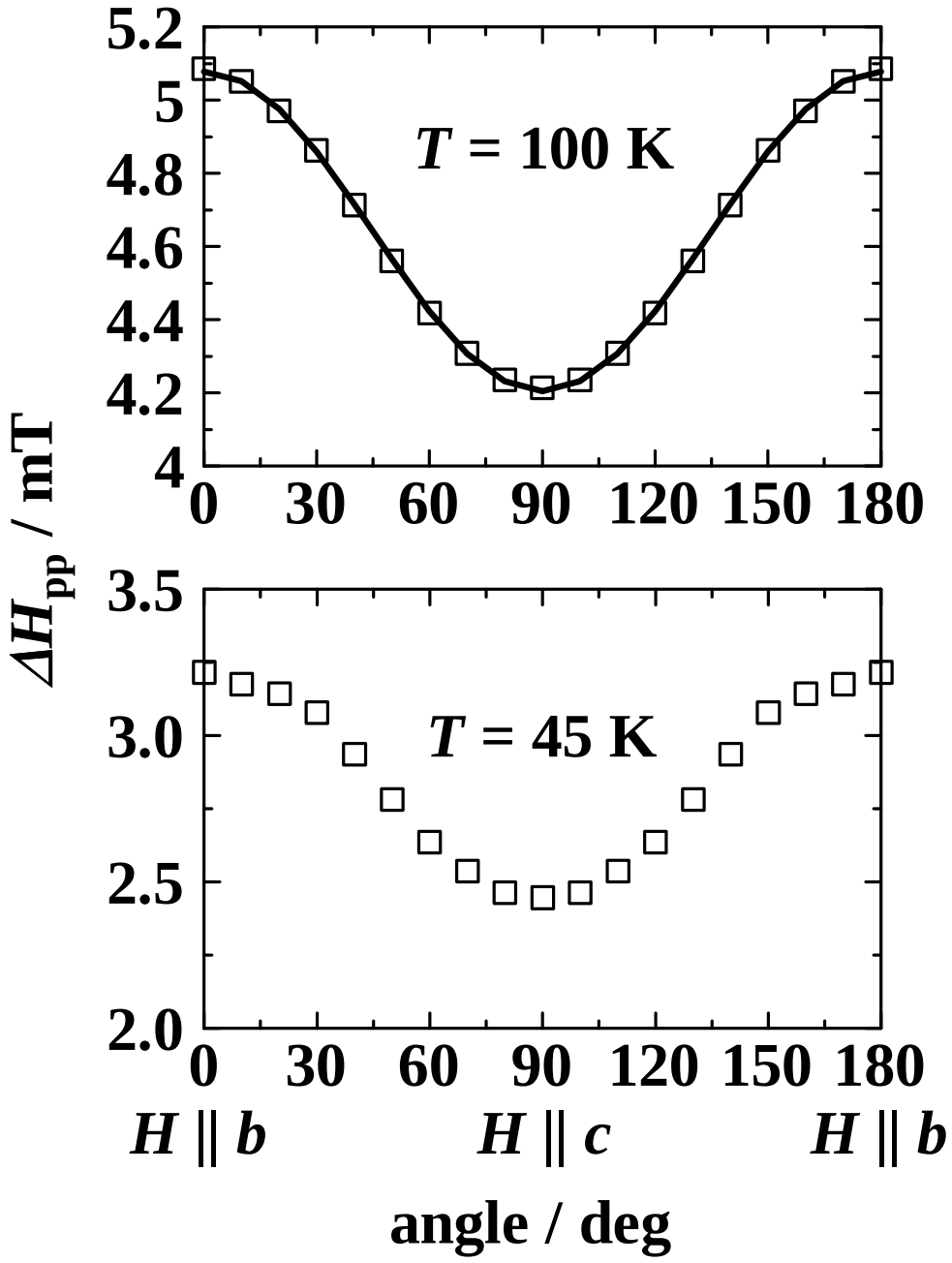

Fig. 3.23. Angular dependence of EPR line width in the *bc*-plane for (EDT-TTFBr$_2$)$_2$GaBr$_4$ at 100 K and 45 K, which are above and below $T_{\rm MI}$, respectively. Solid line is the fitting curve of eq. (3.5) with $\Delta H_{\rm pp}(b) = 5.078$ and $\Delta H_{\rm pp}(c) = 4.210$ mT, respectively.

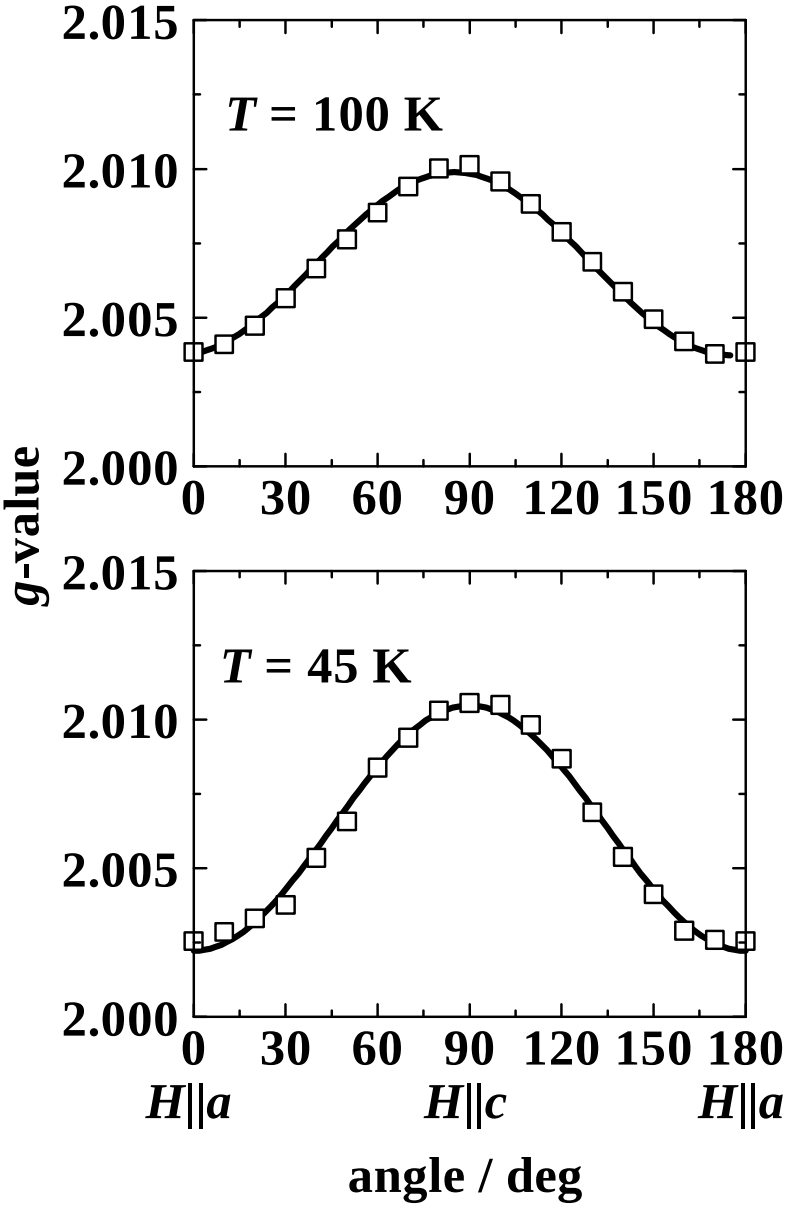

Fig. 3.24. Angular dependencies of g-value with $H \parallel ac$-plane of (EDT-TTFBr$_2$)$_2$GaBr$_4$ at 100 K and 45 K, which are above and below T_{MI}. The solid lines are calculated curves by using the relation $g = g_1 \sin^2\theta + g_2 \cos^2\theta$; $g_1 = 2.010$ and $g_2 = 2.004$ for 100 K, $g_1 = 2.011$ and $g_2 = 2.002$ for 45 K.

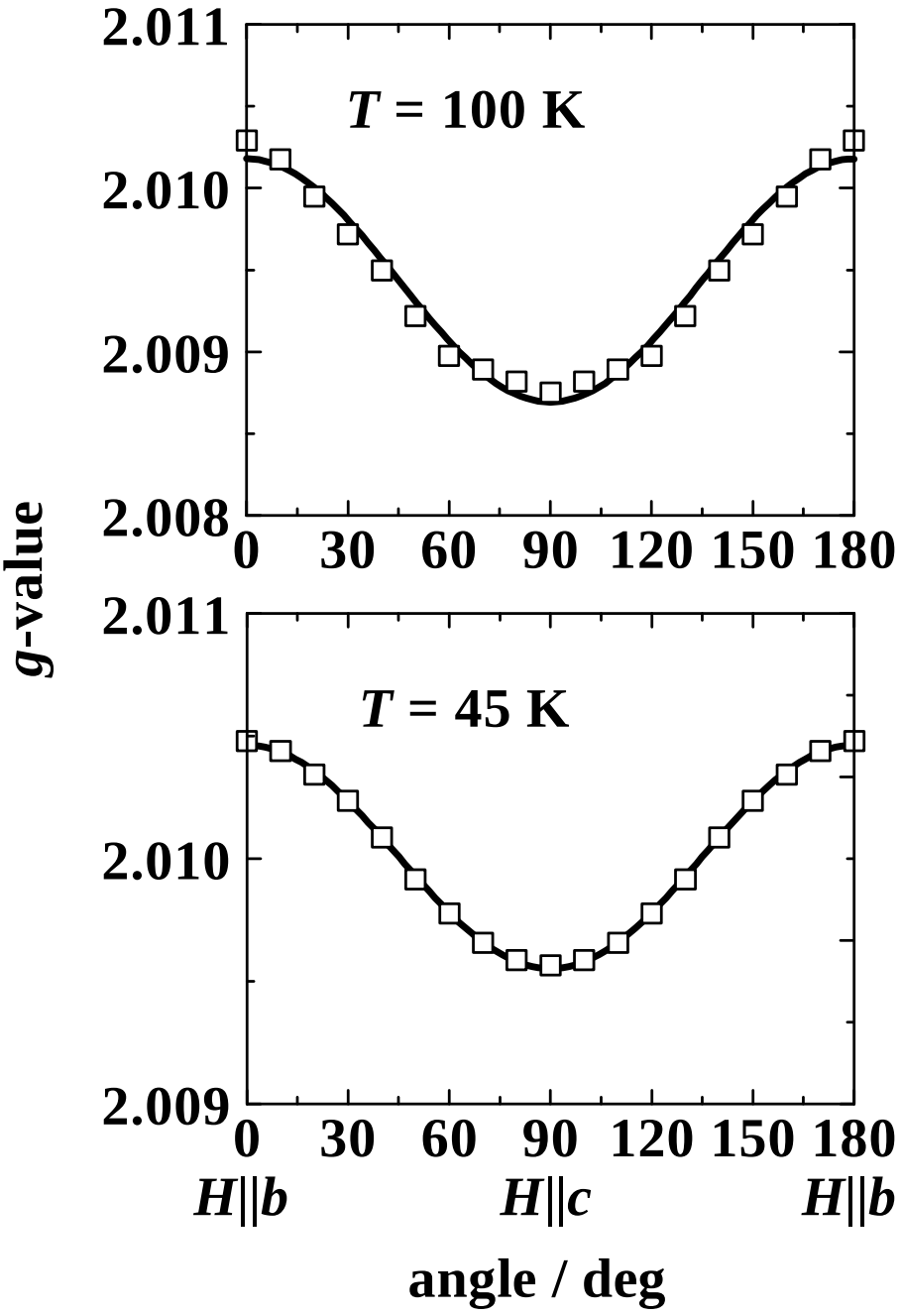

Fig. 3.25. Angular dependencies of g-value with $H \parallel bc$-plane of (EDT-TTFBr$_2$)$_2$GaBr$_4$ at 100 K and 45 K, which are above and below $T_{\rm MI}$. The solid lines are calculated curves by using the relation $g = g_1 \sin^2\theta + g_2 \cos^2\theta$; $g_1 = 2.0102$ and $g_2 = 2.0087$ for 100 K, $g_1 = 2.0105$ and $g_2 = 2.0096$ for 45 K.

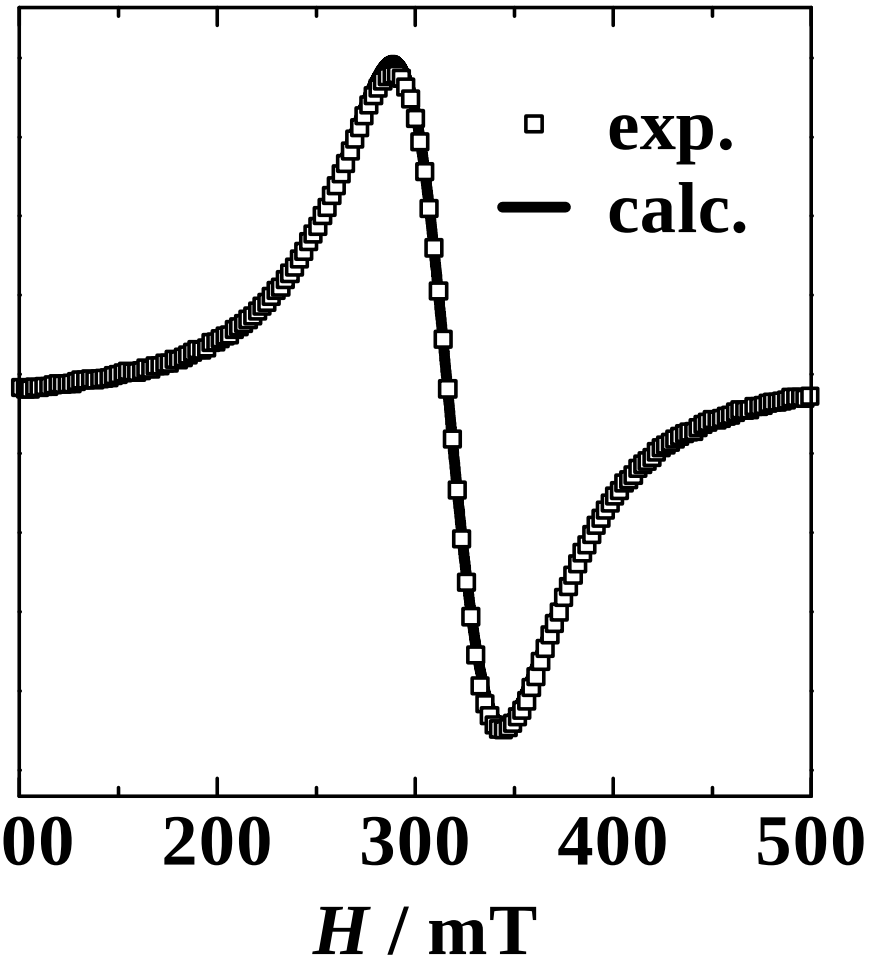

Fig. 3.26. EPR spectrum with external magnetic field $H \parallel c$-axis of (EDT-TTFBr$_2$)$_2$FeBr$_4$. The measured data (rectangles) are well fitted with a single Lorentzian function with $g = 2.048$ and $\Delta H_{\rm pp} = 55.72$ mT (solid line).

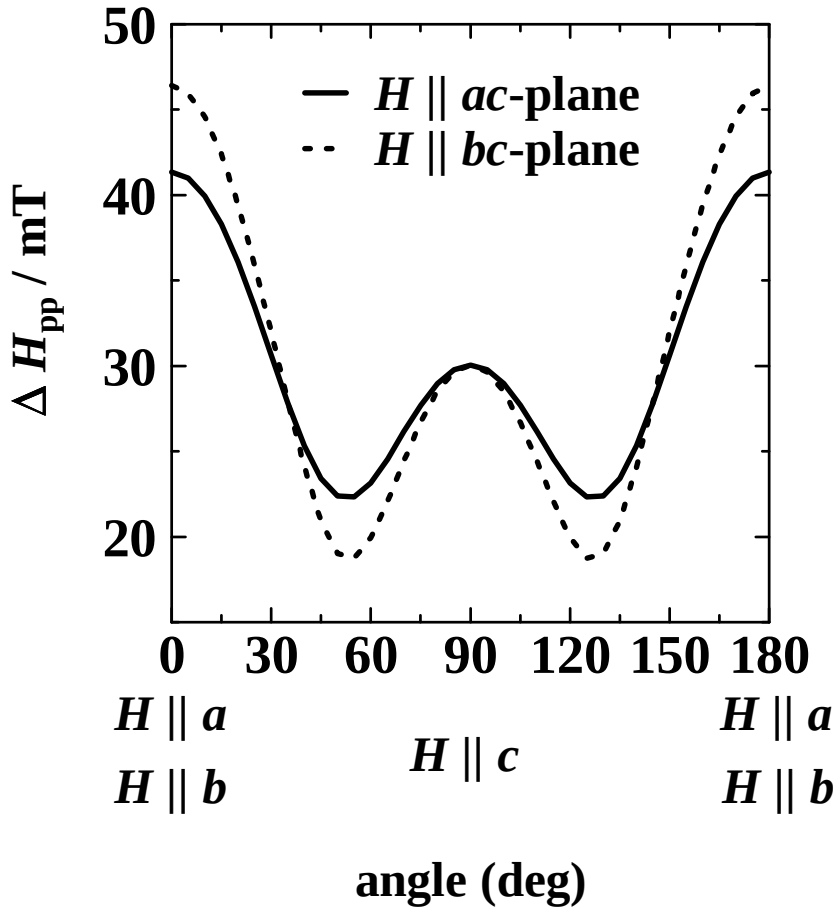

Fig. 3.27. Angular dependence of EPR line width of $(EDT\text{-}TTFBr_2)_2FeBr_4$ calculated based on the dipole-dipole interaction.

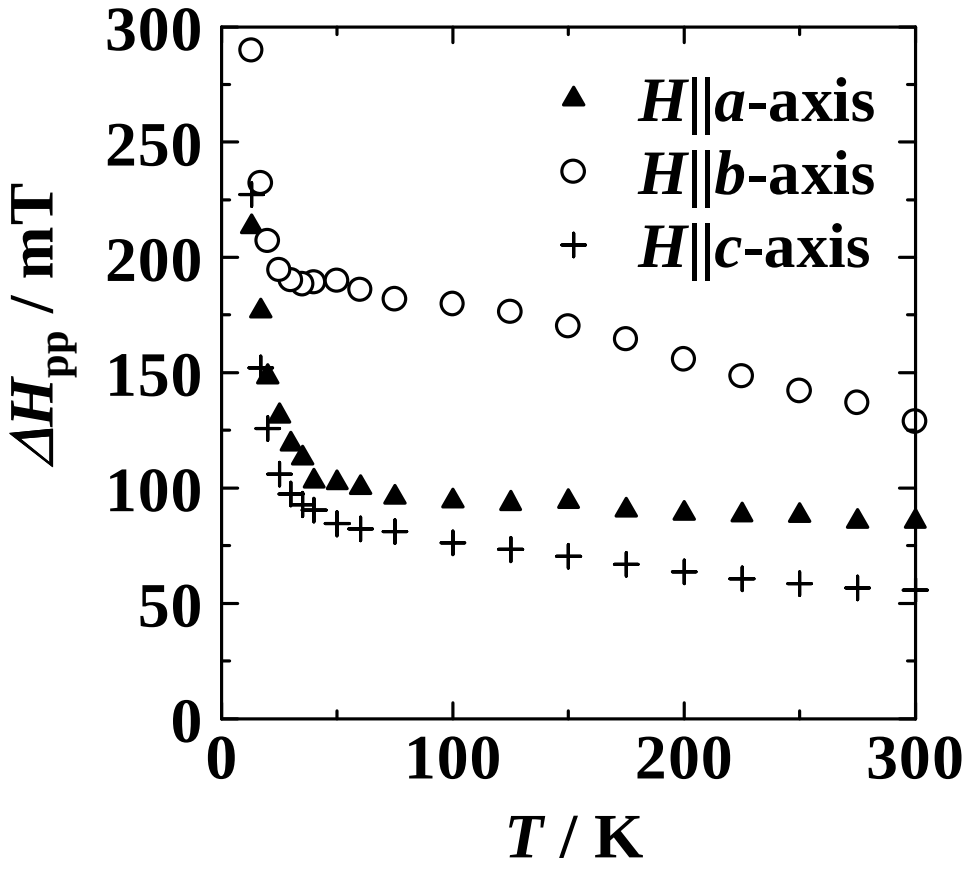

Fig. 3.28. Temperature dependence of the EPR line width $\Delta H_{\rm pp}$ of (EDT-TTFBr$_2$)$_2$FeBr$_4$ along the three crystallographic axes.

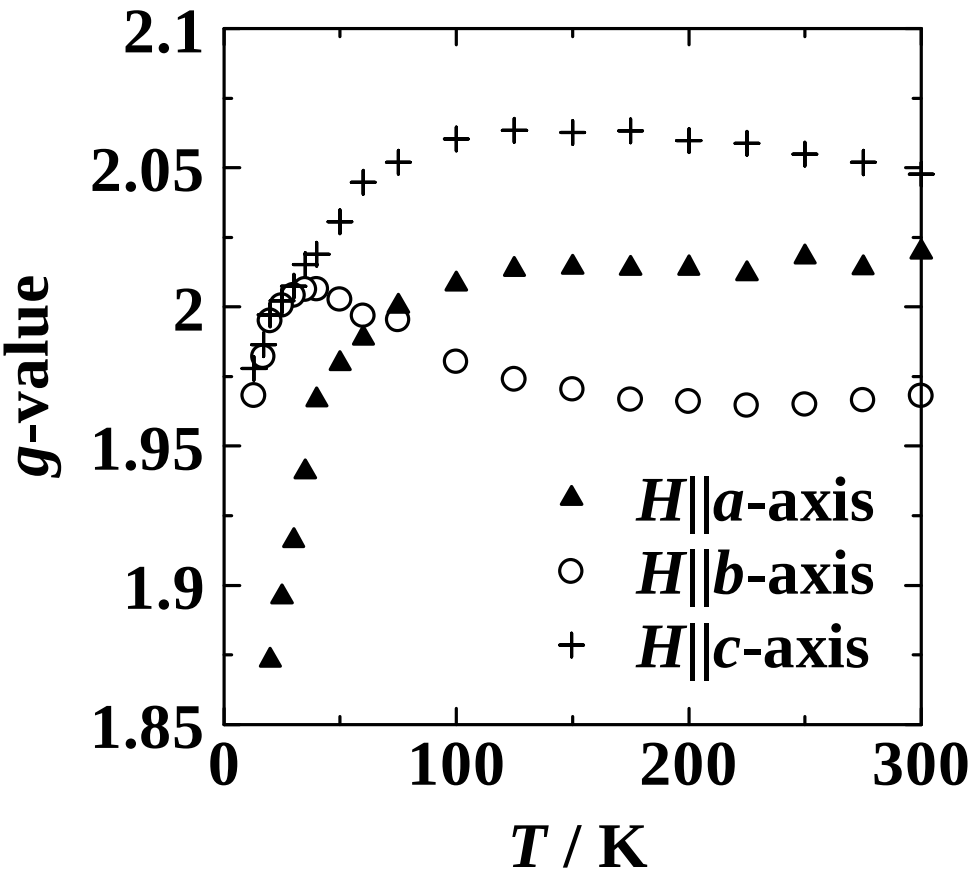

Fig. 3.29. Temperature dependence of the g-value of $(EDT\text{-}TTFBr_2)_2FeBr_4$ along the three crystallographic axes.

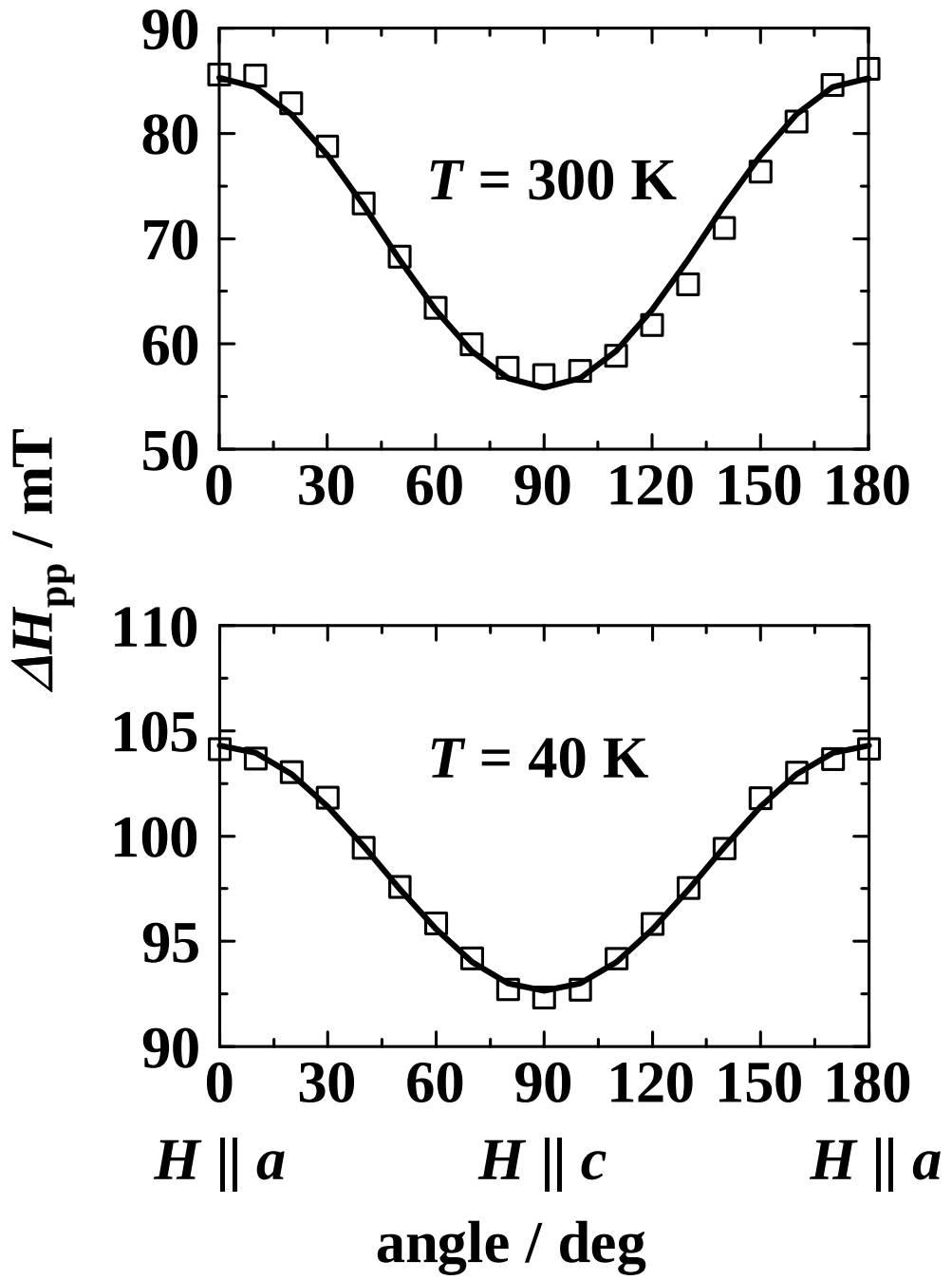

Fig. 3.30. Angular dependencies of the EPR line width $\Delta H_{\rm pp}$ of (EDT-TTFBr$_2$)$_2$FeBr$_4$ at 300 and 40 K with $H \parallel ac$-plane. Solid lines represent the calculated values based on eq. (3.5) with $\Delta H_{\rm pp}(a) = 85.3$ and 104.3 and $\Delta H_{\rm pp}(c) = 55.9$ and 82.7 mT for $T = 300$ and 40 K, respectively.

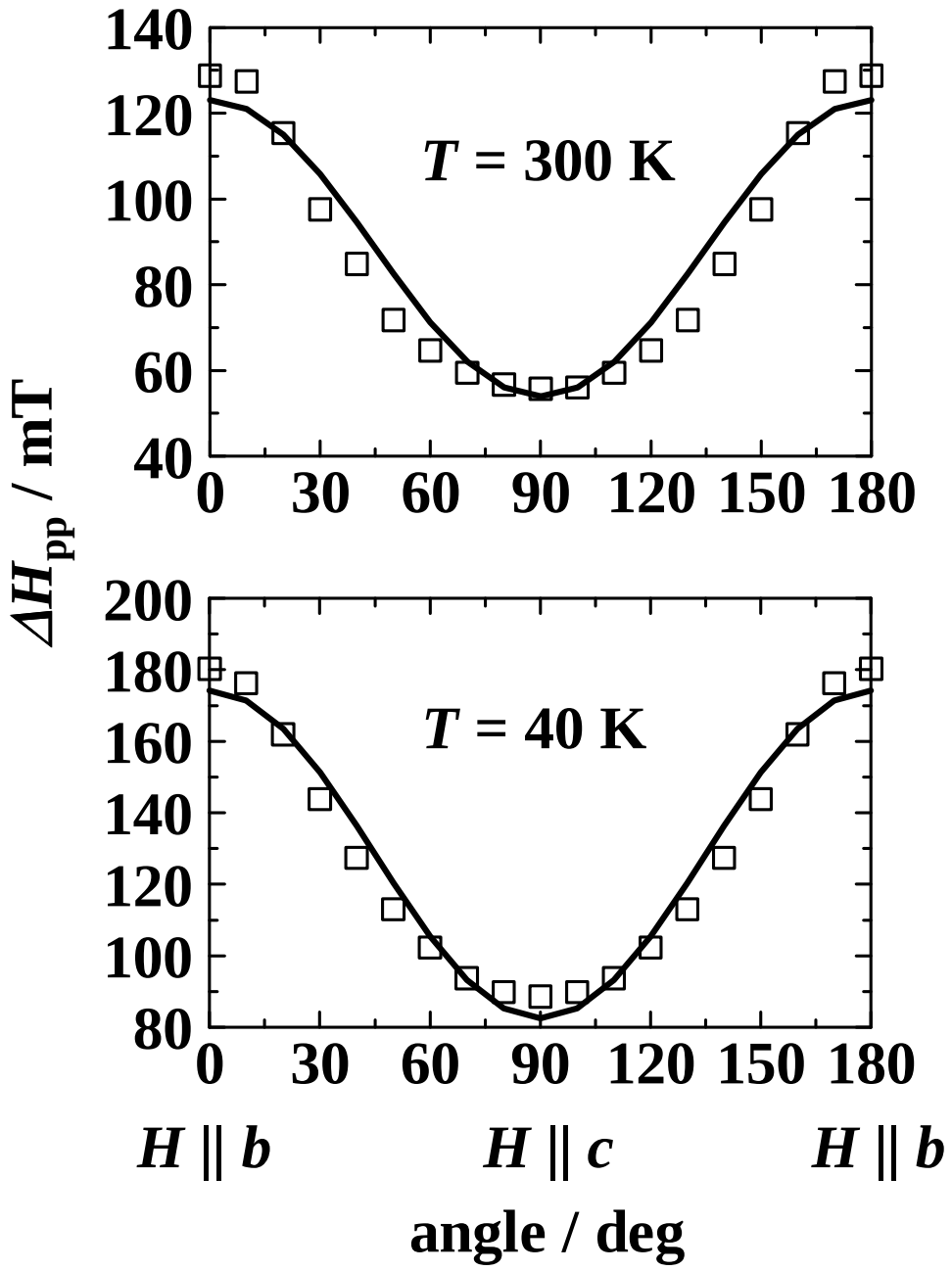

Fig. 3.31. Angular dependencies of EPR line width $\Delta H_{\rm pp}$ of (EDT-TTFBr$_2$)$_2$FeBr$_4$ at 300 and 40 K with $H \parallel bc$-plane. Solid lines represent the calculated values based on eq. (3.5) with $\Delta H_{\rm pp}(b) = 123.1$ and 174.2 and $\Delta H_{\rm pp}(c) = 55.9$ and 82.7 mT for $T = 300$ and 40 K, respectively)

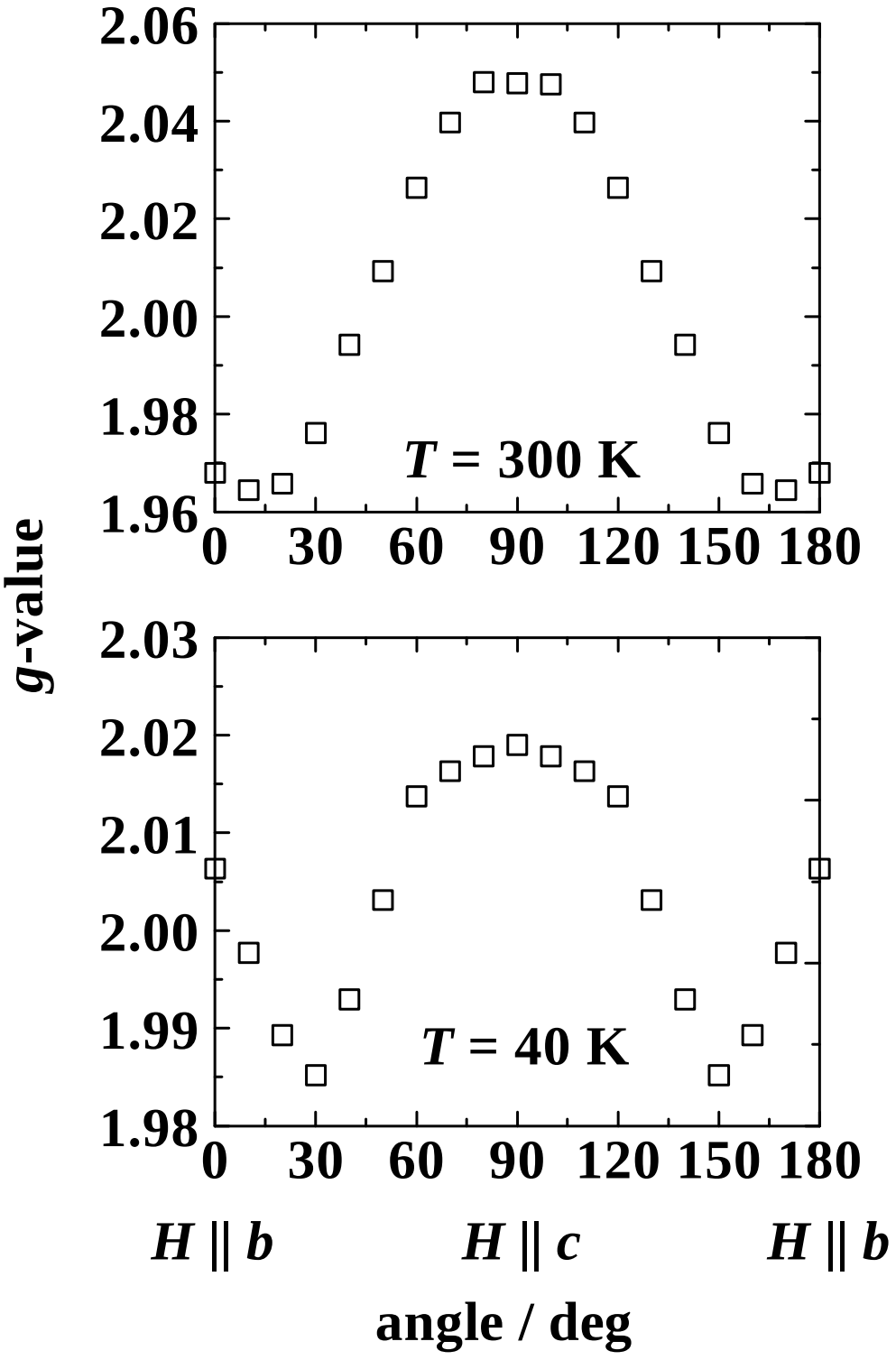

Fig. 3.32. Angular dependence of the g-value with $H \parallel bc$-plane of (EDT-TTFBr$_2$)$_2$FeBr$_4$ at 300 and 40 K.

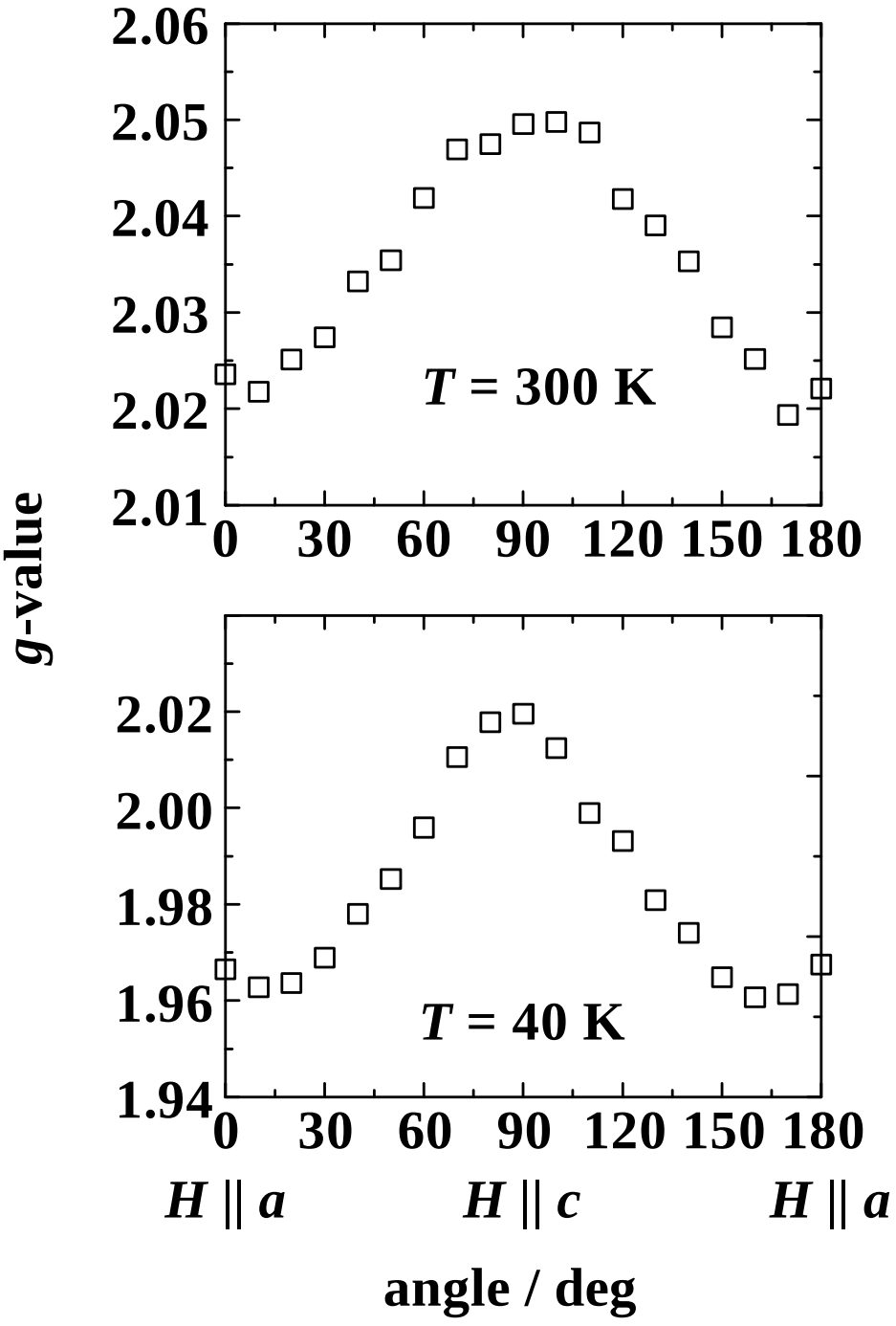

Fig. 3.33. Angular dependencies of the g-value with $H \parallel ac$-plane of (EDT-TTFBr$_2$)$_2$FeBr$_4$ at 300 and 40 K.

3.7 Discussion

In this section, I will discuss the ground state of the π-electron system of (EDT-TTFBr$_2$)$_2$MBr$_4$ (M = Fe, Ga) in the insulating phase, which is the base of the discussion on the magnetism and magnetoresistance. At first, the ground state of the $GaBr_4^-$ salt is discussed on the basis of the EPR results. The ground state of the $FeBr_4^-$ salt is considered to be similar to that of the $GaBr_4^-$ salt because they are isostructural and have resemblance between their resistivity behaviors in the low temperature region below $T_{\rm MI}$. In the next step, the spin polarization and charge disproportionation are calculated by using the tight-binding calculation including on-site Coulomb interaction U. Once the spin structure of the π-electron system is calculated, the spin structure of the localized d-electron, which interacts only with π-electrons, can be determined. In the final step, the negative magnetoresistance observed in (EDT-TTFBr$_2$)$_2$FeBr$_4$ at low temperatures is reproduced qualitatively by using the tight-binding calculation introducing π-d interaction $J_{\pi d}$ in addition to U.

3.7.1 The ground state of (EDT-TTFBr$_2$)$_2$MBr$_4$

For clarifying the ground state, the features of the EPR signal are indispensable. The experimental finding that an EPR signal survives even below $T_{\rm MI}$ followed by the divergent behavior of the line width at ca. 9 K indicates that the $GaBr_4^-$ salt is paramagnetic ($9 < T < 70$ K) and antiferromagnetic ($T < 9K$) in the two low temperature insulating states, where the π-electrons behave as localized magnetic electrons. The existence of the localized π-electrons having a magnetic moment is also suggested from the change of the angular dependence of $\Delta H_{\rm pp}$ at $T_{\rm MI}$.

In the case of metals, the angular dependence of $\Delta H_{\rm pp}$ is owing to the spin-lattice relaxation time T_1, while the spin-spin relaxation time T_2 does not play an important role due to the motion narrowing process in itinerant electrons. Therefore, $\Delta H_{\rm pp}$ is governed by the spin-lattice relaxation time $1/T_1$ and described as

$$\Delta H_{\rm pp} = \Delta H_1 \cos^2\theta + \Delta H_2 \sin^2\theta, \tag{3.7}$$

where ΔH_1 and ΔH_2 are the EPR line widths along the spin principle axes 1 and 2, between which the applied field is directed with declining angle θ with respect to

principle axis 2. Indeed, the angular dependence of $\Delta H_{\rm pp}$ of the $GaBr_4^-$ salt above $T_{\rm MI}$ is well fitted to eq. (3.7), as shown in Figs. 3.22a and 3.23a. The temperature dependence of the $\Delta H_{\rm pp}$ above $T_{\rm MI}$ can also be explained in terms of the Elliot mechanism [33], where the EPR line width is described as

$$\Delta H_{\rm pp} \propto \Delta g^2 \rho, \tag{3.8}$$

where Δg and ρ are the g-value deviation from free electron spin and the resistivity, respectively, the latter of which decreases as the temperature is lowered in metallic state.

In contrast, in the insulating state where the electrons are localized, $\Delta H_{\rm pp}$ is affected not only by T_1 but also by T_2, where the latter is described [34] as

$$\Delta H_{\rm dip} \equiv \frac{1}{T_2} = \frac{7.05 g \mu_{\rm B}}{2} \sqrt{\frac{1}{3} S(S+1)} \sqrt{\sum_j \frac{(3\cos^2\theta_{ij} - 1)^2}{\boldsymbol{r}_{ij}^6}}, \tag{3.9}$$

where $\boldsymbol{r}_{ij}$ and θ_{ij} are the vector between two anions and the angle between the external magnetic field and $\boldsymbol{r}_{ij}$, S is the spin of the magnetic species, and the summation is taken over all magnetic electrons.

Therefore, the π-electron spins in the $GaBr_4^-$ salt below $T_{\rm MI}$ is subjected to the T_1 and T_2 processes;

$$\Delta H_{\rm pp} \propto \frac{1}{2T_1} + \frac{1}{T_2}, \tag{3.10}$$

where $1/T_1$ and $1/T_2$ are in proportion to eq. (3.7) and (3.9), respectively.

Based on the eq. (3.10), the EPR line widths in the ac-plane ($\Delta H_{\rm pp}^{\rm ac}$) and the bc-plane ($\Delta H_{\rm pp}^{\rm bc}$) are described as

$$\Delta H_{\rm pp}^{\rm ac} = a\Delta H_{\rm dip}^{\rm ac}(\theta) + (\Delta H_{\rm pp}(a)\cos^2\theta + \Delta H_{\rm pp}(c)\sin^2\theta) \tag{3.11}$$

$$\Delta H_{\rm pp}^{\rm bc} = a\Delta H_{\rm dip}^{\rm bc}(\theta) + (\Delta H_{\rm pp}(b)\cos^2\theta + \Delta H_{\rm pp}(c)\sin^2\theta), \tag{3.12}$$

where the parameters $\Delta H_{\rm pp}(a)$, $\Delta H_{\rm pp}(b)$ and $\Delta H_{\rm pp}(c)$ are related to line widths owing to the spin-lattice relaxation with $H \parallel a$, b and c-axes, respectively. $\Delta H_{\rm dip}^{\rm ac}(\theta)$ and $H_{\rm dip}^{\rm bc}(\theta)$ are the dipolar line widths in the ac and bc-planes, respectively, given by eq. (3.9). Fig. 3.34 presents the contribution of the dipolar line width in the calculated angular dependence of the line width in the ac- and the bc-planes, where it is assumed that there is a spin $S = 1/2$ for all the donor molecule. Of

course, the value $S = 1/2$ for all the donor molecules is incorrect because of the donor-anion ratio 2:1, where the maximum value of the average spin $\langle S \rangle$ is 1/4. In addition, the average spin $\langle S \rangle$ of a donor molecule can become a smaller than 1/4 if the insulating phase is a charge ordering state, where a paramagnetic electron "localized" in several donor molecules; for example, if a paramagnetic electron localized in four donor molecules, $\langle S_\pi \rangle$ is 1/8 for a donor molecule. Moreover, the exchange narrowing reduces the dipolar line width when spins are coupled by exchange interaction. The correction for the effect of the exchange narrowing and the difference between the spin $S_\pi = 1/2$ per donor molecule and the actual value of the spin are included in fitting parameter a. By using the eqs. (3.11) and (3.12), the angular dependence of the $GaBr_4^-$ salt at 45 K is well fitted as shown in Fig. 3.35, where $a = 0.01273$, $\Delta H_a = 2.8005$, $\Delta H_b = 2.8405$ and $\Delta H_c = 2.0705$ are obtained.

There are two typical candidates for magnetic insulating state, Mott insulator and charge ordering state. When Mott insulator is the case, the dimerization of donor molecules is necessary because it requires one electron per site, taking into account that there is one electron per two donors in the $GaBr_4^-$ salt. When Mott insulator is the case, the dimerization of donor molecules is necessary because Mott insulating state requires one electron per site, taking into account 3/4-filled band of the salts. On the other hand, the donor molecules form crystallographically uniform chains and no dimerization is observed at room temperature, which indicates that the dimerization of donor molecules at low temperature is, if it exists, not so strong. Consequently, charge ordering seems to be the more convincing candidate for the insulating state of π-electrons of the $GaBr_4^-$ salt.

Next, we move on to the $FeBr_4^-$ salt. Though the electronic states below $T_{\rm MI}$ are roughly same in both salts as evidenced by the similar temperature dependences of the resistivities as shown in Fig. 3.36, the large difference between the $FeBr_4^-$ salt and the $GaBr_4^-$ salt is the MI transition temperature; that is, the $FeBr_4^-$ salt undergoes an MI transition at 20 K, while the $GaBr_4^-$ salt undergoes 70 K. These two salts have same crystal structures thanks to the quite similar ionic radii of Fe^{3+} and Ga^{3+}, therefore the difference of $T_{\rm MI}$ is originate from the different electronic structures. Generally speaking, an electronic structure is ruled by the on-site Coulomb

interaction U, inter-site Coulomb interaction V, transfer integral t and electron-phonon coupling. Among the parameters, U, V and electron-phonon coupling are same due to the same crystal structures (V and electron phonon coupling) and using the same donor molecule (U). In addition, the transfer integrals t between donor molecules are same in the both salts because of the same crystal structures. In contrary to these same parameters, the transfer integral $t_{\pi d} = 9.3 \times 10^{-4}$ (see, section 3.1) between donors and anions in the $FeBr_4^-$ salt affects differently from that in the $GaBr_4^-$ salt as followings. The most important feature of the $FeBr_4^-$ anion is the open shell structure of the iron (III) atom, $(e_g)^2(t_{2g})^3$, while the $GaBr_4^-$ anion has the closed shell structure, $(e_g)^4(t_{2g})^6$; that is, an electron can be transfered from a donor column to another donor column throu open shell of the $FeBr_4^-$ anion by $t_{\pi d}$. A $FeBr_4^-$ anion has two short donor-anion S5-Br1 contacts r_d (see, section 3.1) which bridges adjacent donor layers by $t_{\pi d}$ as shown in Fig. 3.1c. The inter-layer transfer integral $t_{\pi d}$ between the donor and the anion is significantly larger than that between the donor molecules (~ 0), resulting in making the electronic structure of the π-electrons three dimensionally as similar to DCNQI-type salts [38] (see, Chapter 1). The MI transition is caused by the low dimensional instability, therefore the little 3D character stabilize the metallic state down to 20 K.

Though the little 3D character of the $FeBr_4^-$ salt, the insulating state of the $FeBr_4^-$ is same as that of the $GaBr_4^-$ salt thanks to the smallness of $t_{\pi d}$ which is only 1/30 and 1/6 of intra- and inter-chain transfer integrals, respectively. Consequently, it is concluded that the ground state of $FeBr_4^-$ is also antiferromagnetically ordered charge ordered state.

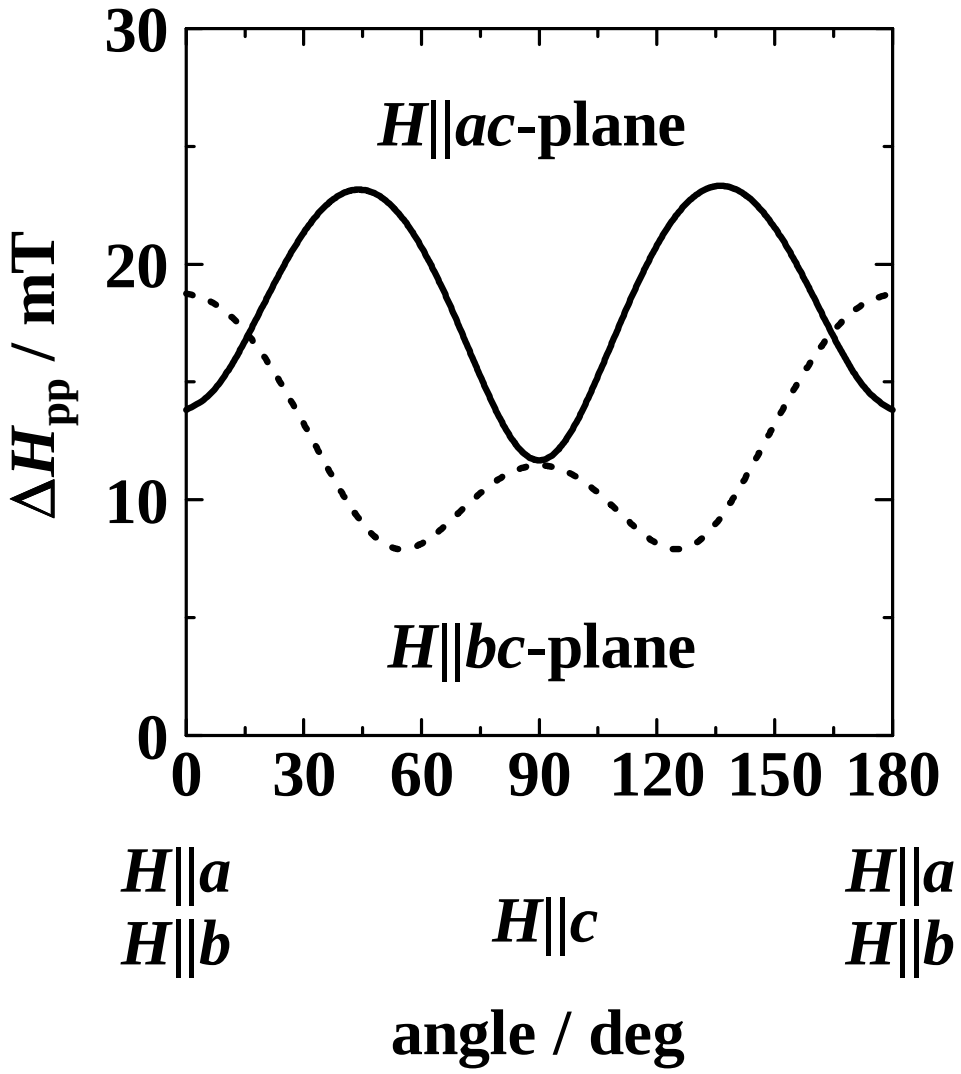

Fig. 3.34. Angular dependence of the line width $\Delta H_{\rm pp}$ with $H \parallel ac$ (solid line) and bc-planes (dotted line) of (EDT-TTFBr_2)$_2$GaBr_4 based on the dipole-dipole interaction.

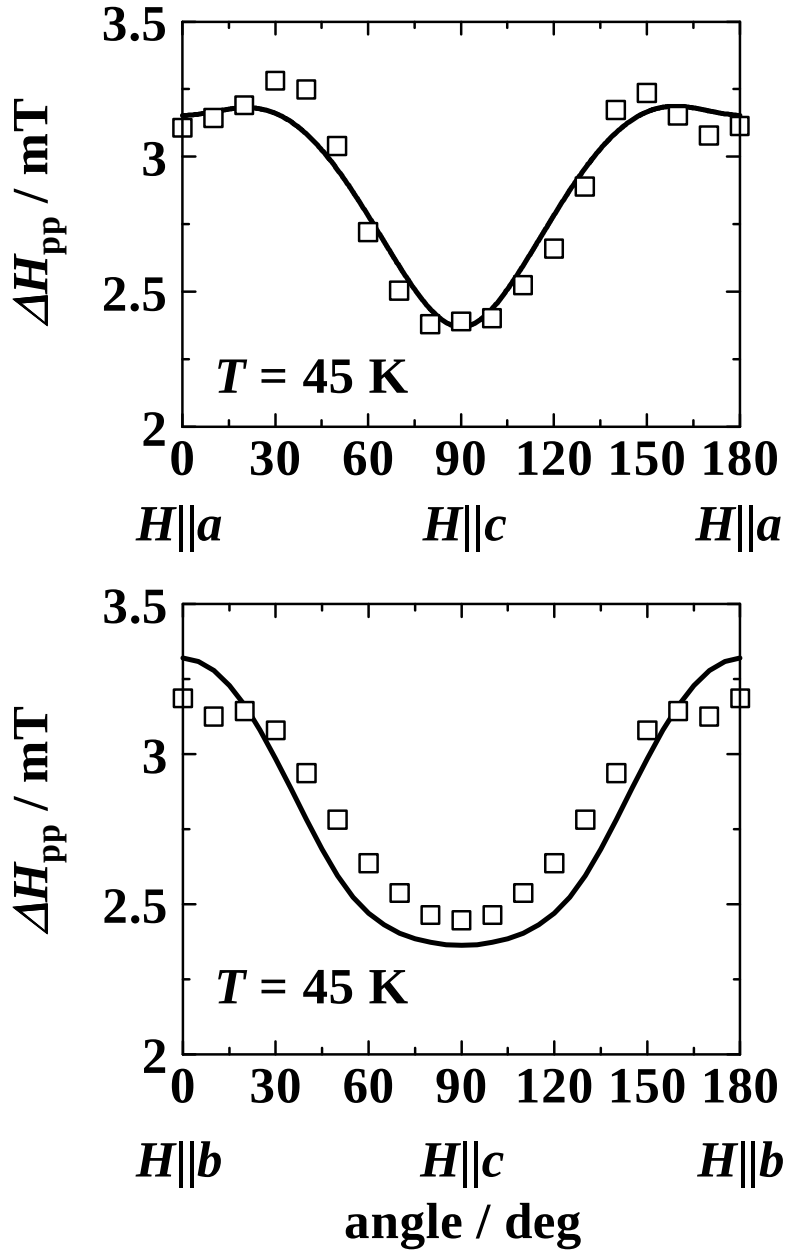

Fig. 3.35. The observed and calculated angular dependence of the line width with $H \parallel ac$ (top) and bc-planes (bottom) of (EDT-TTFBr_2)$_2$GaBr_4. The solid lines represent the calculated fitting curves with eqs. (3.11) and (3.12).

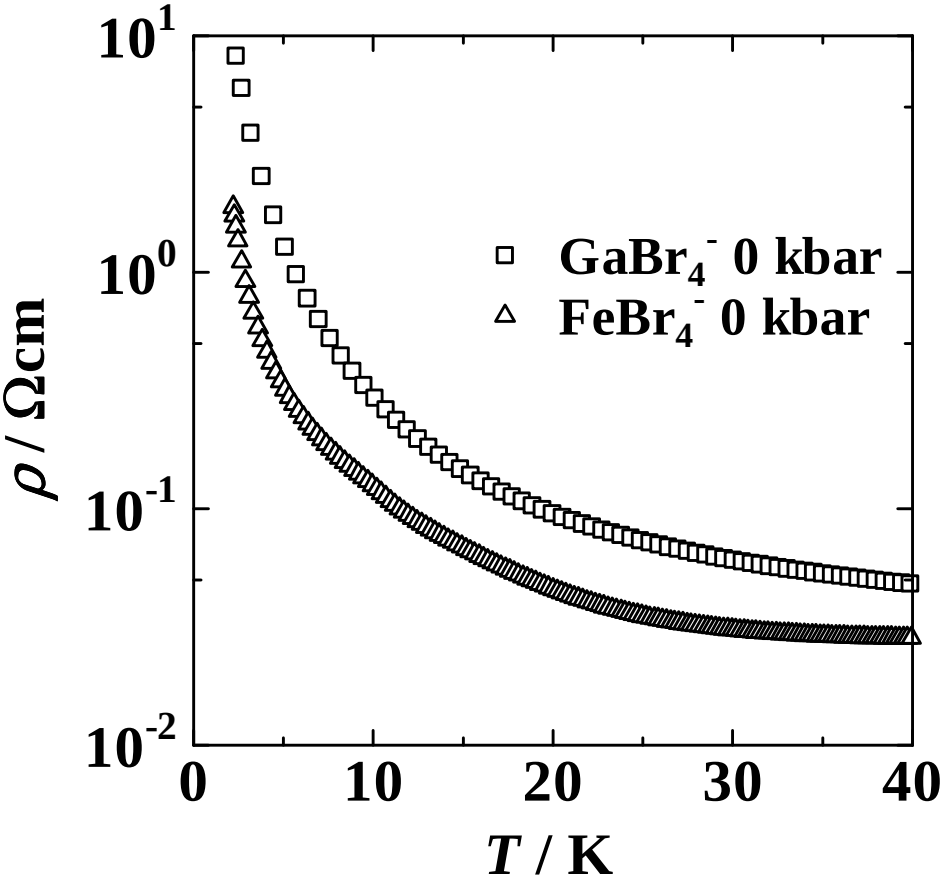

Fig. 3.36. Comparison of the temperature dependence of the resistivity for (EDT-TTFBr$_2$)$_2$MBr$_4$ (M= Fe and Ga) at ambient pressure.

3.7.2 Tight-binding calculation for donor π-electron system

Before to treat theoretically the magnetic structure and negative magnetoresistance of the π-d interaction system $FeBr_4^-$ salt, the magnetic structure of the pure π-electron system is analysed by using tight-binding method including on-site Coulomb repulsion U [39, 40] (see, section 2.3.1). The value of U is varied from 0.4 to 1 eV in the calculation, since the $GaBr_4^-$ salt is considered to have the value of U in this range [41]. In the calculation, only a single 2D donor plane sandwiched between two anion planes is taken into account for simplicity.

According to the Fermi surface as discussed in section 3.2, there is a nesting vector $Q = a^*/2$ indicating that the insulating state has a double-periodicity along the a-axis, where a periodic unit in a donor chain along the a-axis consists of four donor molecules as a natural consequence of the 3/4-filled electronic state. Therefore, the "unit" cell considered in the tight-binding calculation consists of the two crystallographic unit cells, and there are eight non-equivalent sites, which are crystallographically identical to each other, as shown in Fig. 3.37. The spin and charge densities of each site are determined by solving the mean field equation (2.8) and eqs. (2.10) and (2.11). In the calculation, the values $t_p = -297$, $t_{q1} = -13.9$, $t_{q2} = -14.3$, $t_{r1} = 67.1$ and $t_{r2} = 64.2$ meV calculated from the overlap integrals (see, section 3.2) are used. It is noted that the tight-binding calculation, especially that in the organic conductors, often gives a larger energy gap than that observed, therefore, the results is not convincing the quantitative level in general [39].

The band gap ΔE, the spin distribution $S_{\pi i}$ ($\equiv 1/2 \cdot (n_{i\uparrow} - n_{i\downarrow})$; $n_{i\sigma}$ is the charge density of spin σ at i-th donor site) and charge density n_i ($\equiv n_{i\uparrow} + n_{i\downarrow}$) were calculated for various values of U, and the results are shown in Figs. 3.38 and 3.39. As shown in Fig. 3.38, an insulating phase, which is defined with a finite positive value of gap, becomes a ground state in the region of $U > 0.6$ eV as 1st order transition, where the spin polarization and charge disproportionation are generated as shown in Fig. 3.39. In the insulating state, the periodicity of antiferromagnetically ordered π-electron spins is two times of that of a crystallographic unit cell along the a-axis as shown in Fig. 3.40. In the state, donor sites 1, 2, 6 and 7 have positive spin densities and 3, 4, 5, 8 have negative spin densities,

while 1, 3, 5 and 7 have much charge densities and 2, 4, 6 and 8 have less charge densities. The donor spins are characterized as antiferromagnetic arrangement in a chain and between chains. In the donor chain, the spins are aligned as -↑-↑-↓-↓- which is the natural conclusion of the 3/4-filled 1D electronic system, while the spins are antiparallelly coupled to the spins of the adjacent column by inter-column overlap integrals r_1 and r_2, which are larger than q_1 and q_2. The increment of the charge densities increases from 0.001 to 0.01 as U is elevated from 0.6 to 1 eV, but the change is small. These are less than 0.7 % of the mean value of the charge 1.5, which each donor takes in the 3/4 filled state. The absolute values of the spin densities increases from ca. 0.04 to ca. 0.13 as U is elevated from 0.6 to 1 eV. In the following discussion, the value U = 1.0 eV is employed to calculate the effect of the π-d interaction and external magnetic field, though the exact value of U is not so important. Actually, when the calculated results with different values of U are compared, the behavior of the calculated MRs are same in semi-quantitative level.

Then, the inter-site Coulomb repulsion V is introduced to the calculation. In the calculation, it is assumed that V works only between adjacent sites, for example, an electron at site 1 is affected by electrons at 2, 4, 5 and 8, with the same coefficient V for simplicity. Below $V_c = 0.25$ eV, the change of the charge and spin densities take roughly constant values as shown in Fig. 3.41. Above V_c, the charge ordering state is stabilized, where sites 1, 3, 5 and 7 have large spin densities and low charge densities changing from $S_\pi = -0.22$ to -0.35 and from $n_\pi = 1.42$ to 1.24 as V is raised from 0.25 to 0.5 eV, respectively, while the sites 2, 4, 6 and 8 have small spin densities and large charge densities changing from $S_\pi = -0.02$ to -0.01 and from $n_\pi = 1.58$ to 1.76 as V is raised from 0.25 to 0.5 eV, respectively. Though the actual value of the V is not known, the value $V = U/2 = 0.5$ is employed in the following discussion. Similarly to the value of U, the value of the V does not affect so seriously the behavior of the calculated MR in the qualitative level.

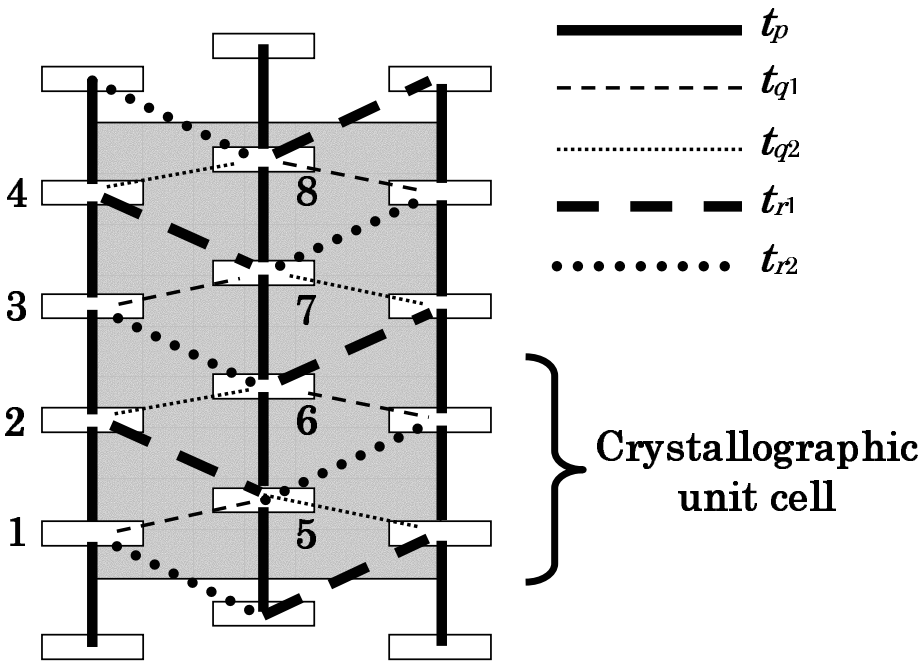

Fig. 3.37. Schematic structure of the donor π-electron system. Rectangles 1 to 8 and lines t_p, t_{q_1}, t_{q_2}, t_{r_1} and t_{r_2} represent eight non-equivalent donor molecules and transfer integrals, respectively; $t_p = -297$, $t_{q1} = -13.9$, $t_{q2} = -14.3$, $t_{r1} = 67.1$ and $t_{r2} = 64.2$ meV.

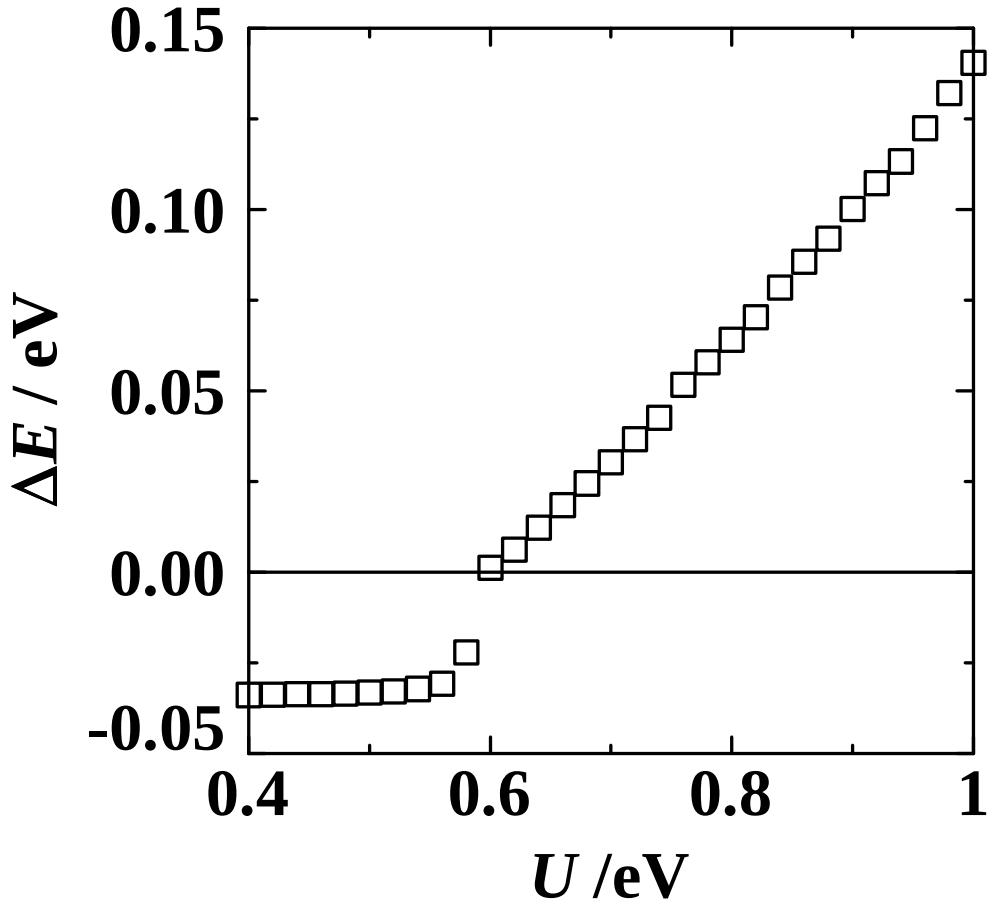

Fig. 3.38. The band gap ΔE calculated for various values of U.

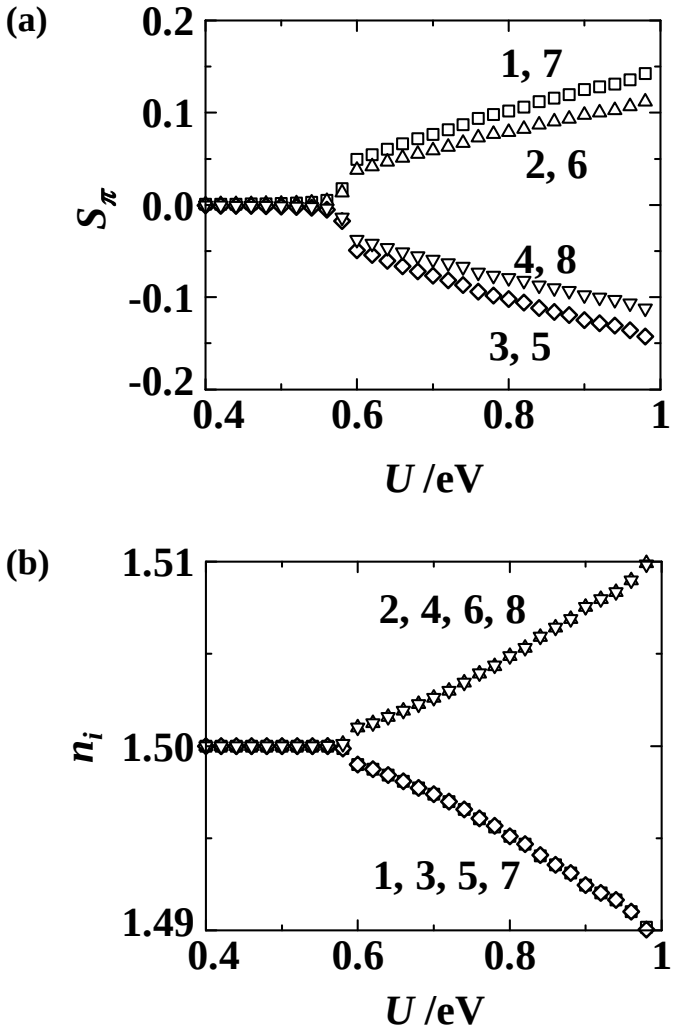

Fig. 3.39. **(a)** The spin density distribution calculated for various values of U. **(b)** The charge density calculated for various values of U. Numbers 1-8 denote non-equivalent donor sites.

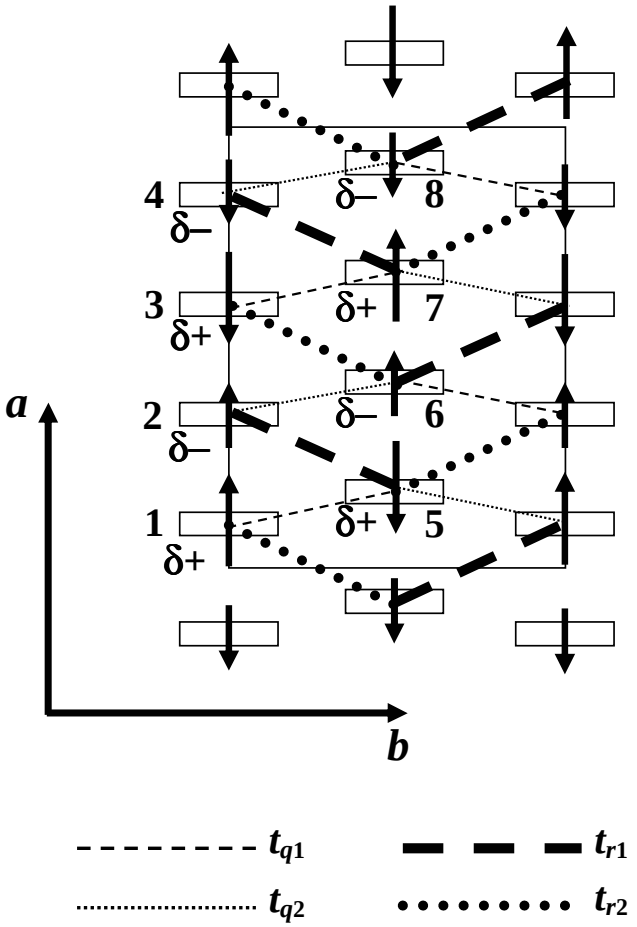

Fig. 3.40. Schematic of the calculated spin densities and electron densities. $\delta+$ and $\delta-$ represent electron poor and rich sites, respectively. Inter-chain transfer integrals t_{q1}, t_{q2}, t_{r1} and t_{r2} are defined in Fig. 3.37

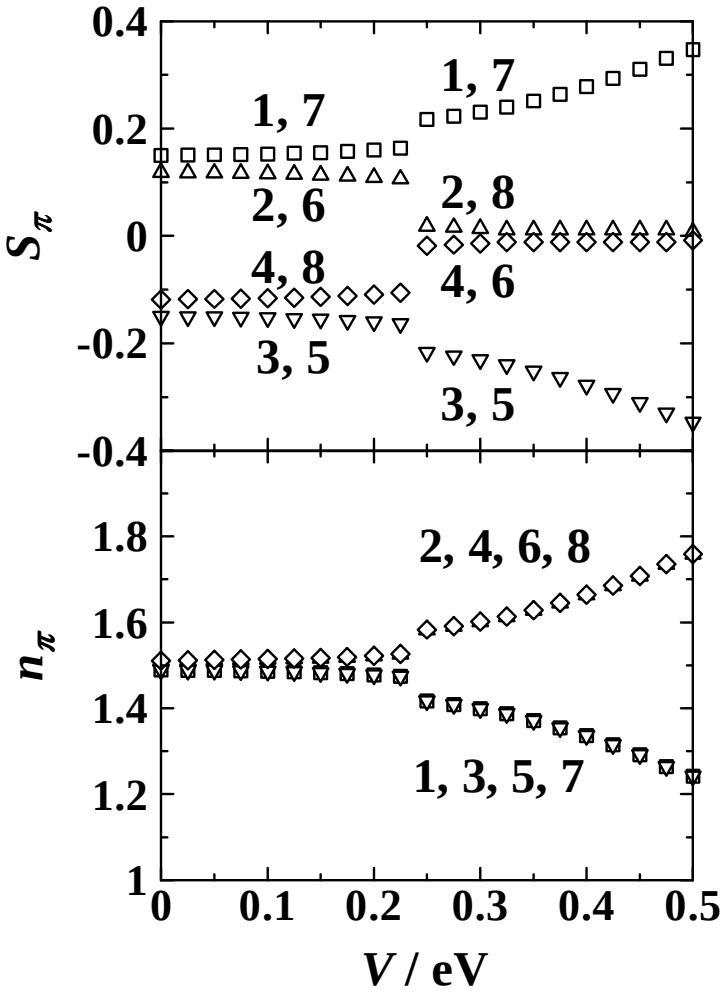

Fig. 3.41. **(a)** The spin density S_π and **(b)** the charge density n_π of the π-donor sites calculated for various values of V at $U = 1.0$ eV. Numbers 1-8 denote non-equivalent donor sites.

3.7.3 Magnetic structure of the $FeBr_4^-$ salt

Once the magnetic structure of the π-electrons is determined as discussed above, the magnetic structure of the $FeBr_4^-$ anions can be characterized. Before the theoretical analysis, it should be important to clarify the structural origin of the π-d interaction. As shown in the section 3.2, the overlap integral between a donor molecule and an anion molecule has a finite value only at the S-Br contacts $r_{\rm d}$. Consequently, each donor molecule in a donor plane has a π-d interaction path of Br-S contact with an adjacent $FeBr_4^-$ anion, while each anion has two interaction paths with two donor molecules belonging to different donor planes (see, Fig. 3.1c).

Based on these π-d interaction paths and the calculated AF spin structure of the donors, the magnetic structure of the $FeBr_4^-$ salt below $T_{\rm N}$ without external field is determined by assuming the following three rules: First, the AF interaction through rd causes an antiparallel arrangement between interacting donor spins and anion spins. This is a natural assumption for the exchange interaction. Second, the d-d direct interaction is negligible thanks to the long anion-anion distances. Third, the spins of the donors and the anions are oriented in the same direction due to the stronger π-d interaction than the anisotropy, where the easy axis is parallel to the b-axis from the experimental results. Judging from the weakness of the anion-anion direct interaction, the π-d interaction is responsible for the high saturation field of the $FeBr_4^-$ salt ($\sim$ 27 T), which is much larger than the spin flop field $H_{\rm SF} \sim 5.8$ T. This fact justifies the collinear spin structure owing to the π-d interaction even if the anisotropies of the π-electrons and d-electrons are different.

Fig. 3.42a shows the magnetic structure based on the three rules. In the magnetic structure, π-d exchange interactions between d-spins d_1, d_3, d_5, d_7 and the π-spins of the donor layer considered are strong because of the large spin densities at the sites 1, 3, 5 and 7. On the other hand, d-spins d_2, d_4, d_6 and d_8 interact with the quite small π-spins of sites 2, 4, 6 and 8 of the donor layer considered, respectively. Judging from the small magnetization of the $FeBr_4^-$ salt below $T_{\rm N}$, all d-spins must interact strongly with π-spins. Consequently, d-spins d_2, d_4, d_6 and d_8 must interact with the donor sites having large spin densities on adjacent donor layers as shown in Fig. 3.42b, or else d-spins d_2, d_4, d_6 and d_8 can be easily rotated by external field and show large magnetic moment. In contrast,

the d-spins d_1, d_3, d_5 and d_7 interact with the donor sites having quite small spin densities on adjacent donor layers in the spin configuration; that is, each anion interact with only one donor site having large spin densities.

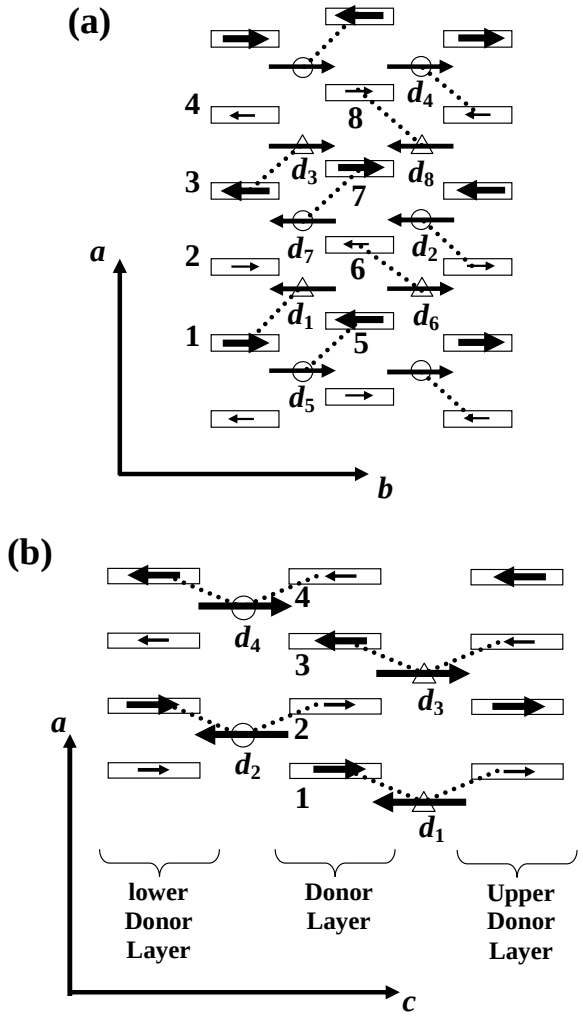

Figure 14
J. Nishijo *et al.*

Fig. 3.42. **(a)** The ab-plane projection of the magnetic structure of the $FeBr_4^-$ salt predicted from the calculated magnetic[63] structure of the pure π-electron system in the $GaBr_4^-$ salt. The antiferromagnetic π-d interactions through short donor-anion S-Br contacts $r_{\rm d}$ is represented as dotted lines. Numbers 1 to 8 represent eight donor sites, and small triangles and small circles represent $FeBr_4^-$ anions which belong to anion sheets above and beneath the sheet of donors depicted by rectangles, respectively. Label d_i indicates that the anion interacts with the i-th donor site. Each anion also interacts with the donors on the adjacent sheets through the other rd. The arrows denote the spins, while the arrows for Fe^{3+} is $S = 5/2$. **(b)** The inter-layer spin configuration of the $FeBr_4^-$ salt viewed perpendicular to the ac-plane, where spins are depicted as being aligned parallel to the c-axis for clarify. Each anion interacts with a donor site having a large spin density and a donor site having a small spin density, which are placed on the adjacent donor layers.

3.7.4 Estimation of the strengths of the π-π and π-d interactions

At first, the strength of the AF π-π interaction is estimated. In general, the AF interaction J_{ij} between donors radicals i and j is roughly in proportion to t_{ij}^2/U, where t_{ij} is the transfer integral between the donors. Though the strength of the interaction in charge ordered state cannot be described such a simple relation, the large intra-chain transfer integral (-298 meV) and small inter-chain transfer integral (-14 to 67 meV) suggest that the magnetic structure of the π-electrons is regarded as 1D Heisenberg AF. The susceptibility of the $GaBr_4^-$ salt shows weak temperature dependence in the temperature range $25 < T < 70$ K, which is the natural consequence of the 1D Heisenberg AF with strong intra-chain AF interaction $J_{\pi\pi}$. Indeed, the temperature dependence of the susceptibility is well fitted by the Bonner-Fisher model [23, 36] with average magnetic moment $\langle S_\pi \rangle = 1/2$ per two donors and $J_{\pi\pi} = -290$ K as shown in Fig. 3.43. When the smaller magnetic moment $\langle S_\pi \rangle = 0.36$ per two donors obtained in the calculation with $U = 1.0$ and $V = 0.5$ eV in previous section is assumed, the fitting gives $J_{\pi\pi} = -425$ K. In the following estimation of the strength of the π-d interaction based on mean-field calculation, the values $\langle S_\pi \rangle = 1/2$ per two donors and $J_{\pi\pi} = -290$ K are used for simplicity.

According to the spin structure shown in Fig. 3.42, the magnetic structure of a sheet of the $FeBr_4^-$ salt is approximately regarded to consist of four sublattices; that is, up ($S_{\pi\uparrow}$; donors 1 and 7) and down ($S_{\pi\downarrow}$; donors 3 and 5) spins of the π-electrons and up ($S_{d\uparrow}$; anions d_3 and d_5) and down ($S_{d\downarrow}$; anions d_1 and d_7) spins of the d-electrons, taking into account that the donors 2, 4, 6 and 8 are substantially non-magnetic and anions d_2, d_4, d_6 and d_8 are magnetically interacts with only the adjacent donor layers as shown in Fig. 3.42. The strength of the π-d interaction $J_{\pi d}$ can be estimated from the magnetization curve of the $FeBr_4^-$ salt by using the mean field calculation of the magnetization. In the calculation, the inter-chain π-π interaction is neglected because of the quasi 1D character of the π-electron system. In this condition, each π-spin interact with two π-spins and one d-spin, for example, $S_{\pi\uparrow}$ at the donor 1 interacts with $S_{\pi\downarrow}$ at the donor 3 placed above and below the chain and with $S_{d\downarrow}$ at d_1. The schematic model of the four magnetic

sublattices is shown in Fig. 3.44a, where the π-spins in the two sublattices $S_{\pi\uparrow}$ and $S_{\pi\downarrow}$ interact with each others with $J_{\pi\pi}$ through the mediation of non-magnetic donors, while a d-spin interacts with only a π-spin through AF interaction $J_{\pi d}$ of S-Br donor-anion contact. Based on this four sublattices model and mean-field approximation, the magnetization along the a- (hard axis) and b-axes (easy axes) at 2 K are fitted. In the calculation, the values $J_{\pi\pi} = -290$ K and $\langle S_\pi \rangle = 1/2$ per two donors, and the same anisotropic energy is assumed for both π and d-spins for simplicity. As shown in Fig. 3.44b, the calculated magnetizations with the values of $J_{\pi d} = -44.5$ K and the anisotropic energy 0.9 K is in good agreement with the observed magnetizations. Of course, strict value of the $\langle S_\pi \rangle$ is unknown, and it can takes a smaller value than 1/2 per two donors. In this case, stronger $J_{\pi d}$ is necessary because the d-spins are rotated more easily by external magnetic field unless the π-d interaction $J_{\pi d}$ is strong. In short, the strength of the $J_{\pi d}$ is estimated as at least -44.5 K.

The calculated magnetic structure of the $FeBr_4^-$ salt in the magnetic field based on the mean-field approximation is shown in Fig. 3.44c, d and e. When the field $H_{\rm ex}$ is applied along the hard axes, both d-spins $S_{d\uparrow}$ and $S_{d\downarrow}$ are canted by the field, while the π-spins hold the antiparallel arrangement owing to their strong AF interaction $J_{\pi\pi}$ as shown in Fig. 16c. On the other hand, only $S_{d\downarrow}$ is canted when the field $H_{\rm ex} < H_{\rm SF}$ is applied parallel to the easy axis, while $S_{d\uparrow}$ is stabilized by the Zeeman energy (Fig. 3.44d). Then the field becomes larger than spin flop field $H_{\rm SF}$, both π- and d-spins are rotated as shown in Fig. 16e, where both d-spins $S_{d\uparrow}$ and $S_{d\downarrow}$ are canted and the π-spins hold antiparallel arrangement similar to the case $H_{\rm ex}$ being applied along the hard axis. In all the case calculated, $S_{\pi\uparrow}$ and $S_{\pi\downarrow}$ hold the antiparallel arrangement, where the angle between $S_{\pi\uparrow}$ and $S_{\pi\downarrow}$ ranges from 176 to 180$^{\rm o}$ in the field region calculated $0 \leq H_{\rm ex} \leq 7$ T.

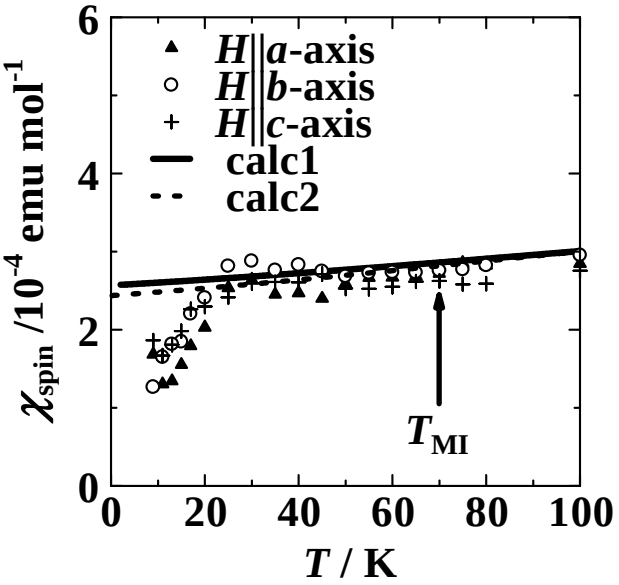

Fig. 3.43. The spin susceptibility of the $GaBr_4^-$ salt fitted by the Bonner-Fisher model with $\langle S_\pi \rangle = 1/2$ and $J_{\pi\pi} = -290$ K (solid line) and with $\langle S_\pi \rangle = 0.36$ and $J_{\pi\pi} = -425$ K (dotted line).

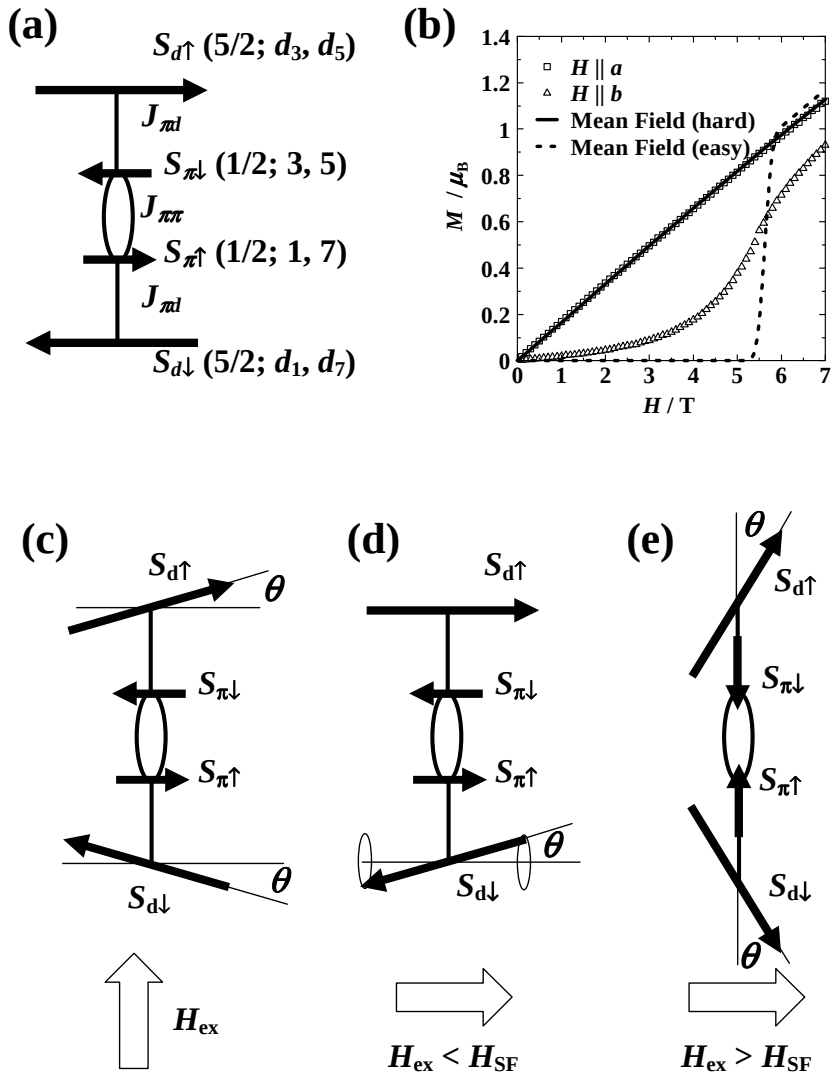

Fig. 3.44. **(a)** The schematic model of the magnetic structure of the $FeBr_4^-$ salt for mean-field calculation of the magnetization. $S_{\pi\uparrow}$ ($S_{\pi\downarrow}$) and $S_{d\uparrow}$ ($S_{d\downarrow}$) represent the $S = 1/2$ π-spins at donor sites 1 and 7 (3 and 5) and $S = 5/2$ d-spins at anion sites $d3$ and $d5$ ($d1$ and $d7$), respectively. The π-spins at donor sites 2, 4, 6 and 8 are neglected because of negligibly small spins at the sites. The d-spins at $d2$, 4, 6 and 8 are also neglected because they interact with only the donor sites 2, 4, 6 and 8 having negligibly small spin densities in this layer, while these d-spins interact with the large donor spins on adjacent donor layers. Intra-chain π-π AF interaction $J_{\pi\pi}$ is mediated through donor 2, 4, 6 and 8. **(b)** Fitting of the magnetization along the a- and b-axes with the values $J_{\pi d} = -44.5$ K and the anisotropic energy $K_u = 0.9$ K for both π- and d-spins. **(c)** The schematic model of the calculated spin structure of the $FeBr_4^-$ salt in the external field applied parallel to the hard axis, and that in the **(d)** external field $H_{ex} < H_{SF}$ and **(e)** $H_{ex} > H_{SF}$ applied parallel to the easy axis.

Figure 16 Nishimoto *et al.*[65]

3.7.5 The origin of the negative magnetoresistance in $FeBr_4^-$ salt

Based on the magnetic structure obtained above, the origin of the negative magnetoresistance observed is discussed in this subsection. Below T_N, the periodic magnetic potential of the $FeBr_4^-$ anions enhance the energy gap of the conducting π-electron system in the low temperature insulating state because of the following reason. The periodic magnetic potential of the d-spins, which is induced by the spin polarization of π-electrons, also counter-affects the π-electron system in the similar manner to the case of SDW state, where the periodic magnetic potential of spin-polarized π-electrons affects the π-electron itself [42]. In addition, the periodicity of the magnetic potential of the d-spins is, certainly, the same as that of the π-electron system resulting in the stabilization of the spin polarized state of the π-electrons. Consequently, the magnetic moments of $FeBr_4^-$ anions can enhance the gap of the insulating π-electron system. When high magnetic field is applied to the system, the periodic magnetic potential is weakened due to the destabilization of the AF structure of the d-spins, where the enhancement of the gap is reduced, resulting in the negative magnetoresistance as observed.

To confirm this idea, the magnetoresistance of the $FeBr_4^-$ salt is calculated by using the tight-binding calculation including not only U and V but also the effective exchange interaction $J_{\pi d}$ and the Zeeman energy of the π-electrons (see Section 2.3.2). As discussed above and shown in Fig. 3.44, it is assumed that the d-spins are classified into the two sublattices; that is, $\boldsymbol{S}_{d\uparrow}$ for d_3, d_4, d_5 and d_6, and $\boldsymbol{S}_{d\downarrow}$ for d_1, d_2, d_7 and d_8, where the d-spins increase or decrease the energy of a π-electron by $-2J_{\pi d}\boldsymbol{S}_d \cdot \boldsymbol{S}_\pi$ depending on the orientation of the d-spins. In the following discussion, the same values of the transfer integrals t given in previous section, $U = 1.0$ eV, $V = 0.5$ eV and $J_{\pi d} = -44.5$ K $= -3.83$ meV is employed to calculate the effect of the π-d interaction, though the exact values of U and V are not so important. In addition, the external field is applied along the easy axis as same as the experimental setting.

The energy of the π-d interaction at i-th donor site is described as $-2J_{\pi d}\boldsymbol{S}_{\pi i}\boldsymbol{S}_{di}$, which means that only the z-component of $\boldsymbol{S}_{di}$ ($\equiv S_{dzi}$) survives in the π-d interaction, where the z-direction is defined as the direction parallel to the spin principle

axis of the π-spin at the i-th donor site. To estimate S_{dzi}, the AF collinear structure of the π-electron spins is assumed, which is justified by the result of the mean-field calculation of the magnetization where the π-electrons hold the antiparallel arrangement owing to the strong intra-chain AF interaction $J_{\pi\pi}$. In this condition, S_{dzi} can be estimated from the magnetization based on the spin structure shown in Fig. 3.44d and 3.44e. In the region of $H_{\rm ex} < H_{\rm SF}$, the magnetization M and S_{dzi} are related to each other as

$$\begin{aligned} M &= \frac{1}{2}g\left(|\boldsymbol{S}_{d\uparrow}| - |\boldsymbol{S}_{d\downarrow}|\sin\theta\right) \\ &= \frac{1}{2}g\left(\frac{5}{2} - \frac{5}{2}\sin\theta\right) \end{aligned} \tag{3.13}$$

$$S_{\rm dzi} = \begin{cases} \frac{5}{2} & i = 3,4,5,6 \\ -\frac{5}{2}\sin\theta & i = 1,2,7,8, \end{cases} \tag{3.14}$$

where the g-value of $FeBr_4^-$ anions $g = 2$ are assumed, and factor 1/2 on the right side of eq. 3.13 means that a formula unit contains a half of the two anion sublattices $\boldsymbol{S}_{d\uparrow}$ and $\boldsymbol{S}_{d\downarrow}$. In contrast, M and S_{dzi} in the field region $H_{\rm ex} > H_{\rm SF}$ are expressed in the following equations;

$$\begin{aligned} M &= \frac{1}{2}g\cdot(|\boldsymbol{S}_{d\uparrow}| + |\boldsymbol{S}_{d\downarrow}|)\sin\theta \\ &= \frac{5}{2}g\sin\theta \end{aligned} \tag{3.15}$$

$$S_{\rm dzi} = \begin{cases} \frac{5}{2}\cos\theta & i = 3,4,5,6 \\ -\frac{5}{2}\cos\theta & i = 1,2,7,8. \end{cases} \tag{3.16}$$

Using eqs. (3.13) - (3.16), S_{dzi} from the observed magnetization M below $H_{\rm SF} = 5.8$ T. Because the magnetization measurement was carried out only in the field region $H_{\rm ex} < 7$ T due to the experimental limitation, linear field dependence of the magnetization is assumed above $H_{\rm SF}$. The estimated values of $|S_{\rm dzi}|$ is shown in Fig. 3.45. Below $H_{\rm SF}$, $|S_{dzi}|$ (i = 1, 2, 7 and 8) decreases as the field is raised, while $|S_{dzi}|$ (i = 3, 4, 5 and 6) keeps the value of 5/2 as discussed in the previous section. When the field becomes larger than $H_{\rm SF}$, all of S_{dzi} takes a same value which is close to the value 5/2 and gradually decreases as the field is raised.

From the values of S_{dzi}, $J_{\pi d}$, transfer integrals, $U = 1.0$ eV and $V = 0.5$ eV, the field dependence of the band gap ΔE is calculated using the tight-binding method as shown in Fig. 3.46. The gap gradually decreases with a convex curvature as the

field is raised followed by a discontinuous jump at H_{SF} owing to the jump of S_{dzi} at H_{SF} as shown in Fig. 3.45b. Above H_{SF}, the gap gradually decreases again. The field dependence of the gap seems to be qualitatively a good representation of the magnetoresistance observed. However, the absolute values of the change of the calculated gap is too large to explain the measured magnetoresistance. Because the tight-binding calculation is a rough approximation, correction parameter α is introduced as $\Delta E' = \alpha \Delta E$ to make the result best fitted to the experiments. The resistivity ρ in the insulating state having a band gap $\Delta E'$ is described as

$$\rho = \rho_0 \exp\left(\frac{\Delta E'}{k_{\mathrm{B}} T}\right), \tag{3.17}$$

where ρ_0 is a constant value. From the calculated band gap $\Delta E'$, eq. (3.17) and the definition of the magnetoresistance

$$\frac{\Delta\rho}{\rho_0} = \frac{\rho(H_{\mathrm{ex}} - \rho(0))}{\rho(0)}, \tag{3.18}$$

the magnetoresistance is calculated with a value of the fitting parameter $\alpha = 0.01$ as shown in Fig. 3.47. The calculated magnetoresistance is in good agreement with that observed semi-quantitatively, proving that the origin of the negative magnetoresistance is the disappearance of the additional gap which is caused by the periodic magnetic potential of the anions and the strong π-d interaction.

Finally, one discrepancy between the calculated and the measured magnetoresistances should be addressed. There is a large quantitative discrepancy between the calculated and the measured energy gaps, which clearly appears in the necessity of introducing the fitting parameter a = 0.01. This means that the observed energy gap caused by the π-d interaction is ca. 1/100 of that calculated. The quantitative discrepancy is partially caused by the limitations of tight-binding calculation and mean field treatment which sometimes overestimates the band gap. However, the discrepancy is too large to be attributed to this reason. Here, there is a clewing fact as follows. In the observed results, applying pressure, which enhances the transfer integrals, reduces the negative magnetoresistance as shown in Fig. 3.16. For example, the MR of the $FeBr_4^-$ salt at ambient pressure takes a value -0.23 at 15 T, 1.5 K, while that under 13.8 kbar takes only -0.04 at the same condition. This behavior indicates that an increase of the transfer integrals weakens the

effect of the π-d interaction on the energy gap. The electron transfer makes the electrons conductive and weaken the localized character of the π-electrons. However, the calculated MR value is roughly independent of the change of the transfer integrals. Actually, when the MR is calculated for several sets of transfer integrals, for example, inter-chain transfer integrals and/or intra-chain transfer integrals are increased by 1.1-1.4 times from those employed in the calculation, the results show quite similar field dependence in the quantitative level where the change of the MR is less than 1 %. The difference of the transfer-integral dependence between the observed and the calculated MR reveals the insensitiveness of the effect of the π-d interaction to the transfer integrals in the tight-binding calculation and/or the mean field treating used in the calculation mentioned above. This fact suggest that the calculation neglects the weakening of the π-d interaction at ambient pressure, resulting in the irrationally large change of the energy gap calculated in the field.

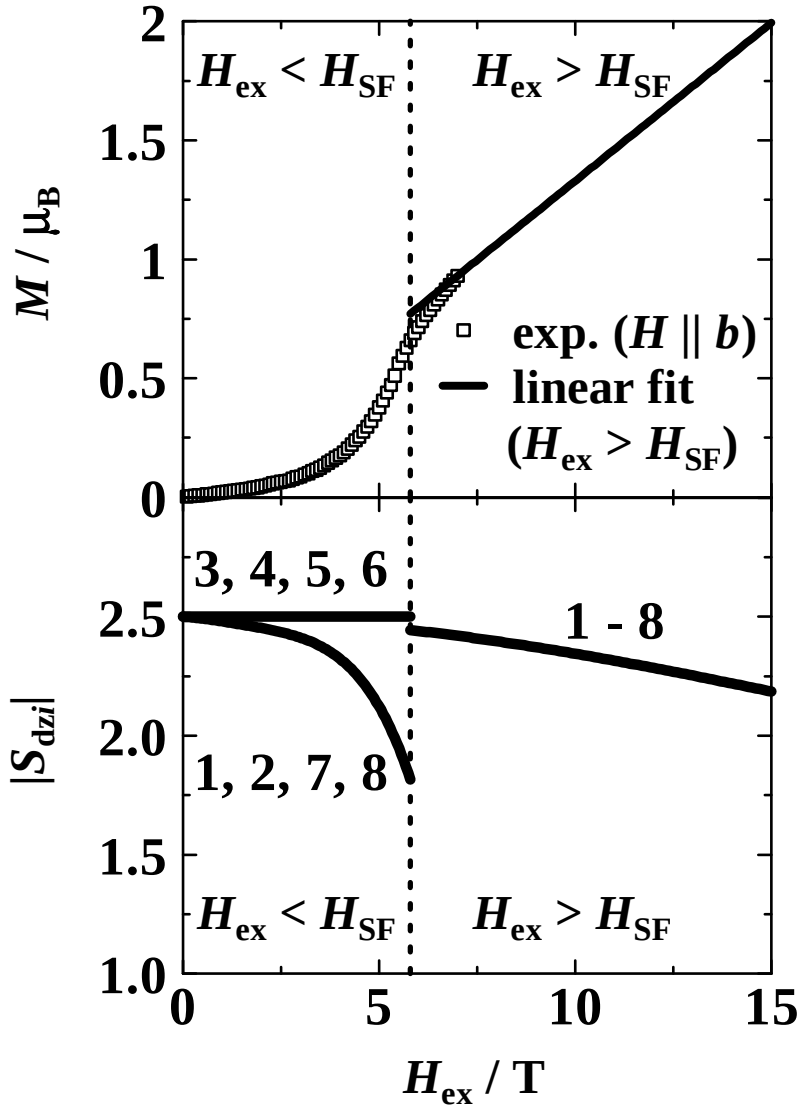

Fig. 3.45. **(a)** The magnetization of the $FeBr_4^-$ salt. To calculate S_{dzi} which is the z-component of the d-spins $\boldsymbol{S}_{di}$, the linear field dependence of the magnetization are assumed above $H_{\rm SF}$. **(b)** The z-component of the d-spins calculated from the fitting of the magnetization curve and eqs. (3.13)-(3.16) (see text).

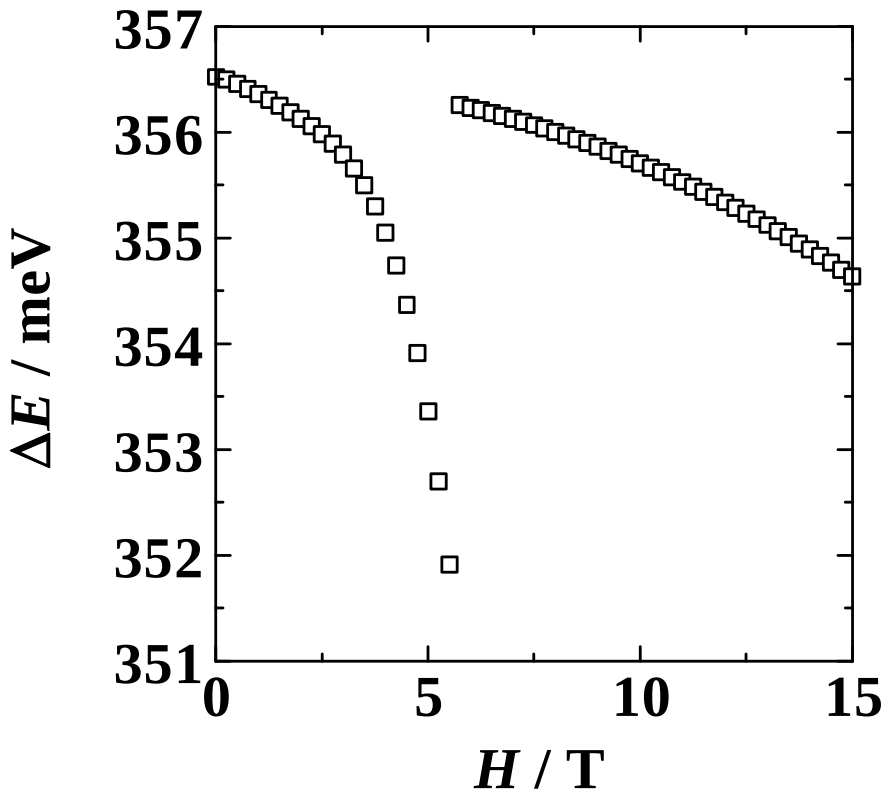

Fig. 3.46. Field dependence of the calculated energy gap ΔE of the $FeBr_4^-$ salt based on the tight binding calculation including U, V and $J_{\pi d}$.

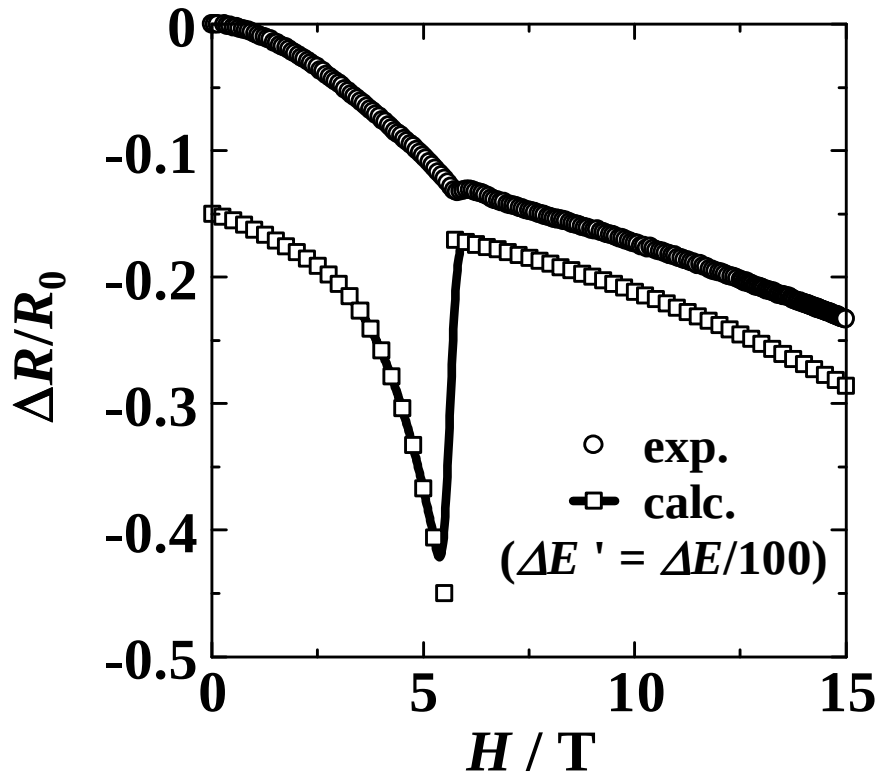

Fig. 3.47. Field dependence of the observed and calculated magnetoresistances with fitting parameter $\alpha = 0.01$. $\Delta E'$ is the energy gap corrected with α. The calculated is vertically shifted down by 0.15 for clarity.

3.8 Summary

Isostructural salts (EDT-TTFBr_2)$_2$MBr_4 (M = Fe, Ga) form a donor-anion sandwiched layer structure, which consists of 1D donor chain elongated parallel to the a-axis and anion chain parallel to b-axis. In the salts, significantly short donor-anion contacts are achieved thanks to the strong attractive coordination-bond-like interaction between bromine atoms of the anion and the donor molecules. The short contacts contributes to the strong donor-anion electronic interaction, whereas the longer inter-anion Br-Br contact is responsible for a weak inter-anion interaction.

In high temperature region, the salts having quasi-1D electronic feature are metallic, where the antiferromagnetic interaction of d-spins is weak, resulting in the small Weiss temperature $\Theta = -3.6$ K. When temperature is lowered, the $GaBr_4^-$ salt undergoes an MI transitions at $T_{\rm MI} = 70$ K, while the $FeBr_4^-$ salt shows a metallic conductivity down to 20 K. The difference of $T_{\rm MI}$ between the salts is owing to the open shell and the closed shell structure of the d-orbitals of the Fe^{3+} and the Ga^{3+}, respectively. As a result of the short donor-anion S-Br contact, π-electrons can be transferred from a donor layer to another through the d-orbital of the $FeBr_4^-$ anion, which makes the π-electron system three dimensionally. MI transition is originated from the low dimensional instability, therefore the three dimensional character of the $FeBr_4^-$ salt reduces $T_{\rm MI}$. In contrary to the $FeBr_4^-$ salt, π-electrons cannot pass though the closed shell of the $GaBr_4^-$, resulting in the low dimensional electronic structure of π-electrons and high $T_{\rm MI}$.

Below $T_{\rm MI}$, the π-electron spins behaves as paramagnetic followed by antiferromagnetic transition, which is evidenced by the EPR spectra of the $GaBr_4^-$ salt. The appearance of the antiferromagnetic localized magnetic moments of π-electrons bring about the strong antiferromagnetic interaction between π and d-spins in the $FeBr_4^-$ salt, resulting in the rapid development of the short range order of d-spins below ca. $T_{\rm MI}$ and antiferromagnetic transition at $T_{\rm N} = 11$ K. The strength of the π-d interaction is estimated as -44.5 K from the magnetization curve below $T_{\rm N}$, which is considerably large among TTF-based magnetic conductors [8,9,13,43–50].

Below $T_{\rm N}$, periodic arrangement of d-spins are caused by the π-electrons, and at the same time, the periodic potential reacts on the insulating π-electrons, where

the periodic potential of d-spins stabilizes the insulating state of the π-electrons through the π-d interaction. The stabilization of the π-electrons is clearly shown in both the temperature dependence of the resistivity and the magnetoresistance of the $FeBr_4^-$ salt. As expected from the stabilization effect of the periodic potential of d-spins, the resistivity shows additive increase at T_N, and large negative magnetoresistance is observed below the temperature. The negative MR is the natural consequence of the gap enhancement by the d-spins. When the high magnetic field is applied, the periodic magnetic potential is weakened by the Zeeman energy of the d-spins, resulting in the reduction of the enhanced gap.

To confirm the model for negative MR, tight-binding calculation including both on-site Coulomb interaction and π-d interaction was carried out. The calculation can reproduce the negative MR semi-quantitatively and evidences the existence of the gap enhancement by d-spins.

In conclusion, (EDT-$TTFBr_2$)$_2FeBr_4$ is a strong π-d interaction system, where the interaction is achieved by the orientation-controlling group of the donor molecule which shortens the donor-anion atomic contacts and strengthen the π-d interaction.

References

[1] E. O. Schlemper and D. Britton, *Acta Crystallogr.*, **18**, 419 (1965).

[2] T. Imakubo, H. Sawa and R. Kato, *J. Chem. Soc., Chem. Commun.*, 1097 and 1667 (1995).

[3] R. Gompper, J. Hock, K. Ploborn, E. Dormann and H. Winter, *Adv. Mater.*, **7**, 41 (1995).

[4] M. Iyoda, Y. Kuwatani, K. Hara, E. Ogura, H. Suzuki, H. Ito and T. Mori, *Chem. Lett.*, 599 (1997).

[5] M. Iyoda, Y. Kuwatani, E. Ogura, K. Hara, H. Suzuki, T. Takano, K. Takeda, J.-I. Takano, K. Ugawa, M. Yoshida, H. Matsuyama, H. Nishikawa, I. Ikemoto, T. Kato, N. Yoneyama, J. Nishijo A. Miyazaki and T. Enoki, *Heterocycles*, **54**, 833 (2001).

[6] T. Imakubo, N. Tajima, M. Tamura, R. Kato, Y. Nishio, and K. Kajita, *J. Mater. Chem.*, **12**, 159 (2002).

[7] T. Suzuki, H. Fujii, Y. Yamashita, C. Kabuto, S. Tanaka, S. Tanaka, M. Harasawa, T. Mukai and T. Miyashi, *J. Am. Chem. Soc.*, **114**, 3034 (1992).

[8] H. Kobayashi, A. Kobayashi and Patrick Cassoux, *Chem. Soc. Rev.*, **29**, 325 (2000).

[9] M. Enomoto, A. Miyazaki, and T. Enoki, *Bull. Chem. Soc. Jpn.*, **74**, 459 (2001).

[10] A. Miyazaki, K. Enomoto, K. Okabe, H. Yamazaki, J. Nishijo, T. Enoki, E. Ogura, K. Ugawa, Y. Kuwatani, and M. Iyoda, *J. Solid State Chem.*, **168**, 547 (2002).

[11] K. Enomoto, J.-I. Yamaura, A. Miyazaki and T. Enoki, *Bull. Chem. Soc. Jpn.*, **76**, 945 (2003).

[12] K. Okabe, K. Enomoto, A. Miyazaki and T. Enoki, *Mol. Cryst. Liq. Cryst.*, **376** 513 (2002).

[13] S. Uji, H. Shinagawa, T. Terashima, T. Yakabe, Y. Terai, M. Tokumoto, A. Kobayashi, H. Tanaka and H. Kobayashi, *Nature*, **410**, 908 (2001).

[14] T. Mori, A. Kobayashi, Y. Sasaki, H. Kobayashi, G. Saito and H. Inokuchi, *Bull. Chem. Soc. Jpn.*, **57**, 627 (1984).

[15] The calculation method is noted in the following article, and I calculated the donor-anion overlap integral by using their program.
T. Mori and M. Katsuhara, *J. Phys. Soc. Jpn.*, **71**, 826 (2002).

[16] L. J. Farrugia, *J. Appl. Cryst.*, **30**, 565 (1997).

[17] J. J. P. Stewart, *J. Comput. Chem.*, **10**, 209 (1989).

[18] R. Kato, H. Kobayashi, T. Mori, A. Kobayashi and Y. Sasaki, *Solid State Commun.*, **55** 387 (1985).

[19] S. D. Obertelli, R. H. Friend, D. R. Talham, M. Kurmoo and P. Day, *J. Phys., Condens. Matt.*, **1**, 5671 (1989)

[20] J. S. Scott, "Semiconductor and Semimetal", Vol. 27, ed. by E. Conwell, Academic Press (1988).

[21] T. Takahashi, D. Jerome, F. Masin, J. M. Fabre, L. Giral, *J. Phys. C*, **17**, 3777 (1984).

[22] K. Kanoda, T. Takahashi, K. Kikuchi, K. Saito, I. Ikemoto and K. Kobayashi, *Phys. Rev. B*, **39**, 3996 (1989).

[23] V. Gama, R. T. Henriques, G. Bonfait, L. C. Pereira, J. C. Waerenborgh, I. C. Santos, M. T. Duarte, J. M. P. Cabral and M. Almeida, *Inorg. Chem.*, **31**, 2598 (1992).

[24] L. Brossard, R. Clerac, C. Coulon, M. Tokumoto, T. Ziman, D. K. Petrov, V. N. Laukhin, M. J. Naughton, A. Audouard, F. Goze, A. Kobayashi, H. Kobayashi and P. Cassoux, *Eur. Phys. J. B*, **1**, 439 (1998).

[25] T. Oguchi, *Phys. Rev.*, **117**, 117 (1960).

[26] T. Sugano, G. Saito and M. Kinoshita, *Phys. Rev. B*, **34**, 117 (1986).

[27] K. Nagata and Y. Tazuke, *J. Phys. Soc. Jpn.*, **32**, 337 (1972).

[28] K. Nagata, *J. Phys. Soc. Jpn.*, **40**, 1209 (1976).

[29] F. Rodriguez and M. Moreno, *Trans. Metal Chem.*, **10**, 351 (1985).

[30] O. Bechstein, D. Hass, E. Uhse, R. Stoesser, *Zeitsch. f r Chem.*, **10**, 351 (1985).

[31] H. Mori, *Prog. Theor. Phys.*, **30**, 578 (1963).

[32] Y. Tazuke and K. Nagata, *J. Phys. Soc. Jpn.*, **38**, 1003 (1975).

[33] R. J. Elliott, *Phys. Rev.* **96**, 266 (1954).

[34] J. H. Van Vleck, *Phys. Rev.* **74**, 1168 (1948).

[35] T. Nakamura, *J. Phys. Soc. Jpn.*, **72**, 213 (2003).

[36] J. C. Bonner and M. E. Fisher, *Phys. Rev.*, **135**, A640 (1964).

[37] D. B. Brown, J. A. Donner, J. W. Hall, S. R. Wilson, R. B. Wilson, D. J. Hodgson and W. E. Hatfield, *Inorg. Chem.*, **18**, 2635 (1979).

[38] S. Uji, T. Terashima, H. Aoki, J. S. Brooks, R. Kato, H. Sawa, S. Aonuma, M. Tamura, and M. Kinoshita, *Phys. Rev. B*, **50**, 15597 (1994).

[39] H. Kino and H. Fukuyama, *J. Phys. Soc. Jpn.*, **65**, 235 (1996).

[40] H. Seo and H. Fukuyama, *J. Phys. Soc. Jpn.*, **66**, 1249 (1997).

[41] J. B. Torrance, *"Low Dimensional Conductors and Superconductors"*, Edited by D. J rome and L. G. Caron, NATO ASI Series B: Physics Vol.155, 1987.

[42] For example, G. Gr ner, *Density Waves in Solids*, Addison-Wesley Longmans Inc., Massachusetts, USA, 1990.

[43] T. Sugano, H. Takenouchi, D. Shiomi and M. Kinoshita, *Synth. Met.* **41**, 2217 (1991).

[44] C. J. Kepert, M. Kurmoo, P. Day and M. R. Truter, *Synth. Met.* **70**, 781 (1995).

[45] P. Day and M. Kurmoo, *Synth. Met.*, **85**, 1445 (1997)

[46] M. Kurmoo, P. Day, P. Guionneau, G. Bravic, D. Chasseau, L. Ducasse, M. L. Allan, I. D. Marsden and R. H. Friend, *Inorg. Chem.*, **35**, 4719 (1996).

[47] H. Oshio, E. Ino, I. Mogi, T. Ito, *Inorg. Chem.*, **32** 5697 (1993).

[48] T. Mallah, C. Hollis, S. Bott, M. Kurmoo and P. Day, *J. Chem. Soc.*, Dalton Trans., 859 (1990).

[49] E. Coronado, J. R. Galan-Mascaros, C. J. Gomez-Garcia and V. Laukhin, *Nature*, **408**, 447 (2000).

[50] A. Sato, E. Ojima, H. Akutsu, Y. Nakazawa, H. Kobayashi, H. Tanaka, A. Kobayashi and P. Cassoux, *Phys. Rev. B*, **61**, 111 (2000).

Chapter 4

Crown thioether complexes

4.1 Introduction

One of the most important issues in designing molecular magnets is to make a magnetic interaction network between constituent molecules as building blocks. From the lesson of traditional transition metal magnets, conduction electrons, which can mediate interactions between magnetic sites, are a promising tool in making these networks. Actually, strong magnetic interactions in iron and manganese oxides are the consequence of conduction electron-mediated exchange interactions. Based on this scheme, molecule-based magnetic conductors are designed to mimic such traditional magnets [1–8]. In the popular molecule-based magnetic conductors developed so far, transition metal magnetic anions containing halogen atoms at ligand sites are incorporated into tetrathiafulvalene (TTF) type charge transfer complexes [1–4]. In these salts, conduction π-electrons of TTF donors can interact with the localized magnetic moments of anions (π-d interaction) through the inter-molecular atomic contact between the sulfur atom of the donor and the halogen sites of the anions. However, π-d interactions are usually very weak in these systems because the spin density at halogen atoms of anions is quite small. To solve this problem, transition metal complexes containing sulfur atoms at ligand sites are used. Indeed, the π-acidity of sulfur-containing ligands, which produce back donation from the central metal atom, increases the spin density at the sulfur atom of the ligands. Furthermore, the large atomic orbitals of sulfur atoms can also enhance the π-d interactions through S-S contacts between donor and anion. The idea of inter-molecular S-S atomic contact is also expected to be applicable in

designing a strong interaction network [9] in insulating molecular magnets where superexchange paths with S-S bridges work in place of π-d interactions.

Under the impetus mentioned above, I have been surveying sulfur-containing magnetic building blocks which can effectively work in the architecture of molecular magnets. Though no attention has yet been paid to crown thioethers in designing molecule-based magnets, the π-acidity of crown thioethers [10, 11] enhancing the spin density at ligand is suitable for building molecular magnets as it contributes to forming an extended electronic structure, which is inferable to enhancing magnetic interactions. In this chapter, I will report a new class of molecule-based magnets with transition metal complexes of crown thioethers having sulfur atoms as the main ingredient. 9S3 = 1,4,7-trithiacyclononane, the crown thioether ligand I employ, is well known and a target of particular focus in the crown thioether area [12, 13]. As counter anions or acceptors to these cations, I used TCNQ (= 7,7,8,8-tetracyanoquinodimethane), Br^- and $[Ni(bdt)_2]^-$ (bdt = 1,2-benzenedithiolato) molecules. TCNQ is a well known acceptor, charge transfer salts of which frequently produce high conductive materials [14–16]. Br^- anions, which are small, can reduce the distances between cations due to the absence of steric hindrance. Therefore, it is expected that a strong interaction between crown thioether complexes will be produced. $[Ni(bdt)_2]^-$ molecules are dithiolate planar complexes which also contain sulfur atoms. As a result, not only strong cation-cation, but also cation-anion interactions are expected through the mediation of intermolecular S-S contacts.

At first, the crystal structures of the salts will be reported, which are helpful to discuss the magnetism of the salts. Then, the electric resistivity and the magnetic susceptibilities of the series of crown thioether complex salts, $[M(9S3)_2]$-$(TCNQ)_n$ (M = Ni, Co; n = 2, 3; 9S3 = 1,4,7-trithiacyclononane; TCNQ = 7,7,8,8-tetracyanoquinodimethane), $[M(9S3)Br_2]$ (M = Cu, $Cu_{1-x}Ni_x$ ($x \sim 0.05$)) and $[M(9S3)_2][Ni(bdt)_2]_2$ (M = Ni, Co), will be shown. The magnetic susceptibilities of the crown thioether complexes of the salts show strong inter-molecular exchange magnetic interaction in spite of its long inter-molecular distances. At last, the origin of the weak-ferromagnetism of $[M(9S3)_2][Ni(bdt)_2]_2$ will be discussed based on the magnetic structure expected from the crystal structure.

4.2 Crystal structures

4.2.1 $[M(9S3)_2](TCNQ)_n$ (M = Ni, Co; n = 2, 3)

The crystals structure of $[Ni(9S3)_2](TCNQ)_2$ and $[Ni(9S3)_2](TCNQ)_3$ are shown in Figs. 4.1 and 4.2, respectively, and their crystallographic data are shown in Table 4.1-4.10. The structures are similar to $[M([9]aneN3)_2](TCNQ)_n$ (M = Ni, Cu; n = 1, 2; $9aneN_3$ = 1,4,7-triazacyclononane) [17]. In the crystal of $[Ni(9S3)_2](TCNQ)_2$, $TCNQ^-$ anions form dimers, which are well separated from each other by the hindrance of $[Ni(9S3)_2]^{2+}$ cations. The feature of the well-separated dimer structure is evidenced by the calculation of intra-dimer and inter-dimer overlap integrals between $TCNQ^-$ molecules based on the extended H ckel method [18], where the former ($= 2.64 \times 10^{-2}$) is overwhelmingly larger than the latter (~ 0) resulting in the singlet state of the dimer. $[Ni(9S3)2]^{2+}$ cations form one-dimensional (1D) chains elongated parallel to the c-axis with an inter-molecular S-S contact of r = 3.838(6) Å, which is slightly longer than the sum of the van der Waals radii of sulfur atoms (3.7 Å).

In contrast, TCNQ molecules form trimers in $[Ni(9S3)_2](TCNQ)_2$, where the trimers are also non-magnetic with two electrons stabilized in the singlet state,as a result of large intra-trimer overlap integrals ($p = 1.82\times10^{-2}$) and small inter-trimer overlap integrals ($q = 9.60\times10^{-4}$). In addition, the presence of large size trimers makes the $[Ni(9S3)_2]^{2+}$ molecules remain apart from each other. Using the empirical relations [19] between the bond length in a TCNQ molecule and its charge state, the valences of the TCNQ molecules can be estimated as -0.69 for TCNQ (A) and -0.71 for TCNQ (B), respectively. It is considered that crystals $[Co(9S3)_2](TCNQ)_2$ and $[Co(9S3)_2](TCNQ)_3$, cobalt (II) analogue of $[Ni(9S3)_2](TCNQ)_2$ and $[Ni(9S3)_2](TCNQ)_2$, respectively, have the same structural featured as those of the nickel (II) complexes.

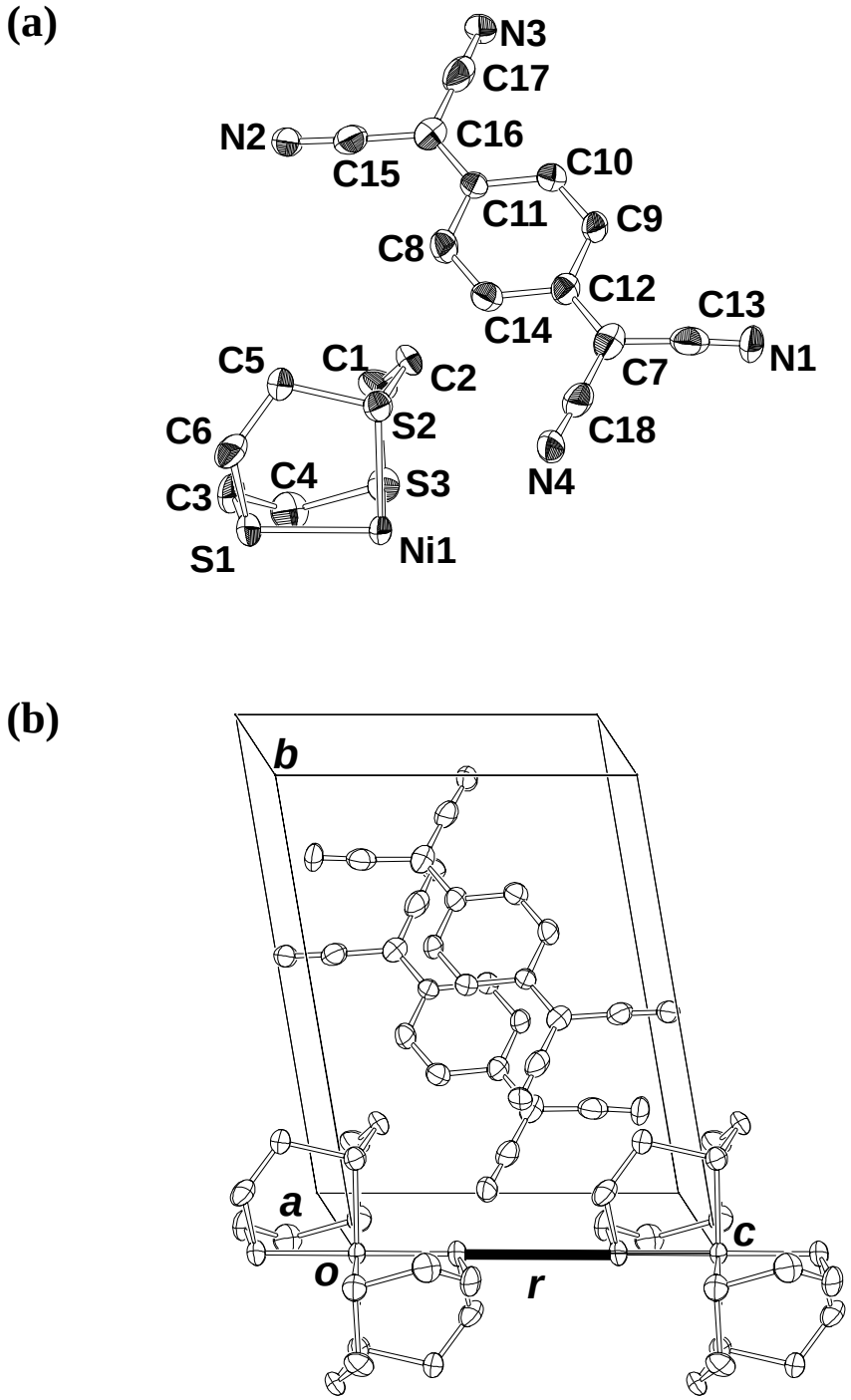

Fig. 4.1. (a) Thermal ellipsoid plot (50 % probability) and (b) the crystal structure of $[Ni(9S3)_2](TCNQ)_2$. The solid line r= 3.838(6) Å represents inter-molecular S1-S1 contact between $[Ni(9S3)_2]^{2+}$ cations.

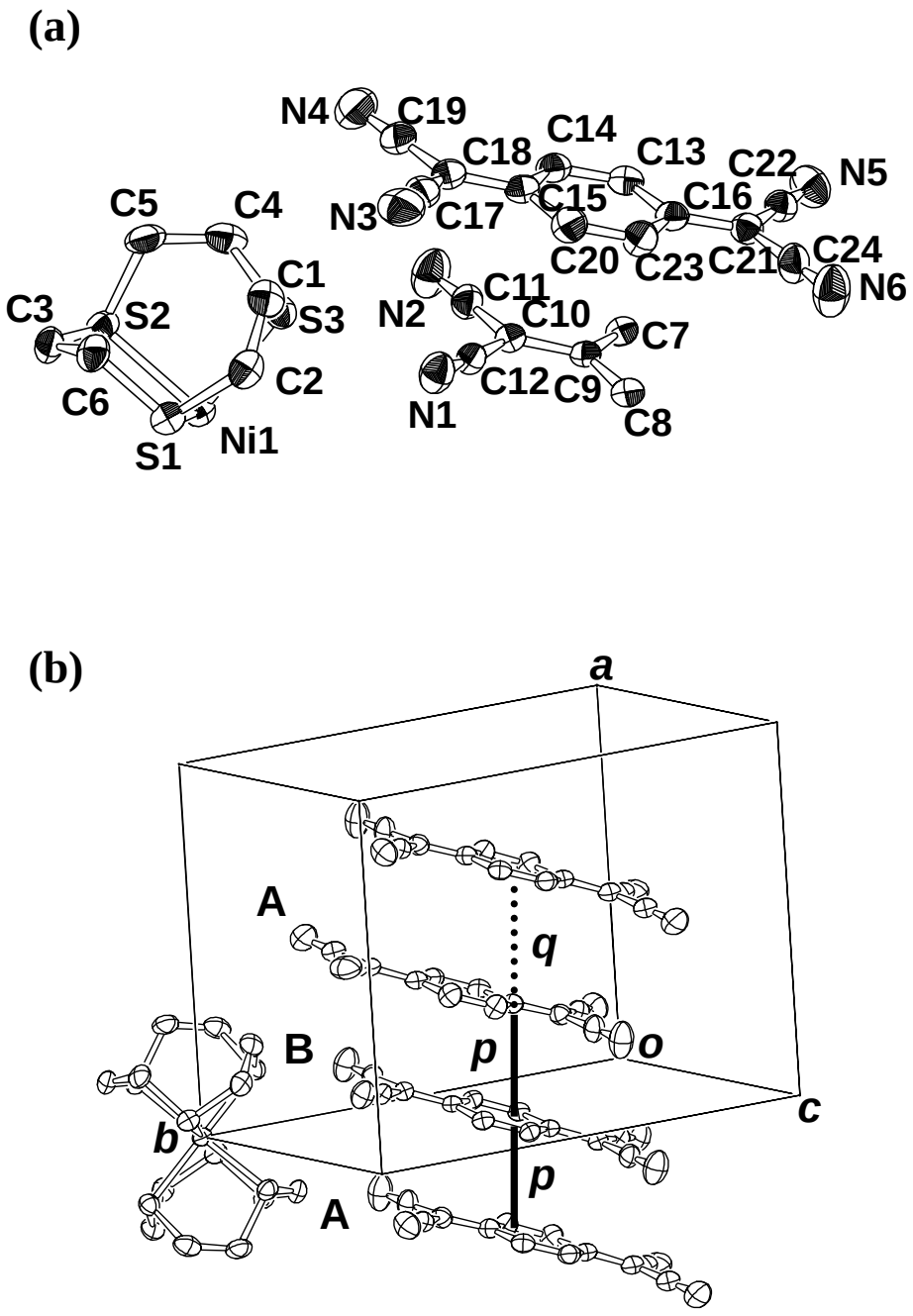

Fig. 4.2. (a) Thermal ellipsoid plot (50 % probability) and (b) the crystal structure of $[Ni(9S3)_2](TCNQ)_3$. Solid lines and dotted line represent overlap large intra-trimer overlap integrals $p = 1.82 \times 10^{-2}$ and small inter-trimer overlap integral $q = 9.60 \times 10^{-4}$), respectively.

Table 4.1. Crystallographic data of $[Ni(9S3)_2](TCNQ)_n$ (n = 2, 3).

	$[Ni(9S3)_2](TCNQ)_2$	$[Ni(9S3)_2](TCNQ)_3$
space group	$P\bar{1}$	$P\bar{1}$
a,Å	9.319(9)	10.418(3)
b,Å	11.555(9)	14.535(4)
c,Å	8.627(9)	7.764(3)
α,deg	99.69(8)	93.04(3)
β,deg	95.86(11)	95.48(3)
γ,deg	80.25(7)	92.38(2)
V,Å^3	899.9(14)	1167.0(6)
Z	1	1
reflections collected ($2\Theta < 55^o$)	1736	4759
reflections unique	1631	4325
R_1 for all data	0.0880	0.0460
wR_2 for all data	0.2266	0.1351

Table 4.2. Atom positions of $[Ni(9S3)_2](TCNQ)_2$.

atom	x	y	z	B_{eq} (Å^3)
Ni1	0.0000	0.0000	0.0000	0.0283(7)
S1	0.0095(4)	-0.0004(3)	-0.2770(3)	0.0364(9)
S2	-0.0826(4)	0.2087(3)	0.0325(4)	0.0331(8)
S3	0.2465(4)	0.0410(3)	0.0427(4)	0.0384(9)
C1	0.2213(15)	0.2042(12)	0.0639(17)	0.041(3)
H1A	0.3009	0.2327	0.1331	0.049
H1B	0.2258	0.2270	-0.0385	0.049
C2	0.0791(15)	0.2632(12)	0.1290(14)	0.038(3)
H2A	0.0683	0.3475	0.1240	0.045
H2B	0.0845	0.2545	0.2394	0.045
C3	0.1905(17)	0.0340(14)	-0.2858(15)	0.047(4)
H3A	0.2264	-0.0025	-0.3871	0.056
H3B	0.1848	0.1193	-0.2783	0.056
C4	0.2938(15)	-0.0070(13)	-0.1609(16)	0.045(3)
H4A	0.3861	0.0182	-0.1707	0.054
H4B	0.3097	-0.0932	-0.1799	0.054
C5	-0.0800(16)	0.2435(11)	-0.1650(14)	0.037(3)
H5A	-0.1536	0.3120	-0.1785	0.045
H5B	0.0144	0.2648	-0.1760	0.045
C6	-0.1086(17)	0.1401(12)	-0.2958(16)	0.045(3)
H6A	-0.0964	0.1622	-0.3967	0.054
H6B	-0.2093	0.1285	-0.2961	0.054
N1	0.5252(16)	0.2323(12)	0.8918(15)	0.062(4)
N2	0.7741(18)	0.5234(11)	0.0069(16)	0.063(4)
C7	0.4933(16)	0.2394(12)	0.5914(16)	0.040(3)
C8	0.6215(15)	0.3763(11)	0.2882(15)	0.036(3)
H8	0.6129	0.3704	0.1789	0.044
C9	0.6337(13)	0.4053(10)	0.6139(14)	0.031(3)
H9	0.6361	0.4154	0.7234	0.037
N3	0.9392(14)	0.6837(12)	0.4690(14)	0.052(3)
N4	0.3443(19)	0.0916(13)	0.4188(15)	0.068(4)
C14	0.5584(14)	0.3038(11)	0.3548(14)	0.032(3)
H14	0.5137	0.2446	0.2913	0.039
C15	0.7739(16)	0.5276(12)	0.1425(16)	0.040(3)
C16	0.7749(15)	0.5364(12)	0.3114(15)	0.039(3)
C17	0.8663(16)	0.6192(12)	0.4000(16)	0.041(3)
C18	0.4118(17)	0.1571(13)	0.4985(16)	0.044(3)
C13	0.5085(16)	0.2385(12)	0.7602(16)	0.042(3)
C12	0.5584(13)	0.3155(11)	0.5239(14)	0.032(3)
C11	0.7028(14)	0.4635(10)	0.3796(13)	0.029(3)
C10	0.7016(15)	0.4761(11)	0.5465(14)	0.035(3)
H10	0.7483	0.5340	0.6100	0.042

Table 4.3. Anisotropic thermal factors of $[Ni(9S3)_2](TCNQ)_2$.

atom	U_{11}	U_{22}	U_{33}	U_{23}	U_{13}	U_{12}
Ni1	0.0390(15)	0.0285(13)	0.0184(11)	0.0043(9)	0.0077(10)	-0.0038(11)
S1	0.051(2)	0.0389(19)	0.0214(15)	0.0032(13)	0.0100(14)	-0.0097(17)
S2	0.039(2)	0.0307(17)	0.0301(16)	0.0034(13)	0.0118(14)	-0.0019(15)
S3	0.040(2)	0.0408(19)	0.0345(17)	0.0066(15)	0.0041(15)	-0.0050(16)
C1	0.036(8)	0.038(7)	0.050(8)	-0.003(6)	-0.002(6)	-0.022(6)
C2	0.059(9)	0.033(7)	0.020(5)	-0.006(5)	0.007(6)	-0.012(7)
C3	0.062(10)	0.053(9)	0.030(7)	0.008(6)	0.024(7)	-0.008(8)
C4	0.037(8)	0.049(8)	0.050(8)	0.005(7)	0.018(7)	-0.001(7)
C5	0.055(9)	0.034(7)	0.026(6)	0.007(5)	0.008(6)	-0.009(6)
C6	0.059(10)	0.039(8)	0.039(7)	0.022(6)	-0.007(7)	-0.007(7)
N1	0.084(11)	0.064(9)	0.039(7)	0.012(6)	0.016(7)	-0.006(8)
N2	0.098(11)	0.046(8)	0.052(8)	-0.001(6)	0.033(8)	-0.023(8)
C7	0.041(8)	0.042(8)	0.040(7)	0.013(6)	0.005(6)	-0.002(6)
C8	0.044(8)	0.035(7)	0.029(6)	0.002(5)	0.012(6)	0.000(6)
C9	0.036(7)	0.030(7)	0.026(6)	0.004(5)	0.012(5)	-0.002(6)
N3	0.062(9)	0.055(8)	0.046(7)	0.004(6)	0.005(6)	-0.033(7)
N4	0.109(13)	0.065(9)	0.040(7)	0.008(7)	0.012(8)	-0.039(9)
C14	0.033(7)	0.030(7)	0.034(6)	0.002(5)	0.004(5)	-0.005(5)
C15	0.058(9)	0.032(7)	0.036(7)	0.008(6)	0.021(6)	-0.007(6)
C16	0.044(8)	0.035(7)	0.039(7)	0.011(6)	0.004(6)	-0.006(6)
C17	0.048(9)	0.037(8)	0.042(7)	0.008(6)	0.019(6)	-0.007(7)
C18	0.063(10)	0.039(8)	0.035(7)	0.005(6)	0.017(7)	-0.018(8)
C13	0.058(10)	0.031(7)	0.039(8)	0.004(6)	0.016(7)	-0.006(6)
C12	0.030(7)	0.033(7)	0.032(6)	0.007(5)	0.013(5)	0.003(6)
C11	0.038(7)	0.023(6)	0.026(6)	0.003(5)	0.008(5)	0.004(5)
C10	0.047(8)	0.026(7)	0.029(6)	0.004(5)	0.001(6)	-0.003(6)

Table 4.4. Bond length of $[Ni(9S3)_2](TCNQ)_2$ (Å).

Ni1-S2	2.383(4)
Ni1-S1	2.400(4)
Ni1-S3	2.403(4)
S1-C3	1.809(15)
S1-C6	1.822(14)
S2-C2	1.802(14)
S2-C5	1.818(12)
S3-C4	1.826(14)
S3-C1	1.841(14)
C1-C2	1.501(19)
C3-C4	1.45(2)
C5-C6	1.537(19)
N1-C13	1.143(18)
N2-C15	1.162(18)
C7-C12	1.380(19)
C7-C18	1.41(2)
C7-C13	1.450(19)
C8-C14	1.333(18)
C8-C11	1.443(19)
C9-C10	1.348(17)
C9-C12	1.428(18)
N3-C17	1.145(18)
N4-C18	1.158(19)
C14-C12	1.442(17)
C15-C16	1.442(18)
C16-C11	1.395(17)
C16-C17	1.46(2)
C11-C10	1.424(16)

Table 4.5. Bond angle of $[Ni(9S3)_2](TCNQ)_2$ (deg).

S2-Ni1-S1	90.68(14)
S2-Ni1-S1	89.32(14)
S1-Ni1-S1	180.0
S1-Ni1-S3	90.73(16)
S1-Ni1-S3	89.27(16)
S2-Ni1-S3	91.47(13)
S2-Ni1-S3	88.53(13)
S3-Ni1-S3	180.0
C3-S1-C6	103.3(7)
C3-S1-Ni1	102.0(4)
C6-S1-Ni1	99.1(5)
C2-S2-C5	101.3(6)
C2-S2-Ni1	100.5(5)
C5-S2-Ni1	102.9(4)
C4-S3-C1	103.5(7)
C4-S3-Ni1	96.4(5)
C1-S3-Ni1	102.7(4)
C2-C1-S3	113.2(9)
C1-C2-S2	116.3(8)
C4-C3-S1	113.0(10)
C3-C4-S3	118.0(10)
C6-C5-S2	113.2(9)
C5-C6-S1	114.7(9)
C12-C7-C18	121.3(12)
C12-C7-C13	121.6(13)
C18-C7-C13	117.1(12)
C14-C8-C11	122.3(12)
C10-C9-C12	122.6(12)
C8-C14-C12	121.1(12)
N2-C15-C16	178.2(14)
C11-C16-C15	121.4(12)
C11-C16-C17	124.2(12)
C15-C16-C17	114.2(11)
N3-C17-C16	179.3(16)
N4-C18-C7	178.0(15)
N1-C13-C7	176.4(15)
C7-C12-C9	123.1(12)
C7-C12-C14	120.5(12)
C9-C12-C14	116.3(11)
C16-C11-C10	120.5(11)
C16-C11-C8	123.0(11)
C10-C11-C8	116.5(11)
C9-C10-C11	121.0(12)

Table 4.6. Atom positions of $[Ni(9S3)_2](TCNQ)_3$.

atom	x	y	z	B_{eq} (Å^3)
Ni1	0.0000	0.0000	0.0000	0.02889(15)
S1	0.08929(7)	0.11688(5)	0.20668(9)	0.03573(18)
S2	0.13515(7)	0.06214(6)	-0.20158(9)	0.03799(19)
S3	0.17060(7)	-0.09673(5)	0.09115(10)	0.03699(18)
C1	0.2668(3)	-0.0229(2)	0.2551(4)	0.0438(7)
H1A	0.3094	-0.0609	0.3402	0.053
H1B	0.3331	0.0107	0.2010	0.053
C2	0.1863(3)	0.0451(2)	0.3461(4)	0.0409(7)
H2A	0.2437	0.0850	0.4261	0.049
H2B	0.1294	0.0110	0.4142	0.049
C3	0.1736(3)	0.1759(2)	-0.0985(4)	0.0433(7)
H3A	0.2453	0.2036	-0.1516	0.052
H3B	0.1000	0.2136	-0.1219	0.052
C4	0.2636(3)	-0.0908(3)	-0.0946(4)	0.0468(8)
H4A	0.3469	-0.1161	-0.0647	0.056
H4B	0.2196	-0.1298	-0.1892	0.056
C5	0.2856(3)	0.0040(3)	-0.1582(5)	0.0492(8)
H5A	0.3286	-0.0010	-0.2635	0.059
H5B	0.3419	0.0408	-0.0717	0.059
C6	0.2086(3)	0.1789(2)	0.0955(4)	0.0420(7)
H6A	0.2165	0.2426	0.1404	0.050
H6B	0.2917	0.1521	0.1193	0.050
C7	0.0241(3)	-0.5071(2)	0.3264(4)	0.0321(6)
H7	0.0407	-0.5115	0.2107	0.039
C8	0.0160(3)	-0.4161(2)	0.5984(4)	0.0323(6)
H8	0.0271	-0.3602	0.6633	0.039
C9	0.0414(2)	-0.4200(2)	0.4200(4)	0.0302(5)
C10	0.0842(3)	-0.3408(2)	0.3415(4)	0.0322(6)
C11	0.1062(3)	-0.3431(2)	0.1630(4)	0.0402(7)
C12	0.1045(3)	-0.2518(2)	0.4290(4)	0.0356(6)
C13	0.3340(3)	-0.4980(2)	0.4248(4)	0.0361(6)
H13	0.3213	-0.5515	0.3532	0.043
C14	0.3738(3)	-0.4183(2)	0.3583(4)	0.0383(6)
H14	0.3869	-0.4182	0.2414	0.046

Table 4.7. Atom positions of $[Ni(9S3)_2](TCNQ)_3$.

atom	x	y	z	B_{eq} (Å^3)
C15	0.3960(3)	-0.3345(2)	0.4647(4)	0.0382(6)
C16	0.3114(3)	-0.5007(2)	0.6023(4)	0.0344(6)
C17	0.4699(3)	-0.1727(3)	0.5161(6)	0.0496(9)
C18	0.4419(3)	-0.2518(2)	0.4015(5)	0.0440(7)
C19	0.4694(3)	-0.2421(3)	0.2282(5)	0.0528(9)
C20	0.3720(3)	-0.3384(2)	0.6412(4)	0.0435(7)
H20	0.3852	-0.2850	0.7133	0.052
C21	0.2724(3)	-0.5824(2)	0.6741(4)	0.0361(6)
C22	0.2549(3)	-0.6674(2)	0.5762(4)	0.0374(6)
C23	0.3309(3)	-0.4164(2)	0.7077(4)	0.0416(7)
H23	0.3149	-0.4158	0.8236	0.050
C24	0.2517(4)	-0.5853(2)	0.8526(5)	0.0462(8)
N1	0.1242(3)	-0.1792(2)	0.4927(4)	0.0512(7)
N2	0.1231(4)	-0.3427(3)	0.0198(4)	0.0657(10)
N3	0.4915(3)	-0.1092(3)	0.6095(6)	0.0672(10)
N4	0.4941(4)	-0.2321(3)	0.0897(5)	0.0738(11)
N5	0.2428(3)	-0.7377(2)	0.5005(4)	0.0550(8)
N6	0.2354(5)	-0.5879(3)	0.9959(5)	0.0722(11)

Table 4.8. Anisotropic thermal factors of $[Ni(9S3)_2](TCNQ)_3$.

atom	U_{11}	U_{22}	U_{33}	U_{23}	U_{13}	U_{12}
Ni1	0.0255(2)	0.0355(3)	0.0254(2)	0.00132(18)	0.00261(17)	-0.00158(19)
S1	0.0345(4)	0.0396(4)	0.0322(4)	-0.0032(3)	0.0036(3)	-0.0029(3)
S2	0.0355(4)	0.0495(5)	0.0302(3)	0.0067(3)	0.0076(3)	0.0001(3)
S3	0.0362(4)	0.0365(4)	0.0374(4)	0.0026(3)	-0.0011(3)	0.0017(3)
C1	0.0368(16)	0.0506(19)	0.0412(16)	0.0058(14)	-0.0100(13)	-0.0021(13)
C2	0.0451(17)	0.0504(19)	0.0253(13)	0.0019(12)	-0.0022(12)	-0.0075(14)
C3	0.0422(17)	0.0395(17)	0.0495(18)	0.0160(14)	0.0062(14)	-0.0038(13)
C4	0.0406(17)	0.057(2)	0.0433(17)	-0.0056(15)	0.0069(13)	0.0152(15)
C5	0.0346(16)	0.069(2)	0.0475(18)	0.0064(16)	0.0170(14)	0.0074(15)
C6	0.0407(16)	0.0345(16)	0.0494(17)	0.0028(13)	0.0027(13)	-0.0111(12)
C7	0.0306(13)	0.0353(14)	0.0305(13)	-0.0005(11)	0.0056(10)	-0.0002(11)
C8	0.0286(13)	0.0348(15)	0.0332(14)	-0.0026(11)	0.0046(10)	0.0005(11)
C9	0.0222(12)	0.0343(14)	0.0343(14)	0.0027(11)	0.0035(10)	0.0018(10)
C10	0.0286(13)	0.0336(14)	0.0351(14)	0.0043(11)	0.0056(10)	0.0015(10)
C11	0.0449(17)	0.0345(16)	0.0423(17)	0.0037(12)	0.0091(13)	0.0006(13)
C12	0.0336(14)	0.0363(16)	0.0380(15)	0.0077(12)	0.0065(11)	-0.0006(11)
C13	0.0310(14)	0.0396(16)	0.0377(15)	-0.0037(12)	0.0044(11)	0.0043(11)
C14	0.0299(14)	0.0462(18)	0.0394(15)	0.0031(13)	0.0057(12)	0.0035(12)
C15	0.0246(13)	0.0430(17)	0.0477(17)	0.0058(13)	0.0050(12)	0.0011(11)
C16	0.0292(13)	0.0353(15)	0.0385(15)	-0.0002(11)	0.0037(11)	0.0021(11)
C17	0.0266(14)	0.0433(19)	0.080(3)	0.0149(18)	0.0042(15)	-0.0014(13)
C18	0.0258(14)	0.0471(19)	0.060(2)	0.0123(15)	0.0054(13)	-0.0001(12)
C19	0.0303(16)	0.061(2)	0.070(2)	0.0224(19)	0.0086(15)	0.0020(14)
C20	0.0466(18)	0.0363(16)	0.0472(18)	-0.0035(13)	0.0076(14)	-0.0020(13)
C21	0.0355(15)	0.0346(15)	0.0384(15)	0.0003(11)	0.0048(12)	0.0029(11)
C22	0.0330(15)	0.0374(16)	0.0419(16)	0.0041(12)	0.0023(12)	0.0029(12)
C23	0.0488(18)	0.0364(16)	0.0398(16)	-0.0032(12)	0.0094(13)	-0.0009(13)
C24	0.062(2)	0.0330(16)	0.0447(18)	0.0041(13)	0.0102(15)	0.0015(14)
N1	0.0640(19)	0.0400(16)	0.0503(16)	0.0011(13)	0.0133(14)	-0.0057(13)
N2	0.096(3)	0.060(2)	0.0435(17)	0.0027(15)	0.0215(17)	-0.0049(19)
N3	0.0410(17)	0.053(2)	0.106(3)	-0.005(2)	0.0071(18)	-0.0060(15)
N4	0.057(2)	0.096(3)	0.074(2)	0.031(2)	0.0155(18)	0.005(2)
N5	0.0594(19)	0.0413(17)	0.0620(19)	-0.0042(14)	-0.0031(15)	0.0032(14)
N6	0.116(3)	0.054(2)	0.0503(19)	0.0063(15)	0.023(2)	0.004(2)

Table 4.9. Bond length of $[Ni(9S3)_2](TCNQ)_3$ (Å).

Ni1-S1	2.3705(11)
Ni1-S3	2.3894(10)
Ni1-S2	2.3896(10)
S1-C2	1.811(3)
S1-C6	1.815(3)
S2-C3	1.811(4)
S2-C5	1.823(4)
S3-C4	1.816(3)
S3-C1	1.816(3)
C1-C2	1.512(5)
C3-C6	1.513(5)
C4-C5	1.503(5)
C7-C9	1.422(4)
C8-C7	1.355(4)
C8-C9	1.433(4)
C9-C10	1.408(4)
C10-C11	1.424(4)
C10-C12	1.427(4)
C11-N2	1.142(4)
C12-N1	1.143(4)
C13-C14	1.357(4)
C13-C16	1.422(4)
C14-C15	1.434(5)
C15-C18	1.404(4)
C15-C20	1.420(5)
C16-C21	1.400(4)
C16-C23	1.433(4)
C17-N3	1.144(5)
C17-C18	1.419(6)
C18-C19	1.414(5)
C19-N4	1.145(5)
C20-C23	1.341(5)
C21-C22	1.411(4)
C21-C24	1.425(5)
C22-N5	1.147(4)
C24-N6	1.143(5)

Table 4.10. Bond angle of $[Ni(9S3)_2](TCNQ)_3$ (deg).

S1-Ni1-S1	180.0	C10-C9-C8	121.1(3)
S1-Ni1-S3	90.50(4)	C7-C9-C8	117.6(3)
S1-Ni1-S3	89.50(4)	C9-C10-C11	121.7(3)
S3-Ni1-S3	180.0	C9-C10-C12	123.9(3)
S1-Ni1-S2	91.89(4)	C11-C10-C12	114.4(3)
S1-Ni1-S2	88.11(4)	N2-C11-C10	178.3(4)
S3-Ni1-S2	88.38(4)	N1-C12-C10	176.6(3)
S3-Ni1-S2	91.62(4)	C14-C13-C16	121.0(3)
S2-Ni1-S2	180.0	C13-C14-C15	121.2(3)
C2-S1-C6	103.10(16)	C18-C15-C20	120.4(3)
C2-S1-Ni1	98.23(11)	C18-C15-C14	122.6(3)
C6-S1-Ni1	104.36(11)	C20-C15-C14	116.9(3)
C3-S2-C5	102.60(18)	C21-C16-C13	121.9(3)
C3-S2-Ni1	99.92(11)	C21-C16-C23	120.4(3)
C5-S2-Ni1	103.39(12)	C13-C16-C23	117.7(3)
C4-S3-C1	102.63(17)	N3-C17-C18	179.3(4)
C4-S3-Ni1	99.26(12)	C15-C18-C19	124.1(3)
C1-S3-Ni1	102.28(12)	C15-C18-C17	119.9(3)
C2-C1-S3	112.3(2)	C19-C18-C17	115.9(3)
C1-C2-S1	115.8(2)	N4-C19-C18	177.9(5)
C6-C3-S2	115.4(2)	C23-C20-C15	122.3(3)
C5-C4-S3	115.6(2)	C16-C21-C22	122.4(3)
C4-C5-S2	112.2(2)	C16-C21-C24	121.8(3)
C3-C6-S1	112.3(2)	C22-C21-C24	115.8(3)
C8-C7-C9	121.6(3)	N5-C22-C21	178.0(4)
C7-C8-C9	120.8(3)	C20-C23-C16	120.8(3)
C10-C9-C7	121.3(3)	N6-C24-C21	179.7(4)

4.2.2 $[M(9S3)Br_2]$ (M = Cu, $Cu_{1-x}Ni_x$)

Fig. 4.3 shows the crystal structure of $[Cu(9S3)Br_2]$, and crystallographic data are summarized in Tables 4.11-4.15. The crystal consists of a five-coordinated complex of Cu, which is the same as that of $[Pt(9S3)X_2]$ (X = Cl, Br, I) crystals [20]. The geometry of the molecule is described as an elongated square pyramid (Fig. 4.3a), where there are two short Cu-S contacts, 2.288(15) and 2.321(14) Å for S1 and S3, respectively, and one long Cu-S contact, 2.614(13) Å for S2. The distances of Cu-Br are 2.406(9) and 2.447(9) Å for Br1 and Br2, respectively. In the crystal, short inter-molecular S2-S3 contacts (r_1 = 3.543(4) Å) connect $[Cu(9S3)Br_2]$ molecules one-dimensionally along the a-axis, while the chains are coupled by very weak inter-chain S1-S3 contacts (r_2 = 4.053(4) Å) along the b-axis. These intra- and inter-molecular S-S distances are ca. 4 % shorter and 10 % longer than the sum of van der Waals radii, respectively.

When I substitute a small amount (∼5 %) of copper (II) with nickel (II), the crystal structure of $[M(9S3)Br_2]$ is changed drastically, as exhibited in Fig. 4.4 and Tables 4.11, 4.16-4.19. In the crystal, intra-molecular Cu-S distances, 2.346(2), 2.601(3) and 2.335(3) Å for S1, S2 and S3, respectively, and Cu-Br distances 2.4193(19) and 2.4241(17) Å for Br1 and Br2, respectively, are not so differ from those of $[Cu(9S3)Br_2]$. In addition, intra-chain structures are also nearly the same between these two materials, where the intra-chain S2-S3 contact (r_1 = 3.495(4) Å) becomes shorter by only 1.4 % by nickel (II) substitution. On the contrary to unchanged intra-molecule and intra-chain structure, the inter-chain coupling is more influenced by the substitution, where the arrangement of the chains changes with a 7.1 % reduction of the inter-chain S1-S3 distance (r_2 = 3.797(4) Å) to that of the latter. Therefore, it is expected that the substitution of nickel (II) ions enhances the inter-chain exchange magnetic interactions, as will be verified by the results of the magnetic susceptibilities.

The cause of the structural difference is not clearly understood. However, the slow crystal growth of $[Cu(9S3)Br_2]$ (ca. 5 weeks) suggests that the arrangement of $[Cu(9S3)Br_2]$ molecules is not well stabilized in $[Cu(9S3)Br_2]$, while the crystal growth of $[Cu_{1-x}Ni_x(9S3)Br_2]$ is significantly fast (1day to 1 week). The addition of a small amount of $[Ni(9S3)2Br_2]$, which has different intra-molecular metal-

sulfur distances, results in an easy change in the molecular arrangement. This is supported by the fact that the [Ni(9S3)Br_2] concentration in [$Cu_{1-x}Ni_x$(9S3)Br_2] is independent of the initial concentration of $NiBr_2$ in the crystal growth. That is, a certain amount of [Ni(9S3)Br2] is suitable for the conversion of the crystal structures.

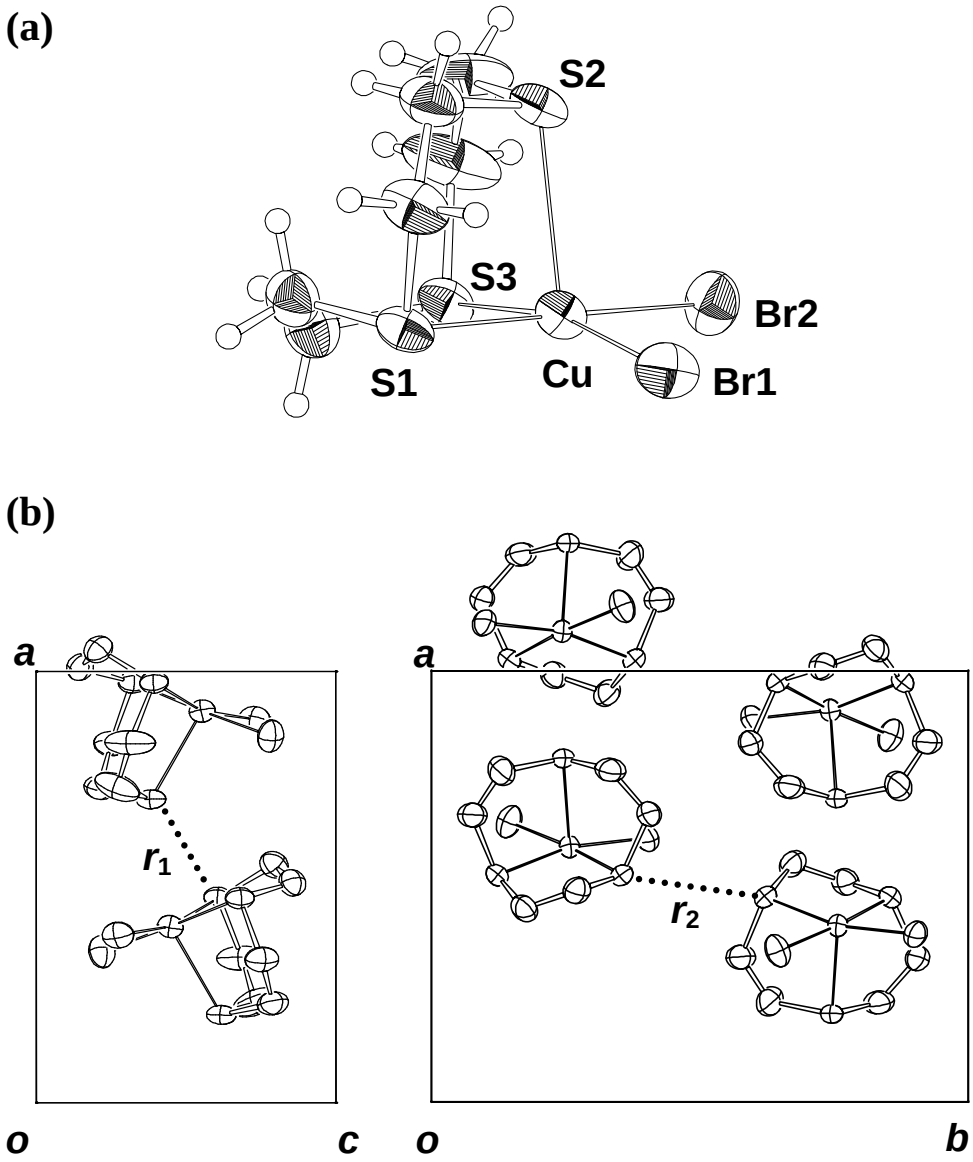

Fig. 4.3. (a) Thermal ellipsoid plot (50 % probability) and (b) the crystal structure of $[Cu(9S3)Br_2]$. The dotted lines $r_1 = 3.543(4)$ Å and $r_2 = 4.053(4)$ Å represent intra- and inter-molecular S2-S3 and S1-S3 contacts between $[Ni(9S3)_2]^{2+}$ cations, respectively.

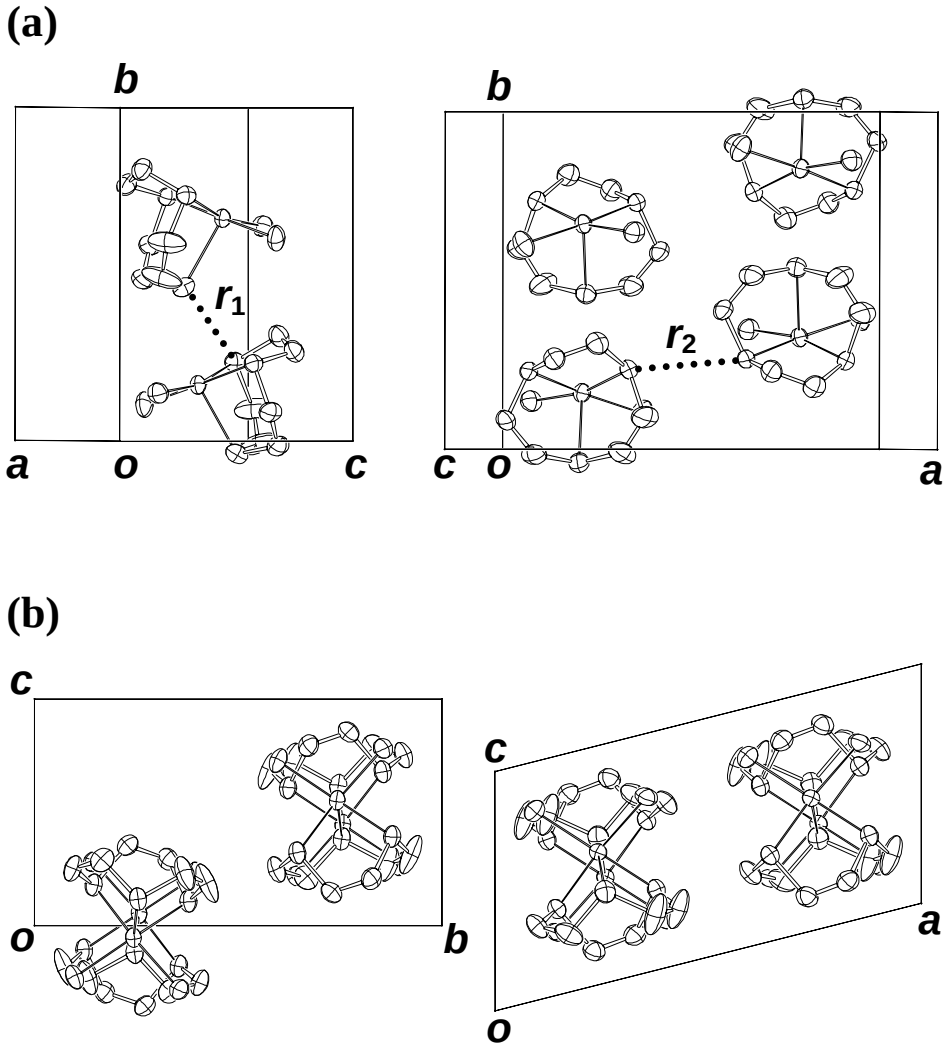

Fig. 4.4. (a) The crystal structure of $[Cu_{1-x}Ni_x(9S3)Br_2]$ (x $\sim$ 0.05). A unit cell contains two chains of $[Cu_{1-x}Ni_x(9S3)Br_2]$ molecules connected by intra-chain short S2-S3 contact r_1 = 3.495(4) Å, while the chains are loosely coupled by inter-chain short S1-S3 contact r_2 = 3.797(4) Å. The labels of atoms are the same as those shown in Fig. 4.3. (b) The projections viewed along the 1D chains of $[Cu(9S3)Br_2]$ (left) and $[Cu_{1-x}Ni_x(9S3)Br_2]$ (right).

Table 4.11. Crystallographic data of [M(9S3)Br_2] (M = Cu, $Cu_{1-x}Ni_x$ (x$\sim$0.05)).

	[Cu(9S3)Br_2]	[$Cu_{1-x}Ni_x$(9S3)Br_2] (x$\sim$0.05)
space group	$P2_12_12_1$	$P2_1/a$
a,Å	11.016(5)	14.000(9)
b,Å	13.702(16)	10.919(6)
c,Å	7.633(3)	7.6261(19)
α,deg	90	90
β,deg	90	104.18(4)
γ,deg	90	90
V,Å^3	1152.1(15)	1130.3(10)
Z	4	4
reflections collected ($2\Theta < 55^o$)	2088	2106
reflections unique	1522	1660
R_1 for all data	0.0417	0.0557
wR_2 for all data	0.1008	0.1406

Table 4.12. Atom positions of[Cu(9S3)Br_2].

atom	x	y	z	B_{eq} (Å^3)
Cu1	0.59163(10)	0.25684(8)	0.05313(16)	0.0363(3)
Br1	0.61121(10)	0.40174(7)	0.22723(17)	0.0512(3)
Br2	0.64977(11)	0.14466(8)	0.28143(16)	0.0546(3)
S1	0.5256(2)	0.35462(18)	-0.1789(4)	0.0409(6)
S2	0.79643(18)	0.24562(18)	-0.1174(4)	0.0398(5)
S3	0.5251(2)	0.12221(18)	-0.1070(4)	0.0408(6)
C1	0.6675(9)	0.4055(7)	-0.2521(18)	0.053(3)
H1A	0.6522	0.4425	-0.3582	0.064
H1B	0.6956	0.4512	-0.1639	0.064
C2	0.4484(10)	0.1728(8)	-0.2934(16)	0.051(3)
H2A	0.4567	0.1274	-0.3902	0.061
H2B	0.3626	0.1772	-0.2658	0.061
C3	0.7698(9)	0.3333(9)	-0.2893(18)	0.056(3)
H3A	0.8440	0.3697	-0.3091	0.068
H3B	0.7510	0.2984	-0.3964	0.068
C4	0.6648(11)	0.0763(9)	-0.187(3)	0.092(6)
H4A	0.6917	0.0289	-0.1006	0.111
H4B	0.6447	0.0393	-0.2912	0.111
C5	0.4901(10)	0.2710(8)	-0.3542(15)	0.050(3)
H5A	0.4272	0.2996	-0.4267	0.060
H5B	0.5617	0.2626	-0.4266	0.060
C6	0.7675(11)	0.1304(9)	-0.230(2)	0.081(5)
H6A	0.7636	0.1443	-0.3544	0.098
H6B	0.8376	0.0889	-0.2115	0.098

Table 4.13. Anisotropic thermal factors of [Cu(9S3)Br_2].

atom	U_{11}	U_{22}	U_{33}	U_{23}	U_{13}	U_{12}
Cu1	0.0344(5)	0.0286(5)	0.0460(6)	-0.0019(5)	-0.0024(5)	-0.0004(5)
Br1	0.0468(5)	0.0387(5)	0.0682(7)	-0.0156(5)	0.0012(5)	-0.0070(5)
Br2	0.0717(7)	0.0451(5)	0.0469(5)	0.0031(5)	-0.0047(6)	0.0142(5)
S1	0.0308(11)	0.0349(11)	0.0571(15)	0.0038(12)	0.0002(10)	0.0051(9)
S2	0.0246(9)	0.0346(11)	0.0602(15)	-0.0037(12)	-0.0015(10)	0.0003(10)
S3	0.0324(11)	0.0342(12)	0.0557(14)	-0.0023(11)	-0.0022(11)	-0.0062(9)
C1	0.041(5)	0.040(5)	0.078(9)	0.018(6)	0.002(6)	-0.003(4)
C2	0.048(6)	0.048(6)	0.056(7)	-0.004(5)	-0.007(6)	-0.011(5)
C3	0.037(5)	0.065(7)	0.067(8)	0.009(7)	0.006(6)	-0.004(5)
C4	0.039(6)	0.060(7)	0.177(18)	-0.065(10)	0.003(9)	0.000(5)
C5	0.048(5)	0.052(6)	0.049(6)	0.011(5)	-0.004(5)	0.003(5)
C6	0.059(7)	0.050(7)	0.136(14)	-0.036(9)	0.039(9)	-0.008(6)

Table 4.14. Bond length of [Cu(9S3)Br_2] (Å).

Cu1-S1	2.337(3)
Cu1-S2	2.609(3)
Cu1-S3	2.331(3)
Cu1-Br1	2.399(2)
Cu1-Br2	2.410(2)
S1-C1	1.800(10)
S1-C5	1.805(12)
S2-C3	1.803(12)
S2-C6	1.825(13)
S3-C4	1.771(12)
S3-C2	1.794(12)
C1-C3	1.526(15)
C2-C5	1.495(14)
C4-C6	1.392(17)

Table 4.15. Bond angle of [Cu(9S3)Br_2] (deg).

S3-Cu1-S1	87.62(12)
S3-Cu1-Br1	166.84(8)
S1-Cu1-Br1	88.47(10)
S3-Cu1-Br2	87.59(10)
S1-Cu1-Br2	175.06(9)
Br1-Cu1-Br2	95.94(9)
S3-Cu1-S2	87.92(9)
S1-Cu1-S2	85.70(10)
Br1-Cu1-S2	104.32(7)
Br2-Cu1-S2	95.35(8)
C1-S1-C5	101.8(6)
C1-S1-Cu1	100.8(4)
C5-S1-Cu1	105.4(4)
C3-S2-C6	101.9(7)
C3-S2-Cu1	100.5(3)
C6-S2-Cu1	97.7(4)-
C4-S3-C2	105.9(8)
C4-S3-Cu1	100.9(4)
C2-S3-Cu1	105.0(3)
C3-C1-S1	116.6(7)
C5-C2-S3	116.7(8)
C1-C3-S2	114.7(9)
C6-C4-S3	126.7(9)
C2-C5-S1	114.1(8)
C4-C6-S2	119.4(10)

Table 4.16. Atom positions of $[Cu_{1-x}Ni_x(9S3)Br_2]$ (x∼0.05).

atom	x	y	z	B_{eq} (Å^3)
Cu	0.24126(8)	0.16777(10)	0.44370(14)	0.0359(3)
Br1	0.09249(7)	0.14383(9)	0.20545(13)	0.0458(3)
Br2	0.35477(8)	0.10835(11)	0.26455(13)	0.0530(3)
S1	0.14485(16)	0.2322(2)	0.6385(3)	0.0365(5)
S3	0.37814(16)	0.2367(2)	0.6622(3)	0.0386(5)
S2	0.25831(18)	-0.0390(2)	0.6180(4)	0.0462(6)
C1	0.2320(7)	0.2680(10)	0.8516(14)	0.049(2)
H1A	0.2031	0.3291	0.9152	0.059
H1B	0.2435	0.1948	0.9259	0.059
C2	0.3278(8)	0.3143(10)	0.8290(14)	0.050(2)
H2A	0.3755	0.3089	0.9449	0.060
H2B	0.3202	0.4003	0.7967	0.060
C3	0.0992(8)	0.0866(9)	0.6906(15)	0.049(2)
H3A	0.0631	0.0997	0.7825	0.059
H3B	0.0523	0.0576	0.5830	0.059
C4	0.1730(9)	-0.0153(10)	0.7559(16)	0.059(3)
H4A	0.1374	-0.0909	0.7604	0.071
H4B	0.2099	0.0034	0.8782	0.071
C5	0.4294(9)	0.0958(11)	0.767(2)	0.088(5)
H5A	0.4837	0.0756	0.7136	0.106
H5B	0.4583	0.1149	0.8926	0.106
C6	0.3769(9)	-0.0100(12)	0.766(2)	0.092(5)
H6A	0.3693	-0.0204	0.8877	0.110
H6B	0.4194	-0.0760	0.7453	0.110

Table 4.17. Anisotropic thermal factors of $[Cu_{1-x}Ni_x(9S3)Br_2]$ (x$\sim$0.05).

atom	U_{11}	U_{22}	U_{33}	U_{23}	U_{13}	U_{12}
Cu	0.0351(6)	0.0416(6)	0.0320(5)	-0.0005(5)	0.0101(4)	0.0014(4)
Br1	0.0437(5)	0.0463(5)	0.0431(5)	-0.0033(4)	0.0021(4)	-0.0037(4)
Br2	0.0538(6)	0.0718(7)	0.0383(5)	0.0027(5)	0.0210(4)	0.0176(5)
S1	0.0351(11)	0.0350(11)	0.0413(11)	0.0001(9)	0.0133(9)	0.0013(9)
S3	0.0340(11)	0.0386(11)	0.0450(12)	0.0006(10)	0.0126(9)	-0.0040(9)
S2	0.0440(13)	0.0413(13)	0.0538(14)	-0.0100(11)	0.0133(11)	-0.0005(10)
C1	0.051(6)	0.052(6)	0.048(5)	-0.009(5)	0.018(4)	-0.003(5)
C2	0.051(6)	0.052(6)	0.044(5)	-0.010(5)	0.009(4)	-0.007(5)
C3	0.050(5)	0.041(5)	0.065(6)	-0.001(5)	0.031(5)	-0.008(4)
C4	0.080(8)	0.044(6)	0.066(7)	0.007(5)	0.041(6)	0.000(5)
C5	0.049(7)	0.048(6)	0.140(13)	0.020(8)	-0.030(7)	0.007(5)
C6	0.052(7)	0.053(7)	0.145(14)	0.044(8)	-0.024(8)	-0.004(6)

Table 4.18. Bond length of $[Cu_{1-x}Ni_x(9S3)Br_2]$ (x$\sim$0.05) (Å).

Cu-S3	2.335(3)
Cu-S1	2.346(2)
Cu-Br1	2.4193(19)
Cu-Br2	2.4241(17)
Cu-S2	2.601(3)
S1-C3	1.794(9)
S1-C1	1.820(10)
S3-C5	1.799(11)
S3-C2	1.808(10)
S2-C6	1.791(12)
S2-C4	1.793(10)
C1-C2	1.483(14)
C3-C4	1.516(15)
C5-C6	1.369(17)

Table 4.19. Bond angle of $[Cu_{1-x}Ni_x(9S3)Br_2]$ (x∼0.05) (deg).

S3-Cu-S1	87.16(9)
S3-Cu-Br1	167.38(8)
S1-Cu-Br1	89.13(8)
S3-Cu-Br2	87.24(8)
S1-Cu-Br2	174.39(8)
Br1-Cu-Br2	96.34(6)
S3-Cu-S2	87.64(9)
S1-Cu-S2	86.08(8)
Br1-Cu-S2	104.14(7)
Br2-Cu-S2	93.73(7)
C3-S1-C1	100.9(5)
C3-S1-Cu	99.5(3)
C1-S1-Cu	105.4(3)
C5-S3-C2	105.8(7)
C5-S3-Cu	102.0(4)
C2-S3-Cu	105.1(3)
C6-S2-C4	104.7(8)
C6-S2-Cu	97.1(4)
C4-S2-Cu	100.6(4)
C2-C1-S1	113.4(7)
C1-C2-S3	116.2(7)
C4-C3-S1	118.2(8)
C3-C4-S2	114.3(7)
C6-C5-S3	124.4(9)
C5-C6-S2	124.5(9)

4.2.3 $[M(9S3)_2][Ni(bdt)_2]_2$ (M = Ni, Co)

Figs. 4.5 and 4.6 show the crystal structures of $[M(9S3)_2][Ni(bdt)_2]_2$ (M = Ni, Co) which are isostructural to each other regardless of the cations, and the crystallographic data are summarized in Tables 4.20 - 4.30. The unit cell consists of two crystallographically independent $[Ni(bdt)_2]^-$ anion molecules (A) and (B) which form a 2D cage-like structure on the plane spanned by the $a + c$ and $b + c$ directions, where a $[M(9S3)_2]^{2+}$ molecule is placed in the center of the cage, as shown in Fig. 4.5b. In the plane, there is a short S3-S5 contact r_1 between $[M(9S3)_2]^{2+}$ and $[Ni(bdt)_2]^-$ (A) (3.772(2) and 3.806(2) Å for M = Ni and Co, respectively), and a C11H-S6 contact r_2 between $[Ni(bdt)_2]^-$ (A) and $[Ni(bdt)_2]^-$ (B) molecules (3.754(5) and 3.705(7) Å for M = Ni and Co, respectively). The 2D planes of the cage-like structure are stacked along the c-axis with the cage-like structure units shifted from each other by a half of the unit, as shown in Fig. 4.6; that is, a $[Ni(bdt)_2]^-$ (A) molecule of a plane lies on top of a $[M(9S3)_2]^{2+}$ molecule of the plane beneath (Fig. 4.6a), while a $[Ni(bdt)_2]^-$ (B) molecule of the upper plane lies on a $[Ni(bdt)_2]^-$ (B) of the lower plane with its center shifted parallel to the plane (Fig. 4.6b). Therefore, there are two kinds of inter-plane contacts generated. One is the contact between $[Ni(bdt)_2]^-$ (B) molecules with a short S7-S7 contact, r_3 = 3.785(2) and 3.778(2) Å for M = Ni and Co, respectively, and the other is the C10H-S2 contact between $[Ni(bdt)_2]^-$ (A) and $[M(9S3)_2]^{2+}$ with r_4 = 3.920(6) and 3.937(6) Å for M = Ni and Co, respectively. Such structural features are the same in both the nickel (II) and cobalt(II) salts, in spite of a difference in the coordination environments of $[M(9S3)_2]^{2+}$. In $[Ni(9S3)_2]^{2+}$, three crystallographically independent Ni-S coordination bonds have almost the same length, 2.3967(11), 2.3849(10) and 2.3836(11) Å for S1, S2 and S3, respectively, whereas $[Co(9S3)_2]^{2+}$ has Jahn-Teller distortions in the Co-S distances; 2.4329(13), 2.285(1) and 2.2521(14) Å for S1, S2 and S3, respectively. The sulfur atoms of the latter two Co-S bonds, S2 and S3, are connected to the adjacent $[Ni(bdt)_2]^-$ through S3-S5 (r_1) and C10H-S2 (r_4) contacts, while that of the former one, S1, does not participate in the inter-molecular contact.

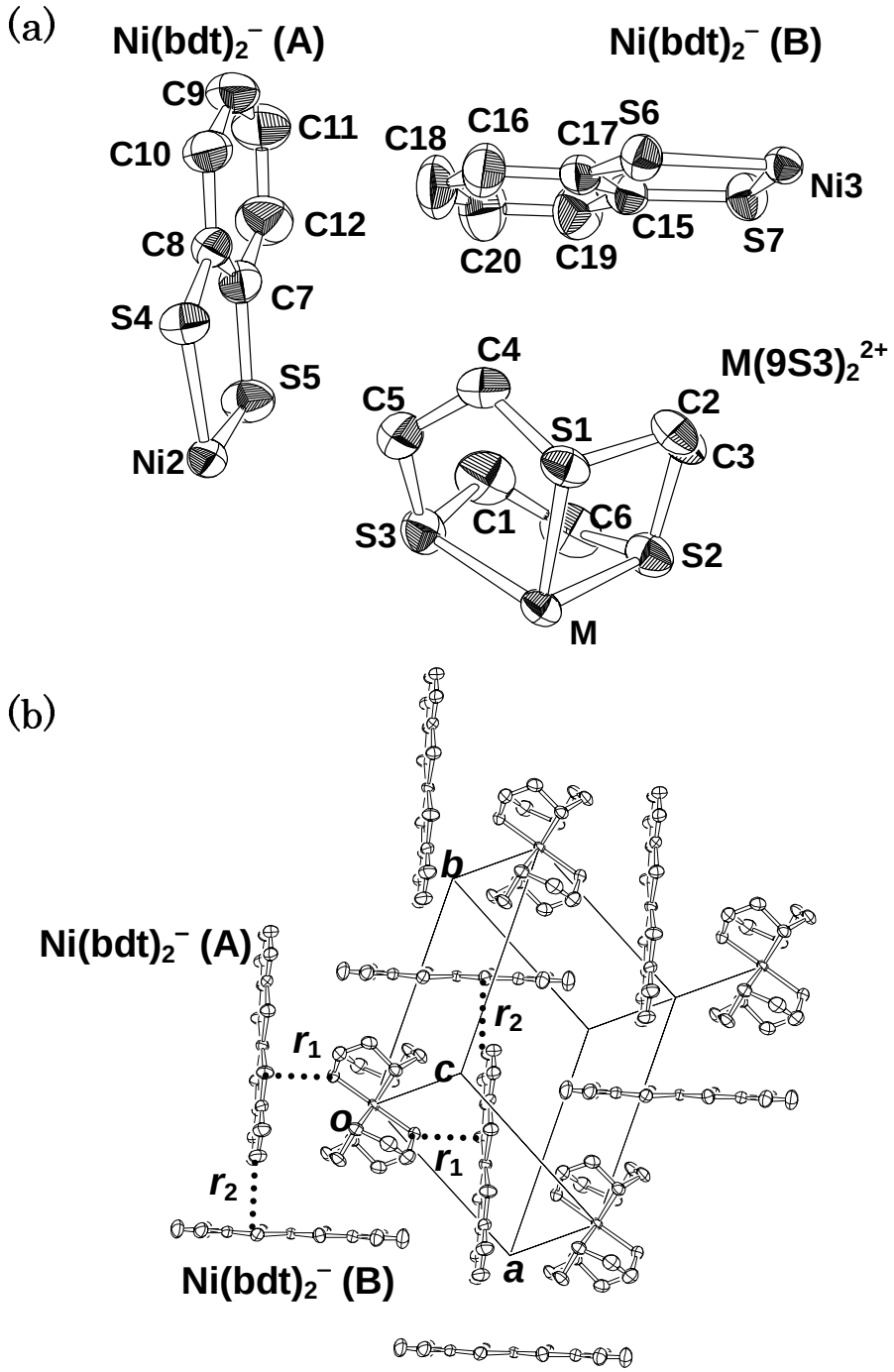

Fig. 4.5. (a) Thermal ellipsoid plot (50 % probability) and (b) the crystal structure of $[M(9S3)_2][Ni(bdt)_2]_2$ (M = Ni, Co), where four formula units on a plane are shown. Dotted line r_1 represents the short S3-S5 contact between $[M(9S3)_2]^{2+}$ and $[Ni(bdt)_2]^-$ (A) molecules, while r_2 represents the C11H-S6 contact between $[Ni(bdt)_2]^-$ (A) and $[Ni(bdt)_2]^-$ (B) anions; $r_1 = 3.772(2)$ and $r_2 = 3.754(5)$ Å for M = Ni and $r_1 = 3.806(2)$ and $r_2 = 3.705(7)$ Å for M = Co.

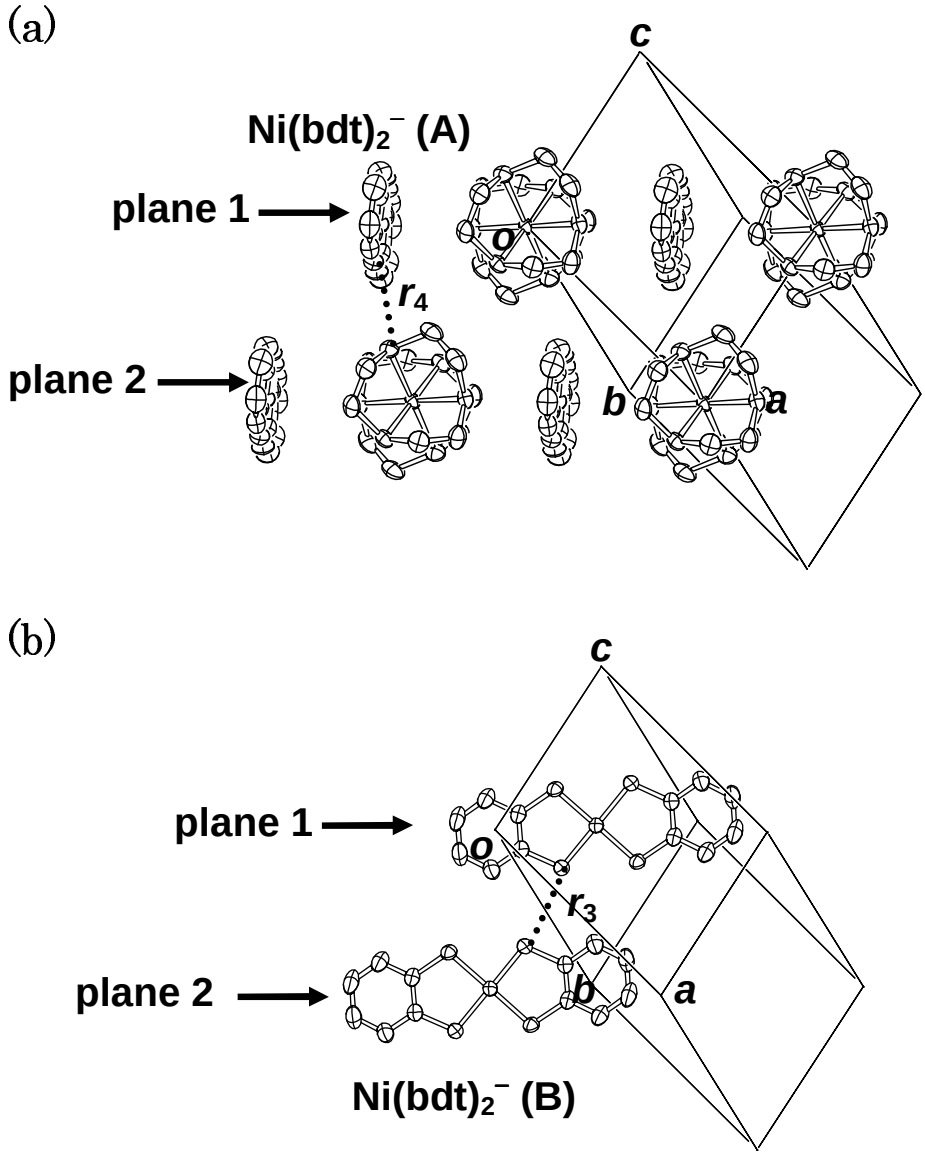

Fig. 4.6. The stacking of the planes along the c-axis direction in $[M(9S3)_2][Ni(bdt)_2]_2$ (M = Ni, Co). (a) $[M(9S3)_2]^{2+}$ and $[Ni(bdt)_2]^-$ (A) molecules and (b) $[Ni(bdt)_2]^-$ (B) molecules are shown. Dotted line r_3 represents the short S7-S7 contacts between $[Ni(bdt)_2]^-$ (B) anions, while r_4 represents the C10H-S2 contacts between $[M(9S3)_2]^{2+}$ and $[Ni(bdt)_2]^-$ (A); $r_3 = 3.78$ and $r_4 = 3.98$ Å for M = Ni, $r_3 = 3.77$ and $r_4 = 3.93$ Å for M = Co.

Table 4.20. Crystallographic data of $[M(9S3)_2][Ni(bdt)_2]_2$ (M = Ni, Co).

	$[Ni(9S3)_2][Ni(bdt)_2]_2$	$[Co(9S3)_2][Ni(bdt)_2]_2$
space group	$P\bar{1}$	$P\bar{1}$
a,Å	11.6629(19)	11.711(3)
b,Å	12.9372(11)	12.8406(16)
c,Å	7.778(2)	7.7989(13)
α,deg	93.859(13)	92.682(12)
β,deg	106.154(17)	107.022(17)
γ,deg	95.185(10)	95.400(15)
V,Å^3	1117.4(4)	1113.0(4)
Z	1	1
reflections collected ($2\Theta < 55^o$)	5167	4149
reflections unique	4018	3141
R_1 for all data	0.0518	0.0426
wR_2 for all data	0.1156	0.0962

Table 4.21. Atom positions of[Ni(9S3)$_2$][Ni(bdt)$_2$]$_2$.

atom	x	y	z	B_{eq} (Å^3)
Ni1	0.0000	0.0000	0.0000	0.03178(16)
S1	-0.04969(10)	0.08652(8)	0.24755(13)	0.0438(2)
S2	0.07521(10)	0.16632(7)	-0.06363(15)	0.0460(2)
S3	-0.19335(10)	0.02609(8)	-0.18616(14)	0.0465(3)
C1	-0.1691(5)	0.1549(4)	-0.2594(7)	0.0628(14)
H1A	-0.2241	0.1579	-0.3778	0.075
H1B	-0.1870	0.2067	-0.1774	0.075
C2	0.0460(5)	0.2090(4)	0.2744(6)	0.0542(11)
H2A	0.0214	0.2586	0.3524	0.065
H2B	0.1279	0.1974	0.3350	0.065
C3	0.0455(5)	0.2572(3)	0.1038(7)	0.0554(12)
H3A	0.1060	0.3172	0.1314	0.066
H3B	-0.0320	0.2815	0.0539	0.066
C4	-0.1992(4)	0.1217(4)	0.1465(7)	0.0567(12)
H4A	-0.2435	0.1208	0.2352	0.068
H4B	-0.1924	0.1924	0.1127	0.068
C5	-0.2693(4)	0.0498(4)	-0.0175(7)	0.0592(12)
H5A	-0.3430	0.0790	-0.0730	0.071
H5B	-0.2917	-0.0166	0.0219	0.071
C6	-0.0424(5)	0.1812(4)	-0.2668(6)	0.0612(13)
H6A	-0.0332	0.2529	-0.2947	0.073
H6B	-0.0305	0.1372	-0.3650	0.073

Table 4.22. Atom positions of[Ni(9S3)$_2$][Ni(bdt)$_2$]$_2$.

atom	x	y	z	B_{eq} (Å^3)
Ni2	-0.5000	0.0000	0.5000	0.03666(17)
S4	-0.60220(10)	0.06340(8)	0.66493(15)	0.0468(2)
S5	-0.50667(11)	0.13525(8)	0.35477(17)	0.0510(3)
C7	-0.5883(4)	0.2169(3)	0.4505(6)	0.0450(9)
C8	-0.6311(3)	0.1847(3)	0.5895(6)	0.0425(9)
C9	-0.7116(5)	0.3479(4)	0.6122(8)	0.0650(15)
H9	-0.7526	0.3921	0.6668	0.078
C10	-0.6940(4)	0.2512(4)	0.6705(7)	0.0538(11)
H10	-0.7235	0.2298	0.7634	0.065
C11	-0.6692(5)	0.3803(4)	0.4734(9)	0.0705(16)
H11	-0.6815	0.4462	0.4361	0.085
C12	-0.6091(5)	0.3162(4)	0.3895(8)	0.0643(13)
H12	-0.5825	0.3378	0.2941	0.077
Ni3	0.0000	-0.5000	0.5000	0.03298(16)
S6	-0.16098(9)	-0.60533(7)	0.45904(14)	0.0416(2)
S7	-0.04074(9)	-0.47965(8)	0.21815(13)	0.0426(2)
C15	-0.1783(4)	-0.5541(3)	0.1207(5)	0.0405(8)
C16	-0.3458(4)	-0.6671(4)	0.1552(7)	0.0578(12)
H16	-0.3835	-0.7028	0.2280	0.069
C17	-0.2336(3)	-0.6086(3)	0.2298(6)	0.0408(9)
C18	-0.3998(5)	-0.6710(4)	-0.0277(9)	0.0731(16)
H18	-0.4745	-0.7096	-0.0777	0.088
C19	-0.2351(5)	-0.5592(4)	-0.0658(7)	0.0605(12)
H19	-0.1989	-0.5230	-0.1399	0.073
C20	-0.3449(5)	-0.6186(5)	-0.1373(8)	0.0739(16)
H20	-0.3820	-0.6233	-0.2604	0.089

Table 4.23. Anisotropic thermal factors of $[Ni(9S3)_2][Ni(bdt)_2]_2$.

atom	U_{11}	U_{22}	U_{33}	U_{23}	U_{13}	U_{12}
Ni1	0.0402(4)	0.0272(3)	0.0262(3)	0.0017(2)	0.0061(3)	0.0063(2)
S1	0.0572(6)	0.0420(5)	0.0321(5)	-0.0013(4)	0.0123(4)	0.0097(4)
S2	0.0580(6)	0.0327(5)	0.0499(6)	0.0060(4)	0.0194(5)	0.0042(4)
S3	0.0457(6)	0.0458(5)	0.0402(5)	0.0002(4)	-0.0004(4)	0.0087(4)
C1	0.075(3)	0.059(3)	0.050(3)	0.019(2)	0.002(2)	0.026(3)
C2	0.060(3)	0.047(2)	0.049(2)	-0.0181(19)	0.012(2)	0.001(2)
C3	0.073(3)	0.0299(19)	0.060(3)	-0.0051(18)	0.017(2)	-0.0001(19)
C4	0.057(3)	0.055(3)	0.062(3)	-0.005(2)	0.024(2)	0.015(2)
C5	0.042(2)	0.064(3)	0.066(3)	-0.009(2)	0.009(2)	0.009(2)
C6	0.092(4)	0.049(2)	0.045(2)	0.019(2)	0.019(2)	0.015(2)
Ni2	0.0359(3)	0.0321(3)	0.0429(4)	0.0028(3)	0.0129(3)	0.0042(3)
S4	0.0501(6)	0.0474(6)	0.0485(6)	0.0063(4)	0.0206(5)	0.0126(4)
S5	0.0600(7)	0.0403(5)	0.0636(7)	0.0139(5)	0.0316(6)	0.0124(5)
C7	0.039(2)	0.038(2)	0.055(2)	0.0031(17)	0.0089(18)	0.0071(16)
C8	0.0330(18)	0.044(2)	0.046(2)	-0.0041(17)	0.0040(16)	0.0081(15)
C9	0.055(3)	0.057(3)	0.077(4)	-0.012(3)	0.008(3)	0.024(2)
C10	0.045(2)	0.061(3)	0.053(3)	-0.007(2)	0.010(2)	0.017(2)
C11	0.068(3)	0.049(3)	0.094(4)	0.008(3)	0.016(3)	0.026(2)
C12	0.070(3)	0.047(3)	0.080(4)	0.017(2)	0.023(3)	0.019(2)
Ni3	0.0350(3)	0.0274(3)	0.0360(3)	0.0025(2)	0.0089(3)	0.0052(2)
S6	0.0401(5)	0.0366(5)	0.0470(5)	0.0113(4)	0.0097(4)	0.0023(4)
S7	0.0448(5)	0.0440(5)	0.0374(5)	0.0031(4)	0.0111(4)	-0.0017(4)
C15	0.040(2)	0.0376(19)	0.042(2)	0.0003(16)	0.0086(16)	0.0071(15)
C16	0.043(2)	0.050(2)	0.074(3)	0.009(2)	0.006(2)	0.0004(19)
C17	0.0365(19)	0.0311(17)	0.051(2)	0.0008(16)	0.0055(17)	0.0074(14)
C18	0.047(3)	0.067(3)	0.085(4)	0.000(3)	-0.009(3)	-0.008(2)
C19	0.055(3)	0.073(3)	0.047(3)	0.004(2)	0.004(2)	0.005(2)
C20	0.060(3)	0.087(4)	0.056(3)	0.000(3)	-0.009(3)	-0.003(3)

Table 4.24. Bond length of $[Ni(9S3)_2][Ni(bdt)_2]_2$ (Å).

Ni1-S3	2.3836(11)
Ni1-S2	2.3849(10)
Ni1-S1	2.3967(11)
S1-C4	1.816(5)
S1-C2	1.818(5)
S2-C6	1.816(5)
S2-C3	1.821(5)
S3-C5	1.801(5)
S3-C1	1.821(5)
C1-C6	1.504(8)
C2-C3	1.503(7)
C4-C5	1.511(7)
Ni2-S5	2.1413(11)
Ni2-S4	2.1505(11)
S4-C8	1.740(4)
S5-C7	1.745(4)
C7-C8	1.385(7)
C7-C12	1.417(6)
C8-C10	1.405(6)
C9-C10	1.372(7)
C9-C11	1.381(9)
C11-C12	1.375(7)
Ni3-S7	2.1497(12)
Ni3-S6	2.1516(10)
S6-C17	1.744(4)
S7-C15	1.739(4)
C15-C17	1.391(6)
C15-C19	1.411(6)
C16-C18	1.382(8)
C16-C17	1.400(6)
C18-C20	1.378(9)
C19-C20	1.381(8)

Table 4.25. Bond angle of $[Ni(9S3)_2][Ni(bdt)_2]_2$ (deg).

S3-Ni1-S3	180.0	S4-Ni2-S4	180.0
S3-Ni1-S2	91.41(4)	C8-S4-Ni2	104.74(15)
S3-Ni1-S2	88.59(4)	C7-S5-Ni2	104.73(16)
S2-Ni1-S2	180.0	C8-C7-C12	119.9(4)
S3-Ni1-S1	88.17(4)	C8-C7-S5	119.3(3)
S2-Ni1-S1	91.80(4)	C12-C7-S5	120.7(4)
S3-Ni1-S1	88.17(4)	C7-C8-C10	119.7(4)
S3-Ni1-S1	91.83(4)	C7-C8-S4	119.2(3)
S2-Ni1-S1	88.20(4)	C10-C8-S4	121.2(4)
S2-Ni1-S1	91.80(4)	C10-C9-C11	120.7(5)
S1-Ni1-S1	180.0	C9-C10-C8	119.8(5)
C4-S1-C2	103.4(2)	C12-C11-C9	120.8(5)
C4-S1-Ni1	103.50(16)	C11-C12-C7	119.1(5)
C2-S1-Ni1	99.41(16)	S7-Ni3-S7	180.0
C6-S2-C3	103.1(2)	S7-Ni3-S6	92.04(4)
C6-S2-Ni1	98.98(18)	S7-Ni3-S6	87.96(4)
C3-S2-Ni1	103.88(16)	S6-Ni3-S6	180.0
C5-S3-C1	103.0(3)	C17-S6-Ni3	104.40(15)
C5-S3-Ni1	100.17(16)	C15-S7-Ni3	104.88(15)
C1-S3-Ni1	103.50(17)	C17-C15-C19	119.7(4)
C6-C1-S3	112.4(3)	C17-C15-S7	119.0(3)
C3-C2-S1	115.8(3)	C19-C15-S7	121.3(4)
C2-C3-S2	112.5(3)	C18-C16-C17	119.2(5)
C5-C4-S1	113.3(3)	C15-C17-C16	120.1(4)
C4-C5-S3	116.0(4)	C15-C17-S6	119.5(3)
C1-C6-S2	115.9(3)	C16-C17-S6	120.3(4)
S5-Ni2-S5	179.999(2)	C20-C18-C16	121.0(5)
S5-Ni2-S4	87.98(4)	C20-C19-C15	119.3(6)
S5-Ni2-S4	92.02(4)	C18-C20-C19	120.6(5)

Table 4.26. Atom positions of$[Co(9S3)_2][Ni(bdt)_2]_2$.

atom	x	y	z	B_{eq} (Å^3)
Co1	0.0000	0.0000	0.0000	0.0300(2)
S1	-0.05068(12)	0.08778(10)	0.24680(16)	0.0442(3)
S2	0.07546(12)	0.15983(9)	-0.06140(17)	0.0442(3)
S3	-0.18307(12)	0.02369(10)	-0.18091(16)	0.0434(3)
C1	-0.1635(6)	0.1520(4)	-0.2677(7)	0.0616(16)
H1A	-0.2173	0.1511	-0.3889	0.074
H1B	-0.1847	0.2050	-0.1934	0.074
C2	0.0446(5)	0.2105(4)	0.2706(7)	0.0515(13)
H2A	0.0177	0.2617	0.3412	0.062
H2B	0.1260	0.1998	0.3377	0.062
C3	0.0471(5)	0.2557(4)	0.0968(7)	0.0513(13)
H3A	0.1093	0.3147	0.1225	0.062
H3B	-0.0293	0.2817	0.0417	0.062
C4	-0.2001(5)	0.1238(4)	0.1362(7)	0.0531(14)
H4A	-0.2462	0.1232	0.2212	0.064
H4B	-0.1928	0.1945	0.0991	0.064
C5	-0.2666(5)	0.0497(5)	-0.0264(7)	0.0558(14)
H5A	-0.3391	0.0788	-0.0909	0.067
H5B	-0.2910	-0.0164	0.0150	0.067
C6	-0.0375(6)	0.1799(4)	-0.2694(7)	0.0590(15)
H6A	-0.0275	0.2530	-0.2938	0.071
H6B	-0.0239	0.1381	-0.3670	0.071
Ni1	-0.5000	0.0000	0.5000	0.0359(2)
S4	-0.60316(12)	0.05747(10)	0.66372(18)	0.0466(3)
S5	-0.51114(13)	0.13833(10)	0.3566(2)	0.0512(3)
C7	-0.5918(4)	0.2178(4)	0.4532(7)	0.0420(11)
C8	-0.6340(4)	0.1818(4)	0.5907(7)	0.0415(11)
C9	-0.7142(5)	0.3443(5)	0.6180(9)	0.0644(17)
H9	-0.7547	0.3874	0.6733	0.077
C10	-0.6965(5)	0.2454(4)	0.6737(7)	0.0526(14)
H10	-0.7256	0.2211	0.7651	0.063
C11	-0.6730(6)	0.3801(5)	0.4826(9)	0.0685(18)
H11	-0.6856	0.4473	0.4473	0.082
C12	-0.6131(5)	0.3183(4)	0.3975(8)	0.0622(16)
H12	-0.5869	0.3430	0.3037	0.075

Table 4.27. Atom positions of$[Co(9S3)_2][Ni(bdt)_2]_2$.

atom	x	y	z	B_{eq} (Å^3)
Ni2	0.0000	-0.5000	0.5000	0.0309(2)
S6	-0.16147(11)	-0.60483(9)	0.45962(17)	0.0398(3)
S7	-0.03959(11)	-0.48151(10)	0.21667(16)	0.0411(3)
C15	-0.1783(4)	-0.5555(4)	0.1186(6)	0.0405(11)
C16	-0.3478(5)	-0.6660(4)	0.1549(8)	0.0549(14)
H16	-0.3861	-0.7005	0.2285	0.066
C17	-0.2350(4)	-0.6084(3)	0.2293(6)	0.0389(11)
C18	-0.4019(6)	-0.6713(5)	-0.0288(10)	0.0757(19)
H18	-0.4770	-0.7094	-0.0793	0.091
C19	-0.2341(5)	-0.5626(5)	-0.0667(7)	0.0590(15)
H19	-0.1967	-0.5286	-0.1418	0.071
C20	-0.3441(6)	-0.6199(6)	-0.1374(9)	0.0763(19)
H20	-0.3807	-0.6244	-0.2610	0.092

Table 4.28. Anisotropic thermal factors of $[Co(9S3)_2][Ni(bdt)_2]_2$.

atom	U_{11}	U_{22}	U_{33}	U_{23}	U_{13}	U_{12}
Co1	0.0405(5)	0.0232(4)	0.0242(4)	-0.0014(3)	0.0066(4)	0.0049(3)
S1	0.0605(8)	0.0381(7)	0.0333(6)	-0.0023(5)	0.0129(6)	0.0081(6)
S2	0.0586(8)	0.0325(6)	0.0435(7)	0.0002(5)	0.0187(6)	0.0050(6)
S3	0.0471(7)	0.0380(6)	0.0381(7)	-0.0037(5)	0.0016(6)	0.0086(5)
C1	0.084(4)	0.046(3)	0.046(3)	0.013(3)	-0.001(3)	0.021(3)
C2	0.058(3)	0.041(3)	0.048(3)	-0.019(2)	0.010(3)	0.000(2)
C3	0.067(4)	0.032(3)	0.052(3)	-0.008(2)	0.017(3)	0.000(2)
C4	0.058(3)	0.051(3)	0.055(3)	-0.009(3)	0.025(3)	0.012(3)
C5	0.045(3)	0.059(4)	0.062(4)	-0.006(3)	0.014(3)	0.012(3)
C6	0.093(5)	0.045(3)	0.040(3)	0.012(2)	0.017(3)	0.014(3)
Ni1	0.0369(5)	0.0295(4)	0.0427(5)	-0.0016(4)	0.0152(4)	0.0027(3)
S4	0.0501(8)	0.0466(7)	0.0490(7)	0.0016(6)	0.0227(6)	0.0103(6)
S5	0.0615(9)	0.0377(7)	0.0664(9)	0.0110(6)	0.0354(7)	0.0101(6)
C7	0.036(3)	0.035(3)	0.053(3)	-0.002(2)	0.012(2)	0.002(2)
C8	0.030(2)	0.040(3)	0.048(3)	-0.010(2)	0.001(2)	0.005(2)
C9	0.058(4)	0.056(4)	0.075(4)	-0.018(3)	0.012(3)	0.027(3)
C10	0.043(3)	0.060(3)	0.051(3)	-0.015(3)	0.009(3)	0.015(3)
C11	0.073(4)	0.042(3)	0.088(5)	-0.004(3)	0.015(4)	0.022(3)
C12	0.066(4)	0.044(3)	0.080(4)	0.008(3)	0.023(3)	0.019(3)
Ni2	0.0347(4)	0.0247(4)	0.0338(4)	-0.0006(3)	0.0113(4)	0.0041(3)
S6	0.0389(6)	0.0339(6)	0.0461(7)	0.0071(5)	0.0123(6)	0.0017(5)
S7	0.0445(7)	0.0417(7)	0.0363(6)	-0.0006(5)	0.0135(6)	-0.0025(5)
C15	0.042(3)	0.036(3)	0.044(3)	-0.005(2)	0.013(2)	0.007(2)
C16	0.034(3)	0.047(3)	0.073(4)	0.004(3)	0.002(3)	-0.005(2)
C17	0.038(3)	0.029(2)	0.048(3)	-0.002(2)	0.009(2)	0.0102(19)
C18	0.048(4)	0.074(5)	0.085(5)	-0.008(4)	-0.003(4)	-0.009(3)
C19	0.061(4)	0.071(4)	0.039(3)	-0.003(3)	0.007(3)	0.003(3)
C20	0.064(4)	0.094(5)	0.054(4)	-0.008(4)	-0.004(3)	0.001(4)

Table 4.29. Bond length of $[Co(9S3)_2][Ni(bdt)_2]_2$ (Å).

Co1-S3	2.2521(14)
Co1-S2	2.2850(13)
Co1-S1	2.4329(13)
S1-C2	1.812(5)
S1-C4	1.824(5)
S2-C6	1.815(5)
S2-C3	1.823(5)
S3-C5	1.798(5)
S3-C1	1.830(5)
C1-C6	1.490(9)
C2-C3	1.506(7)
C4-C5	1.513(7)
Ni1-S5	2.1369(13)
Ni1-S4	2.1487(13)
S4-C8	1.754(5)
S5-C7	1.740(5)
C7-C8	1.386(7)
C7-C12	1.402(7)
C8-C10	1.401(7)
C9-C11	1.363(9)
C9-C10	1.377(8)
C11-C12	1.374(8)
Ni2-S6	2.1493(13)
Ni2-S7	2.1504(12)
S6-C17	1.746(5)
S7-C15	1.744(5)
C15-C19	1.395(7)
C15-C17	1.398(7)
C16-C18	1.382(8)
C16-C17	1.399(7)
C18-C20	1.385(10)
C19-C20	1.368(9)

Table 4.30. Bond angle of $[Co(9S3)_2][Ni(bdt)_2]_2$ (deg).

S3-Co1-S3	180.0	C8-S4-Ni1	104.61(18)
S3-Co1-S2	90.01(5)	C7-S5-Ni1	105.19(18)
S3-Co1-S2	89.99(5)	C8-C7-C12	119.2(5)
S2-Co1-S2	180.0	C8-C7-S5	119.3(4)
S3-Co1-S1	91.61(5)	C12-C7-S5	121.5(4)
S3-Co1-S1	88.39(5)	C7-C8-C10	120.3(5)
S2-Co1-S1	91.52(5)	C7-C8-S4	118.9(4)
S2-Co1-S1	88.48(5)	C10-C8-S4	120.8(4)
S1-Co1-S1	180.0	C11-C9-C10	120.8(5)
C2-S1-C4	102.9(3)	C9-C10-C8	119.0(6)
C2-S1-Co1	99.04(17)	C9-C11-C12	121.0(6)
C4-S1-Co1	102.37(17)	C11-C12-C7	119.5(6)
C6-S2-C3	102.0(3)	S6-Ni2-S6	180.0
C6-S2-Co1	100.6(2)	S6-Ni2-S7	92.05(5)
C3-S2-Co1	105.99(17)	S6-Ni2-S7	87.95(5)
C5-S3-C1	102.3(3)	S7-Ni2-S7	180.0
C5-S3-Co1	103.58(18)	C17-S6-Ni2	104.67(16)
C1-S3-Co1	105.2(2)	C15-S7-Ni2	104.97(17)
C6-C1-S3	111.7(4)	C19-C15-C17	119.4(5)
C3-C2-S1	115.3(3)	C19-C15-S7	121.8(4)
C2-C3-S2	112.5(3)	C17-C15-S7	118.8(4)
C5-C4-S1	112.1(4)	C18-C16-C17	119.6(6)
C4-C5-S3	115.3(4)	C15-C17-C16	120.1(5)
C1-C6-S2	114.2(4)	C15-C17-S6	119.3(4)
S5-Ni1-S5	180.0	C16-C17-S6	120.6(4)
S5-Ni1-S4	87.97(5)	C16-C18-C20	119.8(6)
S5-Ni1-S4	92.03(5)	C20-C19-C15	119.8(6)
S4-Ni1-S4	180.0	C19-C20-C18	121.4(6)

4.3 Electric resistivity

Materials except $[Ni(9S3)_2](TCNQ)_3$ are insulating ($\rho > 10^6$ Ωcm) at room temperature. TCNQ crystal $[Ni(9S3)_2](TCNQ)_3$ shows semiconductive behavior with a resistivity of $\rho = 950$ Ωcm at room temperature and an activation energy of $E_a = 200$ meV. TCNQ molecules have a mixed valence of $-2/3$ in the crystal, though its small overlap integral between $(TCNQ)_3^{2-}$ trimers causes the high resistivity. Comparing with highly conductive or metallic TCNQ mixed valence salts [14–16], it is suggested that the molecular size of the cation is too large for TCNQ acceptor to be stacked compactly, which is necessary to give a highly conductive column. This experimental finding is didactic from the point of achieving a highly conductive molecule-based magnet consisting of transition metal-crown thioether complexes; that is, the molecular sizes should be well balanced between the crown thioether complex and acceptor.

4.4 Magnetic susceptibilities

4.4.1 $[M(9S3)_2](TCNQ)_n$ (M = Ni, Co; n = 2, 3)

The magnetic susceptibilities, χ, of $[M(9S3)_2](TCNQ)_3$ (M = Ni, Co) are characterized as paramagnetic with Curie constants $C = 0.971$ and 0.380 emu·K mol^{-1} for M = Ni and Co, respectively, and a Weiss temperature of $\Theta \sim 0$ K for both salt. The isolated structural features of $[M(9S3)_2]^{2+}$ cations, which are well separated by $(TCNQ)_3^{2-}$ trimers, are responsible for the absence of magnetic interaction.

The temperature dependence of the susceptibilities for $[M(9S3)_2](TCNQ)_2$ (M = Ni, Co) are shown in Fig. 4.7. The susceptibilities of $[M(9S3)_2](TCNQ)_2$ obey the Curie-Weiss law with antiferromagnetic (AF) Weiss temperatures $\Theta = -3.8$ K and -1.6 K, Curie constants $C = 0.967$ and 0.372 emu·K mol-1 for M= Ni and Co, respectively. The Curie constants correspond to one $S = 1$ spin of $[Ni(9S3)_2]^{2+}$ and one $S = 1/2$ spin of $[Co(9S3)_2]^{2+}$ per a formula unit, suggesting the singlet state of $TCNQ^-$ spins due to strong dimerization, as confirmed by the structural features. The susceptibility of the nickel (II) salt is isotropic in the whole measured temperature range. The susceptibility has a broad hump around 10 K accompanied by a

steep drop on the low temperature side of the hump, though no three dimensional (3D) magnetic ordering is observed in the temperature range. On the other hand, no anomaly in the susceptibility is observed in the cobalt (II) salt indicating the weakness of the interaction between $[Co(9S3)_2]^{2+}$ spins.

The susceptibility of $[Ni(9S3)_2](TCNQ)_2$ is well described by the uniform AF Heisenberg chain model [21] with $S = 1$ given by following equation;

$$\chi = \frac{2N_A g^2 \mu_B^2}{6|J|} \cdot \frac{X^2 + 0.5X + 0.1}{X^3 + 1.885382X^2 + 1.812404X + 1.607565}, \tag{4.1}$$

where

$$X = \frac{k_B T}{2|J|}, \tag{4.2}$$

N_A, g, μ_B and k_B are the Avogadro's number, the g-value assumed as $g = 2$ for Ni^{2+}, the Bohr magneton and the Boltzmann's constant, respectively. The exchange interaction J is defined in the following Hamiltonian:

$$H = -2J \sum_{\langle i,j \rangle} \boldsymbol{S}_i \boldsymbol{S}_j. \tag{4.3}$$

The absence of 3D ordering proves the negligible contribution of inter-chain interactions, which is reasonably understood from the absence of close inter-chain molecular contact in the structural consideration (see Fig. 4.1). The intra-chain magnetic interaction $J = -3.9$ K estimated from the fitting is stronger than that expected based on the long inter-molecular distance distance between $[Ni(9S3)_2]^{2+}$ molecules, the value of which 3.838(6) Å is considerably larger than the corresponding van der Waals distance 3.7 Å.

The susceptibility of $[Co(9S3)_2](TCNQ)_2$ is described by the Bonner-Fisher model of a 1D AF chain [22, 23] with $S = 1/2$,

$$\chi = \frac{2N_A g^2 \mu_B^2}{k_B T} \cdot \frac{0.25 + 0.14995X + 0.30094X^2}{1.0 + 1.9862X + 0.68854X^2 + 6.0626X^3}, \tag{4.4}$$

where

$$X = \frac{|J|}{k_B T} \tag{4.5}$$

and I assume $g = 2$. The intra-chain interaction is estimated to be $J = -1.3$ K, which is considerably smaller than that of the isostructural salt having the

$[Ni(9S3)_2]^{2+}$ cation. The origin of the decrease of the intra-chain interaction is considered to be associated with the Jahn-Teller distortion of $[Co(9S3)_2]^{2+}$, as will be discussed in the results of the magnetic susceptibility of $[M(9S3)_2][Ni(bdt)_2]_2$.

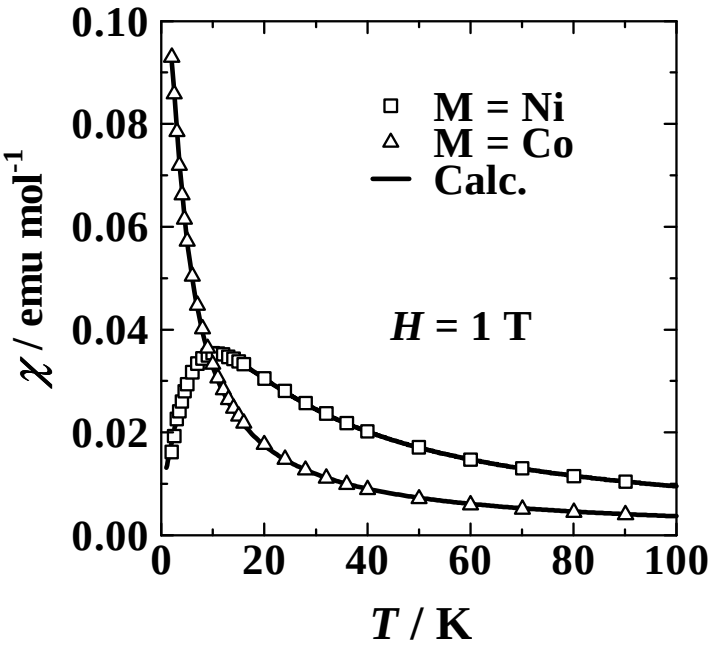

Fig. 4.7. The temperature dependence of isotropic magnetic susceptibilities of $[M(9S3)_2](TCNQ)_2$ (M = Ni, Co) measured in an external magnetic field $H = 1$ T. Solid lines represent the fitting curve calculated by the $S = 1$ 1D AF Heisenberg model and $S = 1/2$ 1D AF Heisenberg model for M = Ni and Co, respectively.

4.4.2 $[M(9S3)Br_2]$ ($M = Cu$, $Cu_{1-x}Ni_x$)

The susceptibilities of $[M(9S3)Br_2]$ ($M = Cu$, $Cu_{1-x}Ni_x$, $x \sim 0.05$) are shown in Fig. 4.8. χ obeys the Curie-Weiss law, where the Curie constants and the AF Weiss temperatures are estimated as $C = 0.381$ emu·K mol^{-1} and $\Theta = -4.2$ K for $M = Cu$ and $C = 0.395$ emu·K mol^{-1} and $\Theta = -3.6$ K for $M = Cu_{1-x}Ni_x$. These values of the Curie constants correspond to one Cu^{2+} $S = 1/2$ spin per formula unit, in addition to a small contribution from Ni^{2+} $S = 1$ in the case of $M = Cu_{1-x}Ni_x$. χ for $M = Cu$ is a isotropic and takes a broad hump around 7 K, while that for $M = Cu_{1-x}Ni_x$ also takes a hump around 6 K and an anisotropic behavior appears in the lower temperature side of the hump. A fitting is made with the Bonner-Fisher model where I assume $g \sim 2$ for both Cu^{2+} and a small amount of Ni^{2+} ions in $[M(9S3)Br_2]$. Intra-chain interaction J is estimated as $J = -5.4$ K and -4.7 K for $M = Cu$ and $Cu_{1-x}Ni_x$, respectively. The nearly equal values of the intra-chain interaction in both salts are considered to be due to the same intra-chain structure of the crystals. The behavior of χ on the low temperature side of the hump is different between the two salts.

In the case of $M = Cu$, χ shows a reduction from that expected with the 1D antiferromagnetic Heisenberg model with weak inter-chain interactions, in addition to the absence of anisotropic behavior. In contrast, for $M = Cu_{1-x}Ni_x$, an anisotropy appears between the field directions parallel to the *b*- and *c*-axes, suggesting an onset of an AF transition at $T_N = 5$ K, where the spin easy axis is oriented parallel to the *b*-axis in the ordered state. The difference is associated with the 2D nature of $M = Cu_{1-x}Ni_x$ salt, which is generated by the modification of the arrangement of the $[M(9S3)Br_2]$ chains by the substitution, as can be seen in the considerable reduction of the S1-S3 contact as shown in section 4.2.2.

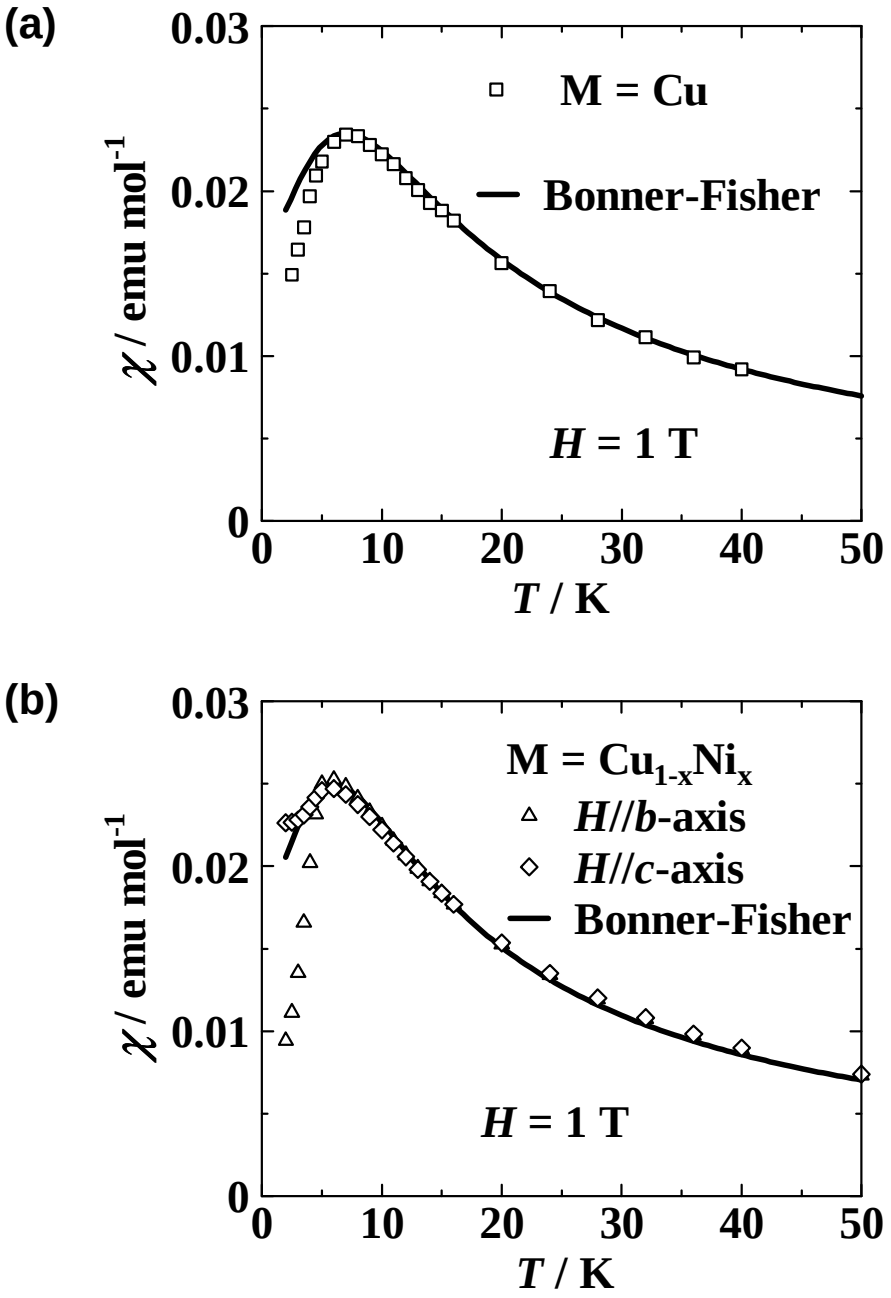

Fig. 4.8. The temperature dependence of the magnetic susceptibility of $[Cu(9S3)Br_2]$ and $[Cu_{1-x}Ni_x(9S3)Br_2]$ ($x \sim 0.05$) measured in an external magnetic field $H = 1$ T. The susceptibility of $[Cu(9S3)Br_2]$ is isotropic in the whole temperature range observed, whereas an anisotropy appears below 5 K in $[Cu_{1-x}Ni_xBr_2]$. The solid lines represent the fitting curves calculated by the $S = 1/2$ 1D AF Heisenberg model.

4.4.3 $[M(9S3)_2][Ni(bdt)_2]_2$ (M = Ni, Co)]

Figure 4.9 shows the temperature dependence of χ of $[Ni(9S3)_2][Ni(bdt)_2]_2$ in the fields applied in the three independent directions defined in Fig. 4.10. χ obeys the Curie-Weiss law at high temperatures above ca. 150 K with negative Weiss temperature $\Theta = -6.5$ K and Curie constant $C = 1.76$ emu·K mol^{-}1, the latter of which corresponds to one $S = 1$ spin of $Ni(9S3)_2^{2+}$ and two $S = 1/2$ spins of $Ni(bdt)_2^{-}$ per formula unit. Below ca. 8 K, anisotropic behavior emerges between the different field directions, where the susceptibility takes sharp peaks at 5.8 and 6.2 K in the x- and z-directions, respectively. In addition, a susceptibility minimum is found at 4.1 K in the z-direction, below which the χ increases as the temperature is lowered. In contrast, only a broad hump is produced at 5.2 K in the y-direction, on the low temperature side of which χ shows a weak decrease. The slight increase of χ below 4.1 K in $H \parallel z$ and non zero value of χ in $H \parallel x$ extrapolated to 0 K is considered to be due to a small misalignment of the crystal and/or the slight deviation of the weak-ferromagnetic axis from the y-direction. The AC susceptibility at 10 Hz shows a sharp peak at 6.2 K. These experimental findings, in addition to the presence of a remanent magnetization which will be discussed in the results of magnetization curves, suggest an onset of a weak-ferromagnetic (WF) transition with a N el temperature $T_N = 6.2$ K, where the x- and y-directions correspond to the spin easy axis and WF axis, respectively.

Fig. 4.11 shows the magnetization curves of $[Ni(9S3)_2][Ni(bdt)_2]_2$ at $T = 2$ K. Below T_N, the magnetization curve of $H \parallel y$ shows a hysteresis loop with a discontinuous change at a coercive force $H_C = 20$ mT and remanent magnetization M_{REM} = 0.18 μ_B, as shown in the inset of Fig. 4.11. The existence of M_{REM} provides evidence of weak-ferromagnetism, though the value is quite large compared to that for ordinary weak-ferromagnets. A spin flop is observed at about $H_{SF} = 1.7$ T in $H \parallel x$, as proved by the S-shaped magnetization curve, which is consistent with the fact that χ steeply approaches zero as the temperature goes to 0 K only in this direction. These suggest that the spin easy axis is oriented in the x-direction. It should be noted that χ increases even for the easy axis in the temperature range $5.8 < T < 6.2$ K ($= T_N$) in a similar fashion as that along the WF axis. This behavior can be understood as the consequence of the XY character of the spin

system. This interpretation is confirmed by the M_{REM} measurement shown in Fig. 4.12a. Judging from the existence of the remanent magnetization in the x and y-directions and its absence in the z-direction, the moment of weak-ferromagnetism is considered to lie on the x-y plane below T_{N}. M_{REM} rapidly increases in $H \parallel x$ in the vicinity of T_{N} as the temperature decreases, followed by the increase in $H \parallel y$. Below that temperature range, the remanent magnetization for $H \parallel x$ decreases after a broad hump around 5.7 K, whereas that for $H \parallel y$ continuously increases and plateaus below ca. 5 K. The overwhelming behavior of the remanent magnetization for $H \parallel y$ below 5.7 K proves a rotation of the moment of the weak-ferromagnetism from the x-direction to the y-direction at ca. 5.7 K. Considering the thin planar crystal shape, as mentioned in the experimental section, the x and y-directions correspond to the thickness and length dimensions of the thin planar crystal, respectively, as shown in Fig. 4.10. The rotation of the WF axis is, therefore, considered to be partly caused by the demagnetization field, which becomes large when the applied field is directed normal to the plane. The demagnetization field H_{dm} is described as

$$H_{\mathrm{dm}} = M \times N, \tag{4.6}$$

where M and N are the value of magnetization and demagnetization factor. N of infinite thin plate takes values $N_{\parallel} = 0$ and $N \perp = 1$ for parallel and perpendicular to the plane, respectively. The demagnetization field is estimated as ca. 0.8 mT calculated based on the remanent magnetization $M_{\mathrm{REM}} = 0.1\ \mu_{\mathrm{B}}$ per a unit cell at 5.7 K in $H \parallel x$, where I assume that the crystal is infinite plate. In contrast, only a negligible demagnetization field is generated when the field is applied along the y-axis because $N = 0$ in this direction. Therefore, the small anisotropy of ca. 1 mT works when the WF direction is rotated between the x and y-axes, as an external perturbation inherited by the crystal shape. This is verified by the change of the rotation, as shown in Fig. 4.12b, when I cut the crystal so as to make the lengths be roughly the same in the x and y-directions. In the cut sample, the rotation temperature changes from 5.7 K to 4.9 K owing to the reduction of the demagnetization field.

The XY character of $[\mathrm{Ni(9S3)_2}][\mathrm{Ni(bdt)_2}]_2$ is also supported by the crystal structure as follows. $[\mathrm{Ni(9S3)_2}]^{2+}$ has the very isotropic octahedral coordination,

which provides isotropic magnetic properties, as confirmed by the isotropic susceptibility of $[Ni(9S3)_2](TCNQ)_2$, to which only $[Ni(9S3)_2]^{2+}$ contributes. On the other hand, the crystal field axes of $[Ni(bdt)_2]^-$ anions (A) and (B) are orthogonal to each other, where molecular planes lie perpendicular to the x and y-directions, respectively. Therefore, the anisotropy of $[Ni(bdt)_2]^-$ molecules does not play a serious role in determining the direction of the weak-ferromagnetic moment in the xy plane. As a result, the WF axis of the thin planar crystal of $[Ni(9S3)_2][Ni(bdt)_2]_2$ is easily rotated to the y-direction by the demagnetization field in the temperature range $4.9 < T < 6.2$ K. However, the WF axis is also rotated below 4.9 K even in the cut sample, where the demagnetization effect is partially present. This fact suggests that there is a small magnetic anisotropy in the xy-plane which governs the WF axis in the low temperature region, though the origin of the anisotropy remains unclear. The anisotropy also causes the enhancement of the spin flop field, the value of which ($H_{SF} = 1.7$ T) is much larger than that expected from the anisotropy caused by the demagnetization field.

The temperature dependence of the susceptibility of $[Co(9S3)_2][Ni(9S3)_2]_2$ is shown in Fig. 4.13. χ obeys the Curie-Weiss law above ca. 100K with Weiss temperature $\Theta = -2.3$ K and Curie constant $C = 1.17$ emu·K mol^{-1}, the latter of which corresponds to one $S = 1/2$ spin of $[Co(9S3)_2]^{2+}$ and two $S = 1/2$ spins of $[Ni(bdt)_2]^-$ per formula unit. Below 4 K, anisotropy emerges between the three field directions, where χ forms a peak at 2.6 K for $H \parallel z$. The AC susceptibility at 10Hz also forms a peak at this temperature, suggesting an onset of an AF (WF) transition at $T_N = 2.6$ K. For the $H \parallel x$ and y-directions, χ increases even below T_N, which is the consequence of the weak-ferromagnetism. The behaviors of the magnetization curves along the three directions at $T = 2$ K shown in Fig. 4.14 are very similar to each other except the hysteresis loop in $H \parallel y$. In $H \parallel y$, the magnetization shows a hysteresis loop with a coercive force $H_C = 1$ mT and remanent magnetization $M_{REM} = 0.015\ \mu_B$, as shown in the inset of Fig. 4.14. These values are about one-twentieth smaller than those of $[Ni(9S3)_2][Ni(9S3)_2]_2$. The WF axis is confirmed to be aligned parallel to the y-direction because a hysteresis loop is observed only when the magnetic field is applied parallel to this direction. However, the increase of χ below T_N not only for $H \parallel y$ but also for $H \parallel x$ suggests that the weak-

ferromagnetic moment of $[Co(9S3)_2][Ni(9S3)_2]_2$ is also rotated in the xy plane when I use a thin planar crystal, as in $[Ni(9S3)_2][Ni(9S3)_2]_2$. In connection to this, the small value of M_{REM} considerably diminishes the demagnetization field effect ($\sim$0.1 mT), which makes the rotation easier. As a result of this easiness in the rotation, a spin flop transition is not observed clearly because the spin is easily rotated in a very weak magnetic field.

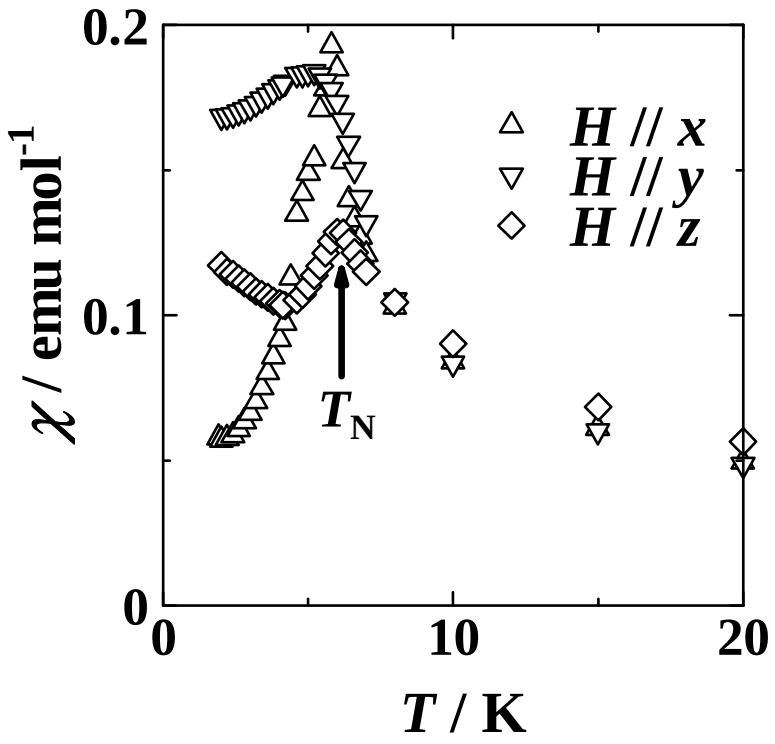

Fig. 4.9. The temperature dependence of the magnetic susceptibility of $[Ni(9S3)_2Br_2]$ in the external magnetic field $H = 0.1$ T applied parallel to the three directions defined as Fig. 4.10. The arrow with T_N is the N el temperature.

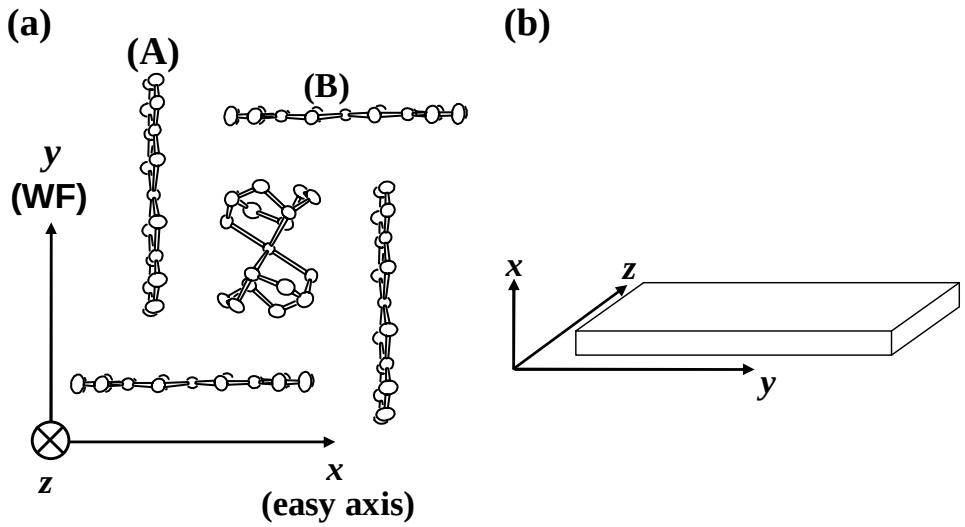

Fig. 4.10. **(a)** The definition of directions x, y and z, where (A) and (B) represent $[Ni(bdt)_2]^-$ (A) and (B) molecules, respectively, in $[M(9S3)_2][Ni(bdt)_2]_2$. "WF" and "easy axis" written in the figure mean that the weak-ferromagnetic axis and the spin easy axis are parallel to the y and x-directions, respectively (see, text). **(b)** The relation between the three directions and the crystal shape.

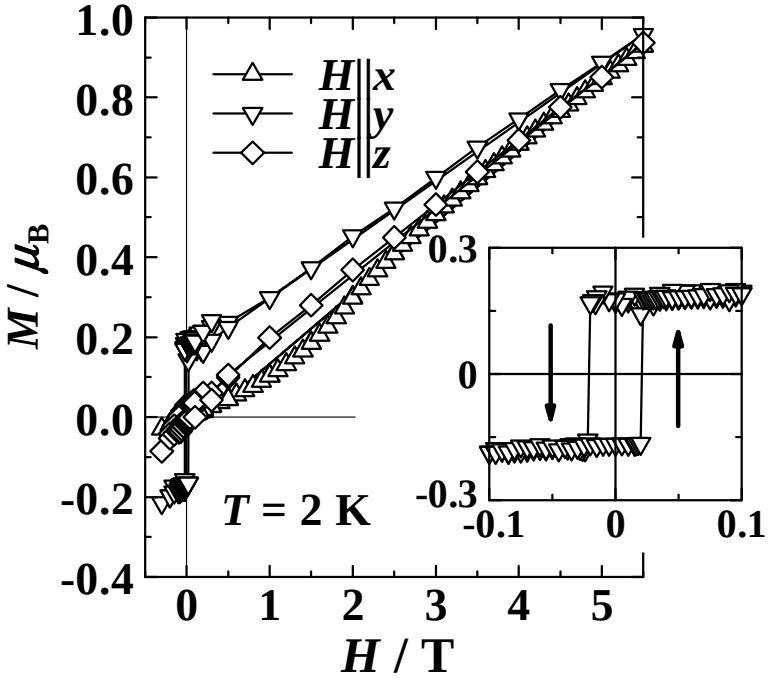

Fig. 4.11. The magnetization curves of $[Ni(9S3)_2][Ni(bdt)_2]_2$ at 2 K in the field applied in the three directions. The inset is the enlargement of the low magnetic field region for $H \parallel y$. The arrows indicate the directions of field sweep.

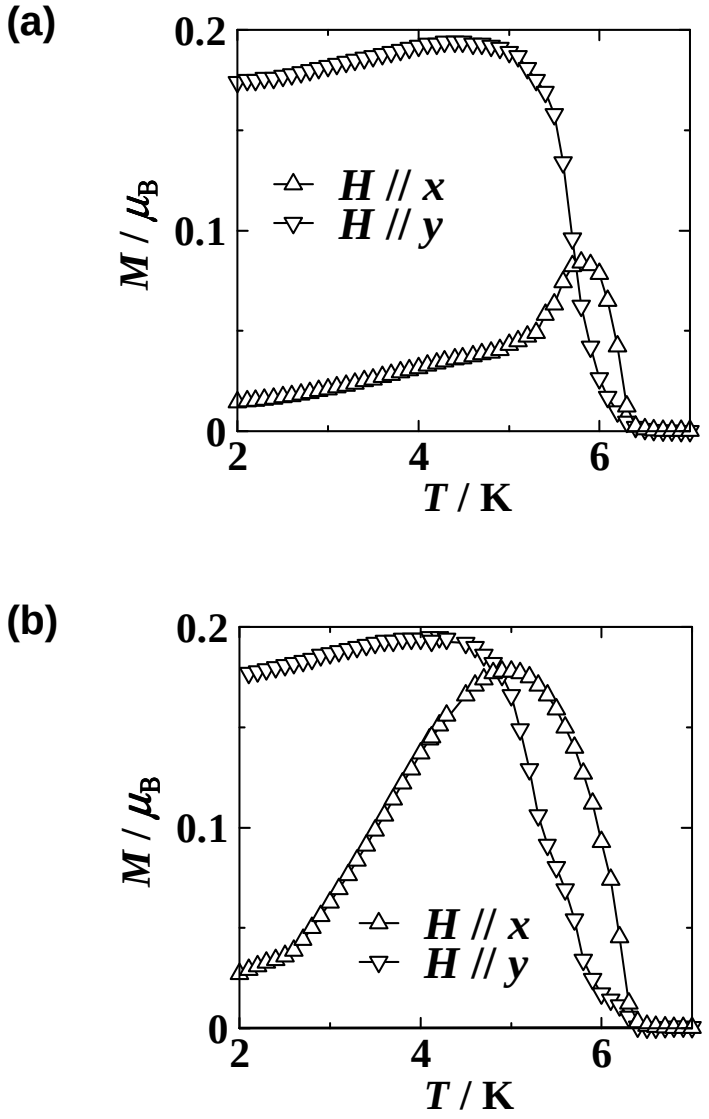

Fig. 4.12. (a) Temperature dependence of the remanent magnetization of $[Ni(9S3)_2][Ni(bdt)_2]_2$ with a weak external magnetic field $H = 0.3$ mT applied parallel to the x and y-directions during heating processes. (b) Remanent magnetization with $H = 0.3$ mT for fractional crystals obtained by cutting the sample of $[Ni(9S3)_2][Ni(bdt)_2]_2$. The crystal lengths of each individual crystal are roughly the same in the x and y-directions.

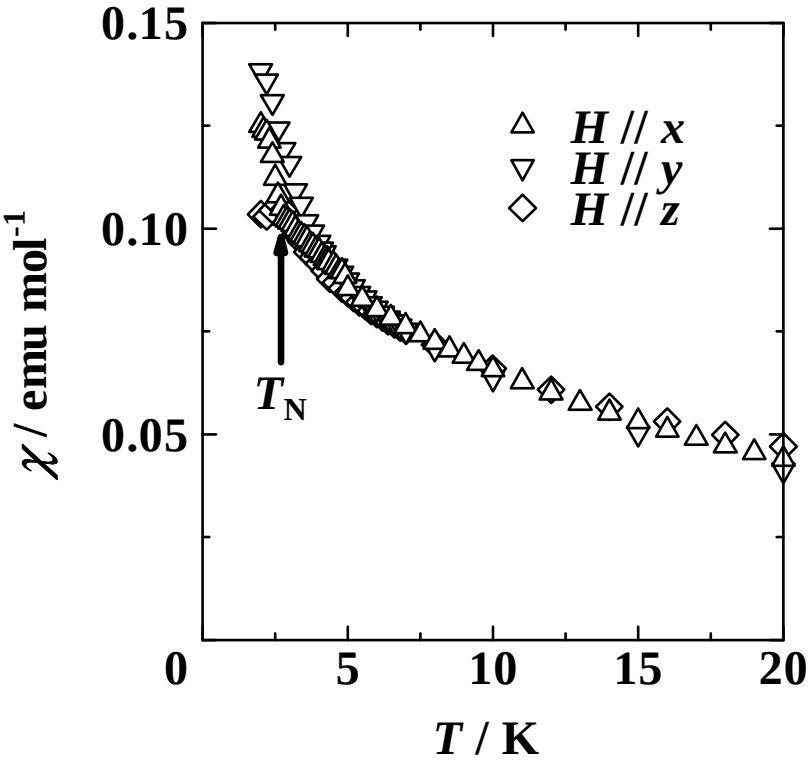

Fig. 4.13. The temperature dependence of the susceptibilities of $[Co(9S3)_2][Ni(bdt)_2]_2$ measured with an external magnetic field $H = 0.1$ T applied parallel to the x, y and z-directions (see Fig. 4.10 for the definitions of x, y and z).

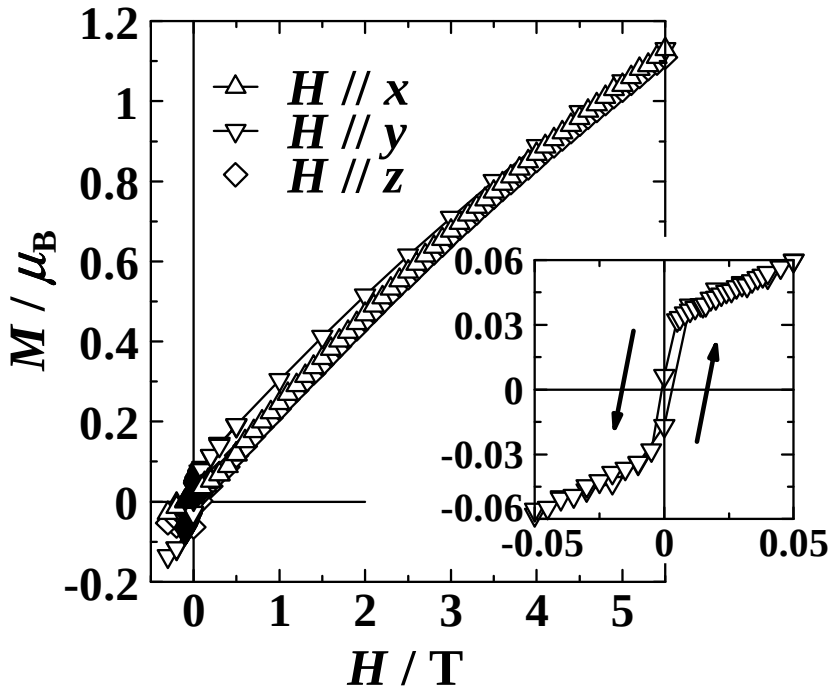

Fig. 4.14. The magnetization curves of $[Co(9S3)_2][Ni(bdt)_2]_2$ at 2 K. Inset is the enlargement of the low magnetic field region of $H \parallel y$. The arrows indicate the directions of field sweep.

4.5 Discussion

The origin of the weak-ferromagnetism of $[M(9S3)_2][Ni(bdt)_2]_2$ is discussed as a main issue in this section, since weak-ferromagnetism is unconventional in molecule-based magnets that have been investigated. For discussing weak-ferromagnetism, I first take $[Ni(9S3)_2][Ni(bdt)_2]_2$, which has the extraordinary large remanent magnetization. Then, the origin of weak-ferromagnetism in the cobalt (II) salt is discussed based on that of the nickel (II) salt. At last, I will discuss the strength of *d*-*d* exchange magnetic interaction, which is useful to design and construct a functional material having strong *d*-*d* and π-*d* interaction.

4.5.1 Weak-ferromagnetism in $[Ni(9S3)_2][Ni(bdt)_2]_2$

For clarifying the origin of weak-ferromagnetism, information on the magnetic structure is necessary. As will be discussed later, the magnetic structure consists of alternate chains of $[M(9S3)_2]^{2+}$ and $[Ni(bdt)_2]^-$ (A) molecules and AF chains of $[Ni(bdt)_2]^-$ (B) molecules. There are two typical candidates for the origin: Dzyaloshinskii-Moriya (DM) interactions and the coexistence of different magnetic sites having different anisotropy axes [24–27]. However, among these, the DM interaction seems to not be suitable for the origin in the present case because of the extraordinary large remanent magnetization of $[Ni(9S3)_2][Ni(bdt)_2]_2$, which corresponds to ca. 7 ° of the canting angle of a ferrimagnetic (FI) chains of $[Ni(9S3)_2]^{2+}$ and $[Ni(bdt)_2]^-$ (A) molecules, while the AF chains of $[Ni(bdt)_2]^-$ (B) molecules cannot take DM interactions because of the presence of an inversion center. In addition, the difference in the anisotropy axes of cations and/or anions is also ruled out, as will be seen in the later discussion.

There are four magnetic interactions J_1, J_2, J_3 and J_4 associated with intermolecular atomic contacts r_1, r_2, r_3 and r_4, respectively (see Figs. 4.5 and 4.6). Judging from the local spin density distributions, which has large values at the central metal atom and adjacent sulfur atom of the ligand because of the mixing of the magnetic *d*-orbital of a central metal and the HOMO of the crown thioether ligands having large distribution of HOMO at the sulfur atoms [10,11,28,29]. Consequently, J_1 and J_3 through short S-S contacts are considered to be strong, while

J_2 and J_4 through CH-S contacts are weak. Comparing J_2 with J_4, J_2 is stronger than J_4 because r_4 is ca. 5 % longer than r_2. In short, $|J_1|, |J_3| \gg |J_2| > |J_4|$. Therefore, two kinds of chains spanned by J_1 and J_3 work as fundamental structural units in explaining the magnetic structure. One is the alternate FI chains (#1 chains) elongated parallel to the (a+c) direction, which consist of $[Ni(9S3)_2]^{2+}$ molecules and $[Ni(bdt)_2]^-$ (A) molecules bonded by J_1, while the other is uniform AF chains (#2 chains) elongated parallel to the c-axis, which consist of $[Ni(bdt)_2]^-$ (B) molecules bonded by J_3. The magnetic structure model is schematically shown in Fig. 4.15. The absence of the spontaneous magnetization associated with the FI structure of #1 chains below T_N indicates an antiparallel arrangement of magnetic moments between FI chains. The magnetic anisotropies of $[Ni(9S3)_2]^{2+}$ and $[Ni(bdt)_2]^-$ (A) are, if they exist, compensated between two #1 chains aligned in antiparallel, resulting in the absence of a spontaneous magnetization. Similarly, the anisotropies of $[Ni(bdt)_2]^-$ (B) molecules in #2 chains are also compensated between adjacent $[Ni(bdt)_2]^-$ (B) molecules in a #2 chain. As a result, the magnetic anisotropies of cations and anions are also excluded from a candidate of the origin of the weak-ferromagnetism.

In contrast, a competition of two AF interactions, J_2 and J_4, can be a candidate for the origin of the weak-ferromagnetism. In the first step of the discussion, I take only J_1, J_2 and J_3 to consider a possible spin structure, as shown in Fig. 4.16. In this structure, the spin of a $[Ni(bdt)_2]^-$ (A) in #1 chain, which is strongly coupled by J_1 with the spins of $[M(9S3)_2]^{2+}$ in the same chain, is connected antiferromagnetically to an AF #2 chain by J_2. In the next step, J_4, the weakest inter-chain interaction between #1 chains, is introduced to the magnetic structure model. The spin configuration of Fig. 4.16b is destabilized because of the parallel spin configuration against AF interaction J_4 between the two FI #1 chains. To reduce the energy caused by the spin conflict, the easy axes of the spins in the #1 chains are forced to be canted (Fig. 4.16c). In this scenario, the collinear structure in the #1 chain is assumed to be conserved against the inter-chain interactions because of strong intra-chain AF interaction J_1. This means that the spins of FI chains are canted in the same direction in concert with respect to the spins of the adjacent FI chain, giving rise to the generation of a spontaneous magnetic moment. The

relaxation of the constraint on the collinear structure will give a slight modification without any loss of validity. In this model, magnetic anisotropies and anisotropic interactions are not necessary, and the extraordinary large remanent magnetization is the natural consequence, as follows. The canting angle of the FI chains rapidly increases when the ratio of J_4/J_2 increases, where the canting of the FI structure is accompanied by a large remanent magnetization. Therefore, this model is suitable to explain the origin of the weak-ferromagnetism of $[Ni(9S3)_2][Ni(bdt)_2]_2$.

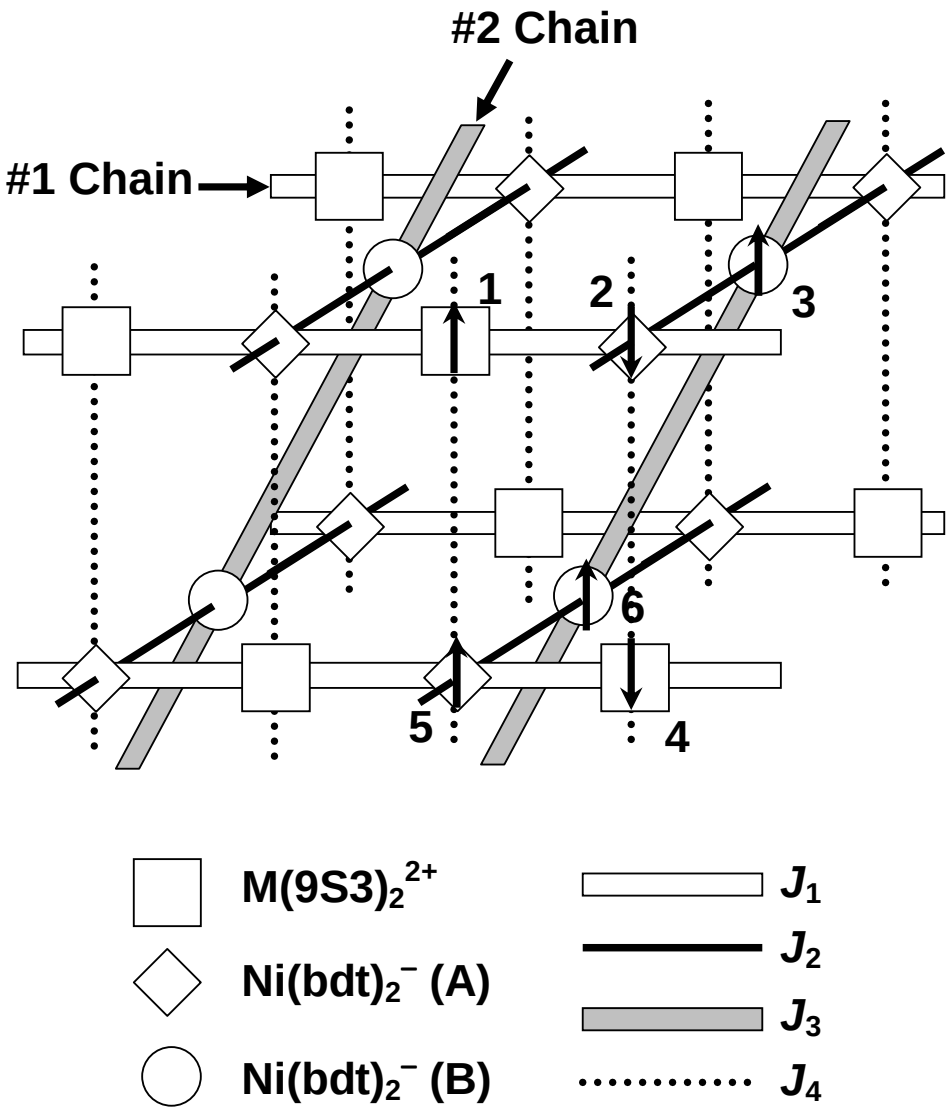

Fig. 4.15. The schematic of the magnetic structure of $[M(9S3)_2][Ni(bdt)_2]_2$, which consists of alternate $[M(9S3)_2]^{2+}$-$[Ni(bdt)_2]^-$ chains (#1 chains) and uniform $[Ni(bdt)_2]^-$ chains (#2 chains). Six arrows numbered with 1 to 6 represent the spins in six sublattices; two $[M(9S3)_2]^{2+}$ (1,4), two $[Ni(bdt)_2]^-$ (A) (2,5) and two $[Ni(bdt)_2]^-$ (B) (3,6).

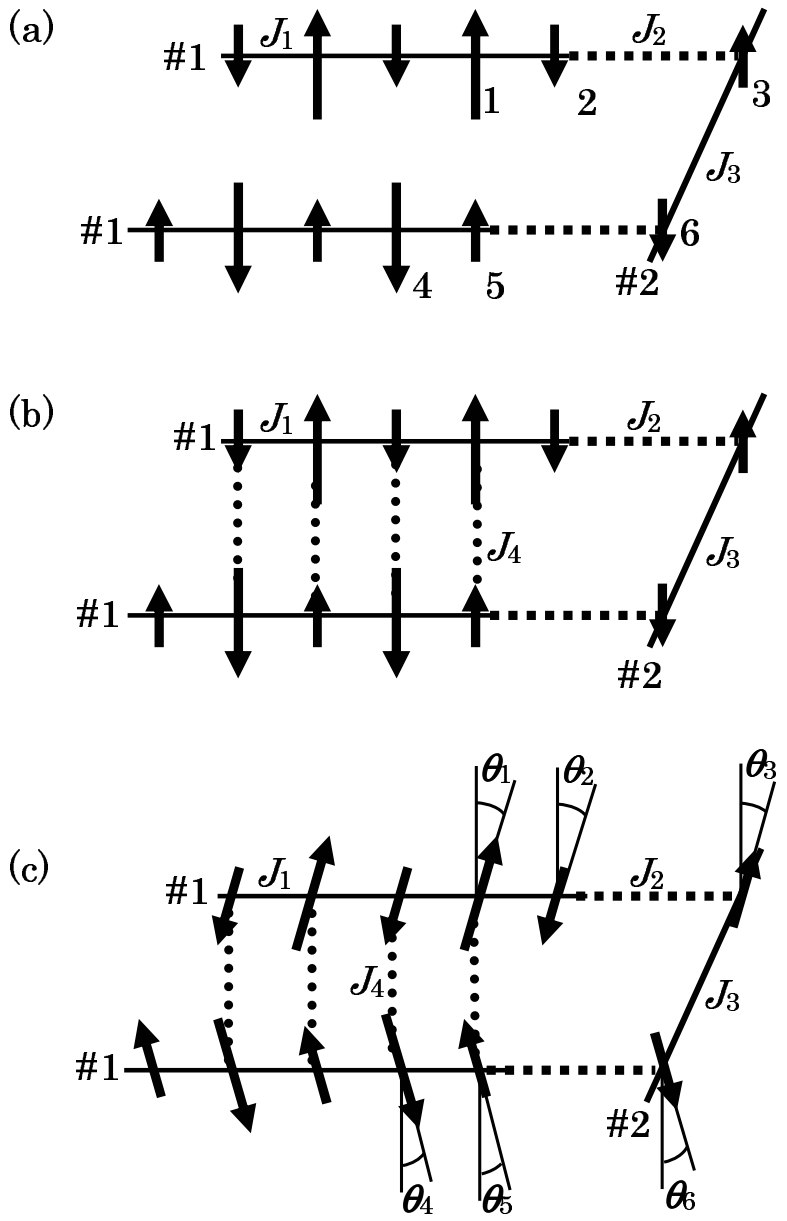

Fig. 4.16. (a) The magnetic structure model of $[Ni(9S3)_2][Ni(bdt)_2]_2$ with three AF exchange interactions J_1, J_2 and J_3 ($|J_1|, |J_3| \gg |J_2|$). Only three chains (two #1 chains and a #2 chain) are shown for clarity. Numbered arrows represent the six sublattices corresponding to those of Fig. 4.15. (b) Introducing the weakest AF inter-chain interaction J_4 destabilizes the spin configuration of (a). (c) Magnetic structure model with J_1, J_2, J_3 and J_4, where spin frustration effect is reduced by canting the spins of #1 and #2 chains. Angle θ_i represents the canting angle of i-th sublattice.

4.5.2 Weak-ferromagnetism in $[Co(9S3)_2][Ni(bdt)_2]_2$

In the cobalt (II) complex salt $[Co(9S3)_2][Ni(bdt)_2]_2$, the spin canting of the #1 chains may also occur, but such a canting cannot cause a spontaneous magnetization because #1 chains have no net magnetic moment. One possible origin is the spin canting of $[Ni(bdt)_2]^-$ (B) in #2 chains (θ_3 and θ_6) and/or the difference of the canting angles between $[Co(9S3)_2]^{2+}$ and $[Ni(bdt)_2]^-$ (A) ($\theta_1 - \theta_2$ and $\theta_4 - \theta_6$) in #1 chains. Though J_3 is stronger than J_2 and J_4, the spin canting of #1 chains, if it exists, can induce a small spin canting in #2 chains. Such a canting also contributes to the weak-ferromagnetism in both the nickel (II) and the cobalt (II) salts, however, strong J_1 and J_3 allows only a very small intra-chain canting angle. Furthermore, the weakening of the inter-chain interaction $2J_4\boldsymbol{S}_1 \cdot \boldsymbol{S}_5$ between #1 chains caused by employing $[Co(9S3)_2]^{2+}$ ($S = 1/2$) in place of $[Ni(9S3)_2]^{2+}$ ($S = 1$) tends to diminish the competition between J_2 and J_4, resulting in the reduction of canting angles. Consequently, only weak weak-ferromagnetism is observed. The reduced remanent magnetization in cobalt(II) salt brings about the decrease of the demagnetization field, resulting in the reduction of the anisotropy energy. Such a small anisotropy energy is the reason for the small coercive force in the cobalt (II) salt. Similar canting of #2 chains induced by #1 chains can also occur in the nickel (II) complex salt, but such a contribution of the canting to the weak-ferromagnetism is not so large in the nickel (II) salt because the weak-ferromagnetism of the salt having an FI structure is mainly governed by the canting between #1 chains. The other candidate for the origin of weak-ferromagnetism in the cobalt (II) salt is the difference of g-values between $[Co(9S3)_2]^{2+}$ and $[Ni(bdt)_2]^-$. The difference of g-values can also causes the FI chain magnetic structure in spite of both components of an alternate chain having $S = 1/2$ magnetic moment. In this case, the remanent magnetization of the cobalt (II) salt is smaller than that of the nickel (II) salt because net magnetization of ferrimagnetic chain described as

$$M_{\mathrm{FI}} = \left| g_{9\mathrm{S3}}\boldsymbol{S}_{9\mathrm{S3}} - g_{\mathrm{bdt}}\boldsymbol{S}_{\mathrm{bdt}} \right|, \tag{4.7}$$

is small in the cobalt (II) salt due to the same $\boldsymbol{S}$ values and small difference of g-values between $[Co(9S3)_2]^{2+}$ and $[Ni(bdt)_2]^-$. The canting angles of the spins of

$[Co(9S3)_2]^{2+}$ and $[Ni(bdt)_2]^-$ are expected to be small when we consider that those of the $[Ni(9S3)_2]^{2+}$ salt is small. In the condition of a small canting angle, the spin of $[Ni(bdt)_2]^-$ in #1 chain is approximately directed to x-axis which is perpendicular to the molecular plane of $[Ni(bdt)_2]^-$, in which direction the g-values of dithiolato complexes are ca. 2.0 [30], while those of $[M(9S3)_2]^{2+}$ are ca. 2.1 [31, 32]. The values of M_{FI} in the $[Co(9S3)_2]^{2+}$ salt calculated from eq. (4.7) is ca. 5% of that of $[Ni(9S3)_2]^{2+}$ salt, the ratio is comparable to obtained value.

4.5.3 Mean-field calculation

Finally, I discuss the magnetic structure on the basis of the mean field approximation. Before calculation, I empirically estimate the values of J_1 and J_3. In the high temperature region, χ is considered to be described as the simple sum of the contributions from a FI #1 chains and an AF #2 chains for the nickel (II) salt or the sum of an AF #1 chains and an AF #2 chains for the cobalt (II) salt because inter-chain interactions are orders of magnitude weaker than intra-chain interactions, where the strength of the inter-chain interactions is considerably small in comparison with the thermal energy. From the fitting of χ by the FI chain model [33] of $S = 1$ and $1/2$,

$$\chi = \frac{N_A \mu_B^2 g^2}{k_B T} \cdot \frac{-0.034146801X^3 + 2.816306411X^2 - 7.2310013697X + 11}{1.29663274X^2 + 0.69719013595X + 12}, \tag{4.8}$$

where

$$X = \frac{2|J|}{k_B T}, \tag{4.9}$$

and the AF chain model (eq. (4.4)) in the region of $50 < T < 300$ K, I obtained J_1 = 12.6 K and J_3 = 4.9 K for the nickel (II) salt and J_1 = 4.1 K and J_3 = 4.5 K for the cobalt (II) salt. The large difference in J_1 between these two salts is explained by the Jahn-Teller distortion of $[Co(9S3)_2]^{2+}$. In the cobalt (II) salt having the electron configuration [31] of an octahedral Co^{2+} ion $(t_{2g})^6(e_g)^1$, only one electron in the e_g state. Only the electron can contribute to the magnetism, while the electron tends to occupy the d_{z^2} orbital directed to the S1 atom having no intermolecular contact as shown in Figs. 4.5 and 4.6. On the other hand, in the electron

configuration of an octahedral Ni^{2+} ion $(t_{2g})^6(e_g)^2$, magnetic electrons occupy not only the d_{z^2} orbital directed at the S1 atom, but also the $d_{x^2-y^2}$ orbital directed at S2 and S3 atoms which have inter-molecular contacts. As a result, the inter-molecular interaction of $[Co(9S3)_2]^{2+}$ becomes weaker than that of $[Ni(9S3)_2]^{2+}$.

Using these J_1 and J_3 values, M_{REM} of the nickel (II) and the cobalt (II) salts at 2 K was calculated for various values of J_2 and J_3 on the basis of the six-sublattices model (two-sublattices of each of $[Ni(9S3)_2]^{2+}$, $[Ni(bdt)_2]^-$ (A) and $[Ni(bdt)_2]^-$ (B), see Fig. 4.15) in the mean field approximation. In the calculation, I assume that the spins can be rotated only in the xy-plane with no in-plane anisotropy for simplicity, which is not contrary to the nature of the salts. The mean field H_i and effective magnetic moment M_i of sublattice i (see Fig. 4.15 for the definitions of i) are represented as follows;

$$\boldsymbol{H}_1 = 2A_1\boldsymbol{M}_2 + 2A4\boldsymbol{M}_5, \tag{4.10}$$

$$\boldsymbol{H}_2 = 2A_1\boldsymbol{M}_1 + 2A2\boldsymbol{M}_3 + 2A4\boldsymbol{M}_4, \tag{4.11}$$

$$\boldsymbol{H}_3 = 2A_2\boldsymbol{M}_2 + 2A3\boldsymbol{M}_6, \tag{4.12}$$

$$\boldsymbol{H}_4 = 2A_1\boldsymbol{M}_5 + 2A4\boldsymbol{M}_2, \tag{4.13}$$

$$\boldsymbol{H}_5 = 2A_1\boldsymbol{M}_4 + 2A2\boldsymbol{M}_6 + 2A4\boldsymbol{M}_1, \tag{4.14}$$

$$\boldsymbol{H}_6 = 2A_2\boldsymbol{M}_5 + 2A3\boldsymbol{M}_3, \tag{4.15}$$

$$\boldsymbol{M}_i = N_A g\mu_B S_i \frac{\boldsymbol{H}_i}{|\boldsymbol{H}_i|} B_S\left(\frac{S_i g\mu_B \boldsymbol{H}_i}{k_B T}\right), \tag{4.16}$$

where $B_s(x)$ and S_i are the Brillouin function and the spin of sublattice i (S_i = 1 for i = 1 and 4, 1/2 for i = 2, 3, 5 and 6 in the nickel (II) salt; S_i = 1/2 for i = 1 to 6 in the cobalt (II) salt), respectively, and I assume $g \sim 2$ or $g \sim 2.1$ for $[Co(9S3)_2]^{2+}$, which is supposed by the EPR results [31], and $g \sim 2$ for all other the spins. The calculation was carried out until $\boldsymbol{M}_i$, the initial value of which were randomly selected, become self-consistently determined.

Figs. 4.17 and 4.18 show the calculated M_{REM} at 2 K of the nickel (II) and the cobalt (II) salt, respectively, which has a non-zero value of M_{REM}. The increase of g-value of $[Co(9S3)_2]^{2+}$ enhances the value of M_{REM}, but the behavior is not so different between g = 2 and g = 2.1. Furthermore, the weak-ferromagnetic region (WFM) exists in both $[Ni(9S3)_2][Ni(bdt)_2]_2$ and $[Co(9S3)_2][Ni(bdt)_2]_2$. The

small value of WFM in $[Co(9S3)_2]^{2+}$ and large value of WFM in $[Ni(9S3)_2]^{2+}$ are in good agreement with the values experimentally obtained. In the WFM region, the calculated spin arrangement can accurately reproduce that shown in Fig. 4.16c. For example, at (J_2, J_4) = (−0.50 K, −0.064 K) in the nickel (II) salt with $M_{\rm REM}$ = 0.18 $\mu_{\rm B}$, the calculated canting angles, θ_i, defined in 4.16c are 10.0^o for i = 1, 2, 4 and 5, 0.25^o for i = 3 and 6, while the sublattice magnetic moments $|\boldsymbol{M}_i|$ calculated are approximately the same as the values of S_i due to the reduced thermal agitation at the low temperatures. The small values of $(\theta_1 - \theta_2)$, $(\theta_4 - \theta_5)$, θ_3 and θ_6 suggest that strong intra-chain interactions stabilize the FI structure of #1 chains and the AF structure of #2 chains in the weak-ferromagnetic region, while weak-ferromagnetism is mainly caused by the canting of the FI chains. In contrast, the calculated $M_{\rm REM}$ of the cobalt (II) salt with g = 2 for $[Co(9S3)_2]^{+2}$ is associated with both the canting of #2 chains (θ_3 and θ_6) and difference between canting angles ($\theta_1 - \theta_2$ and $\theta_4 - \theta_5$), as expected from the model mentioned above. For example, at (J_2, J_4) = (−0.22 K, −0.066 K) in the cobalt (II) salt with $M_{\rm REM}$ = 0.015 $\mu_{\rm B}$, the canting angles defined in Fig. 4.16c are calculated as 35.1^o for i = 1 and 4, 34.6^o for i = 2 and 5, and 0.40^o for i = 3 and 6. It should be noted that a quantitative discrepancy in the absolute value of $M_{\rm REM}$ is present between the calculated and the measured value. Indeed, in the calculation, the region of $M_{\rm REM} \sim 0.18$ $\mu_{\rm B}$, which is the value observed in the actual crystal, is very small and $M_{\rm REM}$ rapidly increases to over 0.6 $\mu_{\rm B}$ when $|J_4|$ increases. This discrepancy may come from the simplification of the mean field approximation.

It is noted that the J_4/J_2 sensitivity of $M_{\rm REM}$ is actually observed in $M_{\rm REM}$ under high pressures. Fig. 4.19 shows pressure dependence of remanent magnetization at 2 K. $M_{\rm REM}$ rapidly decreases from 0.18 to 0.03 $\mu_{\rm B}$ as pressure is raised from 0 to 7.5 kbar. When I apply the pressure to the salt, inter-molecular overlaps are slightly changed. Judging from the calculated results shown in Fig. 4.17, a small change of J_2/J_4 can bring about the large change of the $M_{\rm REM}$ as observed in the Fig. 4.19. The pressure sensitivity of the $M_{\rm REM}$ supports the validity of the model of weak-ferromagnetism.

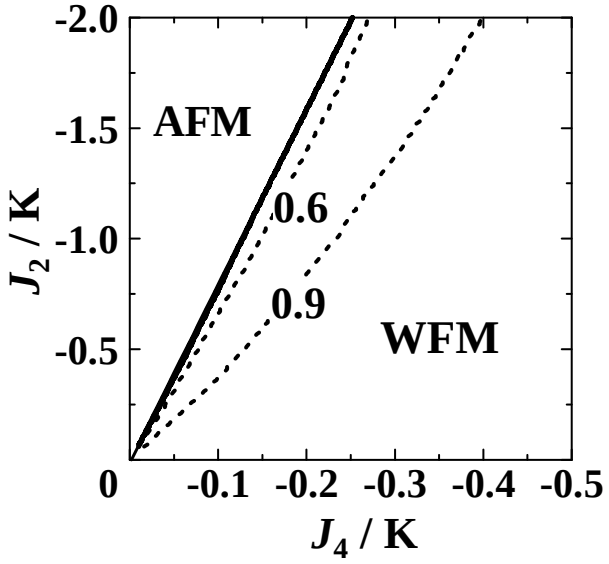

Fig. 4.17. The remanent magnetization (M_{REM}) and phase diagram calculated by mean field approximation at 2 K as functions of J_2 and J_4 for $[\mathrm{Ni(9S3)_2}][\mathrm{Ni(bdt)_2}]_2$. The solid line represents the boundary between weak-ferromagnetic state (WFM) and antiferromagnetic state (AFM). The dotted lines represent $M_{\mathrm{REM}} = 0.3$ (near the boundary of WFM/AFM), 0.6 and 0.9 μ_{B}.

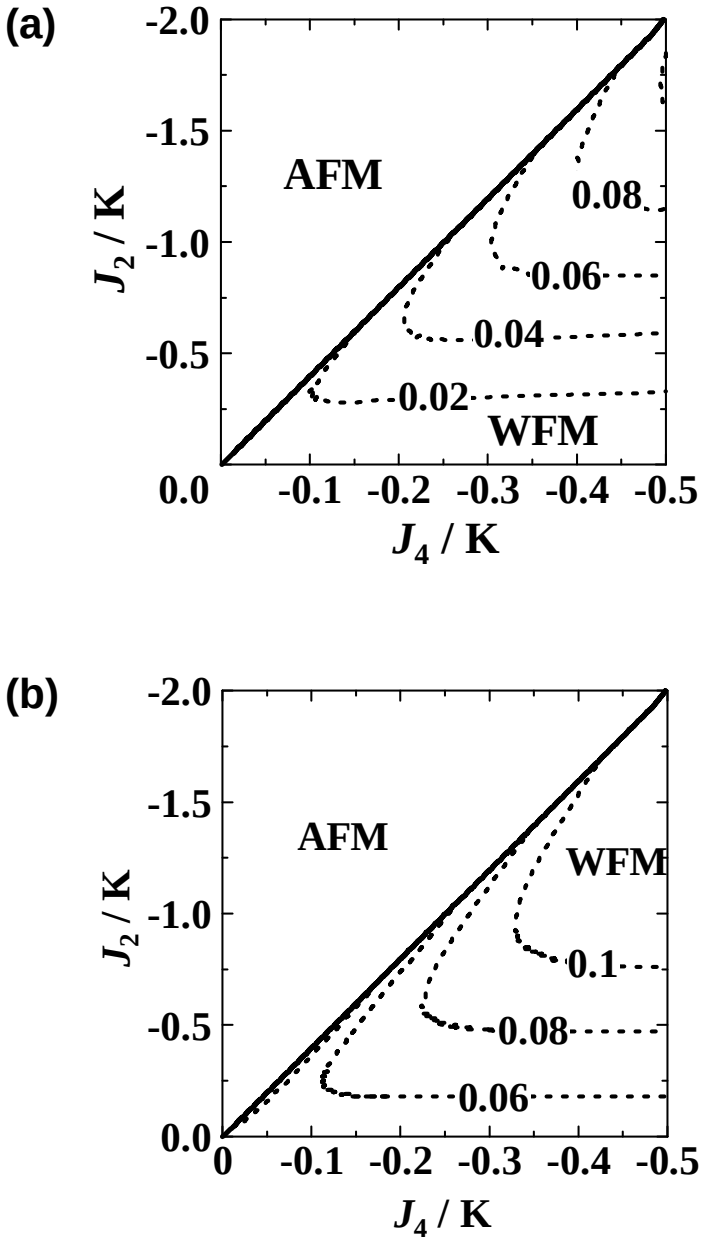

Fig. 4.18. The remanent magnetization (M_{REM}) and phase diagram calculated by mean field approximation at 2 K as functions of J_2 and J_4 for $[Co(9S3)_2][Ni(bdt)_2]_2$ with g-value of $[Co(9S3)_2][Ni(bdt)_2]_2$ (a) 2 and (b) 2.1. The solid lines represent the boundary between weak-ferromagnetic state (WFM) and antiferromagnetic state (AFM). The dotted lines represent $M_{\mathrm{REM}} = 0.02$, 0.04, 0.06 and 0.08 μ_{B} in (a) and 0.04 (near the boundary of WFM/AFM), 0.06, 0.08 and 0.1 μ_{B} in (b).

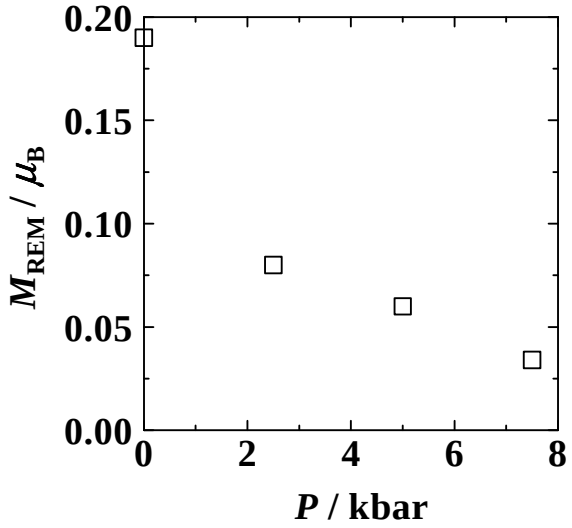

Fig. 4.19. Pressure dependence of the remanent magnetization M_{REM} of $[\mathrm{Ni(9S3)_2}][\mathrm{Ni(bdt)_2}]_2$ at 2 K. The value of M_{REM} rapidly decreases as the pressure increases.

4.5.4 Strength of the exchange interaction of crown thioether complexes

The crown thioether complex salts reported in this thesis often show strong inter-molecular exchange magnetic interactions in spite of their long inter-molecular atomic distances. For examples, $[Ni(9S3)_2](TCNQ)_2$ and $[Ni(9S3)_2][Ni(bdt)_2]_2$ show strong antiferromagnetic intra-chain interactions $J = -3.9$ and -12.6 K, respectively, whereas the inter-molecular sulfur-sulfur distances (3.838(6) and 3.772(2) Å, respectively) are longer than the sum of van der Waals radii (3.7 Å).

When I consider about the strength of exchange magnetic interaction, the spin density of sulfur atoms of ligands and inter-molecular sulfur-sulfur distances are important. The importance is verified by comparing $[Ni(9S3)_2](TCNQ)_2$ with $[Ni(9S3)_2](TCNQ)_3$.

Comparing the inter-molecular distances of these two salts, it is observed that $[Ni(9S3)_2](TCNQ)_2$ has a shorter S-S atomic contact length (3.838(6) Å) and longer Ni^{2+}-Ni^{2+} distance (8.627(9) Å) than those of $[Ni(9S3)_2](TCNQ)_3$ (4.685(3) and 7.761(3) Å), while the intra-molecular Ni^{2+}-S distances have roughly same values (2.383(4), 2.400(4) and 2.403(4) for $[Ni(9S3)_2](TCNQ)_2$ and 2.371(1), 2.389(1) and 2.390(1) for $[Ni(9S3)_2](TCNQ)_3$, respectively). On the other hand, inter-molecular exchange magnetic interaction J of these salts are estimated as $J = -3.9$ and ~ 0 K for $[Ni(9S3)_2](TCNQ)_2$ and $[Ni(9S3)_2](TCNQ)_3$, respectively. The difference in the strength of exchange magnetic interactions and inter-molecular distances between these salts, and the similarity of the intra-molecular distances indicate that the strength of the magnetic interaction mainly depends on the inter-molecular S-S contact in transition metal complexes of crown thioethers, taking into account the difference in the strength of exchange interactions.

Therefore, strong exchange magnetic interaction of crown thioether complexes are due to their electronic structure at sulfur atoms suggested by the molecular orbital calculations, in which a crown thioether ligand has a strong π-acidity resulting in the large spin density at the surrounding sulfur atoms of crown thioether complexes [10, 11].

4.6 Summary

New series of molecule-based magnets including transition metal complexes of crown thioethers were constructed, and their physical properties were investigated.In the crystals, transition metal complexes of the crown thioethers show eminent potential in the exchange interaction.

The crystal $[Ni(9S3)_2](TCNQ)_2$ is a 1D $S = 1$ antiferromagnet with strong antiferromagnetic inter-molecular interaction $J = -3.9$ K, whereas a long inter-molecular contact which is longer than the sum of van der Waals radii. The isostructural salt $[Co(9S3)_2](TCNQ)_2$, which is a $S = 1/2$ analogue of $[Ni(9S3)_2]^{2+}$ salt, is a paramagnet with inter-molecular interaction $J = -1.3$ K, the value of J is weaker than that of $[Ni(9S3)_2]^{+2}$ thanks to Jahn-Teller distortion of $[Co(9S3)_2]^{2+}$.

Contrary to the insulating salts mentioned just before, $[M(9S3)_2](TCNQ)_3$ (M = Ni, Co) are semiconductive paramagnets, where the trimers of partially reduced $TCNQ^{2/3-}$ are well separated each other by the large cations, while the cations are separated by the trimers resulting in the absence of inter-molecular interactions.

[Cu(9S3)Br2] is a 1D antiferromagnet characterized by a strong intra-chain interaction and a weak inter-chain interaction, $J_{\rm intra} = -5.4$ K and $J_{\rm inter} \sim 0$ K, respectively. The substitution of a small amount (~ 5 %) of Cu^{2+} with Ni^{2+} causes a drastic change of a inter-chain arrangement resulting in the inter-chain short S-S contacts, while the intra-chain structure is kept with nearly same intra-chain interaction $J = -4.7$ K. The short inter-chain S-S contacts bring 3D antiferromagnetic transition to $[Cu_{1-x}Ni_x(9S3)Br_2]$ ($x \sim 0.05$) at $T_{\rm N} = 5$ K despite $[Cu(9S3)Br_2]$ having no magnetic transition.

Isostructural salts $[M(9S3)_2][Ni(bdt)_2]_2$ (M = Ni, Co) consist of the two magnetic chains. One is the FI (M = Ni) or AF (M = Co) alternate chain of $[M(9S3)_2]^{2+}$ and $[Ni(bdt)_2]^-$ elongated parallel to the $(a+c)$ direction with intra-chain interaction $J_1 = -12.6$ and -4.1 K for M = Ni and Co, respectively, while the other is the AF uniform chain of $[Ni(bdt)_2]^-$ elongated parallel to the c-axis with intra-chain interaction $J_3 = -4.9$ and -4.5 K for M = Ni and Co, respectively. These two kinds of chains are bound for each other by inter-chain weak AF interaction J_2 and J_4. As a result of these intra- and inter-chain AF interaction, these salts

take place a 3D magnetic transition at T_N = 6.2 and 2.6 K for M = Ni and Co, respectively. Below T_N, these salts show a weak-ferromagnetism featured with the remanent magnetization M_{REM} = 0.18 and 0.015 μ_B and coercive force H_c = 20 and 1 mT for M = Ni and Co, respectively.

The origin of the weak-ferromagnetism is explained as the competition between two AF inter-chain interactions J_2 and J_4 which causes the spin canting of the alternate chain to reduce the energy of the exchange interactions. In the $[Ni(9S3)_2]^{2+}$ salt, the tilted components of the net magnetic moment of FI chains are directed to same direction resulting in extraordinary large remanent magnetic moment. On the other hand, the difference of the g-values between $[Co(9S3)_2]^{2+}$ ($g \sim 2.1$) and $[Ni(bdt)_2]^{-}$ ($g \sim 2.0$) also makes the alternate chain ferrimagnetic, but the net magnetic moment of FI-like chain ($2.1\times1/2$-$2.0\times1/2 = 0.05$) is ca. 1/20 smaller than that of FI chain of $[Ni(9S3)_2]^{2+}$ (2.1×1-$2.0\times1/2 = 1.1$). The model of the weak-ferromagnetism is semi-quantitatively evidenced by mean-field calculation, where the large M_{REM} of $[Ni(9S3)_2]^{2+}$ salt and small that of $[Co(9S3)_2]^{2+}$ are reproduced. In addition, the observed pressure sensitivity of M_{REM} also support the model where slight change of the ratio J_2/J_4 causes a large change of M_{REM}.

Judging from these results, I conclude that the transition metal complexes of crown thioethers are superior building blocks for molecule-based magnet owing to their two features. One of the features is the presence of strong inter-molecular magnetic interactions through S-S atomic contacts owing to the characteristic electronic structure of crown thioethers. Indeed, some of the present samples have strong magnetic interactions (few to ca. -20 K) despite that S-S contacts are longer than the sum of the van der Waals radii. The other important feature is the substitutability between central transition metal ions having different spin states, for example, $S = 1$ component $[Ni(9S3)_2]^{2+}$ and $S = 1/2$ component $[Co(9S3)_2]^{2+}$. As the molecular sizes and structures remain unchanged by the substitution, chemical modification can be done intentionally in the systematic manner of tuning magnetism. From these features, it is concluded that the transition metal complexes of crown thioethers are promising building blocks in designing molecule-based magnets.

References

[1] T. Enoki, J.-I. Yamaura and A. Miyazaki, *Bull. Chem. Soc. Jpn.*, **70**, 2005 (1997).

[2] A. Miyazaki, K. Enomoto, K. Okabe, H. Yamazaki, J. Nishijo, T. Enoki, E. Ogura, K. Ugawa, Y. Kuwatani and M. Iyoda, *J. Solid State Chem.*, **168**, 547 (2002).

[3] H. Kobayashi, A. Kobayashi and Patrick Cassoux, *Chem. Soc. Rev.*, **29**, 325 (2000).

[4] A. Sato, E. Ojima, H. Akutsu, Y. Nakazawa, H. Kobayashi, H. Tanaka, A. Kobayashi and P. Cassoux, *Phys. Rev. B*, **61**, 111 (2000).

[5] S. Uji, H. Shinagawa, T. Terashima, T. Yakabe, Y. Terai, M. Tokumoto, A. Kobayashi, H. Tanaka and H. Kobayashi, *Nature*, **410**, 908 (2001).

[6] N. Hanasaki, H. Tajima, M. Matsuda, T. Naito and T. Inabe, *Phys. Rev. B*, **62**, 5839 (2000).

[7] J. Nishijo, E. Ogura, J. Yamaura, A. Miyazaki, T. Enoki, T. Takano, Y. Kuwatani and M. Iyoda, *Solid State Comm.*, **116**, 661 (2000).

[8] E. Coronado, J. R. Galan-Mascaros, C. J. Gomez-Garcia, V. Laukhin, *Nature*, **408**, 447 (2000).

[9] F. Palacio, G. Antorrena, M. Castro, R. Burriel, J. Rawson, J. N. B. Smith, N. Bricklebank, J. Novoa and C. Ritter, *Phys. Rev. Lett.*, **79**, 2336 (1997).

[10] J. R. Hartman and S. R. Cooper, *J. Am. Chem. Soc.*, **108**, 1202 (1986).

[11] N. Gallego-Planas and M. A. Whitehead, *J. Mol. Struc.; Theochem,* **428**, 67 (1998)

[12] T. W. Hambley, *Inorg. Chem.*, **37**, 3767 (1998).

[13] A. J. Blake, M. J. Bywater, R. D. Crofts, A. M. Gibson, G. Reid and M. Schr der, *J. Chem. Soc., Dalton Trans.*, 2979 (1996).

[14] J. P. Ferraris, D. O. Cowan, V. Walatka Jr and J. H. Prelstein, *J. Am. Chem. Soc.*, **95**, 948 (1973).

[15] Y. Kagami, F. Iwahori, T. Ohishi, T. Hama, T Manabe, M Yamashita, H. Kitagawa, K. Sakai and T. Mitani, *Synthetic Metals*, **86**, 1803 (1997).

[16] N.Gu, X.-M.Yang, H.-Y.Sheng, W.Lu, and Y.Wei, *Synthetic Metals*, **71**, 2221 (1995).

[17] M. T. Azcondo, L. Ballester, S. Golhen, A. Guierrez, L. Ouahab, S. Yartsev and P. Delhaes, *J. Mat. Chem.*, **9**, 1237 (1999).

[18] T. Mori, A. Kobayashi, Y. Sasaki, H. Kobayashi, G. Saito and H. Inokuchi, *Bull. Chem. Soc. Jpn.*, **57**, 627 (1984).

[19] S. Flandrois and D. Chasseau, *Acta. Cryst. B*, **33**, 2744 (1977).

[20] G. J. Grant, C. G. Brandow, D. F. Galas, J. P. Davis, W. T. Pennington, E. J. Valente and J. D. Zubkowski, *Polyhedron*, **20**, 3333 (2001).

[21] J. J. Borr s-Almenar, E. Coronado, J. Curely and R. Georges, *Inorg. Chem.*, **34**, 2699 (1995).

[22] J. C. Bonner and M. E. Fisher, *Phys. Rev.*, **135**, A640 (1964).

[23] D. B. Brown, J. A. Donner, J. W. Hall, S. R. Wilson, R. B. Wilson, D. J. Hodgson and W. E. Hatfield, *Inorg. Chem.*, **18**, 2635 (1979).

[24] I. Dzyaloshinskii, *Sov. Phys. JETP*, **5**, 1259 (1957), and T. Moriya, *Phys. Rev.*, **120**, 91 (1960).

[25] V. Skumryev, F. Ott, J. M. D. Coey, A. Anane, J.-P. Renard, L. Pinsard-Gaudart and A. Revcolevschi, *Eur. Phys. J. B*, **11**, 401 (1999).

[26] M. D. Lumsden, B. C. Sales, D. Mandrus, S. E. Nagler and J. R. Thompson, *Phys. Rev. Lett.*, **86**, 159 (2001).

[27] A. Miyazaki, K. Okabe, T. Enoki, F. Setifi, S. Golhen, L. Ouahab, T. Toita and J. Yamada, *Synth. Metals*, **137**, 1195 (2003).

[28] A. T. Coomber, D. Beljionne, R. H. Friend, J. L. Br das, A. Charlton, N. Robertson, A. E. Underhill, M. Kurmoo and P. Day, *Nature*, **380**, 144 (1996).

[29] S. R. Cooper, S. C. Rawle, J. R. Hartman, E. J. Hintsa and G. A. Admans, *Inorg. Chem.*, **27**, 1209 (1988).

[30] R. Kirmse, J. Stach, W. Dietsch, G. Steinmecke and E. Hoyer, *Inorg. Chem.*, **19**, 2679 (1980).

[31] G. S. Wilson, D. D. Swanson and R. S. Glass, *Inorg. Chem.*, **25**, 3827 (1986).

[32] A. J. Blake, R. O. Gould, M. A. Halcrow, A. J. Holder, T. I. Hyde and M. Schr der, *J. Chem. Soc.*, Dalton Trans., 3427 (1992).

[33] M. Drillon, E. Coronado, R. Georges, J. C. Gianduzzo and J. Currely, *Phys. Rev. B*, **40**, 10992 (1989).

Chapter 5

$(EDO\text{-}TTFI_2)_2[M(mnt)_2]$ (M = Ni, Pt)

5.1 Introduction

Recently, organic charge-transfer complexes including transition-metal-complex anions have been intensively focused with the aim of producing organic molecular metal ferromagnet, which is of great interest from the points of theoretical research of strongly correlated electron systems and application for molecular devices. However, no organic conductor had been reported showing both metallic conductivity and ferromagnetic interaction simultaneously till recent years. In order to obtain such a molecular magnet, I developed a new class of organic complex salt on the basis of donor molecule EDO-$TTFI_2$ (4,5-diiodo-4',5'-ethylenedioxytetrathiafulvalene), which is expected to form strong coordination-bond-like interaction between the iodo group of the donor and cyano group or halogen of acceptors as shown in the Chapters 1 and 3. It is expected that the strong donor-anion interaction shortens the donor-anion distance resulting in the strong π-d interaction as discussed in the Chapter 3. In addition, the strong donor-anion interaction means that the donor-anion interaction plays an important role in the arrangement of the anions, while the arrangement is mainly governed by the Coulomb interaction and the orbital overlaps between anions in ordinal salts. As a result, it becomes easier to realize an unconventional molecular arrangement of anions.

To obtain a ferromagnetic metal, magnetic anions $[M(mnt)_2]^-$ (M = Ni, Pt; mnt=maleonitriledithiolate), which have cyano groups and $S = 1/2$ spin, were

used. The anions frequently forms antiferromagnetic (AF) materials [1–3] except some ferromagnetic materials [4,5]. The antiferromagnetism of the anion is caused by the inter-anion overlap between SOMOs, where the overlap reduce the energy of the electron. Here, if the donor-anion interaction is stronger than the energy of the overlaps of SOMOs, the donor-anion interaction takes precedency over the anion-anion overlaps in the arrangement of the anions. Consequently, there is a possibility to form a ferromagnetic arrangement of anions when the halogenated donor is used.

In this chapter, I will report the structural and physical properties of (EDO-$TTFI_2)_2$[M$(mnt)_2$] (M = Ni, Pt). The salts are the first examples of magnetic organic conductors in which metallic conductivity of π-electrons and ferromagnetic interaction between *d*-electrons coexist.

5.2 Crystal structures

Figs. 5.1-5.3 shows the crystal structure of (EDO-$TTFI_2)_2$[M$(mnt)_2$] (M = Ni, Pt), for which the salts have the same structure regardless of the counter anions. The crystal data are summarized in tables 5.1-5.9. The donor and acceptor molecules form segregate one-dimensional chains elongating parallel to the *c*-axis, where the composition ratio of donor to acceptor is 2:1. Intra-chain molecular orbitals overlaps *p* make donor chains one-dimensional π-electronic systems, where a metallic conductivity of partially oxidized donor molecules is expected. In the acceptor chain, the central metal atom of an acceptor faces the sulfur atoms of the adjacent acceptor molecules located just above and beneath it, as featured with a slipped metal-over-sulfur configuration. The strong attractive interaction between iodo group of donor and cyano group of anion produces short inter-molecular atomic contacts (r_1, r_2, r_3) between donors and acceptors as depicted in Fig. 5.2. At the contacts, the nearest S-S distances r_3 are 4-6 % shorter than the sum of the van der Waals radii (3.70 Å). Therefore, it is probable that the electronic systems interact between conductive donors and magnetic acceptors through the short contact. It is noteworthy that the inter-molecular overlap integral between the SOMOs of intra-chain adjacent acceptors is very small, in spite of a short inter-planar

distance between them (3.69 and 3.73 Åfor M = Ni and Pt, respectively). The presence of a strong interaction between the iodo group of an EDO-$TTFI_2$ and the cyano group of the adjacent $M(mnt)_2^-$ plays an essential role in determining this overlapping mode of acceptors that gives this "pseudo-orthogonality".

5.3 EPR measurement

The EPR measurement of $(EDO\text{-}TTFI_2)_2[Ni(mnt)_2]$ shows only a single Lorentzian shape broad signal with line width $H_{pp} \sim 35$ mT. In general case, a conductive donor molecule shows a sharp EPR signal, therefore the absence of a sharp signal indicates the coalescence of a sharp signal of π-electron with a broad signal of d-electron due to the interaction between these two kinds of spins which is expected from the crystal structure of $(EDO\text{-}TTFI_2)_2[M(mnt)_2]$. On the other hand, no EPR signal is observed in $(EDO\text{-}TTFI_2)_2[Pt(mnt)_2]$ due to the strong spin-orbit coupling of platinum atom, which enhances the spin-lattice relaxation and widen a EPR signal.

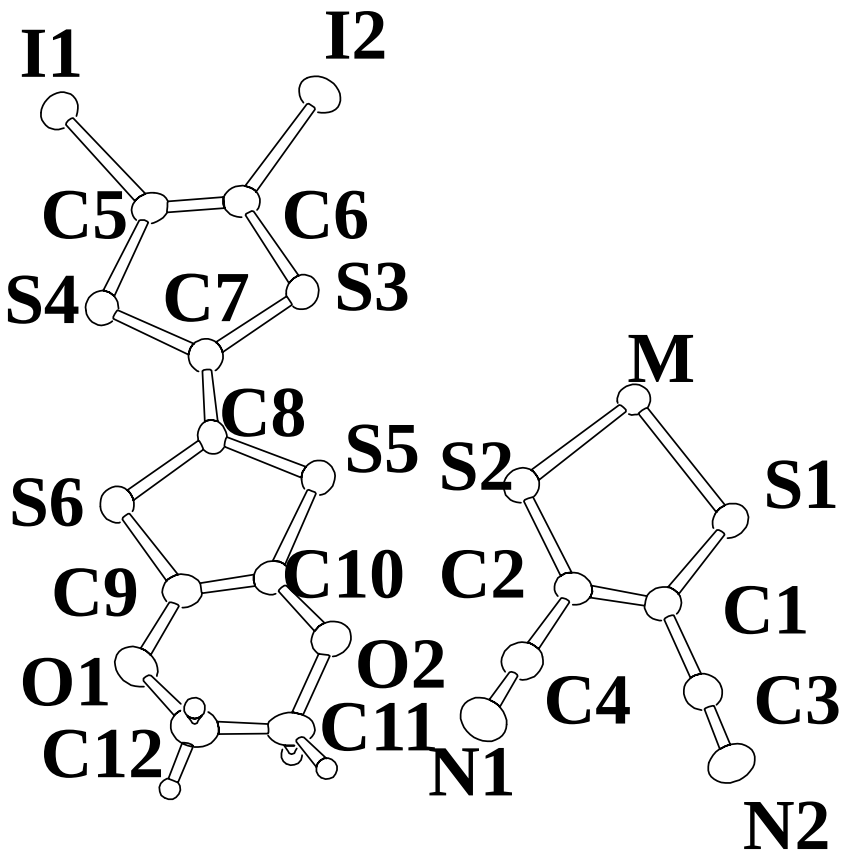

Fig. 5.1. Thermal ellipsoid plot (50 % probability) of (EDO-$TTFI_2$)$_2$[M(mnt)$_2$]

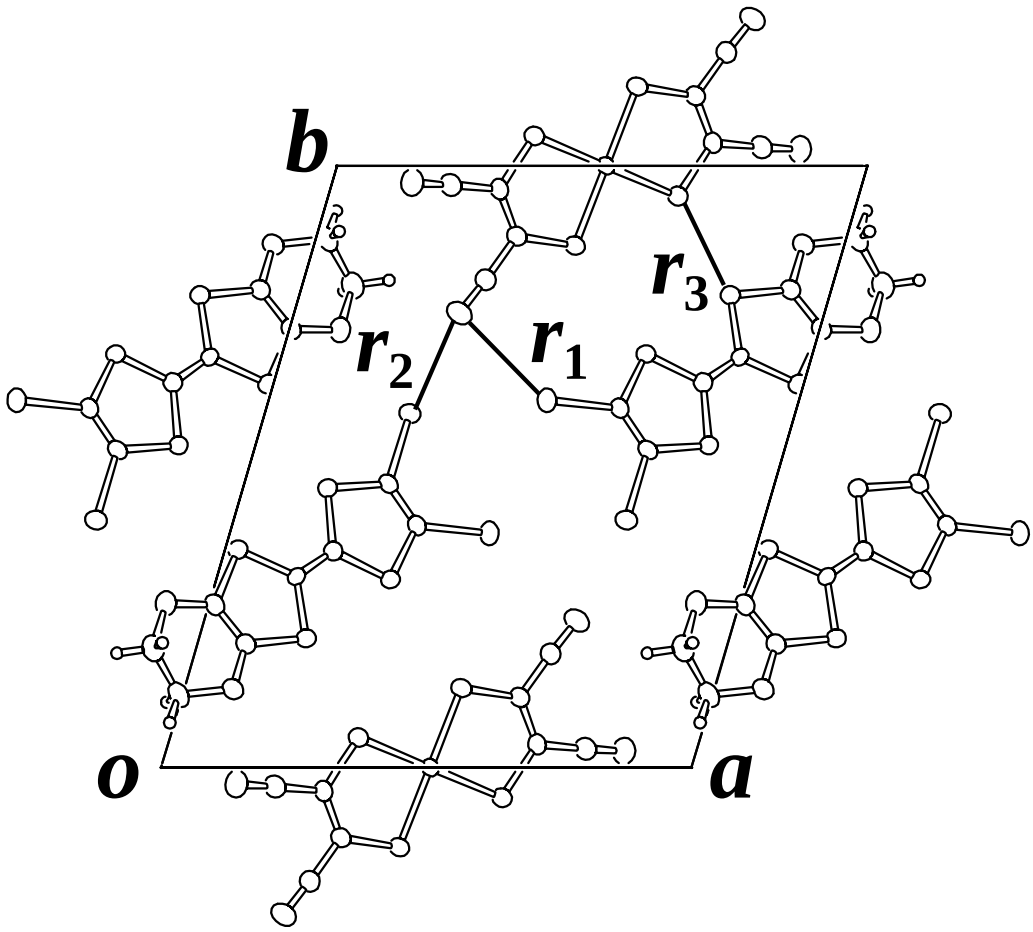

Fig. 5.2. The crystal structure of (EDO-TTFI_2)$_2$[M(mnt)$_2$]. The solid lines represent the short anion-donor contacts between N2-I1 (r_1=3.03 Å), N2-I2 (r_2=3.50 Å) and S2-S5 (r_3=3.54Å).

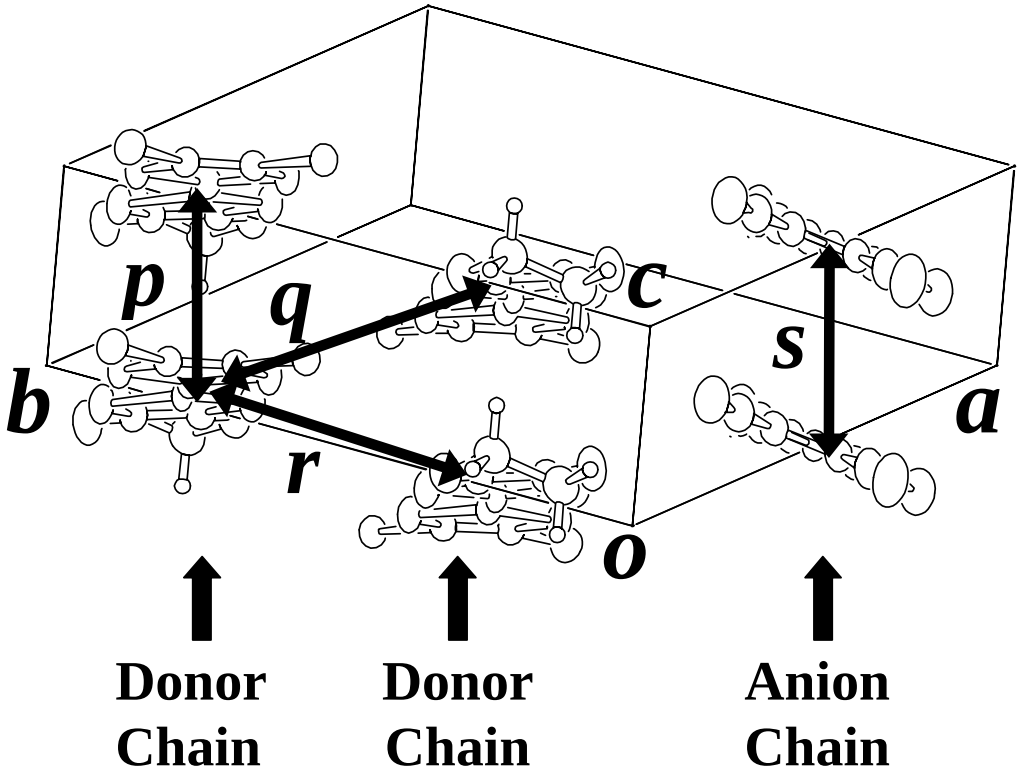

Fig. 5.3. The intra-chain structure and inter-molecular overlap integrals of (EDO-$TTFI_2$)$_2$[M(mnt)$_2$]. The values of overlap integrals are p=16.3×10^{-3} ! \$ q=6.54×10^{-3} ! \$$r$=3.26×10^{-3} between donor molecules and s=0.67×10^{-3} between anions, respectively.

Table 5.1. The crystallographic parameters of (EDO-$TTFI_2$)$_2$[M(mnt)$_2$].

	M = Ni	M = Pt
space group	$P\bar{1}$	$P\bar{1}$
a,Å	16.678(33)	14.077(3)
b,Å	16.590(46)	16.698(5)
c,Å	13.3994(12)	4.158(9)
α,deg	73.89(16)	96.51(2)
β,deg	105.66(16)	91.43(2)
γ,deg	165.54(4)	73.77(4)
V,Å^3	929.2(32)	932.3(4)
Z	1	1
R	0.1088	0.0288
$wR2$	0.2913	0.0792

The cell parameters of $[Ni(mnt)_2]^-$ salt is quite different from those of $[Pt(mnt)_2]^-$, but the difference is due to the different choice of unit cell and these two salts are isostructural.

Table 5.2. Atom positions of (EDO-TTFI_2)$_2$[Ni(mnt)$_2$].

atom	x	y	z	B_{eq} (Å^3)
I1	0.2308(2)	0.3201(2)	0.76847(7)	0.0370(3)
I2	0.3024(3)	0.1916(3)	0.98449(7)	0.0432(3)
Ni	0.5	0	1	0.0336(5)
S1	-0.0085(10)	-0.1963(10)	0.8254(3)	0.0398(7)
S2	-0.0534(10)	-0.0886(10)	0.6561(3)	0.0387(7)
S3	-0.3620(11)	-0.6483(11)	0.7015(3)	0.0434(8)
S4	-0.3803(10)	-0.5178(10)	0.5235(3)	0.0410(8)
S5	0.2413(11)	-0.2090(11)	0.8615(3)	0.0430(8)
S6	0.5509(11)	-0.0753(11)	0.9846(3)	0.0435(8)
O1	-0.6242(30)	-0.8519(29)	0.4195(8)	0.047(3)
O2	-0.6226(33)	-0.9923(32)	0.5922(9)	0.051(3)
N1	0.3435(53)	-0.3998(52)	0.8043(14)	0.071(4)
N2	-0.0598(46)	-0.5852(45)	0.6536(12)	0.063(4)
C1	-0.1308(37)	-0.2708(37)	0.7030(10)	0.035(3)
C2	-0.2750(36)	-0.4572(36)	0.6478(11)	0.035(3)
C3	-0.5245(37)	-0.7530(37)	0.5108(10)	0.036(3)
C4	0.1051(33)	0.0760(33)	0.7700(10)	0.033(3)
C5	-0.5169(37)	-0.8127(36)	0.5914(10)	0.037(3)
C6	-0.6255(46)	-1.0056(45)	0.4934(14)	0.054(4)
C7	-0.7787(43)	-1.0810(42)	0.4195(13)	0.050(4)
C8	0.1241(34)	0.0273(34)	0.8438(10)	0.034(3)
C9	0.0657(45)	-0.4616(44)	0.7265(13)	0.047(3)
C10	0.2230(36)	-0.3151(36)	0.8199(12)	0.039(3)
C11	0.3507(45)	-0.3359(45)	0.8380(11)	0.045(3)
C12	0.3614(38)	-0.2540(38)	0.8748(11)	0.040(3)
H6A	-0.7427(46)	-1.1703(45)	0.4938(14)	0.065
H6B	-0.4069(46)	-0.7994(45)	0.4731(14)	0.065
H7A	-0.7653(43)	-1.0757(42)	0.3535(13)	0.06
H7B	-1.0040(43)	-1.2976(42)	0.4356(13)	0.06

Table 5.3. Anisotropic thermal factors of (EDO-$TTFI_2$)$_2$[Ni(mnt)$_2$](Å^3).

atom	U_{11}	U_{22}	U_{33}	U_{23}	U_{13}	U_{12}
I1	0.0491(5)	0.0462(5)	0.0341(5)	-0.0058(4)	-0.0035(4)	0.0467(4)
I2	0.0571(5)	0.0580(6)	0.0264(5)	-0.0114(4)	-0.0089(4)	0.0560(5)
Ni	0.0524(12)	0.0510(12)	0.0252(12)	-0.0083(10)	-0.0062(10)	0.0509(12)
S1	0.068(2)	0.065(2)	0.024(2)	-0.0075(14)	-0.0065(15)	0.066(2)
S2	0.061(2)	0.058(2)	0.027(2)	-0.0082(14)	-0.0061(14)	0.059(2)
S3	0.071(2)	0.069(2)	0.030(2)	-0.010(2)	-0.008(2)	0.069(2)
S4	0.066(2)	0.062(2)	0.028(2)	-0.0078(15)	-0.0062(15)	0.063(2)
S5	0.066(2)	0.067(2)	0.035(2)	-0.018(2)	-0.015(2)	0.066(2)
S6	0.073(2)	0.073(2)	0.033(2)	-0.016(2)	-0.014(2)	0.072(2)
O1	0.071(6)	0.064(6)	0.026(5)	-0.015(5)	-0.015(5)	0.066(6)
O2	0.086(6)	0.079(6)	0.042(6)	-0.013(5)	-0.010(6)	0.081(6)
N1	0.122(10)	0.115(10)	0.058(10)	-0.010(10)	-0.003(10)	0.117(10)
N2	0.095(10)	0.089(10)	0.044(9)	-0.023(8)	-0.020(8)	0.090(10)
C1	0.059(6)	0.059(7)	0.026(6)	-0.004(6)	-0.001(6)	0.059(6)
C2	0.049(6)	0.048(6)	0.031(7)	-0.001(6)	0.001(6)	0.048(6)
C3	0.053(6)	0.053(7)	0.027(6)	-0.009(6)	-0.007(6)	0.052(6)
C4	0.042(6)	0.039(6)	0.031(6)	-0.005(5)	-0.003(5)	0.040(6)
C5	0.054(7)	0.051(7)	0.028(6)	-0.009(6)	-0.006(6)	0.051(7)
C6	0.064(9)	0.057(8)	0.055(10)	-0.007(8)	0.002(8)	0.058(8)
C7	0.057(8)	0.052(8)	0.041(9)	-0.008(7)	0.001(7)	0.052(8)
C8	0.047(6)	0.046(6)	0.023(6)	-0.005(5)	-0.002(5)	0.045(6)
C9	0.070(8)	0.065(8)	0.040(8)	-0.009(7)	-0.006(7)	0.067(8)
C10	0.049(6)	0.048(7)	0.040(8)	-0.007(6)	-0.001(6)	0.047(6)
C11	0.078(8)	0.075(8)	0.029(7)	-0.009(7)	-0.006(7)	0.075(8)
C12	0.055(7)	0.051(7)	0.035(7)	-0.006(6)	-0.002(6)	0.052(7)

Table 5.4. Bond length of (EDO-$TTFI_2$)$_2$Ni(mnt)$_2$] (Å)

I1-C4	2.08(2)	C1-C2	1.36(2)
I2-C8	2.07(2)	C3-C5	1.35(2)
S1-C1	1.74(2)	C4-C8	1.29(2)
S1-C8	1.75(2)	C6-C7	1.51(3)
S2-C1	1.74(2)	Ni-S6	2.152(5)
S2-C4	1.77(2)	Ni-S5	2.154(14)
S3-C5	1.74(2)	N1-C11	1.17(2)
S3-C2	1.76(2)	N2-C9	1.15(2)
S4-C2	1.74(2)	S5-C10	1.722(15)
S4-C3	1.74(2)	S6-C12	1.70(2)
O1-C3	1.35(2)	C9-C10	1.44(2)
O1-C7	1.46(2)	C10-C12	1.38(2)
O2-C5	1.34(2)	C11-C12	1.42(2)
O2-C6	1.44(2)		

Table 5.5. Bond angles of (EDO-TTFI$_2$)$_2$[Ni(mnt)$_2$] (deg)

C1-S1-C8	94.7(8)	O2-C6-C7	111.7(14)
C1-S2-C4	94.1(8)	O1-C7-C6	111.9(14)
C5-S3-C2	93.4(8)	C4-C8-S1	118.3(11)
C2-S4-C3	93.8(8)	C4-C8-I2	126.9(11)
C3-O1-C7	112.9(13)	S1-C8-I2	114.8(8)
C5-O2-C6	111.0(13)	S6-Ni-S6	180.00(2)
C2-C1-S1	122.1(12)	S6-Ni-S5	87.4(4)
C2-C1-S2	122.6(12)	S6-Ni-S5	92.6(4)
S1-C1-S2	115.3(8)	S6-Ni-S5	92.6(4)
C1-C2-S4	123.0(12)	S6-Ni-S5	87.4(4)
C1-C2-S3	120.2(12)	S5-Ni-S5	180.000(3)
S4-C2-S3	116.8(9)	C10-S5-Ni	103.0(7)
C5-C3-O1	124.7(14)	C12-S6-Ni	103.3(6)
C5-C3-S4	117.9(11)	N2-C9-C10	174.6(17)
O1-C3-S4	117.3(11)	C12-C10-C9	121.9(13)
C8-C4-S2	117.5(11)	C12-C10-S5	120.1(12)
C8-C4-I1	127.8(11)	C9-C10-S5	118.0(12)
S2-C4-I1	114.7(8)	N1-C11-C12	177.6(18)
O2-C5-C3	124.2(13)	C10-C12-C11	119.2(14)
O2-C5-S3	117.9(11)	C10-C12-S6	120.9(12)
C3-C5-S3	118.0(11)	C11-C12-S6	119.9(13)

Table 5.6. Atom positions of (EDO-TTFI$_2$)$_2$[Pt(mnt)$_2$].

atom	x	y	z	B_{eq} (Å^3)
Pt	0.5	0	0	0.02798(8)
I1	0.26866(3)	0.58856(2)	0.28004(9)	0.03408(10)
I2	0.48378(3)	0.38935(2)	0.20249(10)	0.03936(10)
S1	0.48487(10)	-0.13225(9)	-0.0305(4)	0.0398(3)
S2	0.34994(10)	0.04995(8)	0.2457(4)	0.0372(3)
S3	0.32495(10)	0.31257(8)	0.5096(4)	0.0352(3)
S4	0.15661(9)	0.46440(8)	0.5566(4)	0.0343(3)
S5	0.20096(10)	0.21481(8)	0.8589(4)	0.0381(3)
S6	0.02383(10)	0.36229(8)	0.8759(4)	0.0372(3)
O1	-0.0806(3)	0.2726(3)	1.1099(11)	0.0441(10)
O2	0.0926(3)	0.1305(3)	1.1081(12)	0.0466(10)
N1	0.1475(4)	-0.0274(4)	0.5365(17)	0.057(2)
N2	0.3060(5)	-0.2444(4)	0.1795(20)	0.065(2)
C1	0.3713(4)	-0.1167(3)	0.1503(14)	0.0334(11)
C2	0.3136(4)	-0.0387(3)	0.2675(14)	0.0338(11)
C3	0.3370(4)	-0.1890(4)	0.1681(17)	0.0423(13)
C4	0.2206(4)	-0.0314(4)	0.4158(16)	0.0413(13)
C5	0.2678(4)	0.4719(3)	0.4031(13)	0.0295(10)
C6	0.3440(4)	0.4024(3)	0.3798(13)	0.0298(10)
C7	0.2024(4)	0.3599(3)	0.6333(13)	0.0319(10)
C8	0.1481(4)	0.3177(3)	0.7730(13)	0.0298(10)
C9	0.0114(4)	0.2708(4)	1.0133(14)	0.0341(11)
C10	0.0914(4)	0.2056(3)	1.0115(14)	0.0335(11)
C11	-0.0065(5)	0.1214(4)	1.1100(17)	0.0447(14)
C12	-0.0790(5)	0.1984(4)	1.2611(16)	0.0448(14)
H11A	-0.0069(5)	0.0746(4)	1.2281(17)	0.054
H11B	-0.0264(5)	0.1088(4)	0.8893(17)	0.054
H12A	-0.1445(5)	0.1900(4)	1.2482(16)	0.054
H12B	-0.0631(5)	0.2074(4)	1.4883(16)	0.054

Table 5.7. Anisotropic thermal factors of (EDO-$TTFI_2$)$_2$[Pt(mnt)$_2$] (Å^3).

atom	U_{11}	U_{22}	U_{33}	U_{23}	U_{13}	U_{12}
Pt	0.02394(13)	0.02307(14)	0.0388(2)	0.00584(10)	0.00337(10)	-0.00842(10)
I1	0.0364(2)	0.0266(2)	0.0411(2)	0.00881(13)	0.00308(13)	-0.00947(13)
I2	0.0281(2)	0.0429(2)	0.0482(2)	0.0029(2)	0.00804(14)	-0.01196(15)
S1	0.0328(7)	0.0249(6)	0.0632(9)	0.0040(6)	0.0128(6)	-0.0097(5)
S2	0.0306(6)	0.0265(6)	0.0554(8)	0.0042(6)	0.0113(6)	-0.0088(5)
S3	0.0272(6)	0.0232(6)	0.0555(8)	0.0064(5)	0.0047(5)	-0.0060(5)
S4	0.0262(6)	0.0245(6)	0.0523(8)	0.0074(5)	0.0048(5)	-0.0058(5)
S5	0.0284(6)	0.0245(6)	0.0618(9)	0.0080(6)	0.0065(6)	-0.0064(5)
S6	0.0276(6)	0.0268(6)	0.0574(8)	0.0089(6)	0.0067(6)	-0.0056(5)
O1	0.032(2)	0.047(2)	0.057(3)	0.018(2)	0.008(2)	-0.011(2)
O2	0.036(2)	0.031(2)	0.078(3)	0.020(2)	0.002(2)	-0.013(2)
N1	0.038(3)	0.054(4)	0.081(4)	0.013(3)	0.019(3)	-0.013(3)
N2	0.052(3)	0.038(3)	0.113(6)	0.012(3)	0.017(4)	-0.021(3)
C1	0.031(2)	0.028(3)	0.045(3)	0.010(2)	0.003(2)	-0.010(2)
C2	0.026(2)	0.032(3)	0.047(3)	0.009(2)	0.003(2)	-0.011(2)
C3	0.031(3)	0.033(3)	0.065(4)	0.012(3)	0.005(3)	-0.010(2)
C4	0.037(3)	0.037(3)	0.055(3)	0.012(3)	0.007(3)	-0.013(2)
C5	0.030(2)	0.026(2)	0.036(3)	0.007(2)	-0.001(2)	-0.013(2)
C6	0.027(2)	0.029(2)	0.036(3)	0.004(2)	0.003(2)	-0.012(2)
C7	0.027(2)	0.027(2)	0.042(3)	0.003(2)	0.002(2)	-0.008(2)
C8	0.021(2)	0.022(2)	0.044(3)	0.002(2)	0.002(2)	-0.002(2)
C9	0.031(3)	0.033(3)	0.042(3)	0.007(2)	0.003(2)	-0.014(2)
C10	0.031(2)	0.028(3)	0.044(3)	0.006(2)	0.004(2)	-0.011(2)
C11	0.040(3)	0.046(3)	0.059(4)	0.016(3)	0.000(3)	-0.024(3)
C12	0.041(3)	0.051(4)	0.050(3)	0.017(3)	0.004(3)	-0.020(3)

Table 5.8. Bond length of (EDO-$TTFI_2$)$_2$[Pt(mnt)$_2$] (Å)

Pt-S2	2.2652(14)	C6-S3	1.741(5)
Pt-S1	2.2664(15)	C7-C8	1.354(7)
C1-C2	1.371(8)	C7-S4	1.746(5)
C1-C3	1.431(7)	C8-S6	1.743(5)
C2-C4	1.429(7)	C9-C10	1.330(8)
C3-N2	1.133(8)	C9-O1	1.357(6)
C4-N1	1.138(8)	C10-O2	1.355(6)
I1-C5	2.072(5)	C11-O2	1.445(7)
I2-C6	2.063(5)	C11-C12	1.484(9)
C5-C6	1.338(7)	C12-O1	1.446(7)
C5-S4	1.747(5)		

Table 5.9. Bond angle of (EDO-$TTFI_2$)$_2$[Pt(mnt)$_2$] (deg)

S2-Pt-S2	180	C8-C7-S3	122.0(4)
S2-Pt-S1	90.01(5)	S4-C7-S3	114.5(3)
S1-Pt-S1	180	C7-C8-S6	122.4(4)
C2-C1-C3	120.0(5)	C7-C8-S5	120.8(4)
C2-C1-S1	122.6(4)	S6-C8-S5	116.8(3)
C3-C1-S1	117.3(4)	C10-C9-O1	125.7(5)
C1-C2-C4	119.0(5)	C10-C9-S6	118.0(4)
C1-C2-S2	122.0(4)	O1-C9-S6	116.3(4)
C4-C2-S2	119.0(4)	C9-C10-O2	124.4(5)
N2-C3-C1	177.2(7)	C9-C10-S5	118.3(4)
N1-C4-C2	178.4(7)	O2-C10-S5	117.2(4)
C1-S1-Pt	102.3(2)	O2-C11-C12	112.1(5)
C2-S2-Pt	103.1(2)	O1-C12-C11	113.2(5)
C6-C5-S4	117.1(4)	C6-S3-C7	95.4(2)
C6-C5-I1	126.5(4)	C7-S4-C5	95.4(2)
S4-C5-I1	116.4(3)	C10-S5-C8	93.5(2)
C5-C6-S3	117.5(4)	C8-S6-C9	93.3(3)
C5-C6-I2	126.9(4)	C9-O1-C12	111.2(5)
S3-C6-I2	115.6(3)	C10-O2-C11	110.3(4)
C8-C7-S4	123.5(4)		

5.4 Electrical resistivity

The electrical resistivities of (EDO-$TTFI_2$)$_2$[M(mnt)$_2$] along the c-axis are considerably low, ranging 9.1×10^{-3} Ωcm and 5.9×10^{-3} Ωcm at room temperature for M = Ni and Pt, respectively. As shown in Fig. 5.4 and 5.5, the resistivity ρ shows metallic behavior down to 110K, followed by an onset of a metal-insulator (M-I) transition for both salts. The metallic feature is considered to originate from the one-dimensional π-electronic structure of the donor chain with the 3/4 filled state. From the maximum of $d\ln(\rho/\Omega)/d(1/T)$, M-I transition temperatures are estimated at 88 K for M = Ni and 96 K for M = Pt. In the low temperature insulating state, the activation energies of the resistivity are considerably small, as estimated at E_a = 60 and 85 meV for M = Ni and Pt, respectively. Since neither significant superlattice reflection nor discontinuous change in the lattice constant is observed in X-ray oscillation photographs taken in the temperature range 16-300 K, the origin of these transitions can be ascribed to a $4k_F$ charge density wave or spin density wave.

The M-I transition temperature T_{M-I} and the activation energy E_a are decrease as the pressure is raised in the pressure range $P < 10$ kbar, as shown in Fig. 5.6 and 5.7. In the pressure region, applying pressure enhances the intra-chain overlap of HOMOs of donor molecules resulting in the increase of the conductivity and decreasing of T_{M-I} and E_a. In spite of the decreasing of these values in lower pressure region, the M-I transition of these salts cannot be suppressed by applying pressure, while insulating phase of many quasi 1D organic conductors can be suppressed by high pressure owing to the change of their dimensionallity from 1D to 2D. The reason why the insulating phase of (EDO-$TTFI_2$)$_2$[M(mnt)$_2$] is not suppressed under high pressure is attributed to the structural feature of the crystals. In this materials, conductive donor columns are well separated each other by anion chains. Therefore applying pressure cannot enhance the inter-chain electron transfer in the crystals, where the contribution of anion chains to electron transfer is small due to the large difference between energy of molecular orbital of donor and anion.

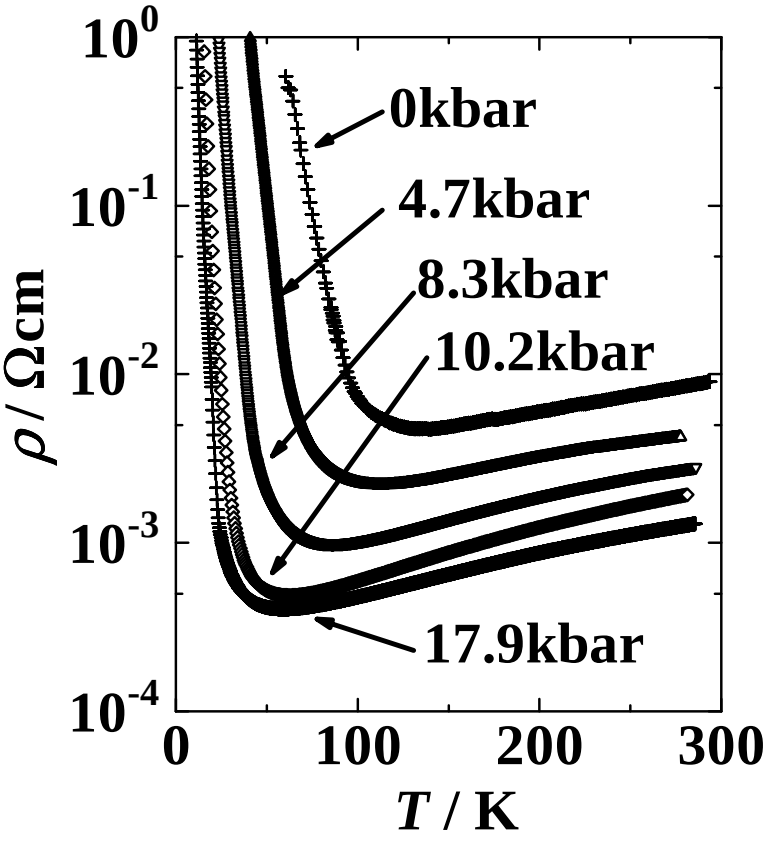

Fig. 5.4. Temperature dependence of resistivities of (EDO-$TTFI_2$)$_2$[Ni(mnt)$_2$] at ambient and high pressures.

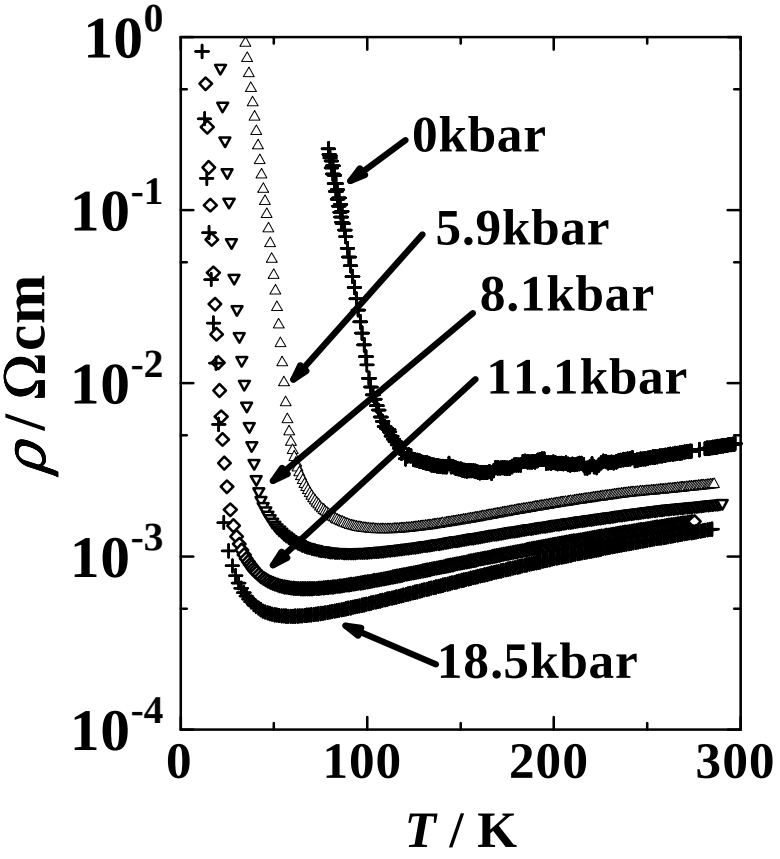

Fig. 5.5. Temperature dependence of resistivities of (EDO-$TTFI_2$)$_2$[Pt(mnt)$_2$] at ambient and high pressures.

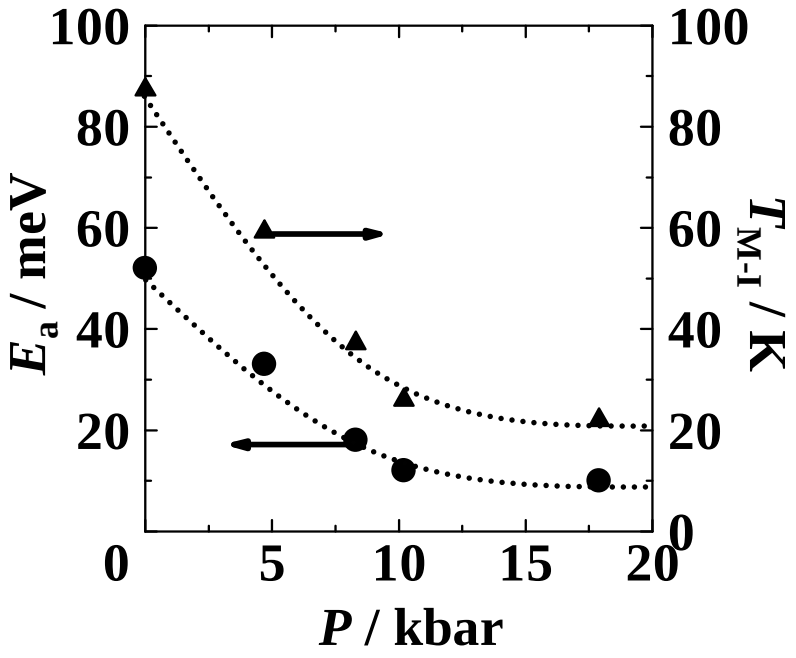

Fig. 5.6. Pressure dependence of M-I transition temperature and activation energy below $T_{\mathrm{M-I}}$ of (EDO-TTFI$_2$)$_2$[Ni(mnt)$_2$]. The dotted lines are guides for the eyes.

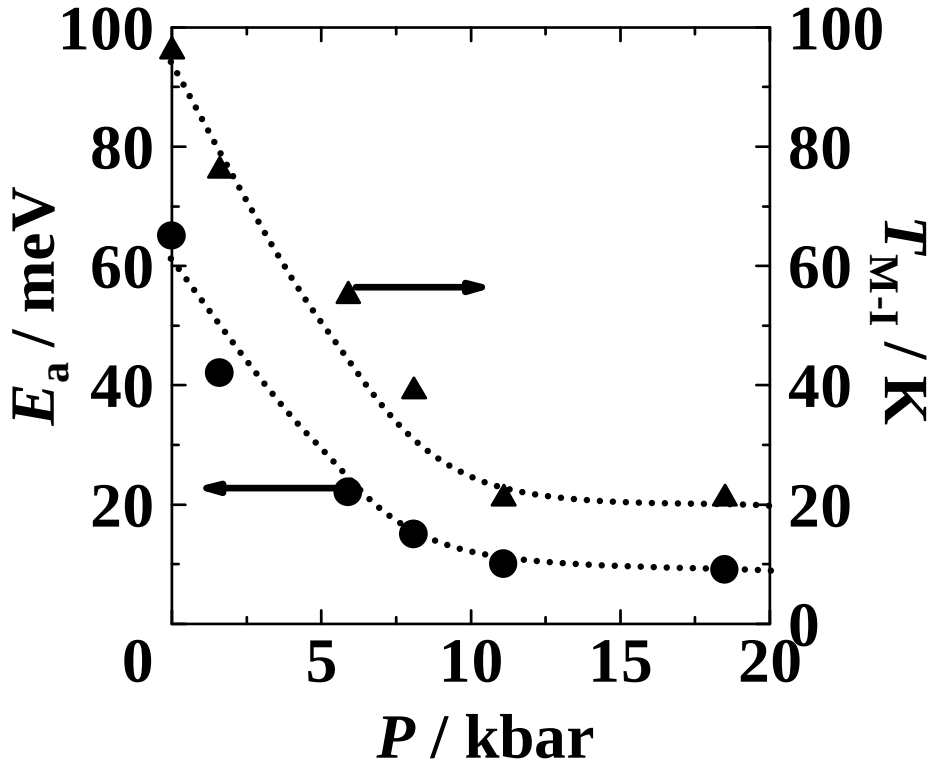

Fig. 5.7. Pressure dependence of M-I transition temperature and activation energy below T_{M-I} of (EDO-TTFI$_2$)$_2$[Pt(mnt)$_2$]. The dotted lines are guides for the eyes.

5.5 Magnetic susceptibilities

Fig. 5.8 shows the temperature dependence of the magnetic susceptibility χ of (EDO-TTFI$_2$)$_2$[Ni(mnt)$_2$] after the subtraction of the core diamagnetic contribution. The value of χT at T = 300 K is estimated at 0.387 emu·K mol^{-1}, which corresponds to one $S = 1/2$ spin per formula unit. Taking into account the 1/2 filled state of [Ni(mnt)$_2$]$^-$, an electron on a [Ni(mnt)$_2$]$^-$ molecule is responsible for the observed localized spin. The χT value monotonously increases as the temperature is lowered, demonstrating the presence of ferromagnetic interaction between the localized spins, with a Weiss temperature Θ = 14 K. The susceptibility is well fitted with the one-dimensional $S = 1/2$ ferromagnetic Heisenberg model [6] with intra-chain ferromagnetic interaction J = 18 K. According to the magnetization curves shown in Fig. 5.9, the spin multiplicity S increases as the temperature decreases, suggesting the development of short-range ordering of ferromagnetic clusters, while no magnetic long range order is observed. The absence of a three-dimensional magnetic ordering, which is evidenced by the absence of an anomaly on the susceptibility in addition to a non-hysteretic trend of the magnetization curves, is the natural consequence of the one-dimensional Heisenberg feature of the spin system suggesting the weakness of the inter-chain interaction.

Next, Fig. 5.10 exhibits the temperature dependence of the magnetic susceptibility of (EDO-TTFI$_2$)$_2$[Pt(mnt)$_2$]. The χT value 0.392emu·K mol^{-1} at T = 300 K is again consistent with an $S = 1/2$ spin per acceptor, and the presence of ferromagnetic interaction is suggested by a Weiss temperature Θ = 15 K. Because of the large spin-orbit interaction of platinum d-electrons, localized spins on [Pt(mnt)$_2$]$^-$ bear an Ising-like character rather than a Heisenberg-like one. In fact, the susceptibility with $H \parallel (a\text{-}b)$ direction is well fitted with the one-dimensional ferromagnetic Ising model [7] with intra-chain interaction J = 20 K in the temperature range from 7.5 to 300 K, while that of other directions shows obviously smaller values. χ takes a maximum at 6 K in all directions, below which χ suddenly decreases due to the AF transition at T_N = 5.5 K caused by weak intra-chain AF interaction. Fig. 5.11 and 5.12 shows the magnetization curves of (EDO-TTFI$_2$)$_2$[Pt(mnt)$_2$] at 6.5 K ($T > T_N$) and 3.5 K ($T < T_N$). A discontinuous upsurge of the magnetization

appears at $H_c = 0.15$ T, $T = 3.5$ K, where the external magnetic field H is applied parallel to the (a-b) axis. The sudden increase of the susceptibility is ascribed as a field-induced antiferromagnet-ferromagnet transition (metamagnet transition) at $H_c = 0.16T$, which is owing to weak inter-chain AF interaction and strong intra-chain ferromagnetic interaction. The spin easy axis is therefore determined as nearly parallel to the (a-b) direction, which corresponds to the side-by-side direction of the $[Pt(mnt)_2]^-$ molecules. From the value of H_c in the magnetization curve below T_N, the magnitude of the inter-chain AF interaction is estimated at $J' \sim 0.05$ K. The fact suggests the origin of inter-chain interaction is dipole-dipole interaction between ferromagnetically ordered anion chains, because the strength of interaction is comparable to dipole-dipole interaction ~ 0.1 T. The large magnetic anisotropy associated with the Pt electrons works to enhance the role of inter-chain AF interaction, resulting in the occurrence of the three-dimensional ordered state. The magnetization with $H \parallel$(a-b) direction is smaller than 1 μ_B, but the difference is originated from the misalignment of the crystals.

In the magnetization curve with $H \parallel$(a-b) direction, a small hysteresis is observed below H_c. Once an external magnetic field larger than H_c is applied to $(EDO\text{-}TTFI_2)_2[Pt(mnt)_2]$, the magnetization of field decreasing process shows ca. 0.1 μ_B larger value than that of increasing process. The difference between the magnetization in field increasing and decreasing process becomes smaller as the external magnetic fields is lowered, and it reaches zero at $H = 0$.

The hysteresis becomes smaller as temperature is raised, as shown in Fig. 5.13. In the measurement, the magnetic field $H = 0.2$ T was applied along the (a-b) direction, then the field is set to $H = 10$ mT and the susceptibility is measured in the heating process. The result shows that the hysteresis is rapidly reduced as temperature is raised, and it takes a minimum at around 3.8 K.

The origin of the ferromagnetic interaction and hysteresis of magnetization curve are discussed in the next chapter.

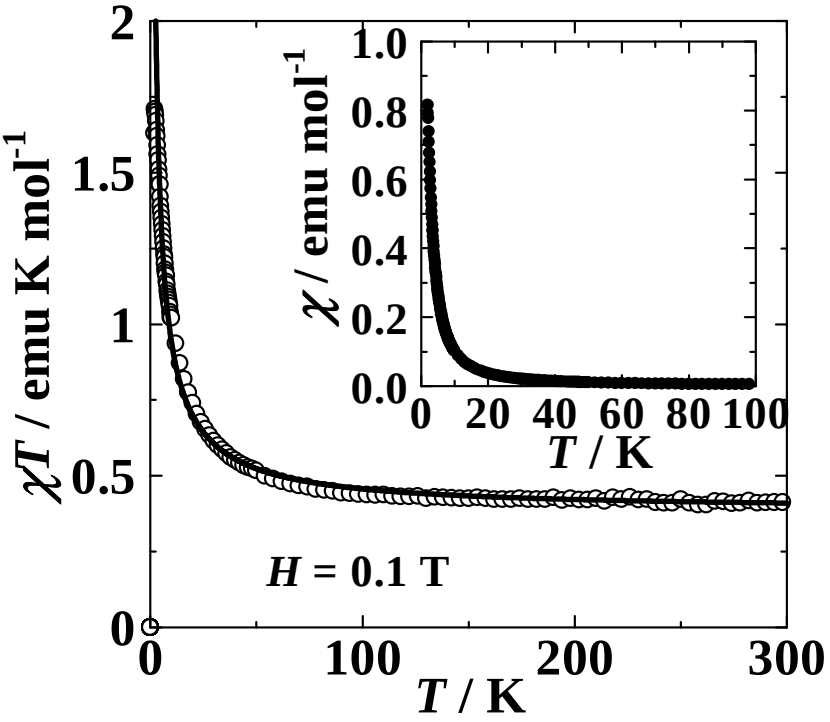

Fig. 5.8. Temperature dependence of the isotropic magnetic susceptibility χ (inset) and χT of (EDO-TTFI$_2$)$_2$[Ni(mnt)$_2$] with external magnetic field $H = 0.1$ T. The solid line represents the $S = 1/2$ 1D ferromagnetic Heisenberg spin system with intra-chain ferromagnetic interaction $J = 18$ K.

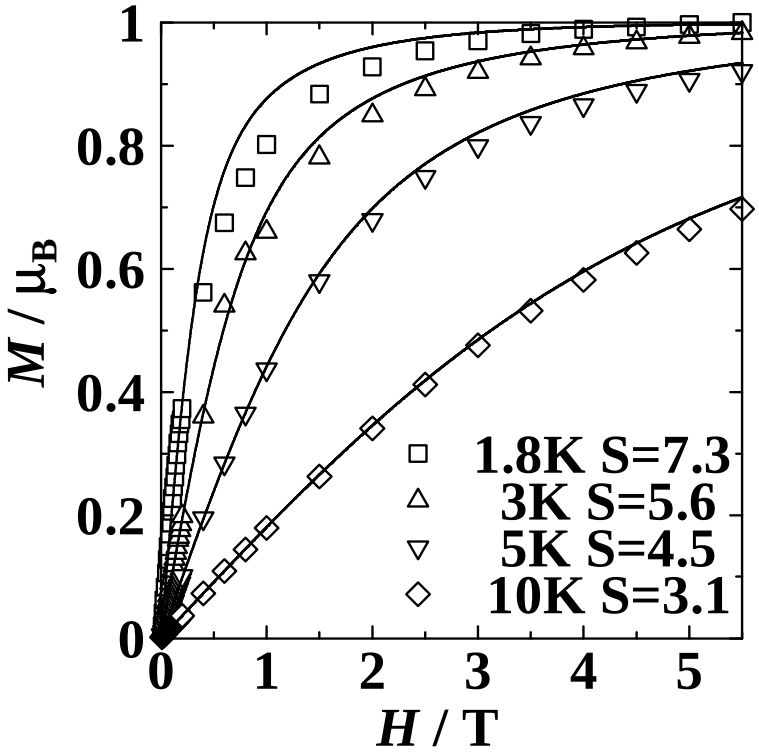

Fig. 5.9. The magnetization curves of (EDO-$TTFI_2$)$_2$[Ni(mnt)$_2$] at various temperatures. The data in each temperatures are fitted with the Brillouin function with effective spin value S (solid lines) which corresponds to the size of short range order.

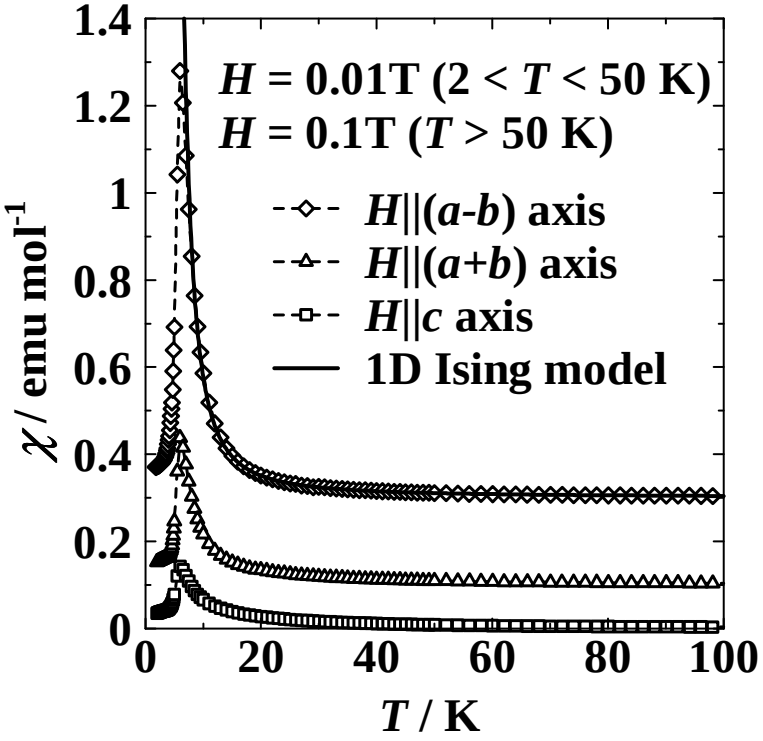

Fig. 5.10. Temperature dependence of the magnetic susceptibility χ (inset) of (EDO-TTFI$_2$)$_2$[Pt(mnt)$_2$] with external magnetic field $H = 0.01$ ($T < 50$ K) and 0.1 T ($50 < T < 300$ K). The data with $H \parallel (a\text{-}c)$ and $(a{+}c)$ are upshifted by 0.3 and 0.1 emu·K mol^{-1}, respectively, for clarify. The solid line represents the $S = 1/2$ 1D ferromagnetic Ising spin system with intra-chain ferromagnetic interaction $J = 20$ K.

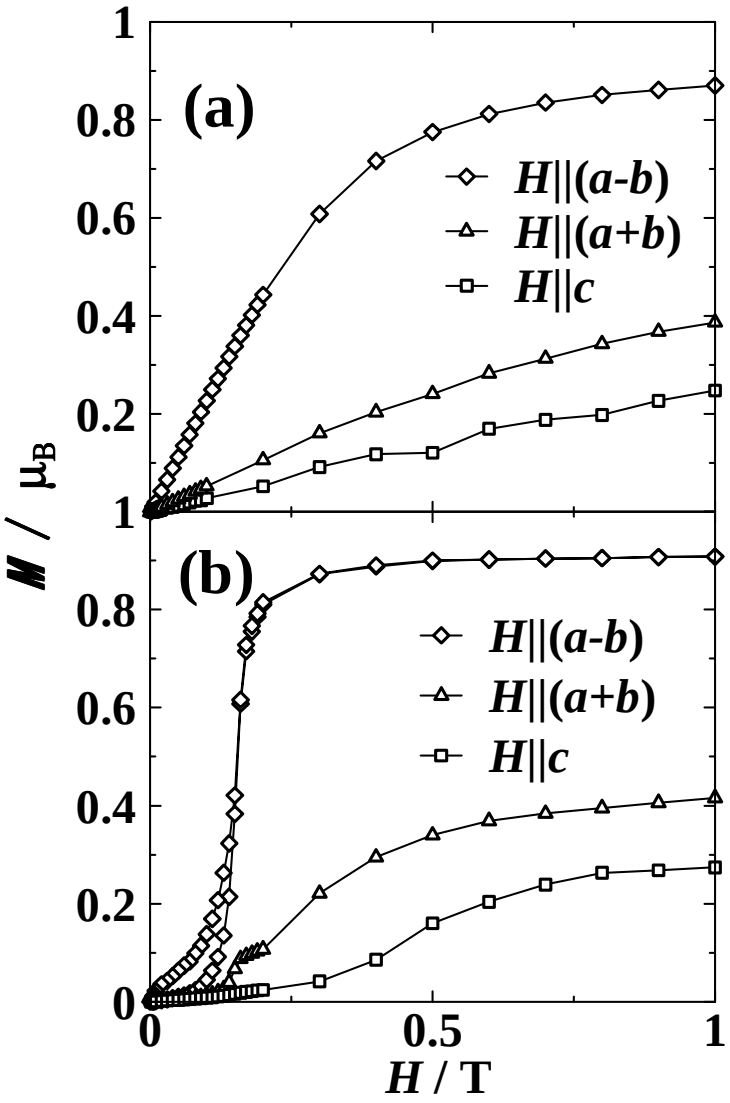

Fig. 5.11. The magnetization curves of (EDO-$TTFI_2$)$_2$[Pt(mnt)$_2$] at (a) 6.5 K (above T_N) and (b) 3.5 K (below T_N).

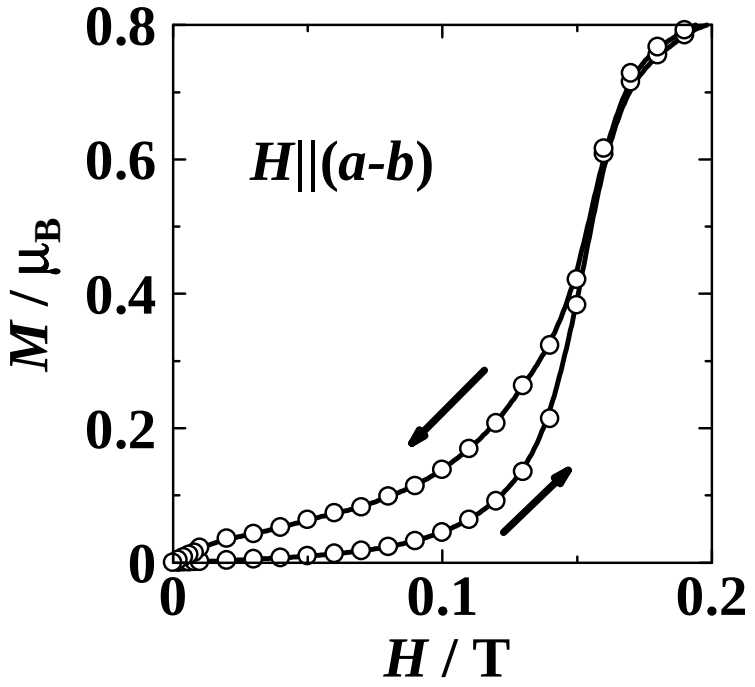

Fig. 5.12. The enlargement of the low magnetic region of the magnetization curves of (EDO-TTFI$_2$)$_2$[Pt(mnt)$_2$] with H $\|(a\text{-}b)$ direction at 2 K. A small hysteresis is observed below metamagnetic transition field $H_c = 0.16$ T.

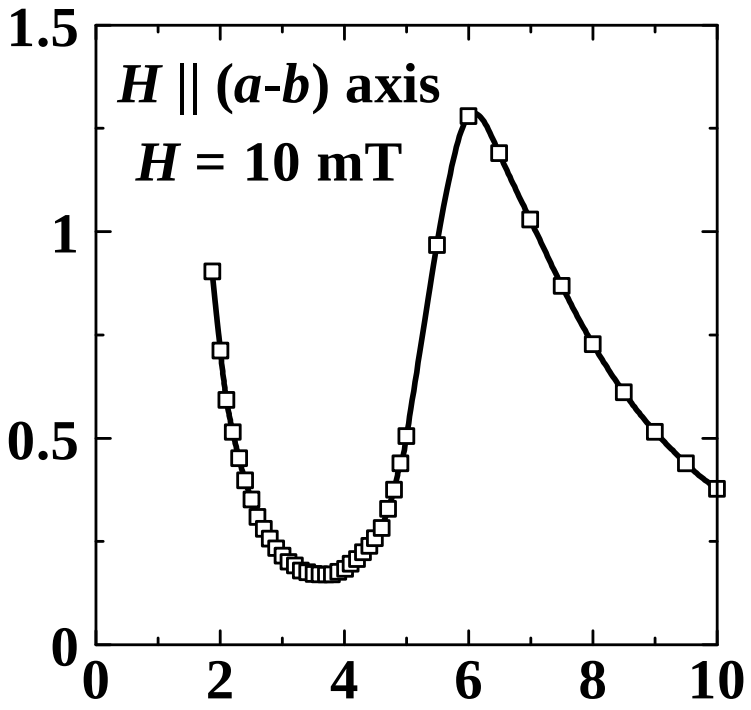

Fig. 5.13. The temperature dependence of the hysteresis of the (EDO-$TTFI_2)_2[Pt(mnt)_2]$ in the heating process. At first, magnetic field $H = 0.2$ T is applied along the (a-b) axis at $T = 2$ K. Then, the field is lowered to 10 mT and the susceptibility was measured in heating process. The large value around 6 K is the effect of the intra-chain ferromagnetic short range order.

5.6 AC susceptibility

To investigate the dynamics of the 1D Ising ferromagnetic chain, AC susceptibility of (EDO-TTFI$_2$)$_2$[Pt(mnt)$_2$] was measured. The AC susceptibility χ' of (EDO-TTFI$_2$)$_2$[Pt(mnt)$_2$] with $H = 0$ T in (a-b)is shown in Fig. 5.14. χ' is independent of the frequency of AC magnetic field, and it takes a large value above $T_{\rm N}$ due to the ferromagnetic intra-chain short range order, while χ'' is ~ 0 in whole temperature range observed. χ' increases as temperature is lowered and forms a peak at ca.6 K followed by steep decrease at $T_{\rm N} = 5.5$ K. Below $T_{\rm N}$, χ' has a shoulder at ca. 3.5 K, then χ' rapidly becomes zero as temperature is lowered.

On the contrary to the results in $H_{\rm DC} = 0$, χ' and χ'' in $H_{\rm DC} = 0.16$ T, the metamagnetic transition field, largely depend on the AC frequency. In the condition $H_{\rm DC} = 0.16$ T, inter-chain AF interaction is just canceled by $H_{\rm DC}$, therefore AC susceptibility under the condition is roughly regarded as a AC susceptibility of a single ferromagnetic Ising chain. χ' with $H_{\rm DC} = 0.16$ T gradually increases regardless of the frequency as shown in Fig. 5.15. Below $T_{\rm N}$, the rate of the increase of χ' is risen, and χ' forms a peak at around 3.5 K, which is roughly same as the temperature where the hysteresis of the magnetization curved disappears. In the lower temperature side of the peak, the rate of the decrease of χ' largely depends on the frequency; that is, χ' decreases more rapidly as frequency is raised. In addition, χ'' shows significant increase below the temperature as shown in Fig. 5.16. These facts mean that the motion of the magnetic spin in the ferromagnetic Ising chain of (EDO-TTFI$_2$)$_2$[Pt(mnt)$_2$] becomes slower below the temperature.

The relaxation time τ of the spin is estimated from the Cole-Cole plot, which is a plot of χ'' vs χ' taking a maximum at the point of $\tau = 1/f$, where f is the frequency of the AC magnetic field. The Cole-Cole plot is shown in Figs. 5.17. The Cole-Cole plot shows a a semicircle-like behavior which is a typical shape of the single relaxation process. The small discrepancy between a semicircle and the plot indicate the small contribution of one or more another spin relaxation process except principal that, but the detail of such relaxation processes is incomprehensible. The relaxation time τ of the main process estimated from the Cole-Cole plot is plotted in Fig. 5.18. The temperature dependence of τ is described as the

following equation;

$$\tau = 1.6 \times 10^{-9} \exp(32/T). \tag{5.1}$$

The activation energy $\Delta E = 32$ K is roughly twice value of the intra-chain ferromagnetic interaction $2J = 40$ K, as expected from the Glauber's theory of 1D Ising ferromagnet [8] confirmed by recent experiments [9–12].

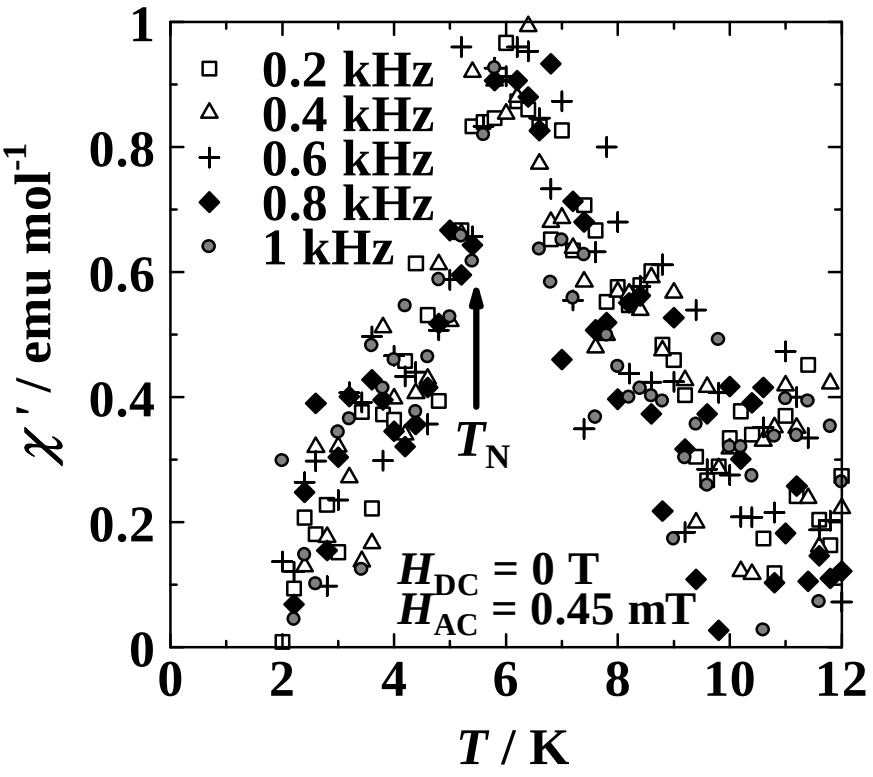

Fig. 5.14. Temperature dependence of AC susceptibility χ' of (EDO-$TTFI_2)_2[Pt(mnt)_2]$ along the (*a*-*b*) direction under DC magnetic field $H_{DC} = 0$ T and AC magnetic field $H_{AC} = 0.45$ mT.

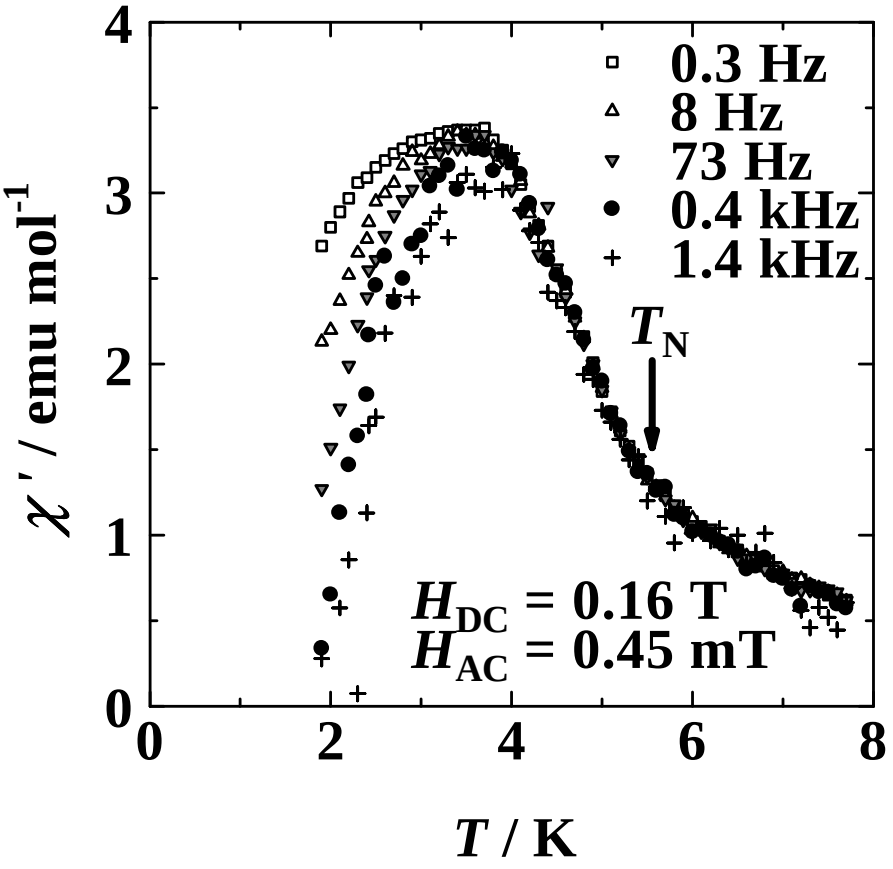

Fig. 5.15. Temperature dependence of AC susceptibility χ' of (EDO-TTFI$_2$)$_2$[Pt(mnt)$_2$] along the (*a*-*b*) direction under DC and AC magnetic field $H_{\rm DC} = 0.16$ T and $H_{\rm AC} = 0.45$ mT, respectively.

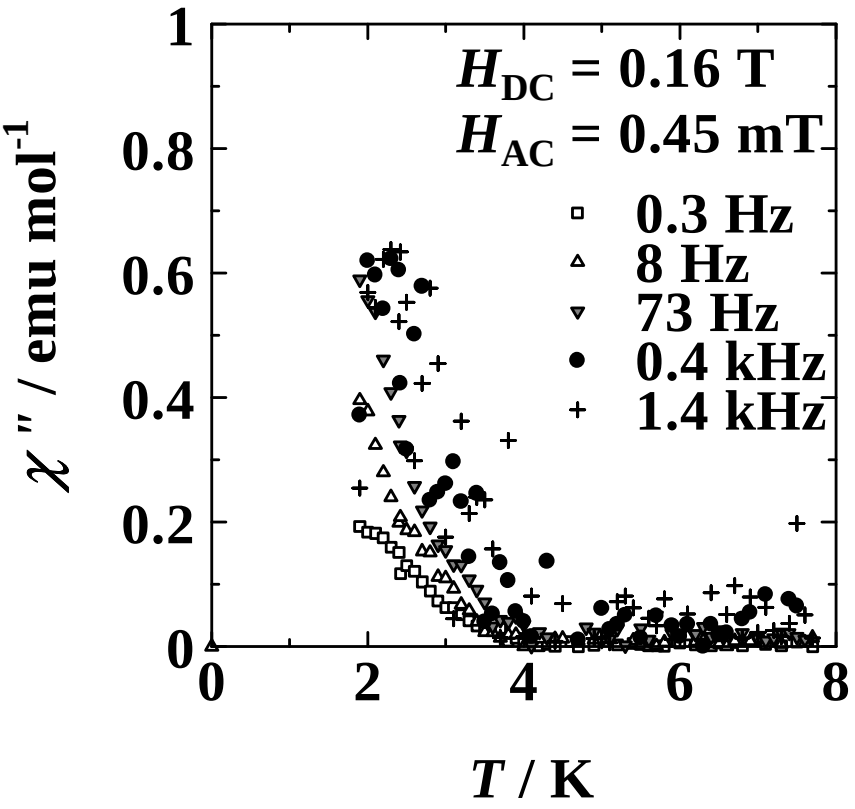

Fig. 5.16. Temperature dependence of AC susceptibility χ'' of (EDO-$TTFI_2)_2[Pt(mnt)_2]$ along the (a-b) direction under DC and AC magnetic field $H_{DC} = 0.16$ T and $H_{AC} = 0.45$ mT, respectively.

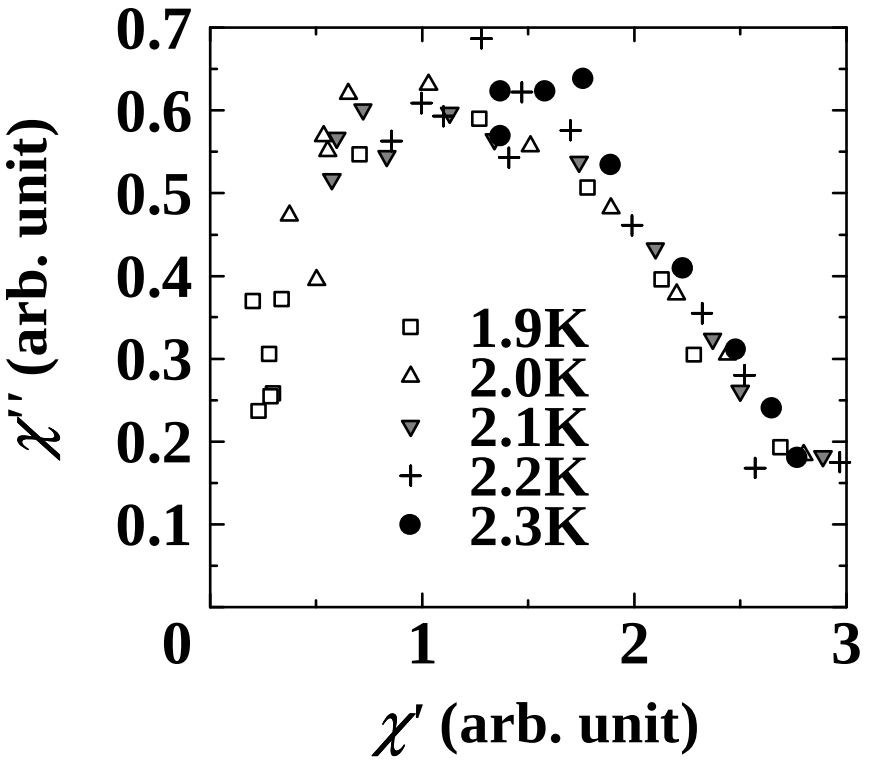

Fig. 5.17. Cole-Cole plot of the AC susceptibility of (EDO-$TTFI_2$)$_2$[Pt(mnt)$_2$] along the (*a*-*b*) direction under DC and AC magnetic field $H_{\rm DC}$ = 0.16 T and $H_{\rm AC}$ = 0.45 mT, respectively.

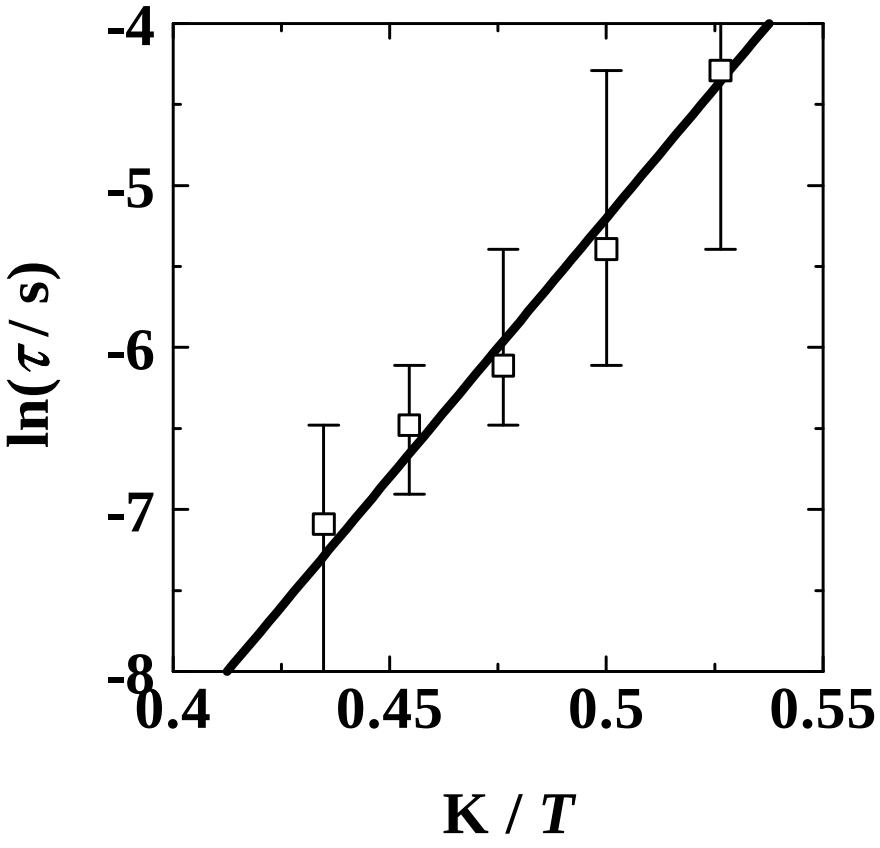

Fig. 5.18. Temperature dependence of the relaxation time of the spin of (EDO-$TTFI_2)_2[Pt(mnt)_2]$ estimated from the Cole-Cole plot shown in Fig. 5.17.

5.7 Magnetic susceptibility under high pressure

To investigate the magnetism of the $[Pt(mnt)_2]^-$ salt, pressure dependence of the magnetization is investigated as shown in Fig. 5.19. In the result, absolute values of the magnetization are meaningless due to the large contribution of the magnetization of the high-pressure cell, which is roughly temperature independent. The temperature dependencies of the magnetization above T_N are roughly temperature independent indicating an unchanged intra-chain ferromagnetic interaction. In contrary to the magnetization above T_N, that below T_N shows a steep increase as the pressure is raised above ca. 5 kbar accompanied by a small hysteresis loop at around 3.8 K.

However, the increase of the magnetization does not mean the stabilization of the ferromagnetic phase as shown below. The magnetization curve of the salt along the (a-b) direction at 8.23 kbar, 1.8 K indicates not a stabilization of the ferromagnetic state but a decrease of the metamagnetic transition field which decreases from ca. 0.16 T to 0.12 T as the pressure is raised from 0 kbar to 8.23 kbar. Therefore, it is concluded that the increase of the magnetization at high pressure with $H = 0.1$ T is the natural consequence of the metamagnetic transition field approaching the external magnetic field.

Regrettably, the origins of the hysteresis loop and the decrease of the metamagnetic transition field are unclear.

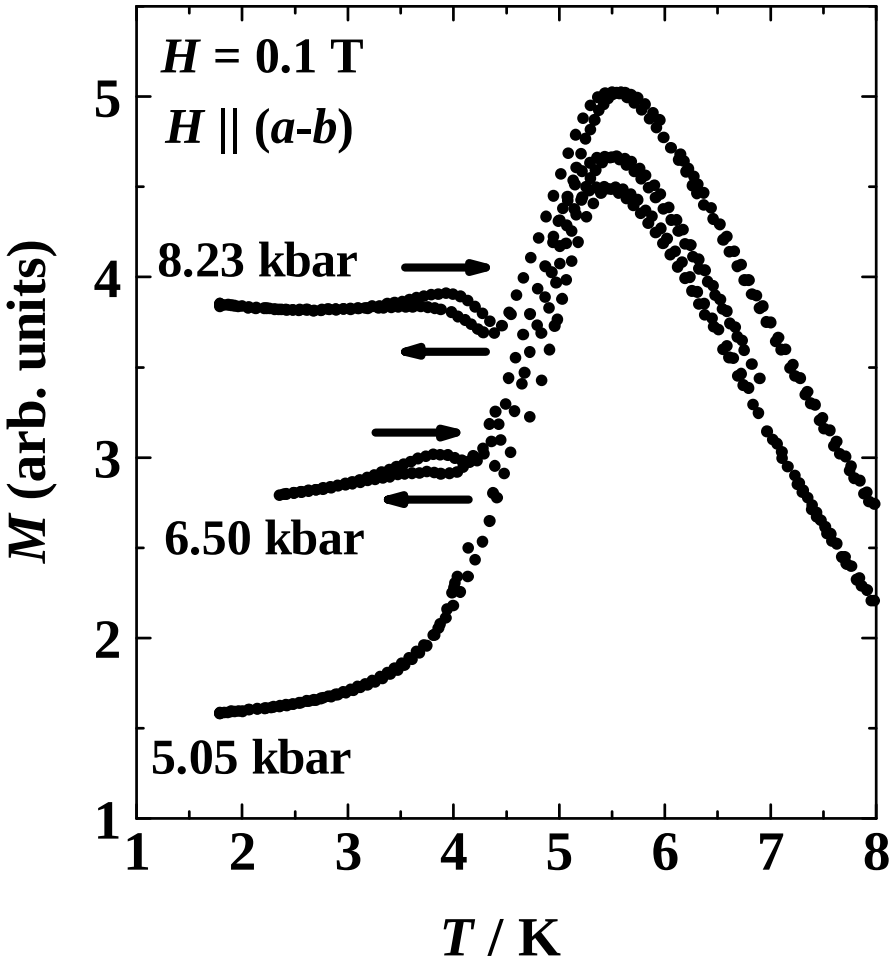

Fig. 5.19. The pressure dependence of the magnetization of (EDO-$TTFI_2)_2[Pt(mnt)_2]$ along the (a-b) direction with $H = 0.1$ T under high pressures.

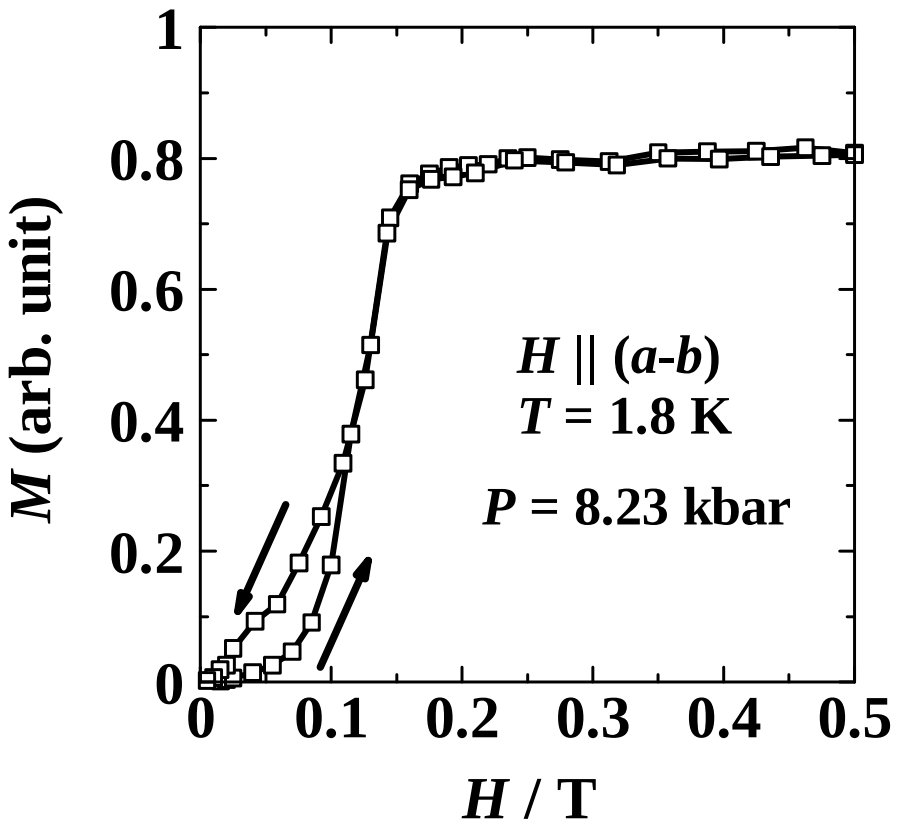

Fig. 5.20. The magnetization curve of (EDO-$TTFI_2$)$_2$[Pt(mnt)$_2$] along the (a-b) direction at 8.23 kbar, 1.8 K.

5.8 Discussion

5.8.1 The origin of the ferromagnetic interaction

The origin of the ferromagnetic interaction can be explained in terms of two factors. First, molecular orbital overlaps is considerably small between SOMOs of $M(mnt)_2^-$ molecules in spite of the presence of short intermolecular atomic contacts, as shown in Fig. 5.3. The orbital overlaps between SOMOs causes an AF interaction, because the inter-molecular interaction J is approximately described as

$$J \sim 2k + 4\beta S, \tag{5.2}$$

where k, β and S are Coulomb integral, resonance integral and overlap integral between SOMOs [13, 14], respectively. The first term gives a small ferromagnetic interaction, while the second term gives an AF interaction. In ordinary molecule-based magnets, overlap integral S is large due to the stabilizing effect of the overlap resulting in the AF inter-molecular interaction [15]. On the contrary to such ordinary molecule-based magnets, S is small in (EDO-$TTFI_2$)$_2$[$M(mnt)_2$] thanks to that the strong donor-anion attractive interaction disturbs the overlap between SOMOs of the anions, resulting in the weakness of the AF interaction between the anions. The effect of this disturbance is clearly evidenced by comparing the magnetism of (EDO-$TTFI_2$)$_2$[$M(mnt)_2$] to that of (DT-TTF)$_2$[$M(mnt)_2$] [16], the crystal structures of these salts are similar to each other. Although the similarity of the crystal structure, there is a important difference between the salts; that is, the SOMOs of the anions overlaps each other in (DT-TTF)$_2$[$M(mnt)_2$] resulting in the AF interaction between anions.

Second, the spin polarization causes ferromagnetic interaction (McConnell's theory [17]). The spin of the $[M(mnt)_2]^-$ anion is described as a large positive spin density at a central metal atom and small negative spin densities at sulfur atoms of the ligand [5]. In the McConnell's model, the net interaction between two magnetic molecules are represented as the sum of the "local" AF interactions. In the (EDO-$TTFI_2$)$_2$[$M(mnt)_2$] salt, the slipped metal-over-sulfur configuration of molecules (Fig. 5.21) causes AF interaction between the sulfur atom of an $[M(mnt)_2]^-$ and

the central metal atom of adjacent $[M(mnt)_2]^-$. When the "local" AF interaction between a metal atom and a sulfur atom is supposed from the McConnell's model, the total interaction becomes ferromagnetic as shown in Fig. 5.21.

After all, the ferromagnetic interaction is due to the suppression of the AF interaction (small overlaps between SOMOs) and ferromagnetic interaction (McConnell's model), which are caused by the strong attractive interaction between a donor and an anion molecules thanks to the iodine atom of the donor.

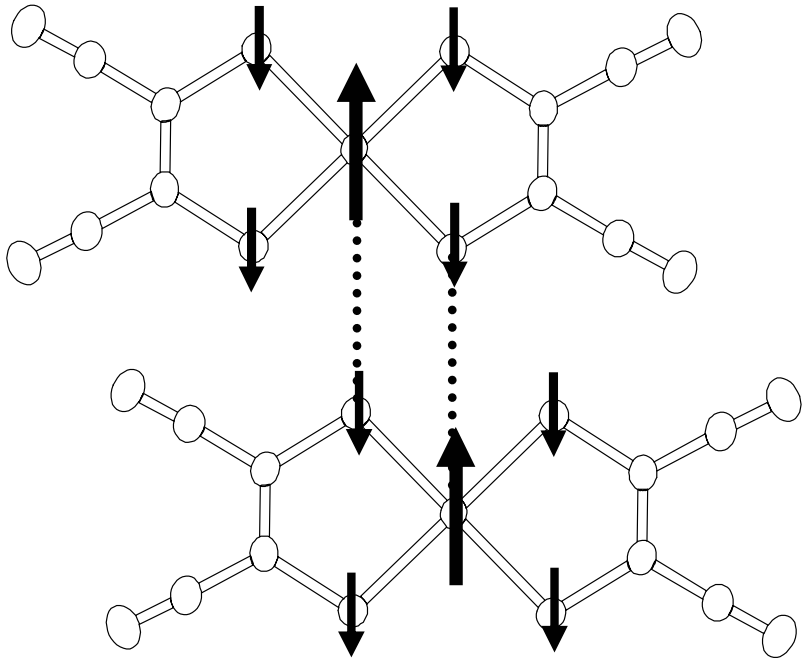

Fig. 5.21. Schematic drawing of the ferromagnetic interaction based on the McConnell's theory. The long arrows at the central metal atoms and short arrows at the sulfur atoms represent the magnetic spin of SOMOs and induced spin density of HOMOs, respectively.

5.8.2 Hysteresis loop of the magnetization curve

The temperature range where the hysteresis is observed is roughly same as that of frequency dependence of AC susceptibility is observed. Consequently, it is natural to regard the dynamics of the spins as relating the origin of the hysteresis.

Below T_{N}, the spins are ordered ferromagnetically in anion chains, as shown in Fig. 5.22a. When the strong magnetic field $H \gg H_{\mathrm{c}}$ is applied along the easy axis, all magnetic spins aligned parallely (Fig. 5.22b). Then, the magnetic field is weakened below H_{c}, the AF domains grow due to the inter-chain AF interaction, and domain walls are formed between the AF domains. The domain walls contribute to the additional magnetization as observed.

The existence of the hysteresis loop is depends on the velocity of the domain walls which is related to the relaxation time of the spins which is estimated from the AC susceptibility. If the domain walls can move easily, a domain wall bump against another domain wall resulting in the disappearance of these two domain walls. Therefore, it is necessary to the hysteresis that the motion of the spins is "frozen", as observed in AC susceptibility below ca. 3.5 K where AC susceptibility χ shows conspicuous frequency dependence. Consequently, The good agreement with the two temperatures, the hysteresis of magnetization existing and frequency dependency of χ' existing, evidences the model of the hysteresis loop mentioned above.

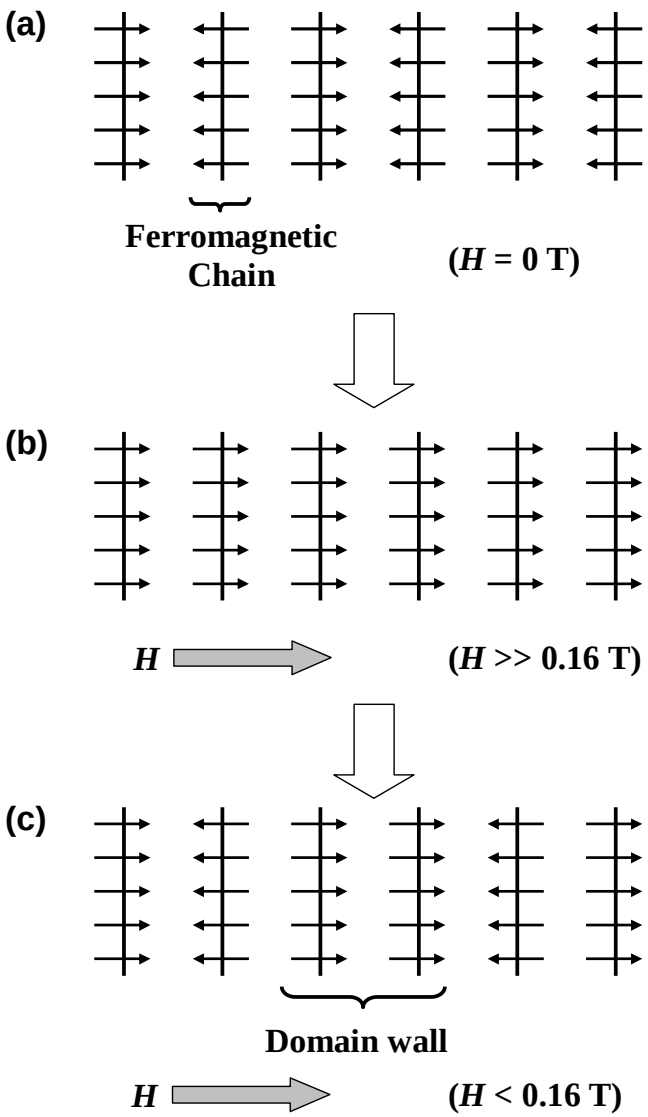

Fig. 5.22. The schematic model of the hysteresis below T_{N}. Arrows and solid lines represent spins of anions and anion chains, respectively. **(a)** The spin are aligned ferromagnetically and antiferromagnetically in intra- and inter-chain, respectively. **(b)** When the external field $H \gg H_{\mathrm{c}} = 0.16$ T is applied, all magnetic moments are aligned parallely. **(c)** Then the field is reduced below H_{c}, the AF regions grow and domain walls showing an additional magnetization are formed.

5.9 Summary

(EDO-$TTFI_2$)$_2$[M(mnt)$_2$] (M = Ni, Pt) consists of 1D metallic donor column and magnetic anion column. The resistivity shows a MI transition doe to the strong 1D character of the donor column, and T_{MI} becomes lowered by applying the high pressure although the transition does not disappear.

The attractive interaction between donor and anion molecules shorten the sulfur-sulfur contact between donor and anion molecules. The existence of the π-d interaction through the contact is evidenced from the EPR spectrum.

On the other hand, the attractive interaction disturbs the orbital overlap between the SOMOs of the anions, resulting in the strong ferromagnetic intra-chain interaction J = 18 and 20 K for M = Ni and Pt, respectively. In the case of [Pt(mnt)$_2$]$^-$ salt, Ising character of the spin enhances the effect of the inter-chain AF dipole-dipole interaction, resulting in the bringing about the AF transition, while the [Ni(mnt)$_2$]$^-$ salt shows no long range ordering down to 2 K owing to the Heisenberg character of the spin.

Below 3.5 K, a hysteresis is observed in the magnetization curve owing to the existence of the domain walls. The dynamics of the domain walls are governed by the strong intra-chain ferromagnetic interaction as pointed out by the Glauber, and the dynamics is confirmed by the AC susceptibility measurement where the large frequency dependence is observed below 3.5 K.

In conclusion, the salts (EDO-$TTFI_2$)$_2$[M(mnt)$_2$] (M = Ni, Pt) are the one of the first examples of the organic conductors in which the metallic conductivity of donors coexists with the ferromagnetic interaction between anions. In addition, the results reveals that the usefulness of the orientation-controlling group, like iodo group of EDO-$TTFI_2$, to construct the novel electron system.

References

[1] R. C. Wheland and J. L. Gillson, *J. Am. Chem. Soc.* **98**, 3916 (1976).

[2] M. G. Miles and J. D. Wilson, *Inorg. Chem.* **14**, 2357(1975).

[3] V. Gama, R. T. Henrique, G. Bonfait, L. C. Pereira, J. C. Waerenborgh, I. C. Santos, M. T. Duarte, J. M. P. Cabral and M. Almeida, *Inorg. Chem.*, **31**, 2598 (1992).

[4] M. Uruichi, K. Yakushi, Y. Yamashita and J. Qin, *J. Mater. Chem.*, **8**, 141 (1998).

[5] A. T. Coomber, D. Beljonne, R. H. Friend, J. L. Br das, A. Charlton, N. Robertson, A. E. Underhill, M. Kurmoo and P. Day, *Nature*, **380**, 144 (1996).

[6] G. Ch. Baker, G. S. Rushbrooke and H. E. Gilbert, *Phys. Rev. A* **135**, 1272 (1964).

[7] E. Ising, *Zeits. Physik.*, **31**, 253 (1925).

[8] R. J. Glauber, *J. Math. Physics*, **4**, 294 (1963).

[9] A. Caneschi, D. Gatteschi, N. Lalioti, C. Sangregorio, R. Sessoli, G. Venturi, A. Vindigni, A. Rettori, M. G. Pini and M. A. Novak, *Angew. Chem. Int. Ed. Engl.* **40**, 1760 (2001).

[10] A. Caneschi, D. Gatteschi, N. Lalioti, C. Sangregorio and R. Sessoli, *J. Chem. Soc. Dalton Trans.*, 3907 (2000).

[11] R. Cl rac, H. Miyasaka, M. Yamashita and C. Coulon, *J. Am. Chem.Soc.*, **124**, 12837 (2002).

[12] A. Kamiyama, T. Noguchi, T. Kajiwara and T. Ito, *Inorg. Chem.*, **41**, 507 (2002),

[13] O. Kahn and B. Briat, *J. Chem. Soc. Faraday Trans.*, **72**, 268 and 1441 (1976).

[14] J.J. Girerd, Y. Journaux and O. Kahn, *Chem. Phys. Lett.*, **82**, 534 (1981).

[15] For example, see "Magnetism: Molecules to Materials" vol. II, eds. J. S. Miller and M. Drillon, *WILEY-VCH*, Weinheim, Germany.

[16] E. Ribera, C. Rovira, J. Veciana, J. Tarr s, E. Canadell, R. Rousseau, E. Molins, M. Mas, J-P. Schoeffel, J-P. Pouget, J. Morgado, R. T. Henriques and M. Almeida, *Chem. Eur. J.*, **5**, 2025 (1999).

[17] H.M. McConnell, *J. Chem. Phys.*, **39** 1910 (1963).

Chapter 6

Conclusion

In the areas of material sciences, many researches have focused on the "hybrid system, which consists of multi-subsystems as shown in Chapter 1. In the hybrid systems where the subsystems having different functions, the change of a property such as electronic, optical, magnetic or chemical property affects another properties, resulting in the system having unconventional properties which cannot be produced only by the individual subsystems. To achieve the hybrid systems, the chemical modification of the organic molecules is the promising way because that can control the intra- and inter-molecular interaction and inter-molecular arrangement. Then, to focus the electronic property of the organic materials, it is well known that the TTF-based organic molecules are superior electronic conductors, where the magnetic conductor, whose localized magnetic moments interact with conduction carriers, have been the one of the most actively investigated research topics (see, section 1.4.2). In the researches, most of the existing magnetic conductors are featured with hybrid system, which consists of magnetic and conductive subsystems. As the interaction between electronic and magnetic properties is weak in the existing magnetic organic conductor unfortunately, how to enhance the interaction is an important task for the guiding principle toward the future perspective. From this viewpoint, I have tried to establish the method for achieving a strong π-d interaction, where the two kinds of materials, halogenated-TTF and crown thioether complexes, are employed.

It is known that the halogenated-TTF donors show strong attractive interaction with a halogen atom or a cyano group of the anion owing to the coordination bond

like interaction (see, Chapter 3 and references therein). By using the halogenated-TTF donor and the anion having halogen atoms or cyano groups, it is expected that the attractive interaction shortens the donor-anion distance and strengthens the π-d interaction, though the halogenated-TTF donors have been employed for only achieving a high conductive organic materials [1–5]. As shown in the Chapter 3, using the brominated-TTF type donor EDT-TTFBr$_4$ with the anion $FeBr_4^-$ having bromine atoms gives a strong π-d interaction system (EDT-TTFBr$_2$)$_2$FeBr$_4$. In the salt, attractive donor-anion interaction between bromine atoms brings about a short donor-anion S-Br contact. The conductive π-electrons can be transferred through the open shell of the d-orbitals of the anion, resulting in the three dimensional character of the electronic system and the low MI transition temperature $T_{MI} = 20$ K, while the closed shell anion analogue (EDT-TTFBr$_2$)$_2$GaBr$_4$ undergoes the MI transition at higher temperature $T_{MI} = 70$ K. The effect of the π-d interaction becomes clear in the insulating state of the π-electron, where the antiferromagnetic interaction of the d-electrons suddenly increases. In addition, the magnetic potential of the anions affects the π-electrons, resulting in the large negative magnetoresistance observed below T_N of the d-electrons, while the non-magnetic anion analogue the $GaBr_4^-$ salt shows only a small positive magnetoresistance. The strength of the π-d interaction estimated as -44.5 K from the magnetization curve is remarkably stronger than that of other π-d systems thanks to the attractive interaction between donors and anions.

In addition, the attractive interaction is useful not only for achieving a short donor-anion contact but also for constructing a novel electronic system of anions. In the magnetic conductor (EDO-TTFI$_2$)$_2$[M(mnt)$_2$] (M = Ni, Pt), the attractive interaction between iodine atoms of donor molecules and cyano groups of anions disturbs the stacking of the anion molecules, resulting in the pseudo-orthogonal overlap between SOMOs of the anions. As a result of the pseudo-orthogonality, a strong ferromagnetic interaction is produced between anion molecules, while the donor chains shows a metallic conductivity; that is, (EDO-TTFI$_2$)$_2$[M(mnt)$_2$] is the first example of the organic metal with strong ferromagnetic interaction of magnetic anions.

The results of the organic metals including both halogenated-TTF donor and

magnetic anion is the certain proof that the introducing a structure-controlling group is the powerful method to achieve a strong π-d interaction and novel electronic structure.

On the other hand, using crown thioether complexes of a transition metal does not shorten the distance between π and d-electron systems but enhances the spin density at the ligands thanks to the strong π-acidity [6, 7]. Indeed, the d-d interaction in the salts discussed in Chapter 4 is more than 10 K in spite of longer inter-molecular distances than the sum of the van der Waals radii. Such strong inter-molecular interaction is appropriate for achieving both molecule-based magnets and magnetic conductors having strong π-d interaction.

Based on the results mentioned above, I concluded that the chemical design of the molecules, such as introducing a structure-controlling-groups and controlling a spin density, is a promising way to achieve a strong inter-molecular interaction and design a multi-functional materials. By using the chemically-designed molecules, we will be able to control the strength of the inter-molecular interaction and arrangement of the molecules, resulting in achieving intentional designing of the physical properties of the material.

Finally, I propose the future scope of my investigations. As shown in this thesis, the strong π-d interaction can be achieved by using a halogenated-TTF donors. However, the interaction of (EDT-TTFBr$_2$)$_2$FeBr$_4$ is a little weak to construct a molecule-based device working at room temperature. In (EDT-TTFBr$_2$)$_2$FeBr$_4$, the magnetic anions interact with the donor molecule at the sulfur atom of the outer six-membered ring of the donor molecule. However, the contribution of the sulfur atom to the HOMO is not so large in the molecule. This fact means that if the HOMO of the donor molecule is well expanded in the outer ring, the π-d interaction becomes stronger. For example, when we employ not an ethylenedithio but a vinylenedithio group, the HOMO of the donor molecule is expanded in outer ring as shown in Fig. 6.1. In the donor molecule VDT-TTFBr$_2$, the contribution of the sulfur atoms at the outer six-membered ring is significantly large, where it is expected that the π-d interaction of (VDT-TTFBr$_2$)$_2$FeBr$_4$ is greatly stronger than that of (EDT-TTFBr$_2$)$_2$FeBr$_4$. To synthesize this kind of donor molecules is a way to achieve stronger π-d interaction.

On the other hand, the strong π-d interaction is also expected by using the crown thioether complexes with large acceptor molecules such as [Ni(tmdt)$_2$] [8]. Regrettably, [Ni(9S3)$_2$](TCNQ)$_3$ is a semiconductor as shown in this thesis, but the result clues to achieve an organic metal including the crown thioether complex; that is, using large acceptors is recommended because the large acceptor is insensitive to the crown thioether complex disturbing the stacking of the acceptor.

Furthermore, there is another promising way to achieve strong π-d interaction based on the crown thioether complexes; that is, the crown thioether ring is introduced to the TTF-type donor. There are several trials to enhance the interaction between conductive electrons and localized magnetic moments by using a donor molecule containing organic-radical part as a localized magnetic moments. In this case, the distance between conductive and magnetic electrons is remarkably short because both electrons are in the same molecule. For examples, the donor molecules including nitronyl nitroxide radical [9, 10] or proxyl radical [11] was synthesized, where radical spin and donor spin are strongly interacted to each other. However, generally speaking, organic radicals are unstable and the spin is small (usually, $S = 1/2$). In contrary to the ordinary organic radicals, transition metal ions are stable even in air and have a larger magnetic moment. Therefore, it seems to be a promising way to enhance π-d interaction by introducing functional groups, which work as ligand of transition metals, into the TTF-frame. The distance between conductive donor and transition metal is remarkably short in such "ligand-donor", resulting in the strong π-d interaction. Fundamental researches of this type donors have been started [12, 13], and some of them are successfully in obtaining coordination bond with transition metal cations. Especially, considering the strong π-acidity of the crown thioether, the crown thioether ring is a strong candidate for a ligand part of such hybrid-donor molecule. The TTF-crown thioether hybrid type donor molecule is, to the best of my knowledge, not synthesized yet except its precursor shown in Fig. 6.2. If we can construct the conductive organic materials with TTF-crown thioether hybrid donor, the strong π-d interaction is promised.

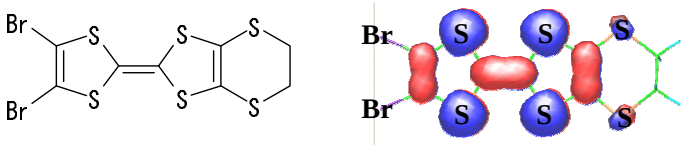

EDT-TTFBr$_2$

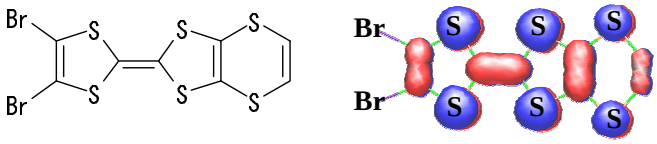

VDT-TTFBr$_2$

Fig. 6.1. The molecular structures of EDT-TTFBr$_2$ and VDT-TTFBr$_2$, and HOMOs calculated based on PM3 [15].

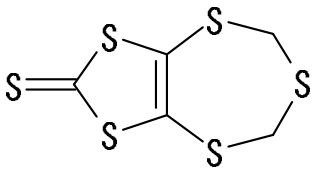

Fig. 6.2. The molecular structure of 2,5,8,10,12-pentathiabicyclo[7.3.0]dodec-1(9)-en-11-thion [14].

References

[1] T. Imakubo, H. Sawa and R. Kato, *J. Chem. Soc., Chem. Commun.*, 1097 and 1667 (1995).

[2] R. Gompper, J. Hock, K. Ploborn, E. Dormann and H. Winter, *Adv. Mater.*, **7**, 41 (1995).

[3] M. Iyoda, Y. Kuwatani, K. Hara, E. Ogura, H. Suzuki, H. Ito and T. Mori, *Chem. Lett.*, 599 (1997).

[4] M. Iyoda, Y. Kuwatani, E. Ogura, K. Hara, H. Suzuki, T. Takano, K. Takeda, J.-I. Takano, K. Ugawa, M. Yoshida, H. Matsuyama, H. Nishikawa, I. Ikemoto, T. Kato, N. Yoneyama, J. Nishijo A. Miyazaki and T. Enoki, *Heterocycles*, **54**, 833 (2001).

[5] T. Imakubo, N. Tajima, M. Tamura, R. Kato, Y. Nishio, and K. Kajita, *J. Mater. Chem.*, **12**, 159 (2002).

[6] J. R. Hartman and S. R. Cooper, *J. Am. Chem. Soc.*, **108**, 1202 (1986).

[7] N. Gallego-Planas and M. A. Whitehead, *J. Mol. Struc.; Theochem,* **428**, 67 (1998)

[8] H. Tanaka, Y. Okano, H. Kobayashi, W. Suzuki and A. Kobayashi, *Science*, **291**, 285 (2001).

[9] H. Sakurai, A. Izuoka and T. Sugawara, *J. Am. Chem. Soc.*, **122**, 9723 (2000).

[10] J. Nakazaki, Y. Ishikawa, A. Izuoka, T. Sugawara and Y. Kawada, *Chem. Phys. Lett.* **319**, 385 (2000).

[11] H. Fujiwara, H.-J. Lee, H. Kobayashi, E. Fujiwara, and A. Kobayashi, *Chem. Lett.*, **32**, 482 (2003).

[12] F. Iwahori, S. Golhen, L. Ouahab, R. Carlier, J-P. Sutter, *Inorg. Chem.*, textbf40, 6541 (2001).

[13] S-X. Liu, S. Dolder, M. Pilkington, S. Decurtins, *J. Org. Chem.*, **67**, 3160 (2002).

[14] M. Wagner, *J. Prakt. Chem.*, **336**, 177 (1994).

[15] J. J. P. Stewart, *J. Comput. Chem.*, **10**, 209 (1989).